Novel infrared and Raman spectroscopic imaging for the elucidation of specific changes in breast microcalcifications

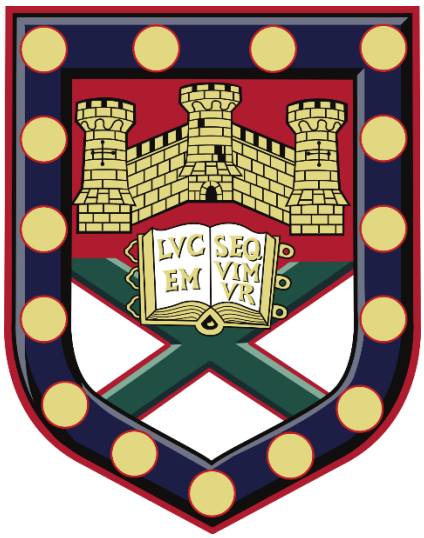

Submitted by

Pascaline BOUZY

to the University of Exeter

as a thesis for the degree of

Doctor of Philosophy in Physics

I certify that all material in this thesis which is not my own work has been identified and that no material has previously been submitted and approved for the award of a degree by this or any other University.

Pascaline BOUZY

April 2020

Abstract

Breast cancer is the second most common cause of death from cancer in women, accounting for more than 1 million deaths globally per year. Current detection is based on X-ray mammographic screening, which involves the use of ionising radiation with potentially detrimental effects, or MRI scans, which have limited spatial resolution. The presence of microcalcifications in breast tissue has been associated with malignant disease. Unfortunately, X-ray mammography and MRI scanning techniques are not able to discriminate between microcalcifications from a benign lesion and those from a malignant lesion.

The aim of this project was to use optical techniques based on vibrational spectroscopy, such as Fourier Transform Infrared (FTIR) absorption and Raman scattering, which are non-destructive, label-free and chemically specific, to investigate the composition of microcalcifications in breast tissue for augmented diagnostics and improved outcome for the patient.

This work involved the characterisation of mineral standards of the type that can be found in the breast, in order to identify the precise composition of the microcalcifications. A series of calcium hydroxyapatite (Hap) compounds was used for calibration of the micro-FTIR and Raman spectra. The ratio of carbonate-to-phosphate band intensity for each individual Hap powder was determined and the data were used to assess the level of carbonate substitution in each breast tissue biopsy. In parallel, the analysis of potential precursor mineral phases (namely octacalcium phosphate and amorphous calcium phosphate) revealed similar features to Hap in both FTIR and Raman spectra, which can be translated to the biopsy samples.

The accessibility to diverse panels of breast tissue sections (frozen and paraffin-embedded) was a great opportunity to test different approaches. A deparaffinisation protocol was applied to a set of samples for Raman analysis and the process was found not to affect the microcalcification composition. The FTIR analysis of the frozen tissues provided information on the carbonate peak in the short wavelength range

(1500-1400 cm^{-1}), which normally contains a strong contribution from paraffin in standard histological specimens. The study of breast tissue sections showed the heterogeneity in composition of microcalcifications between different samples from the same stage of pathology in terms of protein, lipid - which is usually not observed in formalin-fixed paraffin-preserved (FFPE) sections - and carbonate content.

The mineralisation of the MDA-MB-231 breast cell line induced by two osteogenic agents: inorganic phosphate (Pi) and β-Glycerophosphate (βG) was investigated using Raman micro-spectroscopy. The uptake of osteogenic agent induced a faster mineralisation for cells cultured with a medium supplemented in Pi (day 3) than βG (day 11). A shift (± 3 cm^{-1}) of the phosphate peak at 956 cm^{-1} in the Raman spectra was apparent when the culture medium was supplemented with βG, indicating the presence of precursor phase (octacalcium phosphate) during Hap crystal formation.

New IR technologies such as bright laser sources e.g. quantum cascade laser (QCL) open possibilities for the analysis of biological samples. They allowed us to achieve a better signal-to-noise ratio than Globar thermal sources used in traditional FTIR systems, particularly on optically dense samples such as calcifications. The ability of selecting specific incident wavelengths allows significant improvements in the acquisition time. This work illustrates for the first time the identification of microcalcifications using a QCL source in the long wavelength range coupled to an upconversion system with a silicon detector for efficient sensing. The upconverted images showed a good agreement with the micro-FTIR images.

Vibrational spectroscopy has been shown to be a powerful tool for discrimination of mineral species in breast calcification. These techniques can provide complementary information for the pathologist to be able to classify breast pathologies - benign, ductal carcinoma *in situ* (DCIS) and invasive cancer - with higher accuracy.

Acknowledgments

This thesis was conducted as part of the Mid-TECH project with the generous support from the European Union Horizon 2020 Research and Innovation programme under the Grant Agreement No. 642661.

I would like to thank my supervisors Prof. Nick Stone and Prof. Francesca Palombo for their support. Nick, I can tell you how grateful I am for the opportunity that you gave me to be part of this adventure. Your passion for research has no limit and gave me the energy to be fully involved in this project. Thank you for always helping me and believing in me when I am lost. Francesca, you are fantastic. I am really grateful to have you as supervisor. You always have the patience and the kindness to guide me. Your door is always open when I need you. Thank you so much for everything.

I would also like to thank Dr Maria Morgan, my third supervisor at the Royal College of Surgeons in Ireland, for being involved in this study, to take time to meet me and to give me a lot of advice. Thanks to Dr Shane O'Grady, who helped me with the cell study and for training me in tissue culture.

I would like to thank all the partners involved in the Mid-TECH project, especially Prof. Peter Tidemand-Lichtenberg from DTU, for your patience when you taught me the basics of coherent light sources. All the PhD students involved in the programme, especially Yu-Pei for all the nights we spent in the lab to get some coherent results.

A big thanks to the BioSpec team for their support: Ben, thank you for your help with everything, in the lab or Matlab when I was lost, Rikke, always kind and ready to help me and also Krups, Alex, Suzy, Priyanka, Michelle, Adrian, Tanveer, Jenni, Hannah, and Doriana, I appreciated your help when preparing the samples and collecting the FTIR data for the study with DTU.

I would like to thank Dave, the best one, without you the Physics building cannot hold, but also Ellen, always kind and with a lot of advice, and the rest of Biophysics people.

A little thought to my family, especially my grandmother that I lost after a long battle with breast cancer.

Enfin, à toi Simon, mon époux, je te dédie cette thèse. Sans ton soutien constant dans ma vie et mes projets, je n’aurais pas pu achever un tel travail. Je te dis simplement merci. Je ne remercierai jamais assez le destin d’avoir fait nos chemins se croiser.

Table of contents

List of figures

List of tables

List of appendices

Abbreviations

AA	Ascorbic acid
ACP	Amorphous calcium phosphate
ACR	American College of Radiology
$AgGaS_2$	Silver gallium sulphide
AJCC	American Joint Committee on Cancer
Al	Aluminium
ALP	Alkaline phosphatase
AR	Alizarin red staining
ATR	Attenuated total reflection
βG	β-glycerophosphate
β-TCMP	Magnesium-substituted tricalcium phosphate
β-TCP	β-tricalcium phosphate
BaF_2	Barium fluoride
BI-RADS	Breast imaging reporting and data system
BMP-2	Bone morphogenetic protein 2
BRCA 1, 2	Breast cancer 1 and 2 genes
CaF_2	Calcium fluoride
CCD	Charge coupled device
COD	Calcium oxalate dihydrate
C:P ratio	Carbonate-to-phosphate ratio
DCIS	Ductal carcinoma *in situ*
DCPD	Dicalcium phosphate dihydrate
Dex	Dexamethasone
DMEM	Dulbecco's modified Eagle medium
DNA	Deoxyribonucleic acid
DTU	Technical University of Denmark
ECM	Extracellular matrix
EMSC	Extended multiplicative signal correction
EMT	Epithelial mesenchymal transition
ER	Oestrogen receptor
ETD	Extralobular terminal duct

FBS	Foetal bovine serum
FFPP	Formalin-fixed paraffin-preserved
FPA-MCT	Focal plane array - mercury cadmium telluride
FTIR	Fourier transform infrared
FWHM	Full width at half maximum
H&E	Haematoxylin and eosin
Hap	Hydroxyapatite
HER2	Human epidermal growth factor receptor 2
HRT	Hormonal replacement therapy
IARC	International Agency for Research on Cancer
IDC	Invasive ductal carcinoma
IHC	Immunohistochemistry
IR	Infrared
ITD	Intralobular terminal duct
KBr	Potassium bromide
LCIS	Lobular carcinoma *in situ*
LWIR	Long wavelength infrared
Mg	Magnesium
MMP	Matrix metalloproteinase
MRI	Magnetic resonance imaging
MVs	Matrix vesicles
Na	Sodium
NHS	National Health Service
NIR	Near infrared
OC	Osteogenic cocktail
OCP	Octacalcium phosphate
O-PTIR	Optical photothermal infrared
PBS	Phosphate buffered saline
PCA	Principal component analysis
PCs	Principal components
Pi	Inorganic phosphate
PLS	Partial least square
PPi	Inorganic pyrophosphate
PR	Progesterone receptor

QCL	Quantum cascade laser
RCSI	Royal College of Surgeons in Ireland
SC	Supercontinuum
SHG	Second harmonic generation
SNR	Signal-to-noise ratio
TMA	Tissue microarray
TNM	Tumour node metastasis
TP53	Tumour protein 53
WLE	Wide local excision
XRD	X-ray diffraction

Chapter 1 : Introduction

1.1. Generalities

1.1.1. Anatomy of the breast

Breasts or mammary glands are part of the female reproductive system. In women, two mammary glands are developed during puberty with the secretion of oestrogen and progesterone hormones. The size varies from 30 to 1000g, depending on the individual's lifestyle. In contrast, men do not have a mammary gland as developed as women but a rudimentary form, composed mainly of collagen and adipose tissue [1].
From an anatomical point of view, the breast extends on the anterior chest wall and the pectoralis major muscle. In the horizontal axis, its projection lies from the second to the sixth rib. The suspensory ligaments or Cooper's ligaments stretch over the skin to the pectoralis fascia providing support and mobility of the breast [1] (Figure 1.1a).
The breast is well-vascularised by many arteries and veins, which transport oxygen and nutrients to the tissue. The essential blood supply of breast is the internal thoracic artery and its different branches [2] (Figure 1.1b). The breast is also well-drained via the lymphatic system formed by different lymphatic vessels and lymph nodes describing a circle around the nipple (Figure 1.1c). Their function, for instance, consists of draining tissues from dissolved substances (e.g. plasma proteins), and their involvement in the immune response consists of producing and maturing immune cells (e.g. lymphocyte and white blood cells) [3].
Unfortunately, if these systems (vascular and lymphatic) allow connecting mammary glands with the rest of the body, cancer cells could also use them to spread and colonise other sites (e.g. brain, lungs).

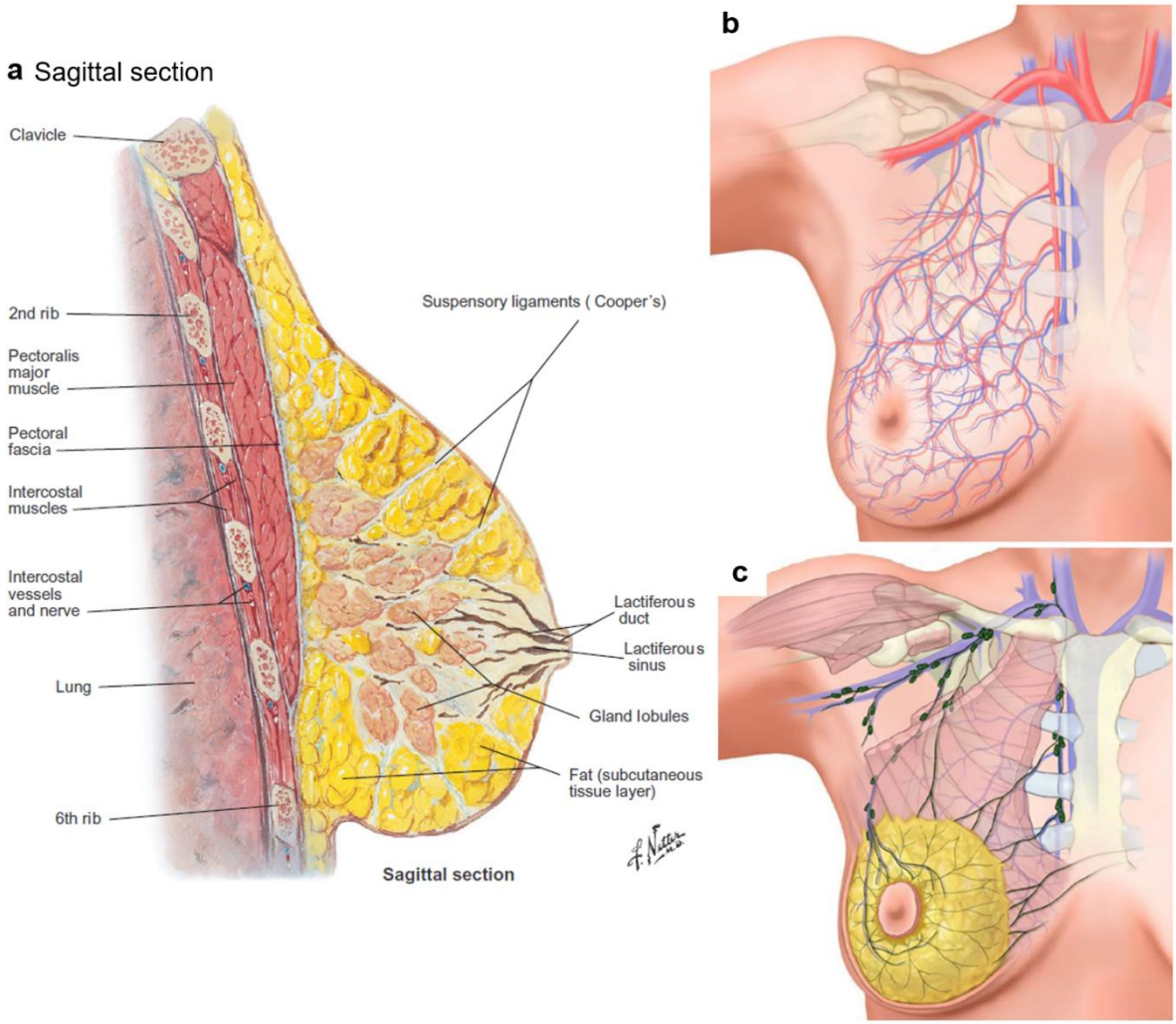

Figure 1.1 Anatomy of a female breast. (a) Sagittal section. (b) Blood supply with arteries and veins. (c) Lymphatic system with lymph nodes. Figure adapted from [2], [4].

1.1.2. Histology and physiology of the breast

As illustrated in Figure 1.1a, the breast is composed of adipose and fibrous (stroma) tissues surrounded by 15 to 20 lobes, corresponding to a glandular tissue. During lactation, the milk is drained via these lobes by lactiferous ducts through the nipple [4]. Each lobe is composed of 20-40 lobules. A lobule is made of around 10 to 100 acini that open into an intralobular terminal duct (ITD), which continues into an extralobular terminal duct (ETD) (Figure 1.2a and b), the lactiferous duct and the nipple. The size of lobules and the number of acini are different for each individual and vary according to the age and individual lifestyle (e.g. pregnancy, lactation) [1]. The activity and the growth of mammary glands depend on many hormones. For instance, oestrogen

stimulates the growth and multiplication of ducts, while progesterone increases the size of the glandular tissue (lobules and acini) [5]. As a woman gets older, her lobes and ducts tend to decrease and be replaced by connective and adipose tissues [2].

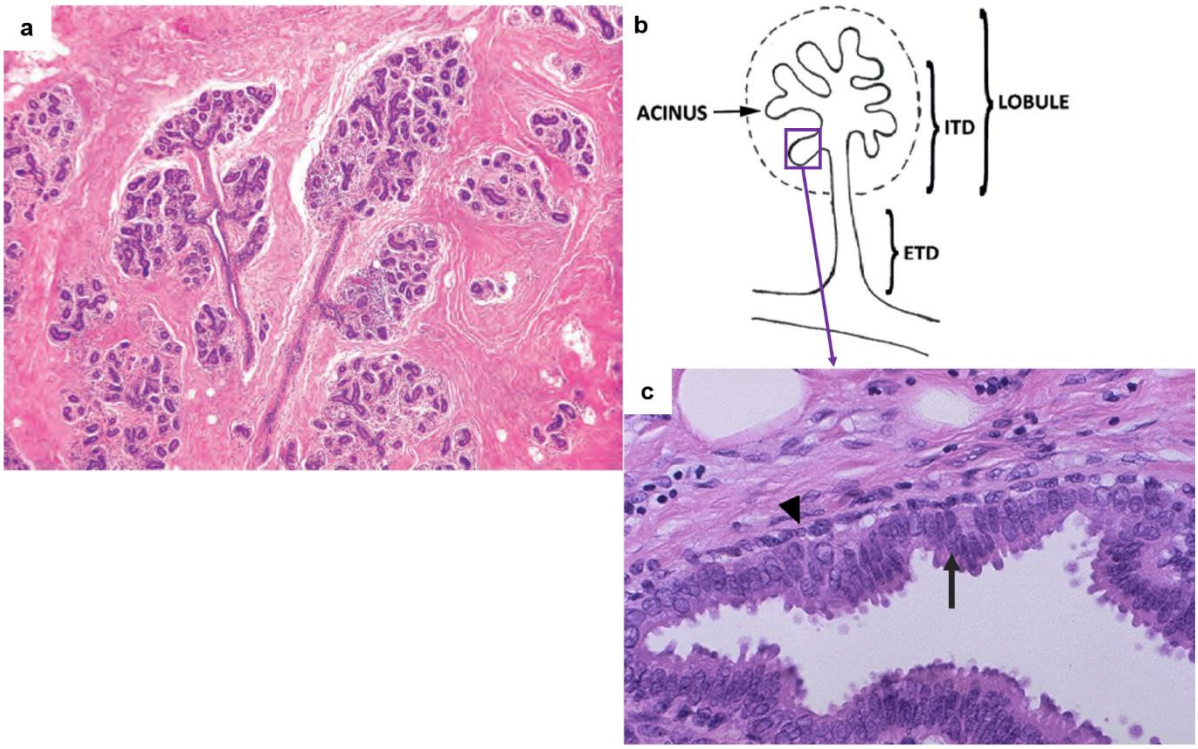

Figure 1.2 Normal breast tissue section stained with Haematoxylin and Eosin (H&E). (a) Portion comprising lobules composed of acini and the intralobular terminal duct (ITD) leading to the extralobular terminal duct (ETD). (b) Diagram of a mammary gland unit showing an acinus, the ITD and the ETD. (c) Illustration of an acinus (x100 magnification) with a layer of myoepithelial cells (black arrowhead). In the lumen, layer of epithelial cells (black arrow). Figure adapted from [1], [2], [4].

In general, two primary cell types line ducts and lobules: a basal layer of myoepithelial cells (stellate shape) and luminal epithelial cells, as shown in Figure 1.2c. However, the shape of the cells appears different depending on their location within the breast. For instance, the major ducts (e.g. lactiferous ducts) are lined by tall columnar cells, whereas the smaller terminal ducts are lined by cuboidal cells [4].

The childbirth produces different hormones allowing the activation of these cells. For example, prolactin stimulates secretion of milk proteins via the lobular epithelial cells, and oxytocin induces the contraction of the myoepithelial cells for the milk during lactation [2]. Besides, other cells are found in the breast (especially in the stroma) including fibroblasts, inflammatory cells, immune cells (namely macrophages) or microvessels, which have important functions for the breast [4].

1.2. Breast cancer

1.2.1. Epidemiology

In 2018, the International Agency for Research on Cancer (IARC) estimated that breast cancer is the fifth most common cause of death from cancer in the world with 627,000 deaths. In women, it is the most commonly diagnosed cancer, with 2.1 million new cancer cases worldwide per year followed by lung cancer (Figure 1.3). Among all new cases of cancer diagnosed in women, 30% is for breast cancer [6]. In the UK, in 2016, the death rate was estimated around 11,500 in women, and around 80 for men and the number of new cases of female breast cancer was around 54,000. Overall it is the second most common cause of death from cancer after lung cancer [7].

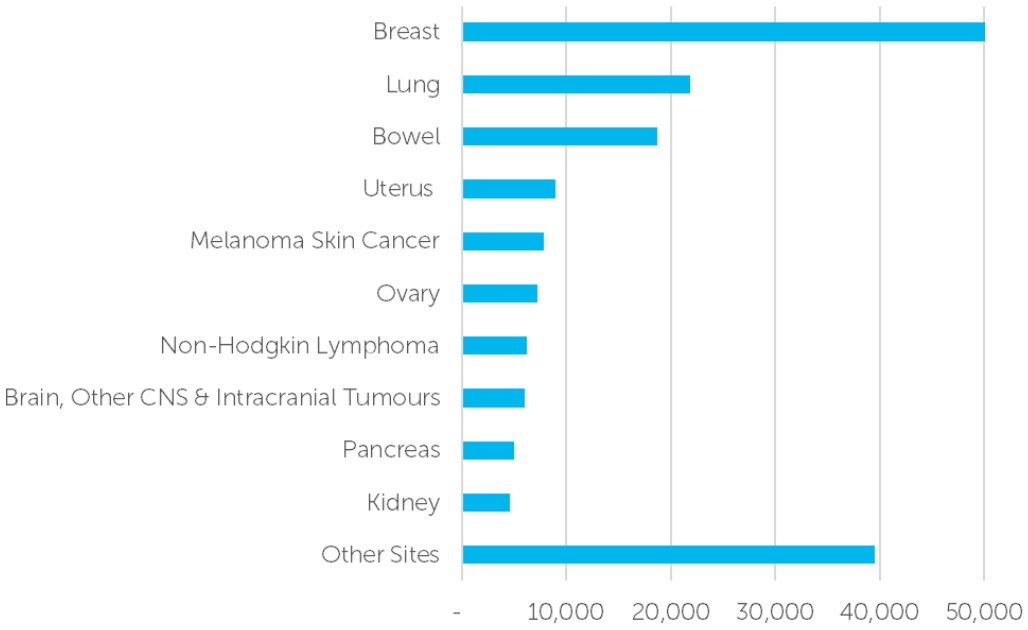

Figure 1.3 Ten most common causes of cancer for women associated with their number of new cases in 2016 [7].

Survival rates tend to increase over a few decades, mainly due to changes in detection practice by screening population more often and earlier [6]. As illustrated in Figure 1.4, early diagnosis is essential for the patient to have a better response to treatment. In fact, the survival rate in UK is close to 100% when cancer is detected at stages I, II and III compared to a patient with a stage IV with only 60% survival rate [7].

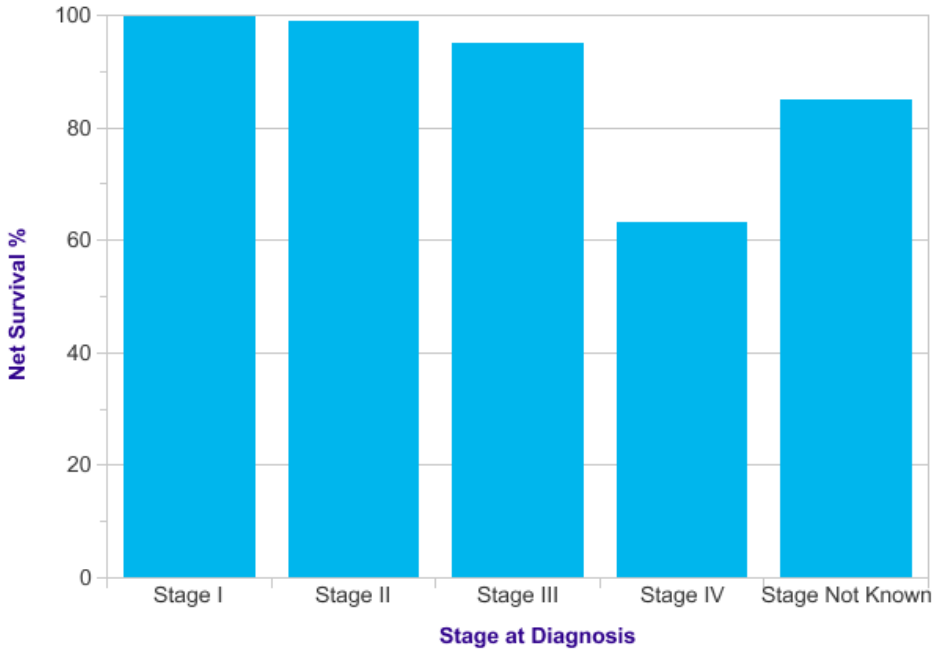

Figure 1.4 One-year survival rate according to the breast cancer stage in women (15 to 99 years) in 2016 [7].

Early diagnosis is important to improve the survival rate and treatment response, and in this context, microcalcifications (as described below) appear to be the unique early marker to detect breast cancer.

1.2.2. Breast cancer: Definition

Due to numerous factors, changes can appear in the breast. A cell from a normal breast epithelium may acquire specific abilities to form a primary tumour and colonise other sites in the body. As shown in Figure 1.5a, over time and under control of different factors, cells escape from the mammary duct by Epithelial-Mesenchymal Transition (EMT) process; they change their phenotype from epithelial to mesenchymal and express different proteins to induce cell migration. In the worst-case

scenario, some cells can migrate from their original site and colonise other organs (e.g. lungs, brain …) via lymph nodes or blood vessels; these are the so-called metastases. In fact, during the EMT, epithelial cells must infiltrate the extracellular matrix (ECM) through the basal membrane in order to penetrate the blood vessel (intravasation). Once inside of the blood vessel, cells exit through the membrane (extravasation) and can interact with the microenvironment (e.g. fibroblasts …) to form a new tumour site [8].

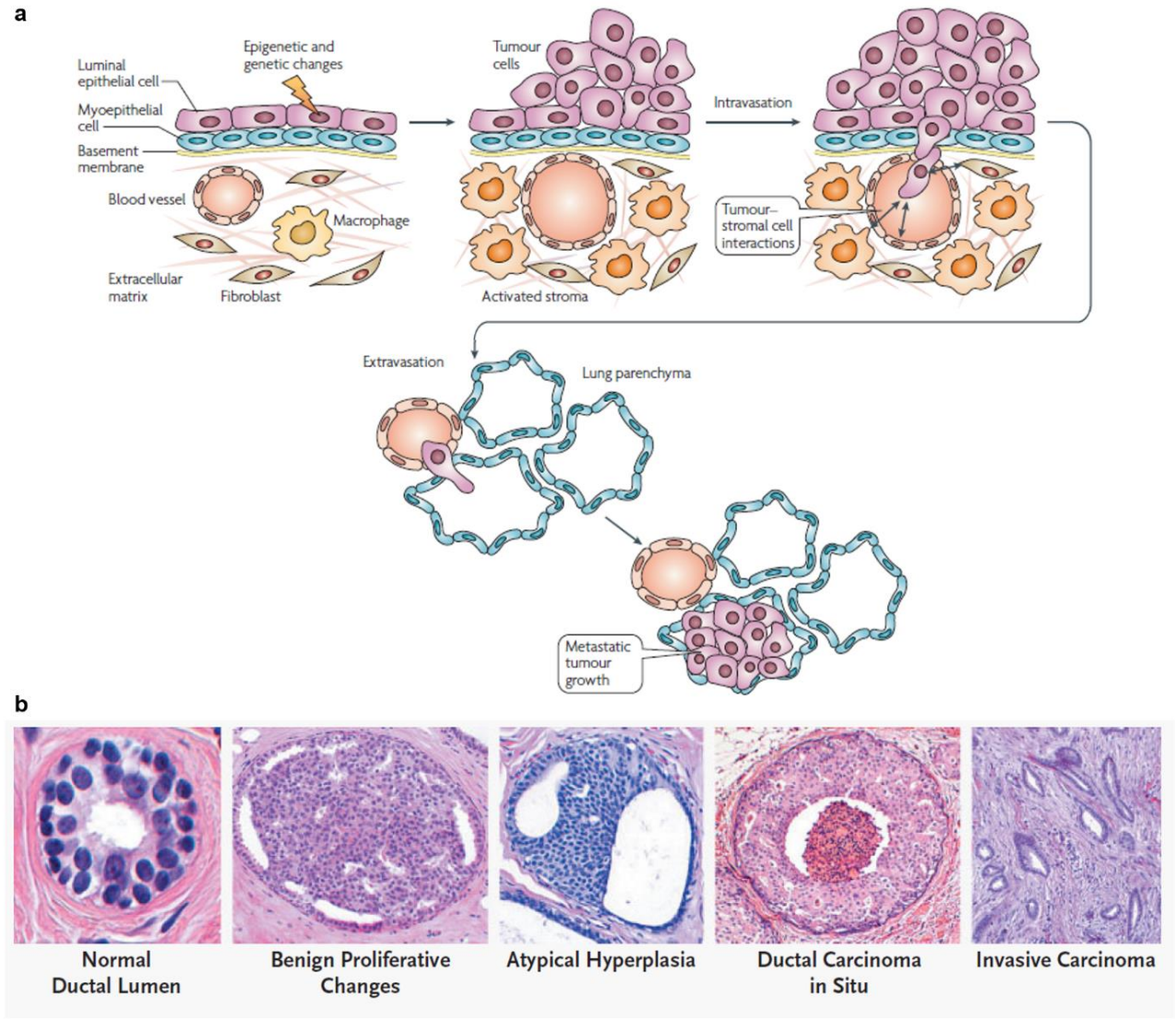

Figure 1.5 (a) Schematic representation of cancer progression in breast tissue. (b) Different intermediates of ductal carcinoma. Figure adapted from [9], [10].

Breast cancer is a heterogeneous disease, and its progression and outcome vary between individuals. This process is subject to changes in gene expression (e.g. loss of p53 function, overexpression of the oncogene HER2 …) [9] for modification of cell adhesion or cell motility or even invasion. To illustrate this heterogeneity in breast cancer, Figure 1.5b shows the cancer progression in mammary ducts. At the beginning, a normal ductal lumen contains cohesive epithelial cells (purple nucleus) but a group of these cells can increase their proliferation within the duct without any cancerous risk also called benign proliferative changes. The atypical hyperplasia, which is a premalignant lesion characterised by an abnormal proliferation of cells in healthy breast parenchyma, could lead to a ductal carcinoma *in situ* (DCIS) and eventually an invasive carcinoma. The risk of developing an invasive ductal cancer (IDC) increases for each stage of the disease, but for the pathologist, it is still challenging to discriminate which case will evolve into a malignant lesion [9].

1.2.3. Histological and molecular classification

In order to standardise the disease, to help clinicians and histopathologists but also to improve diagnosis and treatment, different classifications have been introduced. The morphological and histological appearance of breast tumours can be associated with the degree of malignancy of the lesions. Classifications can also be based on the molecular marker expression of tumour and the metastatic process.

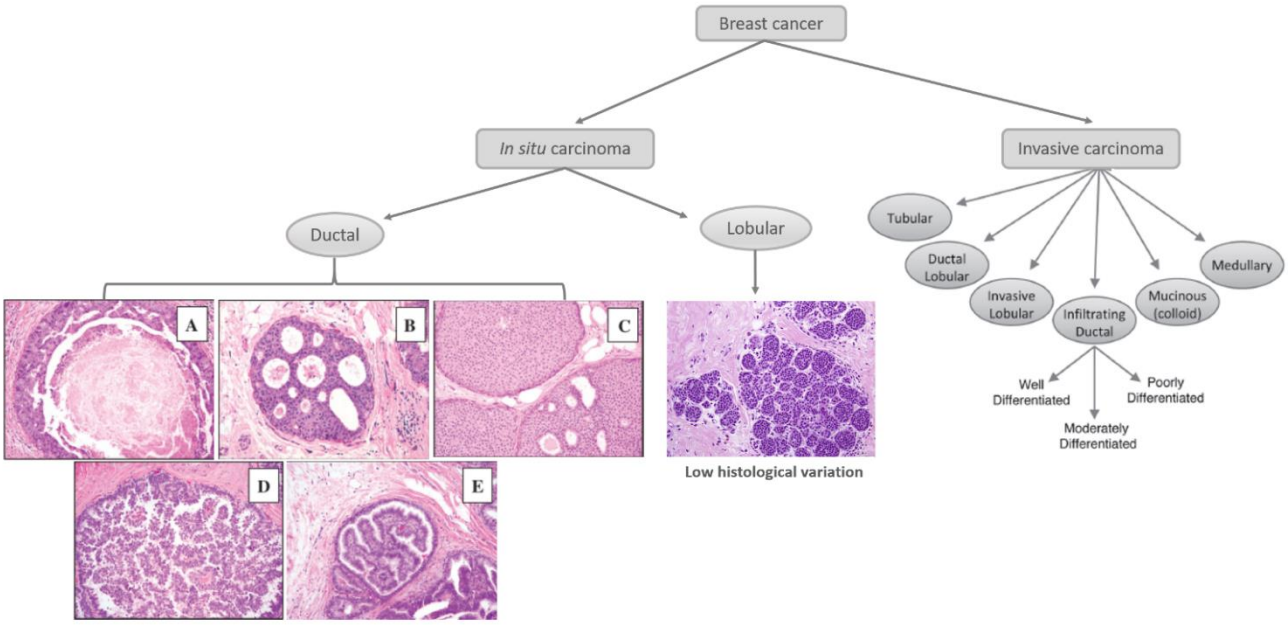

Figure 1.6 Classification of breast cancer subtypes. (H&E staining) A: Comedo, B: Cribiform, C: Solid, D: Micropapillary and E: Papillary. Figure adapted from [11]–[13].

As shown in Figure 1.6, breast cancer is divided into two main groups: carcinoma *in situ* and invasive carcinoma.

Firstly, carcinoma *in situ* is separated into two types according to the original site of the primary tumour. When the tumour takes place in ducts, it is called ductal carcinoma *in situ* (DCIS), whilst when it originates in the lobules, it is called lobular carcinoma *in situ* (LCIS) [11]. DCIS is the most common carcinoma in the breast with around 80-90% of all *in situ* carcinomas [12]. The DCIS group is more heterogeneous than LCIS with six subtypes based on histopathology characteristics: Comedo, Cribiform, Micropapillary, Papillary and Solid types [11].

Secondly, the invasive carcinoma group is also classified in six subtypes: tubular, ductal or lobular, invasive lobular, IDC (which is involved in 70-80% [12] of all invasive lesions), mucinous and medullary [11].

Elston and Ellis have also subclassified DCIS, LCIS and all invasive tumours in three grades [14]. A score reflects the differentiation and proliferation of tumour cells [12]:
- Grade 1: well-differentiated. Tumour cells appear normal and are not overgrowing.
- Grade 2: moderately differentiated. Cells appear slightly different than normal.
- Grade 3: poorly differentiated. Cells appear abnormal and tend to grow and spread more aggressively.

Clinicians can also stage breast cancer and guide the surgery using the Tumour Node Metastasis (TNM) staging system. This system, which is the “gold standard”, has been developed by the American Joint Committee on Cancer (AJCC) to standardise diagnostics, estimate prognosis and select an appropriate treatment for each individual. Three parameters are taken into account in this system: the size of the primary tumour (T), the involvement of the lymph node (N) and the spreading of cancer. (M) describes the presence of distant metastases, which colonise other organs. More details of this classification are presented in Table 1.1.

Table 1.1 TNM staging system adapted from [15].

(T) Primary tumour
Tx- Primary tumour cannot be assessed
T0- No evidence of primary tumour
Tis- Carcinoma *in situ* (DCIS, LCIS, Paget's disease)
T1- Tumour ≤ 2 cm
T1mic- Microinvasion ≤ 0.1 cm
T1a- Tumour 0.1-0.5 cm
T1b- Tumour 0.5-1 cm
T1c- Tumour 1-2 cm
T2- Tumour 2-5 cm
T3- Tumour > 5 cm
T4- Tumour of any size with direct extension to chest wall or skin
T4a- Extension to chest wall
T4b- Oedema or ulceration of the skin or satellite skin nodules
T4c- Extension to the chest wall and the skin
T4d- Inflammatory carcinoma
(N) Regional lymph Node
Nx- Regional lymph nodes cannot be assessed
N0- No regional lymph node metastasis
N1- Metastasis in axillary lymph nodes mobile
N2a- Metastasis in axillary lymph nodes fixed
N2b- Metastasis in internal mammary node but not in axillary lymph node
N3a- Metastasis in infraclavicular lymph node and axillary lymph node
N3b- Metastasis in internal mammary lymph node and axillary lymph node
N3c- Metastasis in supraclavicular lymph node
(M) Metastasis
Mx- Distant metastasis cannot be assessed
M0- No distant metastasis
M1- Distant metastasis

1.2.4. Biomarkers of breast tumour

All these classifications are not enough to have an adequate and successful treatment for each patient. The search for predictive biomarkers associated with breast cancer and expressed by tumour cells are necessary [9]. Amongst these biomarkers, the well-known and well-established are: oestrogen receptor (ER), progesterone receptor (PR) and Human Epidermal Growth Factor Receptor 2 (HER2) [11]. For instance, ER, which is the most important predictive marker in breast cancer [16], [17], is overexpressed (ER^+) by luminal epithelial cells in over 70% of DCIS cases [9]. In fact, its expression determines the patient response to hormone therapy. In the case of PR, its expression is often associated with ER expression [18]. Less than 1% of all cancers is ER^-/PR^+ [17]. HER2 is a proto-oncogene enabling cell growth and proliferation and overexpressed ($HER2^+$) by epithelial cells in 50% of DCIS lesions [9]. Slamon et al. suggested that the HER2 subtype is related to a poor prognosis for the patient [17], [19].

According to the expression of these biomarkers, breast cancer is divided in molecular subtypes. The predictive markers are evaluated by immunohistochemistry. Table 1.2 summarises the breast cancer molecular subtypes according to their immunohistochemistry status (IHC), the expression of their genes of proliferation (i.e. Ki67), histologic grade and prognostic. Six molecular subtypes were identified: luminal subtypes A and B, normal breast-like, HER2 enriched, basal-like and claudin-low [11], [18], [20], [21].

Table 1.2 Classification of molecular subtypes of breast cancer. IHC: Immunochemistry status. Adapted from [11], [18], [20], [21].

Molecular subtype	IHC status	Genes of proliferation	Histologic grade	Prognostic
Luminal A	ER^+ PR^+ $Her2^-$	Low	Low	Good
Luminal B	$ER^{+/-}$ $PR^{+/-}$ $Her2^-$	High	Intermediate/High	Intermediate or poor
Normal Breast-like	ER^+ PR^+ $Her2^-$	Low	Low	Intermediate
HER2 enriched	ER^- PR^- $Her2^+$	High	High	Poor
Basal-like	ER^- PR^- $Her2^-$	High	High	Poor
Claudin-low	ER^- PR^- $Her2^-$	High	High	Poor

The clinical tests of these biomarkers are important to evaluate the treatment and the outcome of the patient. For instance, the luminal subtype A and B of breast cancer have different outcomes. In fact, patients with luminal A subtype of breast cancer have a good prognosis while luminal subtype B is more aggressive, with a higher expression of gene proliferation [20]. The normal breast-like subtypes are not well characterised and represent 5 to 10% of all breast carcinomas [20]. The tumours with HER2 enriched subtype have a high proliferation level with a high histological grade [20]. In the case of a basal-like subtype (triple-negative), the prognostic is poor [11]. In this case, hormone therapy appears useless and requires surgery or chemotherapy. The claudin-low subtypes are identified by a low expression of genes responsible for tight junctions, the cohesion between cells. These tumours express genes involved in the EMT [20]. The tumours presenting this subtype have a high histologic grade and poor prognosis.

The heterogeneity of breast tumours tends to challenge the treatment. These biomarkers are considered as a reference and need to be identified to improve the patient outcome.

1.3. Risk factors

In 2012, it was estimated that around 10-12% of women worldwide would have breast cancer during their life. Many studies highlight the fact that the risk for developing breast cancer increases with genetic, lifestyle and hormonal factors.

1.3.1. Genetic factors

Family history is significant for breast screening. In fact, in those cases where there is a high-risk potential, a screening mammography every year is recommended. It has been estimated that family history is responsible for 27% of all breast cancer cases [22]. In 1866, Broca highlighted a correlation between breast cancer and inheritance [23].

Numerous genes are responsible for the development of breast cancer and they are classified in different categories according to their involvement in breast cancer. The most known genes are BRCA 1 and BRCA 2 (Breast Cancer 1 and 2) and are the

high-risk breast cancer susceptibility genes [23]. They are involved in 3-6% of all breast cancers [22]. These genes are considered as the “caretaker” of DNA because of their involvement in its repair process. A mutation in these genes could lead to cancer [23].

It has also been demonstrated that a combination of high breast tissue density observed by mammography with a nulliparity, increases by seven fold the risk to develop breast cancer [22]. These cases are considered as having a high-risk potential and need to be considered for breast screening. The breast density is classified according to the American College of Radiology Breast imaging reporting and data system (ACR BI-RADS) classification (Figure 1.7).

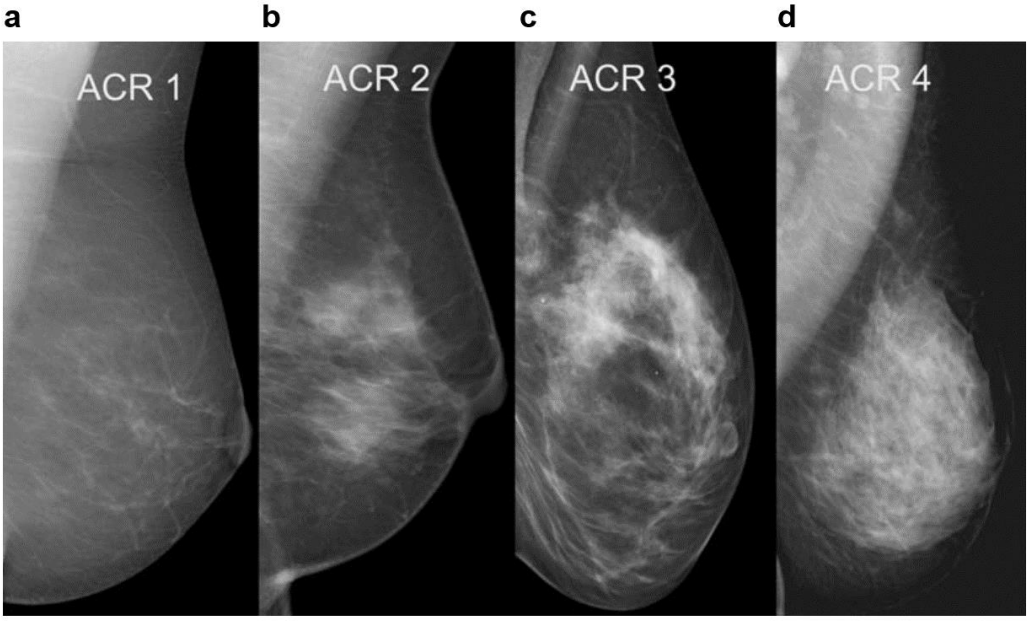

Figure 1.7 Mammograms showing different breast densities classified according to the American College of Radiology (ACR). (a) ACR 1: fatty tissue, (b) ACR 2: fibroglandular tissue, (c) ACR 3: heterogeneously dense and (d) ACR 4: extremely dense, [24].

Surprisingly, height could also be a factor for developing breast cancer. In fact, tall women (1.70 m) have a higher potential to develop cancer than smaller women (1.55 m) [22].

1.3.2. Lifestyle risk factors

Numerous factors could induce breast cancer. Among these factors, alcohol, smoking, obesity and fat diet. Physical activity can reduce the risk of breast cancer by 20% [23]. Furthermore, pregnancy after 35 years old increases the risk, whilst pregnancy before 29 years old decreases the risk [22]. Radiation exposure or pollution have been demonstrated to increase the risk of breast cancer in women [23].

1.3.3. Hormonal factors

Endogenous hormones (menstrual cycle) and exogenous hormones (Hormonal Replacement Therapy (HRT) and contraceptive pills), and in particular the oestrogens, play a role in breast cancer. A long exposure to this hormone has been identified to be a risk factor. In fact, the oestrogen receptors related to the hormonal activity are able to stimulate the cell proliferation increasing risks for developing breast cancer [23].

1.4. Microcalcifications

Microcalcifications consist of abnormal calcium deposits in the mammary gland and were described for the first time in 1951 by R. Leborgne. They are, at some point, a risk factor to develop a breast cancer. Microcalcifications have a small size (< 0.5 mm in diameter) and are evidenced in mammographic screening as tiny and clustered inclusions. When a breast tumour is not palpable, search for microcalcifications could be a predictive marker for breast cancer. In fact, it has been demonstrated that microcalcifications are correlated with breast cancer [25]. Tabar et al. have shown over 20 years, that a regular invitation for screening reduces by 30% the breast cancer mortality. A comparison has been made between a group of populations without invitation for screening and a group with a regular follow-up. The results demonstrated that mammography is a tool for an early detection of tumours based on microcalcification features and also by discriminating high risk tumours (small or non-palpable). This improves chances for survival and the ability to discriminate cancer with poor or good prognostic [26], [27].

1.4.1. Classifications

Microcalcifications are considered as the unique early marker of breast cancer [28]. Many studies suggest that there is a correlation between the appearance of microcalcifications and lesion malignancy.

1.4.1.1. Le Gal's classification

Le Gal's classification was introduced in 1984 and aims to distinguish microcalcifications based on their morphological appearance by associating a predictive value of malignancy [29]. In this classification, microcalcifications are grouped in five categories, as illustrated in Figure 1.8. For instance, ring shaped microcalcifications are involved in 100% of benign lesions whilst vermicular microcalcifications are observed in 100% of malignant lesions [25].

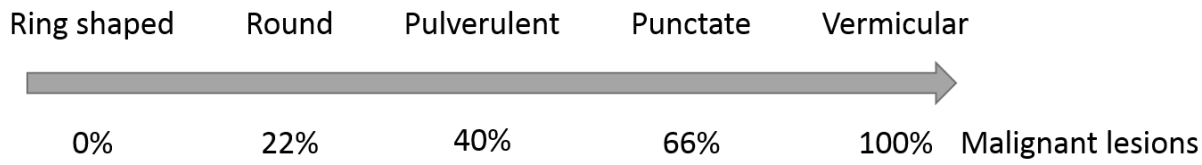

Figure 1.8 Le Gal's classification of microcalcifications based on their mammographic appearance and related percentage of correlation with malignant lesions in breast cancer.

Le Gal's classification is easy to use for classifying microcalcifications; however, it does not consider the spatial distribution of microcalcifications in a mass or even their margins. In this context, another classification is needed to include these parameters.

1.4.1.2. BI-RADS classification

The American College of Radiology (ACR) Breast and Imaging Reporting and Data System (BI-RADS) has been introduced in 1993. The purpose of this report was to standardise the results from mammographic images, within the radiologist community. A description and classification, in specific terms, of the breast lesions and microcalcifications associated with a predictive value of malignancy help clinicians to

establish an adapted treatment for the patient. In this classification, microcalcifications are defined by their morphology, size and distribution within the mammary gland.
The morphology of microcalcifications is classified into two main categories [24], [30], [31]:

1. Typically benign

The calcifications are grouped into nine categories, and few examples are illustrated in Figure 1.9:
- Skin or dermal: Lucent centre and usually localised near or within the skin (from the sebaceous gland).
- Vascular: Tubular structure and a railroad form. They are associated with blood vessels.
- Coarse or “popcorn-like”: Large size (< 2-3 mm diameter) and usually associated with fibroadenomas.
- Large rod-like: calcium deposit into a dilated duct leading to the nipple. The size is usually more than 1 mm.
- Round: Spherical shape with different sizes. When they are smaller than 0.5 mm, they are called “punctate” or “pulverulent”.
- Rim (“lucent-centred” and “eggshell” calcifications): Deposit of calcium at the surface of a sphere. The eggshell shape has less than 1 mm size, whereas lucent-centered calcifications have a size comprised between 1 mm and more than 1 cm.
- Suture: calcium deposit on suture material.
- Dystrophic: Associated with a prior trauma surgery or radiation; this type represents most of the cases in breast pathology. They are larger than 1 mm.
- Milk of calcium: Sedimented calcifications in cysts. They have different appearance such as linear, curved or “tea-cup” shape.

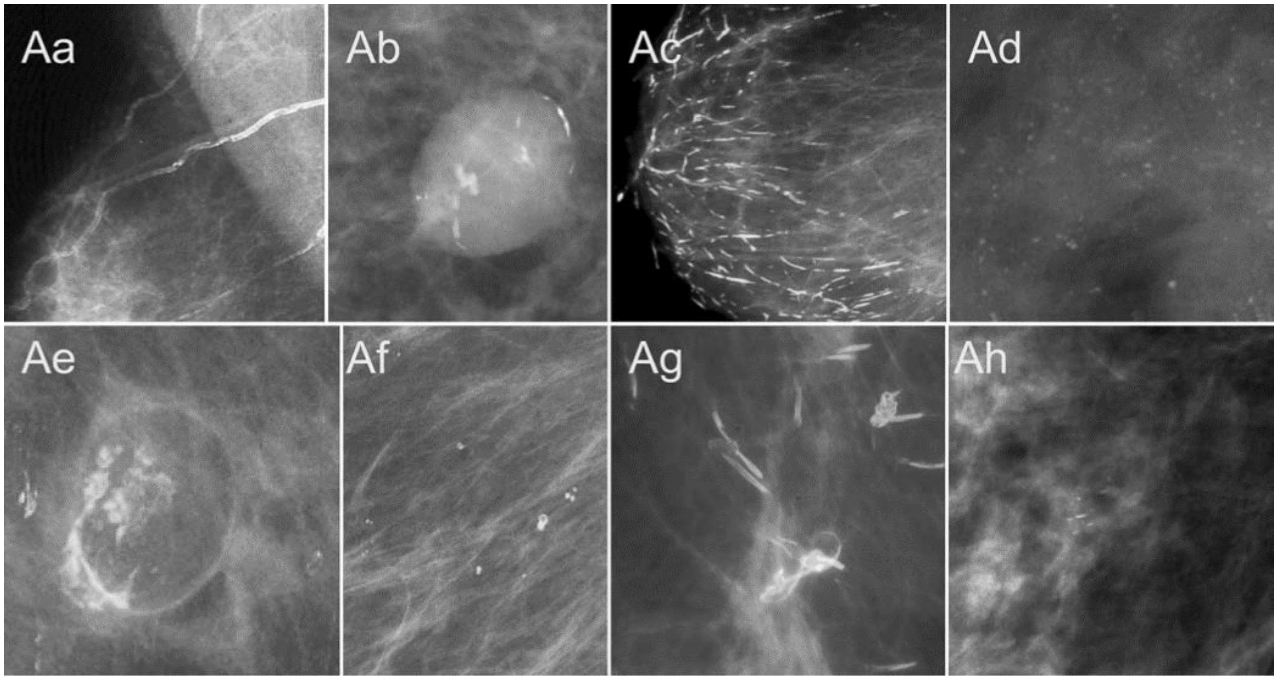

Figure 1.9 Different type of typically benign calcifications based on the BI-RADS classification using mammographic images. (Aa) Vascular, (Ab) coarse or popcorn-like, (Ac) large rod-like and (Ad) round calcifications. Rim type is represented by (Ae) “eggshell”, (Af) lucent-centred. Finally, (Ag) suture and (Ah) milk of calcium calcifications, [24].

2. Suspicious morphology

In this group, the calcifications have a low or high risk of malignancy [30], and they are illustrated in Figure 1.10:

- Coarse heterogeneous: Irregular and usually between 0.5-1 mm in size (13% risk of malignancy).
- Amorphous: They do not have any specific form, usually tiny and hazy. There is 27% risk of malignancy.
- Fine pleomorphic: Irregular shape and smaller than 0.5 mm. There is 78% risk of malignancy.
- Fine linear or fine linear branching (casting type calcification): Smaller than 0.5 mm, they can be linear, curved or branched. They represent 78% risk of malignancy and are usually associated with a very poor prognosis for the patient [32].

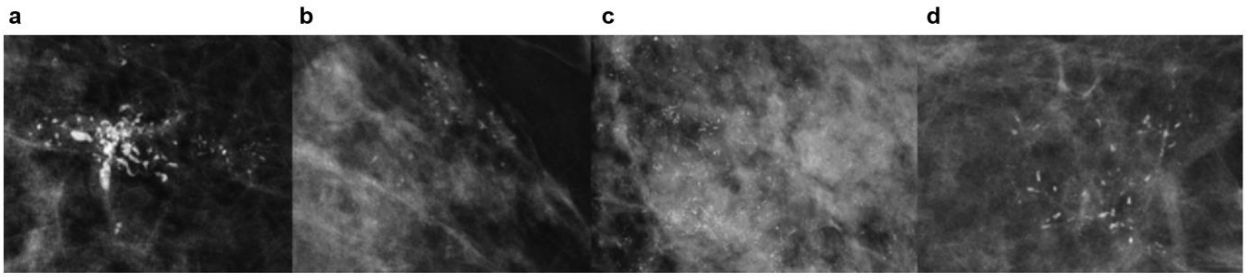

Figure 1.10 Mammographic images of calcifications with suspicious morphology based on the BI-RADS classification. (a) Coarse heterogeneous, (b) amorphous, (c) fine pleomorphic and (d) fine linear or fine linear branching calcifications, [30].

According to the BI-RADS classification for mammography reports, the radiologist classifies calcifications based on their spatial distribution. They are divided into five groups [33] and illustrated in Figure 1.11:

- Diffuse: Calcifications are randomly distributed in the breast.
- Regional: Calcifications are localised in a larger area of the breast (larger than 2 cm).
- Linear: Calcifications present a linear arrangement. The calcium deposit was mainly in a duct.
- Segmental: The calcium deposit is localised in ducts and branching.
- Grouped: Several calcifications (usually five) are grouped in a small area of the breast (1 cm) or a larger number clustered in 2 cm of breast tissue.

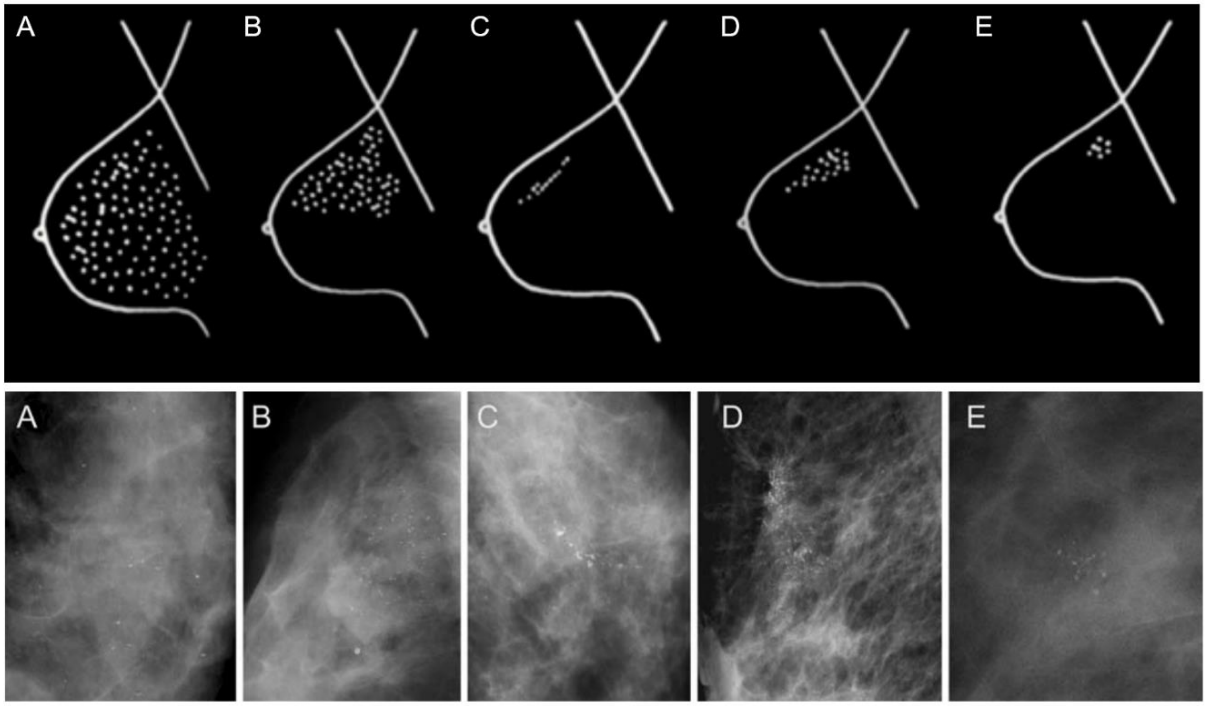

Figure 1.11 Classification of calcifications based on their spatial distribution according to the BI-RADS classification. (A) Diffuse, (B) regional, (C) linear, (C) segmental and (D, E) grouped. Figure adapted from [24], [33].

All these calcification features enable to improve the clinical outcome of the patient when they are detectable by mammography. Based on the morphology and the spatial distribution of calcifications, radiologists are able to manage mammography reports into five mammographic grades (normal, benign, probably benign, suspicious of malignancy and highly suspicious) [34] summarised in Table 1.3.

Table 1.3 BI-RADS categories for mammography reports. Categories based on the calcification appearance and their distribution in the breast tissue. Adapted from [24], [34].

Mammographic grade	**Description**		
M1	Normal		
M2	Benign		
M3	Intermediate/probably benign		
M4	Suspicious of malignancy		
M5	Highly suspicious of malignancy		
Features	**Category ≤ 3**	**Category 4**	**Category 5**
Calcifications			
Typically benign group	x		
Suspicious morphology group:			
Amorphous		x	
Coarse heterogeneous		x	
Fine pleomorphic		x	x
Fine linear/branching			x
Distribution			
Linear			x
Segmental		x	x
Regional		x	
Diffuse	x		
Grouped	x		

For instance, in diffuse distribution, an amorphous calcification is always benign. Conversely, a linear or segmental distribution (a calcium deposit is localised in ducts and branching) could be indicative of a high risk of malignancy. However, it depends on the morphology of the calcifications: a vascular shape in a linear distribution is benign, and it is the same case for a regional distribution [33].

These features show the complexity of mammogram interpretation to predict the malignancy of breast lesions. Further complementary analysis such as a biopsy is often required to establish a diagnosis.

1.4.2. Composition of microcalcifications

In 1984, Frappart et al. demonstrated the existence of two types of microcalcifications by X-ray diffraction according to their chemical composition. Type I microcalcifications are composed of calcium oxalate dihydrate (COD), whilst type II microcalcifications are mainly composed of hydroxyapatite (Hap) [35].

1.4.2.1. Calcium oxalate dihydrate (COD)

The COD crystal (so-called “weddelite”) is amber, crystalline and bi-refringent. The formula is $CaC_2O_4 \bullet 2H_2O$. They are observed in benign breast lesions [35]. It has been mentioned that calcifications with a “milk of calcium” morphology are small particles of COD [33].

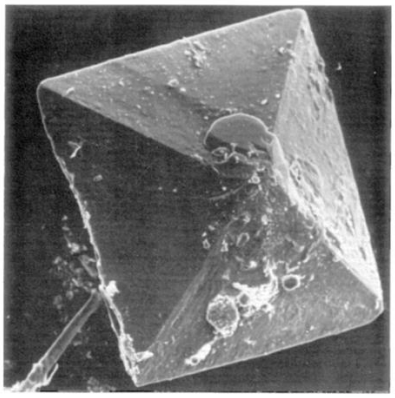

Figure 1.12 Example of type I microcalcification from a sclerocystic mastopathy observed by scanning electron microscopy, x980 magnification. Image from [35].

Figure 1.12 shows a well-defined crystal with homogeneous surface and a typical pyramidal shape.

1.4.2.2. Calcium Hydroxyapatite (Hap)

The Hap crystal is white, opaque and non-refringent under polarised light. The formula is $Ca_{10}(PO_4)_6(OH)_2$ [35].

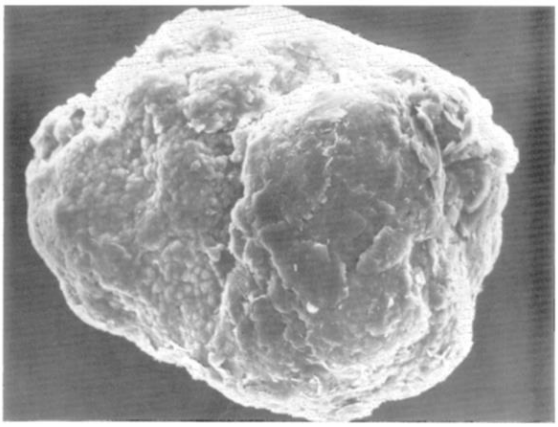

Figure 1.13 Example of type II microcalcification from an infiltrating adenocarcinoma of the breast observed by scanning electron microscopy, x1800 magnification. Image from [35].

Figure 1.13 illustrates a microcalcification with an irregular surface, with oolites (egg stones) composed of Hap without any crystallinity.
Frappart et al. also demonstrated that type II microcalcifications are associated with benign and malignant lesions. They appear to be smaller in the case of suspicious lesions and larger with a specific appearance in benign lesions [33].

Hap crystal is the main compound found in bone and teeth. The study of biological tissues containing Hap suggests that Hap crystals are not found in their pure form, but are mainly carbonated Hap (cHap). Two carbonate ion subtitutions are found in the crystal. When OH^- ion is replaced with CO_3^{2-} ion, we talk about type A substitution, and when PO_4^{3-} ion is repaced with CO_3^{2-} ion, we talk about type B substitution [36]. Sometimes, type L (labile) substitution can be found when the CO_3^{2-} ion is at the surface of the hydration layer of Hap [37]. Different levels of substitution are found in the body: 5.6 wt% of CO_3^{2-} ion substituted in bone, 4.6 wt% of CO_3^{2-} ion in dentine and 3.2 wt% of CO_3^{2-} ion in enamel [38]. The formulae of Hap containing different substitutions are:

- Type A: $Ca_{10}(PO_4)_6(OH)_{2-2y}(CO_3)_y$
- Type B: $Ca_{10}(PO_4)_{6-x}(OH)_x(CO_3)_{2-x}$

Figure 1.14 illustrates an example of two types of CO_3^{2-} ion substitution in a Hap crystal.

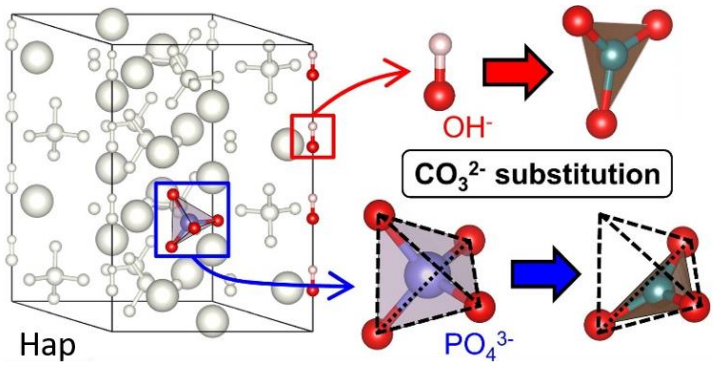

Figure 1.14 Schematic diagram illustrating type A and type B CO_3^{2-} substitutions in Hap crystal. Image from [39].

However, other elements can be incorporated in the carbonated apatites directly in the crystal lattice or just absorbed at the surface of the crystal, including F^-, Cl^-, SiO_4^{4-}, CO_3^{2-}, Na^+, Mg^{2+}, K^+, Sr^{2+}, Zn^{2+}, Ba^{2+} and Al^{3+} [40]. These substitutions are possible due to a rich environment in various ions. In fact, it has been demonstrated that breast tumours are rich in magnesium, potassium, zinc etc. and could potentially interact with the Hap crystal [40], [41]. Anionic substitutions can replace PO_4^{3-} or OH^- ions, whereas cationic substitutions replace only Ca^{2+} ion. The incorporation of these elements in the Hap lattice affects crystal structure but also crystallinity and solubility, inducing changes in the surrounding environment [40].

1.4.3. Formation of microcalcifications

The mechanisms involved in microcalcification formation and the relationship between their occurrence and cancer progression are still poorly understood [25]. This section is an overview of different models of microcalcification formation found in the literature, even though the different mechanisms have not been fully clarified yet.

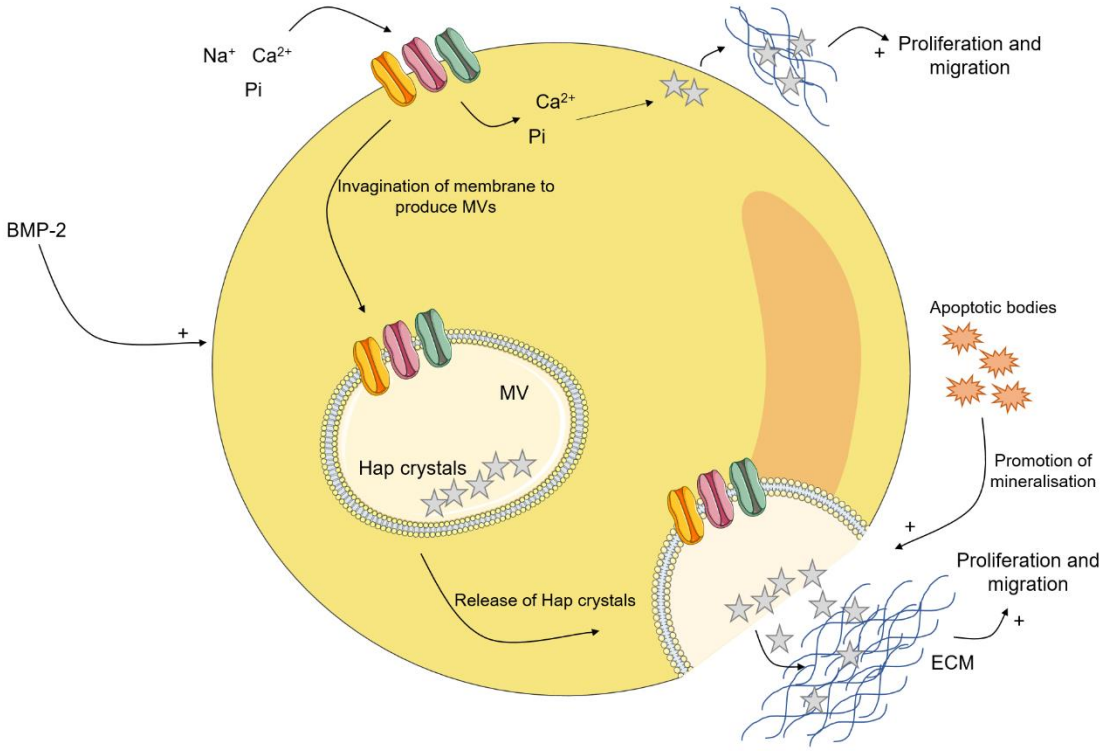

Figure 1.15 Different mechanisms of microcalcification formation in breast cancer cells. MV: matrix vesicle, ECM: extracellular matrix, Pi: inorganic phosphate.

1.4.3.1. Matrix vesicles (MVs)

MVs are generally found in cells and they are able to induce mineralisation in a physiological process, e.g. osteoblasts and chondrocytes, but it has not been excluded that they could also be involved in a pathological process. Their size varies between 20 and 200 nm in diameter [25]. As illustrated in Figure 1.15, MVs are the result of the invagination of the cell membrane at specific sites. They contain at their surface different channels (specific to calcium or phosphate ions) that facilitate Hap crystal formation, but the exact composition of these crystals is unknown. Finally, once the first Hap crystals are produced, they are released through endocytosis into the ECM followed by maturation.

1.4.3.2. Role of Bone Morphogenetic Proteins (BMPs)

Breast cancer cells must acquire osteoblastic characteristics to induce the mineralisation process (Figure 1.16). Some breast epithelial cells undergo the EMT and acquire a mesenchymal phenotype. Following these changes, and under the overexpression of the bone morphogenetic protein 2 (BMP-2), which is an osteogenic inducer, the mesenchymal cells appear to change their phenotype into osteoblast-like and are able to secrete Hap crystal [25], [42].

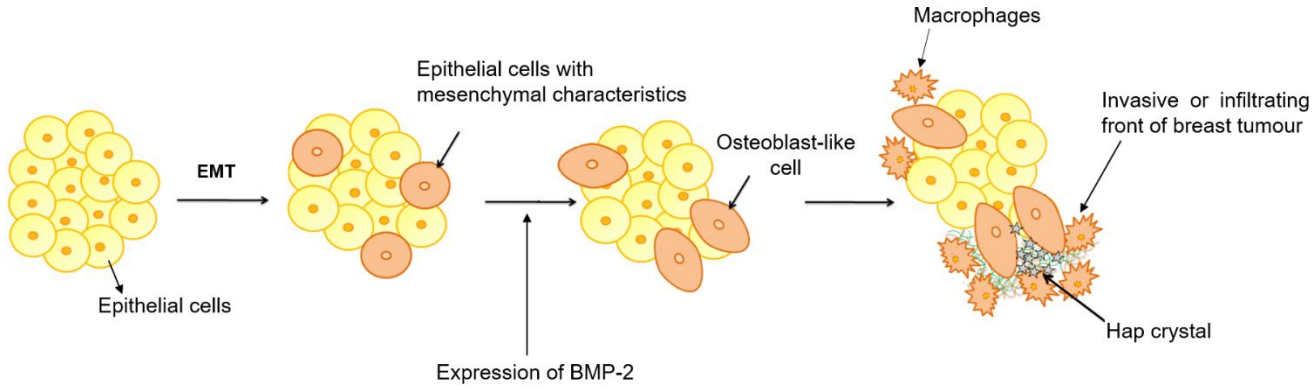

Figure 1.16 Simplified model of breast epithelial cells that acquire osteoblast characteristics via EMT, followed by expression of bone morphogenetic protein 2 (BMP-2) and then secretion of Hap crystal from the invasive/infiltrating front of a breast tumour. EMT: Epithelial mesenchymal transition. Adapted from [25], [42].

Although there are many osteoblastic matrix proteins, e.g. osteocalcin and osteopontin, that are capable to induce mineralisation, BMP-2 seems to play an important role in breast microcalcification regulation [25]. For example, BMP-2 expression increases calcium channel expression at the surface of breast cancer cells, which increase Ca^{2+} ions content into the MVs.

1.4.3.3. Apoptotic bodies

They come from programmed cell death (necrotic areas) and promote microcalcification formation by accumulating calcium and phosphate ions at their surface. Their role in the mineralisation has not been investigated [28].

1.4.3.4. Intracellular mineralisation

As illustrated in Figure 1.15, it has been demonstrated that calcium and phosphate ions can precipitate into the cytoplasm of osteoblast-like cells and, after release in the ECM, the maturation process takes place.
The MVs and the intracellular mechanisms tend to confirm that microcalcification formation is a secretory process rather than mineralisation from necrotic areas [28], [43] but it is subject to controversy in the literature and is still not clear.

To summarise the mineralisation process, three pathways of pathological mineralisation are considered [43] (Figure 1.17):
- Unregulated: including the formation of apoptotic bodies and formation of microcalcifications in a necrotic area.
- Regulated: breast cancer cells undergo the EMT and change their phenotype to become osteoblast-like cells (involving BMPs expression and MVs).
- Dysregulated: imbalance between inducers (e.g. BMPs) and inhibitors (e.g. osteopontin).

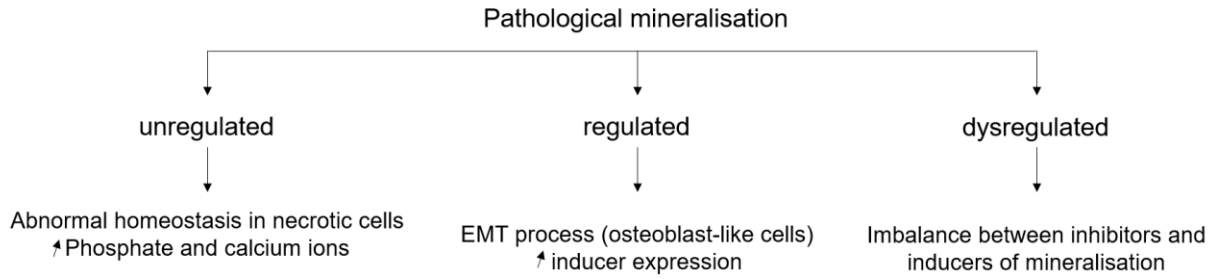

Figure 1.17 Scheme of the three different pathways of pathological mineralisation: unregulated, regulated and dysregulated.

1.4.4. Models of in vitro mammary cell mineralisation

To improve the understanding of the pathological process, Morgan et al. developed an *in vitro* model of mineralisation based on the secretory theory (Figure 1.18) [28]. To produce Hap crystals, cells need a source of inorganic phosphate (Pi). In this model, they added in the culture medium β-glycerophosphate (βG), which is an osteogenic agent, commonly used in literature. It has been demonstrated that the enzyme ALP (alkaline phosphatase) present at the surface of mammary cells can hydrolyse βG to Pi and glycerol. The Pi produced is then absorbed by cells via Na-Pi co-transporters. Once inside the cell, Pi can precipitate with calcium to produce the first Hap crystals. The primary crystals are then released in the ECM by different mechanisms, as discussed above. To regulate this process, osteopontin (OPN) can be produced to inhibit Hap growth as well as inorganic pyrophosphate (PPi). In pathological conditions, both can be inhibited by ALP to regulate the crystal growth and enhance cell malignancy. This model is based on a secretory process of pathological mineralisation.

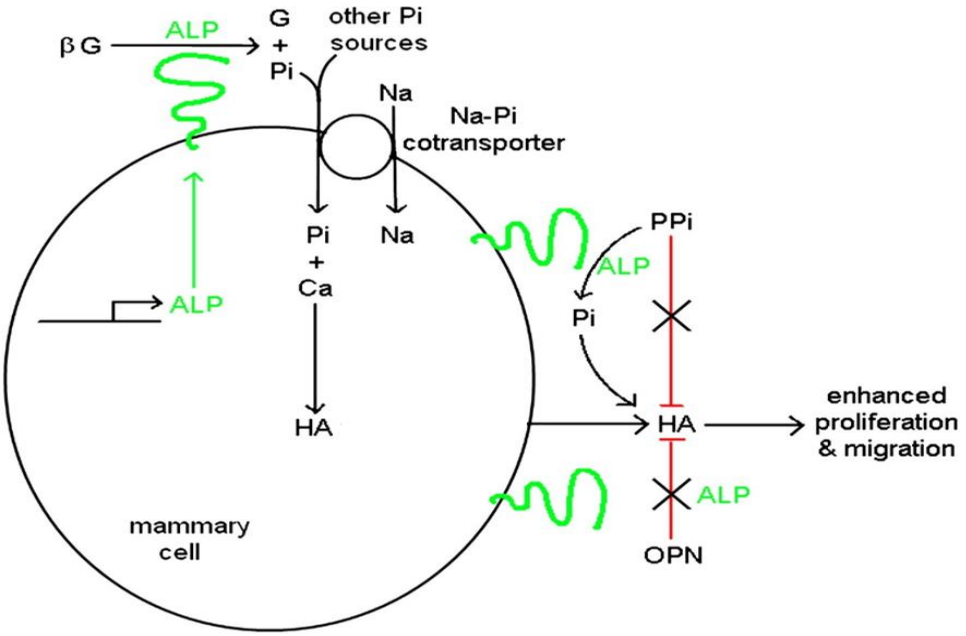

Figure 1.18 Model of *in vitro* mammary cell mineralisation. βG: β-glycerophosphate, G: glycerol, Pi: inorganic phosphate, PPi: inorganic pyrophosphate, Ca: calcium, ALP: alkaline phosphatase, Na: sodium, HA: hydroxyapatite and OPN: osteopontin, [28].

Vidavsky et al. suggested that this model constrains mineralisation to upregulate ALP expression. They developed an alternative model of mineralisation based on 3D culture, which they consider more appropriate than 2D culture. Their model is based on the development of microcalcifications in necrotic areas. They formed different spheroids with a necrotic core and could simulate benign, DCIS and invasive lesions.

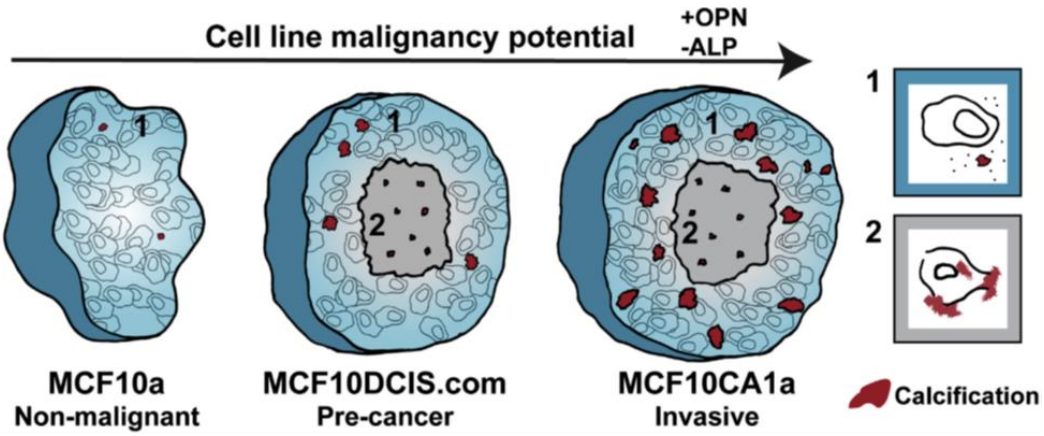

Figure 1.19 Model of 3D *in vitro* mammary cell mineralisation. OPN: osteopontin and ALP: alkaline phosphatase, [43].

In this model (Figure 1.19), MCF-10a cells (normal breast epithelial cells) are considered as a benign lesion. Before the experiments, they modified genetically the MCF-10a cells to have MCF10DCIS and MCF10CA1a cell lines. At the end, they obtained three different cell lines, which simulate the different stages of cancer: benign, *in situ* and invasive breast cancer. Then, they started to grow the cells in a culture medium supplemented in magnesium, calcium and phosphate at physiological concentrations to induce the microcalcification formation. By avoiding the use of osteogenic agents (e.g. βG), they recreated physiological conditions to induce microcalcifications which is maybe not the case by using osteogenic cocktails. However, the formation of microcalcifications *in vivo* or how they interfere during cancer progression is still unknown.

1.4.5. Relationship between microcalcification and breast cancer

As discussed above, the shape and the composition of microcalcifications are associated with the pathology outcome. In this context, it is interesting to find the relationship between microcalcifications and the occurrence of breast cancer. For instance, Morgan et al. have demonstrated that Hap crystal could induce matrix metalloproteinases (MMPs) expression in MCF-7 and Hs578T cell lines (two malignant breast cancer cell lines). MMPs are involved in the degradation of ECM components and promote invasion of breast cancer cells [44], [45]. In addition, the same team found that Hap crystals are involved in cell proliferation by enhancing mitogenesis in normal and malignant breast cancer cell lines [45]. Finally, it has also been demonstrated that Hap crystals induce an inflammatory process and upregulate different factors to enhance breast tumour development [45].

1.4.6. Involvement of microcalcifications in other diseases

The pathological mineralisation occurs in different locations of the body such as vasculature, lung, prostate, kidney or brain. Investigation of other forms of calcification is useful to understand the phenomenon that occurs in breast cancer. Scimeca et al. demonstrated that calcifications involved in prostate cancer are produced via cells acquiring osteoblast phenotype through the EMT [42]. However, in this pathology,

calcifications are often associated with benign lesions and rarely with malignant lesions [46]. In lung calcifications, the shape is important to determine the degree of pathology. A benign pulmonary nodule generally presents calcifications with a dense core, or they are laminated or diffuse, whilst malignant lesions contain punctate or eccentric calcifications [47]. The mineral composition varies in kidney calcifications. Monk et al. have suggested that the composition changes based on geographical distribution. In Europe 75% of calcifications are made of uric acid, while in the US they are made of calcium oxalate or calcium phosphate; in the UK struvite stones (magnesium ammonium phosphate) are more important [48]. These examples show that the occurrence of calcifications is complex, and the maturation of calcifications is not a linear process and not well-known.
In the meantime, regarding this lack of knowledge, a screening of the population is the best option to identify and rapidly treat those individuals affected by breast cancer.

1.5. Screening, diagnostics and prevention

In England, all women aged 50 up to 71 years old receive a letter for a routine screening every three years. The cost for routine screening is around £169 million per year but mammography is a powerful tool for detecting breast cancer. According to the report from the National Health Service (NHS) in England, in 2017-18, 2.5 million women were invited, around 1.8 million attended their appointment for mammography, and 18000 cancer cases were detected (14000 of those cancers were invasive) [49].

1.5.1. Clinical exam

The first step towards detection of breast cancer is any change in breast appearance or the presence of a fluid discharge as illustrated in Figure 1.20. If that is noticed, an appointment with a doctor could be necessary, and the GP can recommend further investigations, e.g. breast palpation and/or screening mammography.

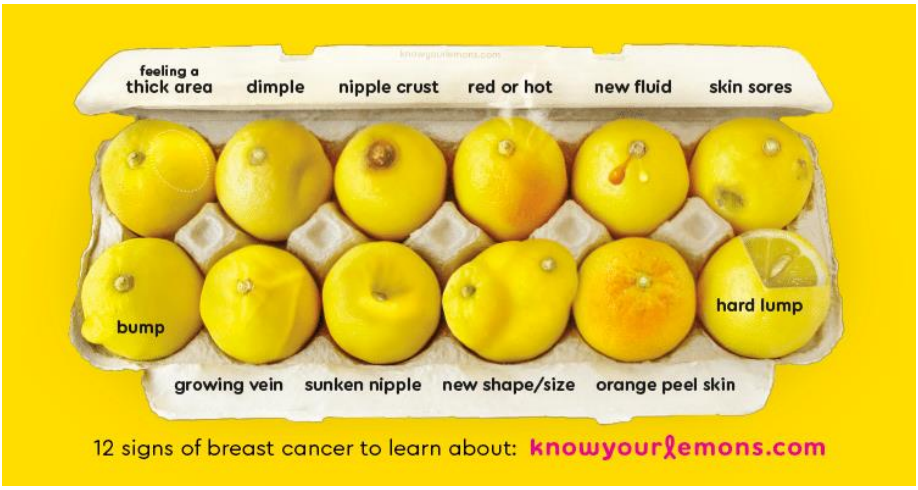

Figure 1.20 Different breast changes that require consulting a GP, [50].

1.5.2. Mammography

Mammography is a medical imaging test that uses low-dose X-rays to visualise breast tissue (Figure 1.21). As illustrated in Figure 1.21, a mammogram presents fat tissue in a very dark colour, water in dark, connective tissue is lighter, and calcium is white. A good quality mammogram is generally obtained with a strong compression of the breast. The compression helps to immobilise the breast, decrease the thickness and have a tissue imaged with high contrast [27]. Low energy X-rays are used to provide a contrast in soft tissues, but limited penetration can impact on the quality of the images when measuring thick or dense breasts.

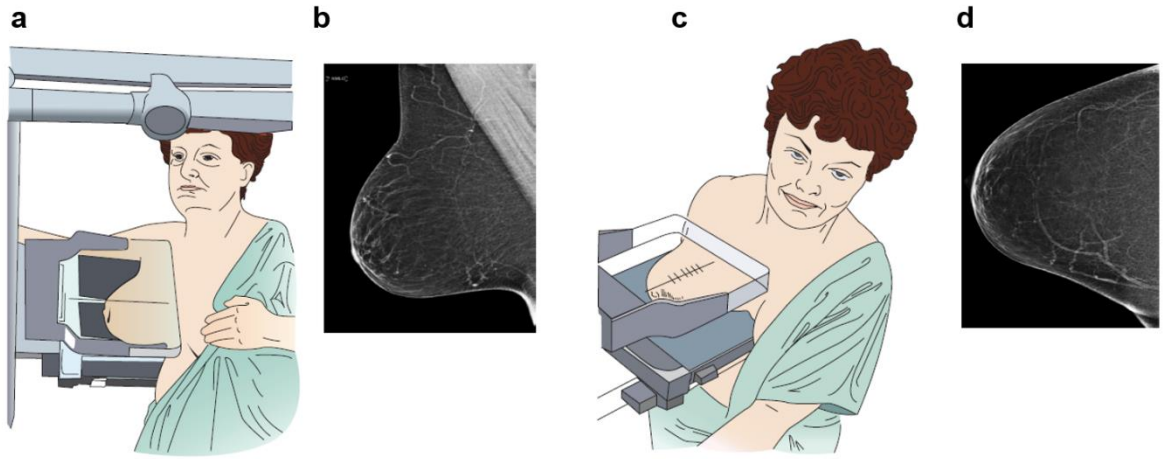

Figure 1.21 A typical screening mammography. (a) Mammography in mediolateral oblique position and (b) related mammogram. (c) Mammography in craniocaudal position and (d) related mammogram, [27].

Mammography assists the early detection and diagnosis of breast cancer because it can screen non-palpable breast lesions by detecting microcalcifications. However, it is impossible by mammography to distinguish type I or II microcalcifications or discriminate between benign and malignant lesions. Therefore, if an area appears suspicious in mammography, further investigation such as a biopsy is necessary. Breast cancer cannot be accurately diagnosed without a biopsy that can help the surgeon to identify and delimit a suspicious area.

1.5.3. Biopsy

If a suspicious area is found during routine screening, a protocol has been established to manage patients and their outcome, as shown in Figure 1.22.

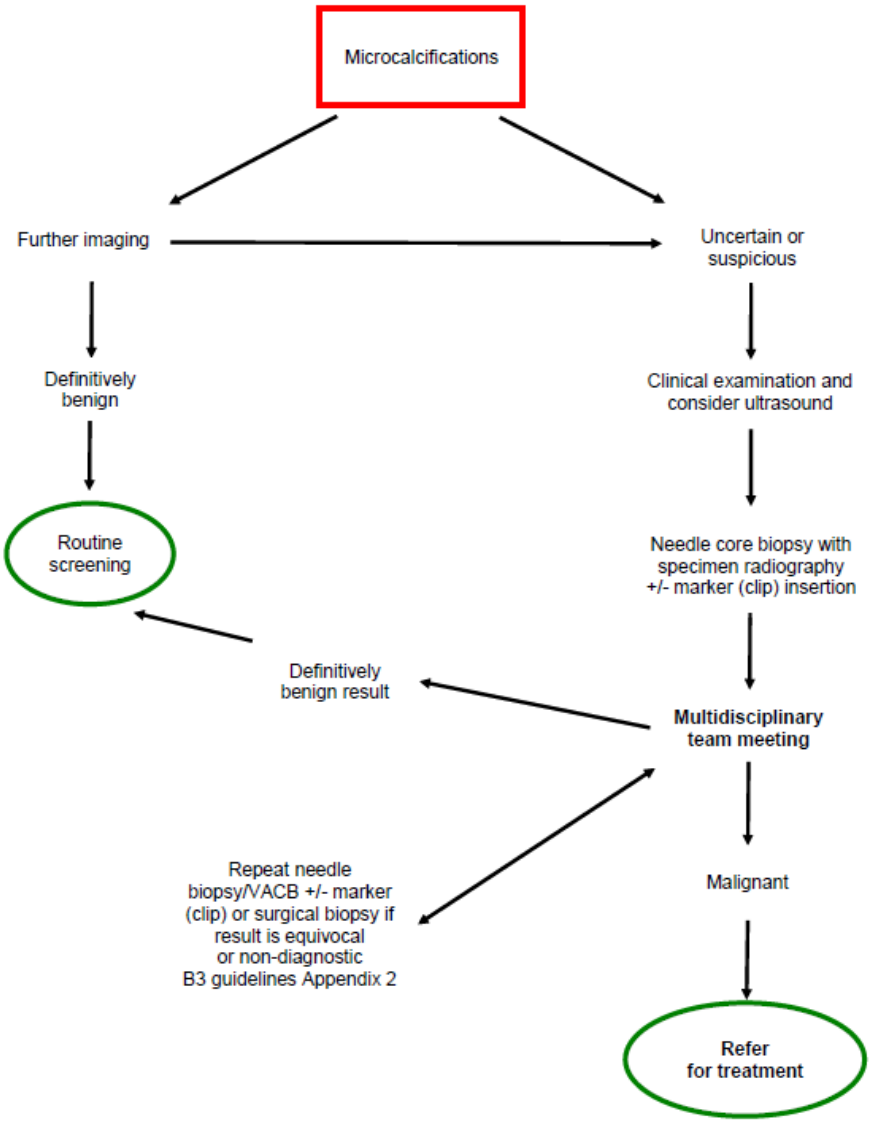

Figure 1.22 Protocol of assessment following the evidence of abnormalities (microcalcifications) during routine screening. VACB: vacuum-assisted core biopsy, [51].

According to the NHS Breast screening programme, if a microcalcification is detected during routine screening, a new mammography is performed (unless the abnormality is easily identifiable). If the lesion is benign, the patient will be recalled for routine screening every three years. If not, a clinical examination and ultrasound analysis are performed. During this analysis, a marker clip is inserted in the lesion area to guide the needle biopsy procedure.

Once the biopsy procedure has been performed, an H&E staining, which is the “gold standard” for histological diagnosis, is realised on samples to help the pathologist to discriminate between different tissue structures. Biopsies are then classified into five categories (B1 to B5b) based on their potential malignancy (Table 1.4).

Table 1.4 Classification based on percutaneous breast biopsy established by the Royal College of Pathologist. Adapted from [34], [52].

Normal tissue (B1)
Artefact, bleeding, microcalcification, …
Benign proliferative change (B2)
Fibroadenoma
Fibrocystic change
Sclerosing adenosis
Columnar cell change
Indeterminate lesions (B3)
Atypical epithelial ductal proliferation (AEDIP)
In situ lobular neoplasia, including lobular carcinoma *in situ* and atypical lobular hyperplasia (ILN)
Papillary lesion
Radial scar
Mucinous lesion
Suspicious for malignancy (B4)
Neoplastic cells contained within blood clots
Very small foci of invasive carcinoma
Non high grade intraductal proliferation with high degree of atypia
Non-invasive cancer (B5a)
Ductal carcinoma *in situ* (DCIS) and intracystic carcinoma
Pleomorphic lobular carcinoma *in situ* (LCIS)
Invasive cancer (B5b)
Invasive ductal carcinoma (IDC)
Invasive lobular carcinoma (ILC)
Special type including papillary, tubular and mucinous carcinomas

This classification takes into account the histological features. Biopsies are classified as: normal (B1), benign (B2) or malignant (B5). However, some samples are difficult or impossible to classify in these groups and have their own categories (B3 and B4). The B3 category regroups usually benign lesions but sometimes their histology shows a risk of malignancy (e.g. atypical epithelial ductal proliferation or papillary lesion). The B4 category is not attributed to a specific pathology but for instance can be accredited to the procedure issues or containing artefacts with a potential carcinoma [52].

1.5.4. Consequences of the procedure

Mammography and biopsy procedures are necessary steps to detect a pathology or refine a diagnosis but not without consequences for the patient. All women with mammographically suspicious lesions are recalled for further testing. If they do not have a malignant lesion, they have been subjected to unnecessary procedures, high risks of complication due to the procedure, emotional stress and anxiety. Only 10-25% of mammographically suspicious lesions are malignant [53]. Moreover, the cost of a false positive can be considerable for the NHS. For instance, in 2016, a standard needle biopsy and guides (i.e. marker clips) costed around £20 whilst a vacuum needle with guides around £300 [34]. Besides, it has to take into account the pathologist cost to prepare biopsies (embedded in paraffin, cut to a specific thickness, stained) and their analyses.

1.6. Other procedures

Different forms of biomedical imaging are the main tools for the detection of cancer at an early stage, evaluate the cancer progression, or response therapy, in real-time without tissue destruction. Many techniques are used for different purposes such as screening (i.e. mammography) or biopsy guidance (i.e. ultrasounds) [54] and are often supplementary to each other and adapted to the patient (often challenging in case of high breast density or obesity) [54].

Breast imaging in routine screening is based on X-ray mammography but other tools such as magnetic resonance imaging (RMI), tomography (i.e. positron emission tomography) or ultrasounds [54] are often used in breast cancer detection.
Contrary to mammography, which uses X-rays, MRI is based on applying an external magnetic field. By using a contrast agent (i.e. gadolinium) [55], MRI has the ability to evaluate patients with a high breast tissue density, and can detect malignancy when it is difficult with mammography and also useful for patient with mammary implants [56]. Unfortunately, due to an expensive cost of the device, hospitals are not often equipped for MRI and, due to a high number of false positives, this technique is not used in the screening routine [54].
Positron emission tomography (PET) is based on the detection of radioactivity emitted by a radiopharmaceutical agent (often used ^{18}Fluorodeoxyglucose or FDG) injected in the veins [57]. PET reflects metabolic changes and blood flow in the body. In contrast to X-ray or mammography, this technique evaluates the functionality and not the structure of breast [58], in particular by evaluating the rate of glucose consumption [57]. In fact, breast cancer is associated with an increase of glucose consumption in malignant lesions.
Ultrasound can discriminate different tissues based on their elasticity according to the speed of propagation of the acoustic waves [54]. It has been proved that the elasticity of cancerous tissue is lower than that of normal tissue. Based on their elasticity and stiffness, breast tissues are discriminated between benign and malignant lesions [54], [56].

In parallel, imaging techniques i.e. ultrasound, MRI or positron emission mammography are also used to guide biopsy procedure [56].

The use of these techniques does not improve detection of microcalcifications in the breast, and their small size tends to challenge their recognition. Many studies evidence the ability of vibrational spectroscopy to identify chemical composition of microcalcifications in breast by using FTIR [59] and Raman spectroscopy [60]. Crystal powders of calcium Hap in tissue phantom could be also detected using a deep Raman instrument [61]. This, opens the possibility for the analysis of *in vivo* breast microcalcifications and could be used as a supplementary technique to mammography [62], [63].

In a context of emergence of new tools for breast cancer screening, vibrational spectroscopy can help with the understanding and characterisation of specific changes in microcalcifications and therefore diagnose benign and malignant lesions.

1.7. Vibrational spectroscopy

1.7.1. Fourier Transform Infrared (FTIR) spectroscopy

1.7.1.1. Principle of FTIR spectroscopy

Vibrational spectroscopy is a family of non-invasive and non-destructive methods that are increasingly used in the analysis of biological samples such as tissues, cells and biofluids. Vibrational spectroscopy techniques detect the molecular composition and structure of a sample, based on the use of visible or infrared (IR) light to interrogate the vibrational modes of chemical moieties in molecules. In the case of IR absorption, by virtue of these vibrational modes, the molecules in a sample absorb IR light at certain frequencies and are promoted to excited vibrational levels. These energy transitions are different for different chemical groups in molecules, and hence an IR spectrum with patterns of signals at different frequencies is recorded. Using charts of known frequencies for specific functional groups, it is possible to assign the bands to particular types of vibrations, stretching or bending (Figure 1.23), of specific chemical bonds, e.g. O-H stretching (~3300 cm^{-1}). Therefore, a vibrational spectrum is a chemical 'fingerprint' of a material and can be used to identify its molecular composition. It also provides a measure of the concentration of a sample based on the Beer-Lambert law: $A_\lambda=\varepsilon_\lambda$ c *l*, where A_λ is the absorbance at a given wavelength, ε_λ the molar absorption coefficient at that wavelength, c the molar concentration, and *l* the optical path length (thickness of the sample or cuvette size).

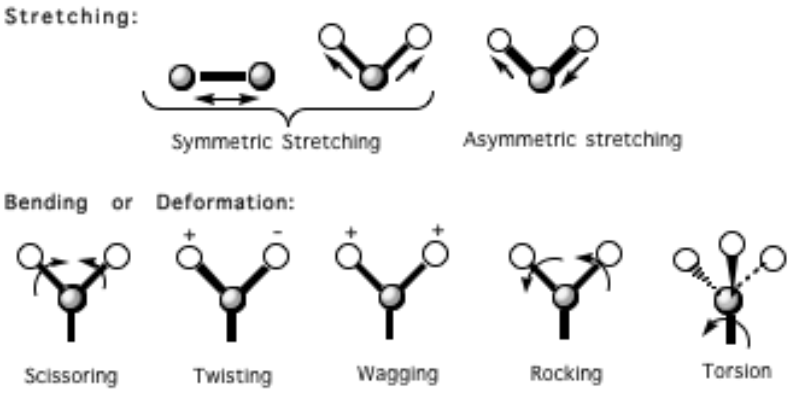

Figure 1.23 Different types of vibrational modes of molecules. From Colombia University, New York.

1.7.1.2. Quantum cascade laser (QCL) coupled to upconversion detector

Developments including QCL and upconversion imaging approaches can make a transformation of the FTIR imaging technique from a benchtop to a rapid and sensitive tool for real-time screening. QCLs are semiconductor lasers constructed for the first time by Faist et al. in 1994 to perform hyperspectral imaging. Unlike FTIR spectroscopy with a Globar thermal source, which records the whole mid-infrared spectrum, QCL systems record images at a single frequency [64]. In fact, the system can be tuned to a particular wavelength range of interest, such as phosphate or carbonate regions in our case. If only a few discrete frequencies are required, this approach is faster than current FTIR spectroscopic imaging and focuses only on specific signatures, such as those from microcalcifications in breast cancer. Moreover, it has also been demonstrated that QCL systems can provide extremely fast scanning of large tissue areas when compared with FTIR imaging [64]. Another modification of standard spectroscopic approaches involves the use upconversion detection. Investigated in 1960s, upconversion imaging is based on replacing the hyperspectral imaging in the mid-IR using an FPA-MCT (Focal Plane Array-Mercury Cadmium Telluride) detector with a CCD (Charge-Coupled Device) camera. This technique proposes an alternative procedure using a non-linear crystal of lithium niobate that allows conversion of photons with a long wavelength into photons with a shorter wavelength that can be measured with a CCD camera [65]. The advantages of using a CCD camera is that it has a higher number of pixels (Megapixels) than the FPA-MCT detector (128x128 pixels), does not require liquid nitrogen cooling and is cheaper to manufacture.

1.7.2. Raman microspectroscopy

Raman spectroscopy is based on the inelastic scattering of light from matter, and vibrational Raman spectroscopy is sensitive to vibrational modes in molecules causing a change in polarizability (whilst IR absorption is sensitive to the modes causing a change in dipole moment, making the two techniques complementary for molecules with a centre of inversion). It is a scattering process whereby the molecule is promoted to a virtual state (Figure 1.24) from which it drops back to the same initial vibrational level (Rayleigh scattering) or to a higher (Stokes Raman) or lower (anti-Stokes Raman) level. In Raman microspectroscopy, a Stokes spectrum is measured where vibrational resonances correspond to frequency shifts in the mid-IR region, so the spectra from Raman and IR techniques can be compared and contrasted.

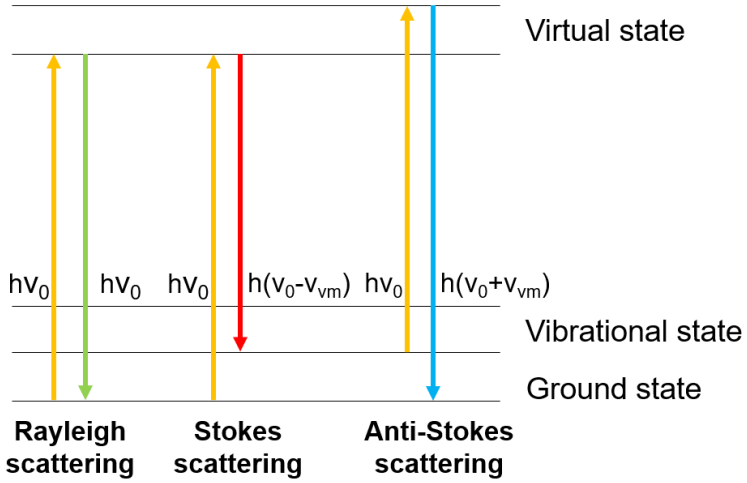

Figure 1.24 Jablonski diagram showing the vibrational energy levels in molecules and the cases of elastic and inelastic light scattering. $h\nu_0$: incident photon energy, $h\nu_{vm}$: Raman shift or difference in vibrational energy between final and initial state.

1.7.3. Spectroscopy and clinical applications

The important advantage of these vibrational techniques is that they are non-destructive, label-free and chemically specific, providing molecular information about a sample. They can be applied in combination with microscopy, imaging approaches, and the use of probes to enable minimally invasive clinical applications.

1.7.3.1. Breast tissue

The potential for biomedical applications of these techniques has been demonstrated through several proof-of-concept studies [66]; in particular, Lyng et al. demonstrated that Raman microspectroscopy could be applied to breast cancer for discrimination between benign and malignant lesions [67]. Many studies show that vibrational spectroscopy can be used to analyse mineral components of bone and other calcified tissues and to identify the mineralisation [68]. In Raman microspectroscopy, the specific peak for Hap is at 960 cm^{-1} for phosphate and 1070 cm^{-1} for carbonate [37]. In FTIR spectroscopy, the peak positions are around 1020 cm^{-1} for phosphate and 1410, 1450, 1423, 875 and 881 cm^{-1} for carbonate [59]. A few studies have focused on the analysis of breast microcalcifications. Haka et al. have demonstrated that Raman spectroscopy reveals differences in the chemical composition and structure of 90 microcalcifications (from 11 patients) in the different types of lesions in the breast. In fact, the results of principal component analysis (PCA) show a larger amount of carbonate substitution in benign lesion, whilst a malignant lesion presents a higher content of proteins (by calculating the matrix-to-mineral ratio) [60]. Baker et al. have confirmed the previous results using FTIR spectroscopy and a cohort of 110 patients and 236 microcalcifications. They have also found that microcalcifications are separated into three distinct groups according to their carbonate and protein contents. In fact, malignant lesions present elevated protein and reduced carbonate level; *vice versa* benign lesions have reduced protein and elevated carbonate. The percentage of carbonate substitution has been found to be 2.08, 1.83 and 1.41% in benign, DCIS and IDC, respectively [59].

Furthermore, a study led by Kerssens et al. using deep Raman spectroscopy in porcine tissue has demonstrated that it is possible to determine the level of carbonate substitution. This study shows that, in a thick layer of tissue, deep Raman can discriminate microcalcifications [37] and can be a good complement to the mammography screening.

1.7.3.2. Cell mineralisation

Several studies suggest that Raman microspectroscopy is a useful tool to assess *in vitro* mineralisation. Smith et al. have demonstrated that this technique provides specific information about early mineralisation (phosphate peak at 960 cm^{-1}) in murine osteoblast calvarial cells. They were able to distinguish different precursors in Hap formation after three days of mineralisation [69]. Another study by E. Brauchle et al. confirms the previous results and shows a perfect discrimination between different stages of differentiation of MSCA-1^{+} JPCs using PCA [70]. Moreover, Raman microscopy was able to discriminate between two breast cancer cell lines (MCF-7 and MDA-MB-436) and normal breast cells (MCF-10a) [71]. These findings suggest that Raman microspectroscopy is capable to assess breast cancer mineralisation.

1.8. Aims of the thesis

This thesis aims to evaluate the chemical composition of microcalcifications in the mammary gland. It will explore different aspects of mineralisation in the breast, in particular using an *in vitro* approach of mineralisation or biopsy samples directly. This model of mineralisation is essential to understand the maturation process of the Hap crystal in a biological context and link the findings with the microcalcifications found in breast biopsy samples. For the first time, this work analyses the Hap crystal formation over time by using vibrational spectroscopy and evidences other actors involved in their formation.

Furthermore, this work will explore novel spectroscopic methods to measure the composition of microcalcifications in breast tissue sections. In fact, for the first time, breast microcalcifications have been analysed in the long-wave infrared regime using upconversion detection combined with a QCL laser. The use of this unique setup may

have an impact on clinical translation of these approaches by allowing a selection of specific wavelengths of interest and also a simple detection using silicon based detectors more sensitive and cost efficient compared to MCT detectors commonly used in commercial systems. This may lead to a new diagnostic tool for identifying breast microcalcification changes during cancer progression.

This thesis is divided into six chapters: Chapter 1 is a general introduction to breast cancer and microcalcifications. Chapter 2 is focused on the materials and methods. Chapters 3 to 6 are dedicated to the results, with a brief context of the study, relevant data and discussion. Chapter 7 is a general conclusion, which also covers future work. The themes of Chapter 3 to 6 are listed below:

- Chapter 3 investigates different standard minerals typically found during the mineralisation process. It will focus on spectral characteristics of different components found in breast microcalcifications.

- Chapter 4 examines breast biopsy samples using FTIR imaging and Raman microspectroscopy and comparison with the spectra of standard minerals.

- Chapter 5 explores an *in vitro* model of breast cell mineralisation and compares its characteristics with those of standard minerals and breast biopsies.

- Chapter 6 examines new IR technologies such as those based on QCL source and upconversion detection for rapid imaging of breast biopsy samples.

Chapter 2 : Materials and Methods

2.1. Sample collection

2.1.1. Frozen tissue

Female breast tissue samples were collected from the NIHR Exeter Clinical Research Facility at the Royal Devon and Exeter (RD&E) NHS Foundation Trust, under the tissue bank ethical approval (No 16/SC/0162). Samples were collected at the time of routine clinical care between 2011 and 2017 and the patients consented for research (see consent form in Appendix, supplementary data 1, Figure A.1). Samples were collected after surgery (mastectomy or wide local excision, WLE) and were tested by immunochemistry for ER and HER2 status. A total of 290 samples were stored at the tissue bank containing 145 biopsies taken at distance of the tumour (set considered as benign) and 145 taken in the tumour (set considered as malignant). The clinical data about the patients and the breast samples were collected by the hospital according to template for each patient. The form is illustrated in Appendix, supplementary data 1, Figure A.2. The age of patients is ranges between 41 and 96 years.

Amongst 145 breast cancer samples (malignant), only 16 samples contained microcalcifications after a reading under a microscope the consecutive H&E stained sections using an optical microscope with x4, x10 and x40 objectives in the lab. The sample size is around 5 mm diameter. Samples were classified according to their histological report: benign (n=1), DCIS (n=2), IDC (n=11), ILC (n=1) and mixed IC (n=1). For each sample, three adjacent sections were cut without cutting agent and mounted onto barium fluoride (BaF_2) slides for Raman and FTIR imaging analysis, and one stained with H&E for histological analysis, i.e. the “gold standard” for diagnosis. Each section was 5 µm thick. The sections were stored at -80°C prior to the spectroscopic analysis. For clarity, the protocol is summarised in Figure 2.1a.

2.1.2. Paraffinised tissue

Two batches of paraffinised breast cancer tissue were collected for this study. Dr Renzo Vanna from the Insituti Clinici Scientifici Maugeri in Pavia, Italy, provided the first batch of 11 samples. They were classified according to the degree of pathology into: benign (n=5) and malignant, including DCIS (n=5) and IDC (n=1) with microcalcifications. Three adjacent sections embedded in paraffin were prepared: one (3 µm thick) was mounted onto a BaF_2 slide for FTIR analysis, one (10 µm thick) mounted onto stainless steel for Raman, and the last one was mounted onto a glass slide and stained with H&E.

The second batch of 13 samples with microcalcifications was previously collected from the Gloucestershire Royal Hospitals NHS Foundation Trust. As the other batch, samples were classified and analysed according to the degree of pathology: benign (n=5), DCIS (n=5) and IDC (n=5) lesions with microcalcifications. For each sample, two adjacent sections of 3 µm thickness were analysed: two sections mounted onto a BaF_2 slide for FTIR and QCL spectroscopy analysis and one section mounted on a glass slide and stained with H&E. For clarity, the protocol is summarised in Figure 2.1b.

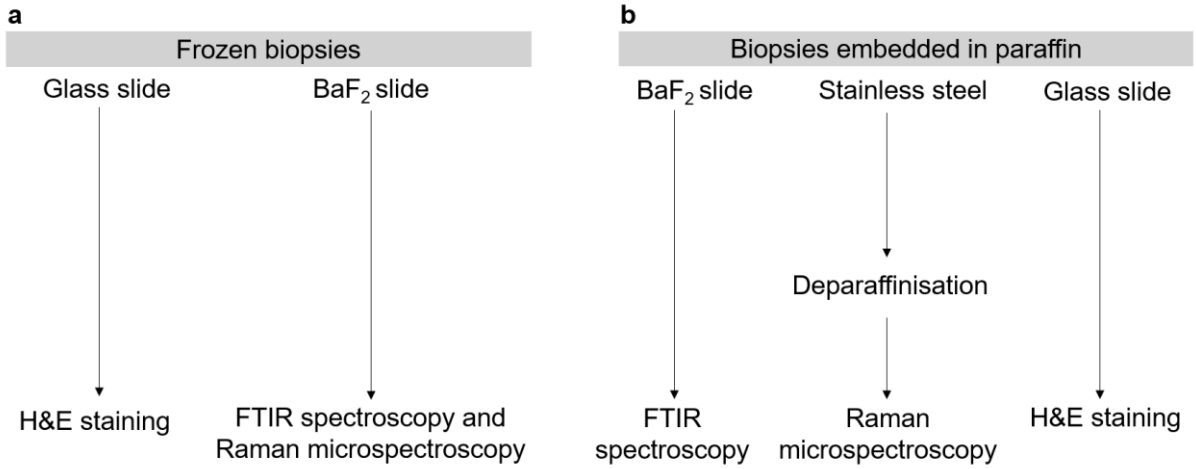

Figure 2.1 Experimental protocols used for the preparation of biopsy tissue samples for FTIR and Raman microspectroscopy measurements.

2.1.3. Mineral standards

Prof. Mary Tecklenburg from Central Michigan University, USA, generously provided home-made B-type cHap powders. These standards were made by incorporating different levels of CO_3^{2-} (1.24, 2.92, 4.43, 5.24, 7.52 and 8.12 wt.%) in the Hap lattice as part of the synthesis process. In parallel, pure Hap powder (97% pure, Sigma-Aldrich) was used to perform a calibration curve.
Another set of standards was generously given by Prof. Keith Rogers from Cranfield University: Amorphous Calcium Phosphate (ACP), Octacalcium Phosphate (OCP) and β-Tricalcium Phosphate (β-TCP).

2.1.4. Breast cancer cell line

The human MDA-MB-231 cell line, which is a highly invasive metastatic cell line obtained from an adenocarcinoma in the mammary gland, was used in this study. This sample was a gift from Dr Maria Morgan at the Royal College of Surgeons in Ireland (RCSI). Cells were stored in sterile cryovials kept in liquid nitrogen prior to the experiments. The procedure of cell culture and the mineralisation induction are detailed in section 2.3.6.

2.2. Instrumentation

2.2.1. Raman microspectroscopy

Micro-Raman measurements were acquired using a Renishaw inVia confocal Raman microscope, comprising a 50x long working distance objective (N.A. 0.5) for illumination and for collection of the backscattered light, xyz motorized stage, 600 lines/mm grating and CCD camera (Figure 2.2). The excitation beam was from a NIR diode laser source with 830 nm wavelength.

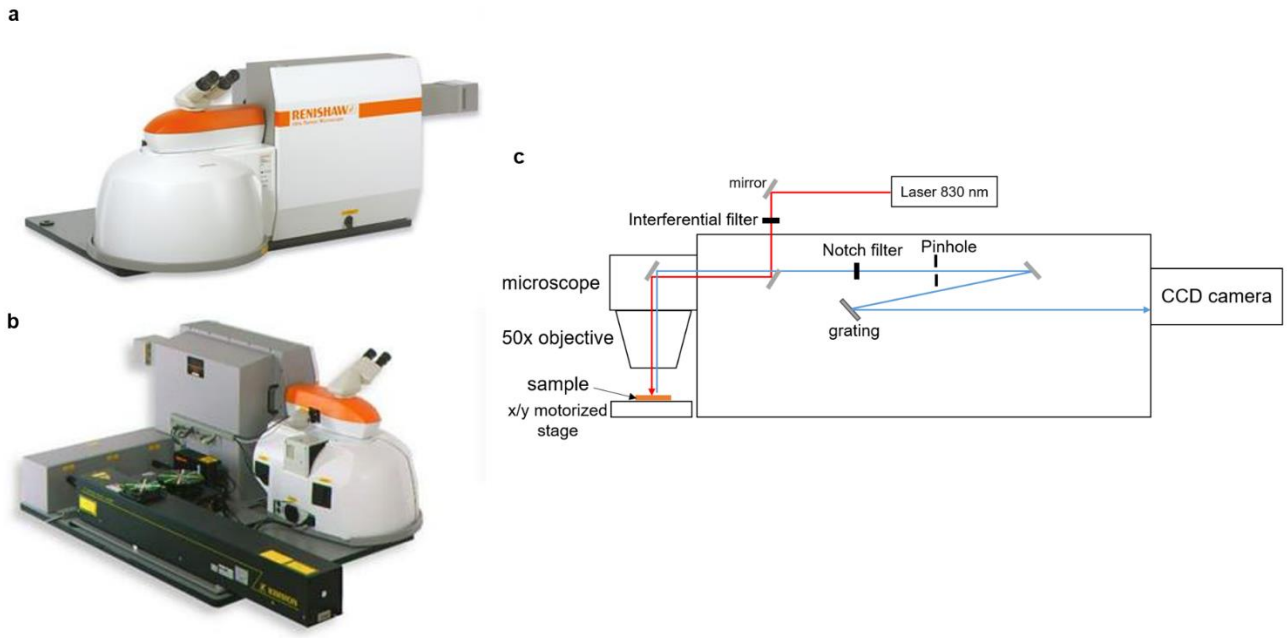

Figure 2.2 (a) Raman confocal microscope coupled to a spectrometer and CCD camera. (b) Diode laser source at 830 nm used in these measurements. (c) Schematic diagram of the Raman setup. Red line: laser beam. Blue line: scattered light (Stokes part) dispersed by the grating and detected by the CCD camera.

Before each set of measurements, a system calibration was performed using three standards: silicon wafer, neon-argon lamp and green glass.

2.2.2. IR microspectroscopy

All samples were measured using an Agilent 670 FTIR spectrometer, containing a Michelson interferometer (Figure 2.3) and coupled to an Agilent 620 FTIR microscope equipped with both 4x and 15x Cassegrain objectives and an MCT-FPA detector (128x128 pixels).

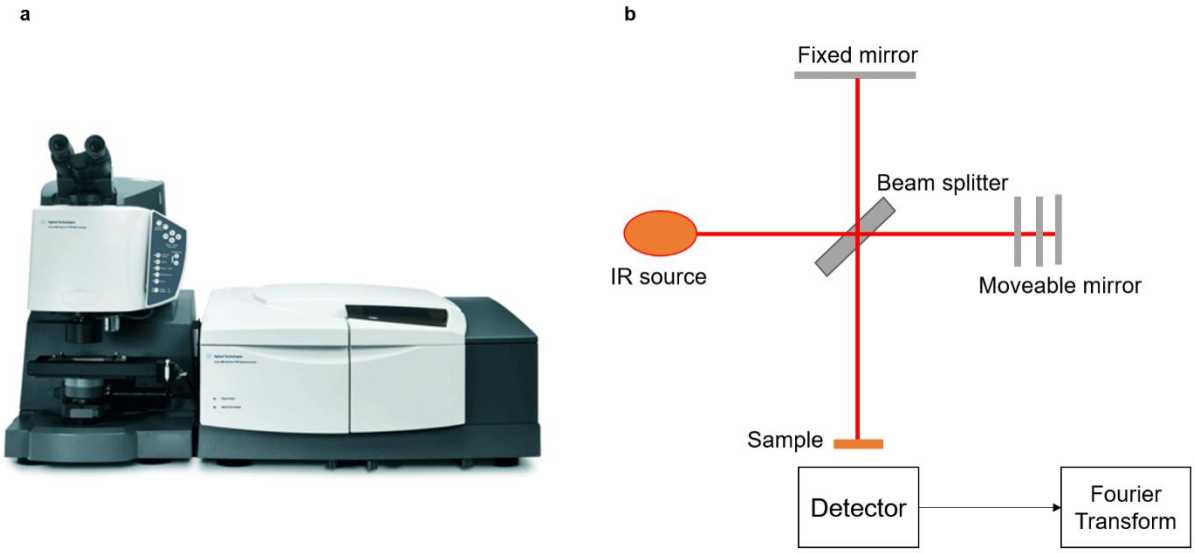

Figure 2.3 (a) Agilent Cary 670 FTIR spectrometer coupled to an Agilent Cary 620 FTIR microscope. (b) Schematic diagram of a Michelson interferometer. The IR beam is separated in two by a beam-splitter, one beam is sent to a fixed mirror and the other one to a moveable mirror so that a path length difference is introduced. When the beams recombine at the beam-splitter, an interferogram is produced which contains all wavelengths from the source at once. As the light travels across the sample, some wavelengths are absorbed owing to vibrational modes of molecules in the material. A background and sample measurements are performed in succession to ensure minimisation of any absorption of IR light arising from the environment and optical setup. A mid-IR spectrum of the sample is then obtained and plotted for analysis [72].

2.2.3. QCL system coupled to upconversion detector

IR measurements were also conducted using a lab-built QCL system developed by Pedersen et al. from the Denmark Technical University. It is composed of three parts: a QCL source, a microscopy unit and an upconverter unit (Figure 2.4).

The QCL source was used as long-wavelength infrared (LWIR) source, widely tuneable within the range 9.34 to 12 µm. In this setup, the QCL beam is focused by a lens to a spot of approximately 82 µm diameter (spatial resolution) onto the sample which is located on a microscope stage. The transmitted light is coupled to a mixing source (Near-infrared, NIR) which is a diode-pumped 1064 nm laser operating in continuous wave which generates an average power of up to 3 W. These combined laser (LWIR and NIR) beams are focused into a nonlinear crystal ($AgGaS_2$), which is the up-converter unit. At the end, a NIR signal is detected by a silicon power meter.

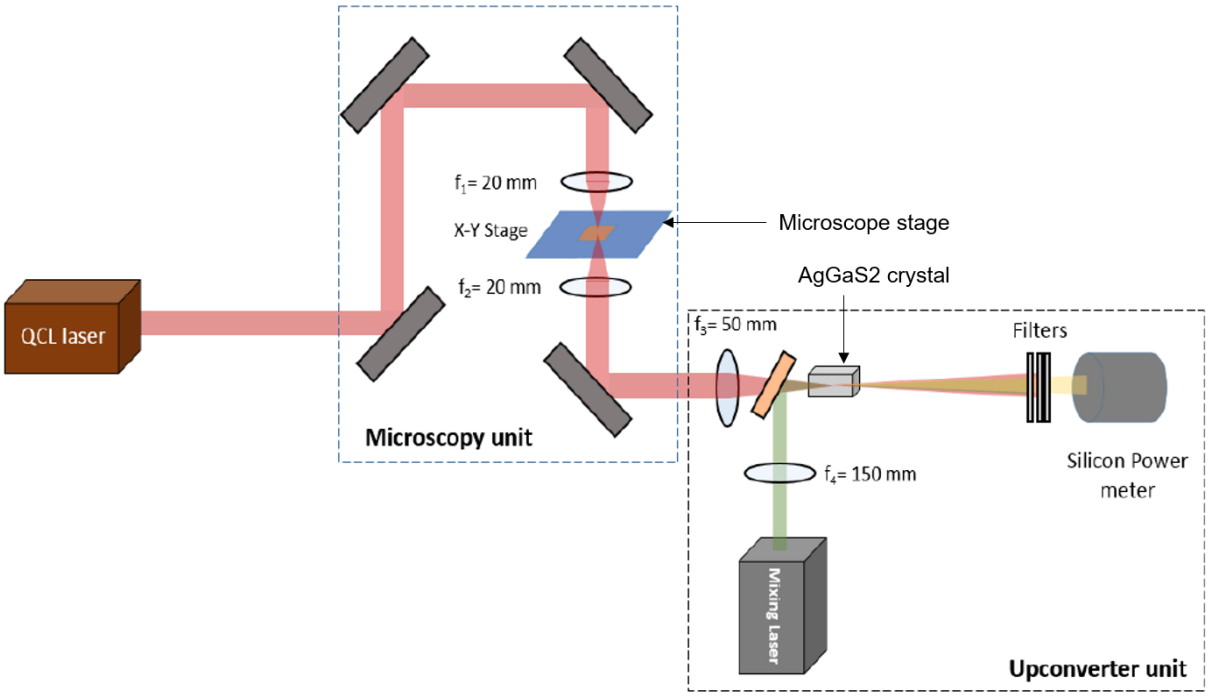

Figure 2.4 Schematic diagram of the experimental setup comprising a QCL source, a motorised xy microscope stage, mixing laser, nonlinear crystal and silicon power meter, [73].

The upconverted images obtained are in false colours, where red corresponds to high intensity and blue to low intensity of absorption.

2.3. Methods

2.3.1. Raman analysis of mineral standards

For the Raman measurements, standards were analysed in their powder form on calcium fluoride (CaF_2) substrates using the parameters listed in Table 2.1

Table 2.1 Raman parameters for the analysis of mineral standards, breast tissue sections and breast cancer cells.

Parameters	
Diode laser	830 nm
Output power	100%
Grating	600 lines/mm
Centre	1500 Raman shift/ cm^{-1}

Ten spectra were recorded for each mineral with 5 s exposure time and 5 accumulations using WiRE software. Two replicates were performed.

2.3.2. Raman mapping of tissue samples

2.3.2.1. Frozen tissues

A micro-Raman map of each sample which contained microcalcifications was recorded using the streamline mode of the Renishaw inVia microscope, as summarised in Table 2.1. The acquisition time was 15 s with a step size of 1.4 µm. Raman maps were recorded using WiRE software.

2.3.2.2. De-paraffinised sections

A de-paraffinisation procedure was performed before the Raman mapping measurement to prevent artifacts due to the strong contribution of paraffin in Raman spectra. Samples were deparaffinised using a protocol suggested by Dr Vanna involving consecutive washing:

- Two baths of 95% hexane for 5 minutes
- Two baths of 100% ethanol for 5 minutes
- One bath of 95% ethanol for 5 minutes
- Slides are air-dried at room temperature overnight.

Biopsies were analysed using the following parameters: a map of each sample with microcalcification areas was recorded using streamline mode, with an 830 nm diode laser source at 100% laser power, a grating of 1200 lines/mm and centred to 1250 cm^{-1}. The acquisition time was 3 s with a step size of 8.4 µm and a bin of 6. Raman maps were recorded using WiRE software.

2.3.3. FTIR analysis of mineral standards

Pellets of minerals were prepared according to the following protocol: 99 mg of KBr powder was added to 0.5 mg of cHap, mixed and grounded together to a fine powder using a mortar and pestle. The mixture was transferred into a manual hydraulic press (Specac) and compressed for 1 h with a pressure of 10 t. In order to be analysed by FTIR spectroscopy in transmission mode, each pellet should contain the appropriate amount of sample so that the IR light is not fully absorbed. For the background spectrum, a pellet containing only 100 mg of KBr (transparent) was also prepared. The KBr/cHap pellets were analysed in single-point spectrum mode. Spectra were recorded in the spectral range comprised between 4000 and 700 cm^{-1} with a spectral resolution of 4 cm^{-1}. Each spectrum was obtained by averaging 32 scans, whilst the background spectrum was recorded with 64 scans. Spectra were collected using Agilent Resolutions Pro software. Five spectra were recorded for each sample. Two replicates were performed.

2.3.4. FTIR analysis of tissue samples

A map of each sample with microcalcification areas was recorded using the Agilent FTIR imaging system. The parameters are listed in Table 2.2. A background spectrum was recorded using a clean area of BaF_2 for each sample.
Biopsies were also analysed in single-point mode and the parameters are summarised in Table 2.2. Five spectra were recorded for each sample and collected using Agilent Resolutions Pro software.

Table 2.2 FTIR parameters for the analysis of biopsy samples, frozen and paraffinised tissue.

	X4 objective	X15 objective	Point mode
Spectral range	3800-1000 cm^{-1}	3800-900 cm^{-1}	4000-700 cm^{-1}
Spectral resolution	4 cm^{-1}	4 cm^{-1}	4 cm^{-1}
Pixel size	20.6 μm^2	5.5 μm^2	-
Background (BaF_2)	256 scans	64 scans	64 scans
Sample	64 scans	32 scans	32 scans

2.3.5. QCL analysis of mineral and biological samples

Pellets of standards (as previously described in section 2.3.3) and paraffinised biopsies were analysed with the same parameters as the breast tissue samples using the QCL system described previously (section 2.2.3).

Spectra were recorded in the spectral range comprised between 1066 and 830 cm^{-1}, with a spectral resolution of 4 cm^{-1}. Background (pure KBr pellet) and cHap spectra were recorded at each discrete wavenumber. In these conditions, five spectra were recorded for each sample.

2.3.6. Analysis of breast cancer cell mineralisation

2.3.6.1. Induction of cell mineralisation

Before the study, MDA-MB-231 cells were maintained in sterile 75 cm^2 flasks with a standard growth media of DMEM (Thermofisher Scientific) supplemented with 10% of foetal bovine serum (FBS, Thermofisher Scientific) and 1% Penicillin/Streptomycin (Thermofisher Scientific) at 37°C and 5% CO_2 atmosphere in an incubator for few days. After removing the media, cells were trypsinised (Thermofisher Scientific) and washed with PBS. Cells were seeded at 0.8 x 10^6 cells/well in 3 mL/well of media (DMEM and FBS) within 6-well plates. Cells were grown overnight at 37°C, 5% CO_2 onto calcium fluoride (CaF_2) slides inserted into the 6-well plates. The next day (day 1), the mineralisation was induced by two pathways using different osteogenic agents (Figure 2.5). The first pathway consists of adding an osteogenic cocktail (OC) coupled to Dexamethasone (Dex) (Sigma Aldrich, D4902) to the media. The OC is composed

of β-glycerophosphate (βG) (Sigma Aldrich, 50020), which is a source of inorganic phosphate, and ascorbic acid (AA) (Sigma Aldrich, 49752), which promotes collagen production. Dex is considered an inducer of osteoblastic differentiation. The second pathway uses Pi directly into the media, coupled with Dex, to induce faster mineralisation (Figure 2.5).

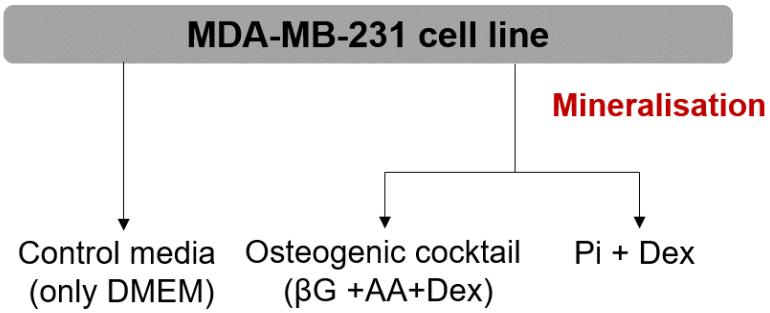

Figure 2.5 Protocol for mineralisation of the MDA-MB-231 cell line using different osteogenic agents. βG: β-glycerophosphate, AA: ascorbic acid, Dex: Dexamethasone, Pi: inorganic phosphate.

Osteogenic agents (βG, AA and Dex) were added to 3 mL/well of media at different concentrations (Table 2.3). Pi was also added to 3 mL/well of media but prepared from Na_2HPO_4 + NaH_2PO_4 (Sigma Aldrich S5136, 71496) powders in a 4:1 molar ratio as a 1 M stock solution. The solution was diluted in pyrogen-free water (Thermofisher, H20CC0106). Solutions of osteogenic agents were prepared in advance, divided in aliquots and kept at -80°C for further experiments. Media were changed every three days.

Table 2.3 Concentrations of osteogenic agents employed to induce mineralisation. βG: β-glycerophosphate, AA: ascorbic acid, Dex: Dexamethasone, Pi: inorganic phosphate.

	Stock solution	Final solution
βG	1M	10 mM
AA	5 mg/mL	50 µg/mL
Dex	1nM	100 nM
Pi	1M	10 mM

The mineralisation process was stopped at day 3, 7, 11 and 14 (Figure 2.6) and the samples were analysed using IR and Raman microscopy. Cells were washed three times with PBS, fixed with 4% paraformaldehyde (Thermofisher Scientific, A11313) for 30 minutes and air-dried at room temperature. In parallel, cells were grown onto CaF_2 substrates submerged in 6-well plates using regular growth media and fixed on the same days. Three replicates were performed in this study.

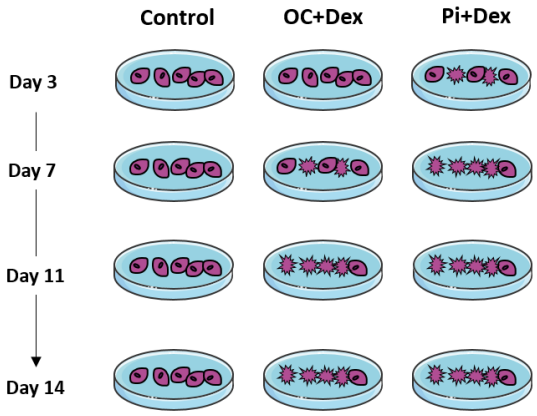

Figure 2.6 Illustration of the mineralisation process for each condition (Control: only DMEM), OC and Dex, and Pi and Dex. Cells were fixed at day 3, 7, 11 and 14.

2.3.6.2. Raman mapping of breast cancer cells

Raman maps of different areas of mineralised cells at specific days of mineralisation (Day 3, 7, 11 and 14) were recorded using streamline mode, and the parameters are summarised in Table 2.1. The acquisition time was 30 s with a step size of 9 µm and a bin of 7.

2.3.6.3. FTIR imaging of breast cancer cells

FTIR maps of different areas of mineralised cells at specific days of mineralisation (Day 3, 7, 11 and 14) were recorded using a spectral resolution of 4 cm^{-1} and a spatial resolution of 5.5 µm/pixel with x15 objective. Spectra were acquired over a spectral range comprised between 3800 and 900 cm^{-1}. Each spectrum was obtained by averaging 256 scans, and a background spectrum was also recorded with 512 scans.

2.4. Data analysis

2.4.1. Selection of spectra

Datasets were analysed using a home-made program in Matlab software (Mathworks, USA). Spectra were selected from a central location within the microcalcification in Raman maps and IR images based on the phosphate peak intensity at 960 cm^{-1} and 1030 cm^{-1}, respectively.

2.4.2. Peak decomposition analysis

Curve fitting analysis of spectral band shapes was performed using OriginPro software (OriginLab, USA). A mix of Gaussian and Lorentzian functions were used to fit the FTIR and Raman spectra in different carbonate and phosphate regions. The Levenberg-Marquardt algorithm was used to minimize the χ^2 value. The peak positions were fixed whilst the peak widths were free fitting parameters.

A mean spectrum was calculated from ten spectra of each sample (mineral standards, cells or biopsies). Raman spectra were truncated in the spectral range of interest for phosphate (985-900 cm^{-1}) and carbonate (1100-1010 cm^{-1}) bands. IR spectra were truncated in the spectral range 1200-900 cm^{-1} for phosphate and 890-830 cm^{-1} and 1480-1330 cm^{-1} for carbonate bands. Raman spectra were smoothed with the Savitzky-Golay algorithm, second polynomial order with 9 points, using OPUS software (Bruker Optics, Ettlingen, Germany). A baseline correction using the rubber-band method with 64 data points was also performed on each spectrum. After baseline correction, a second derivative was calculated for each IR spectrum to identify sub-band positions to be used in the curve fitting analysis.

2.4.3. Principal Component Analysis (PCA)

PCA is a method that has proved capable of discriminating small variations between spectra contained in large datasets. It is an unsupervised classification method which simplifies a complex dataset by reducing the number of variables and removing all redundancy in the information. The new dataset is divided in principal components (PC 1, 2, 3 …) and classified according to the importance of information in the dataset [74]. PCA was applied to the spectra and maps using a home-made program written in Matlab (Mathworks, USA).

2.4.3.1. PCA applied to set of single spectra from FTIR and Raman maps

In this analysis, PCA classifies information in groups by producing a cloud of points according to PCs. Each point corresponding to a spectrum. Spectra from the *in vitro* mineralisation study were selected for each sample (as described in Section 1.4.1), and then a PCA was performed on both Raman and IR spectra. Prior to PCA, Raman spectra were smoothed (Savitzky-Golay algorithm, second polynomial order, 9 points), and baseline corrected using OPUS software (Bruker Optics, Ettlingen, Germany). Owing to a strong scattering background in the IR spectra, Mie scattering correction was performed accordingly to A. Kholer's program in Matlab. In fact, when the IR light goes through a scattering particle (e.g. microcalcification), its path is deviated, which induces consequences in FTIR spectroscopy. The IR spectra, containing the biochemical information are distorted and the analysis is challenging. In consequence of which, a Mie scattering correction is applied before the processing [75], [76]. It is an algorithm, which corrects distortion in spectra based on the extended multiplicative signal correction (EMSC). In this correction, a target spectrum of Matrigel, which contains pure proteins of the ECM [76], was used to reproduce the baseline. Then, spectra were truncated in the spectral region between 1800 and 900 cm^{-1}.

2.4.3.2. PCA applied to Raman and IR maps

Prior to applying a PCA to Raman spectra, a cosmic ray removal was performed by using a median filter, followed by a baseline correction with asymmetric least squares smoothing and a vector normalisation in Matlab, whilst IR spectra were truncated to the fingerprint region (1800-900 cm^{-1}) and vector normalised (Matlab). A PCA was performed on Raman and IR maps of breast tissue samples using a toolbox in Matlab.

2.4.4. Partial Least Square (PLS) model

PLS is a supervised method which identifies the relationship between several variables [77]. In the context of the measurements presented here, the model was built to be able to determine the amount of carbonate within microcalcifications in breast tissue biopsies based on spectral analysis performed with the different mineral standards. The advantage of using this model is that it takes into account the statistical variance, e.g. variation between the concentration (carbonate ion substitution) given by the manufacturer and the real percentage of carbonate in the Hap powders or the variation between biopsies from different patients or different stages of pathology [77]. The PLS model was performed using a program in Matlab software (Mathworks, USA). The aim was to use a model spectrum based on the cHap standards in order to obtain the most relevant information also called latent factors or variables. The next step was to decompose the dataset from breast tissues to extract the relevant information that fit the model spectrum. The PLS model was built for a given number of latent factors and then used to predict the percentage of carbonate ion substitution in each microcalcification contained in breast tissue sections [78]. Raman and IR spectra were truncated to the phosphate and carbonate region, as described before. Raman spectra were baseline corrected and normalised in Matlab. FTIR spectra were normalised and a second derivative analysis was applied in Matlab.

Chapter 3 : Mineral standards as a model for microcalcifications

3.1. Introduction

As discussed previously, mineralisation is a complex mechanism which occurs in normal physiology in bone formation or bone remodelling but also in pathological processes, e.g. vascular calcifications, urinary stones, mammary microcalcifications etc. It appears that mineralisation found in different diseases is not defined as a linear process, but instead is complex and composed of different phases. The timeline and different stages of mineralisation for breast microcalcifications are still unknown.

3.1.1. Mineral phase and precursors

The mineral phase of a normal calcification corresponds to the formation of cHap crystal and is considered as the main compound of calcifications [79]. However, many studies suggest that different components are involved during this mineral phase. In fact, different calcium phosphates are considered as playing a role in cHap formation [80], such as amorphous calcium phosphate (ACP), octacalcium phosphate (OCP), dicalcium phosphate dehydrate (DCPD), or tricalcium phosphate (β-TCP) [40], [80], [81]. A few examples of phosphate minerals occurring in biological tissues with their chemical formula are listed in Table 3.1.

Following the example of Hap crystal, which is not found in its pure form but carbonated, β-TCP is not pure but always magnesium-substituted (β-TCMP) in biological tissue [82].

Table 3.1 Phosphate minerals in biological human tissues. In cHap, x = other cation substitutions for Ca^{2+} and y= other anion substitutions for OH^-. In ACP, the calcium-to-phosphate ratio is variable. Adapted from [40], [80]–[82].

Minerals	Chemical formula	Location in Human tissues
Carbonated apatite (cHap), A or B-type	$(Ca, Na, Mg, X)_{10} (PO_4)_6 CO_3$ $(Ca, Na, Mg, X)_{10} (PO_4, CO_3)_6 (OH, Y)_2$	Enamel, dentine, bone, urinary stone, breast microcalcifications, soft tissue deposits
Amorphous calcium phosphate (ACP)	$Ca_X (PO_4)_y$, variable composition	Heart calcifications with uremia, aortic valves
Octacalcium calcium phosphate (OCP)	$Ca_8 H_2 (PO_4)_6 \cdot 5H_2O$	Dental and urinary calculi
Dicalcium phosphate Dihydrate (DCPD) or Brushite	$Ca_8 HPO_4 \cdot 2H_2O$	Dental calculi, chondrocalcinosis
Mg-substituted β-tricalcium calcium phosphate (β-TCMP) or Mg-substituted Whitlockite	$\beta\text{-}Ca_{3-x} Mg_x (PO_4)_2$	Dental calculi, arthritic cartilage, and breast microcalcifications
Magnesium Ammonium phosphate or Struvite	$MgNH_4 PO_4 \cdot 4H_2O$	Urinary stone
Acid Magnesium Ammonium phosphate or Newberyite	$MgHPO_4 \cdot 3H_2O$	Urinary stone

These elements are involved in several physiological or pathological processes such as bone formation or vascular calcifications [83]. A study has reported the case of a dog with dental calculus containing mainly calcium carbonate (or calcite), which is not the case in human where OCP is mainly found. The conclusion was that the dog saliva has a higher pH than human and could be responsible for calcite formation [80]. Hence, pH variation can also interfere with the mineralisation process.

Finally, depending on pH variation or temperature, these different elements of the mineral phase can contribute to the transformation of one compound into another, e.g. OCP or ACP can transform into cHap and cHap into ACP or β-TCP [80], and the question here is whether these results can correlate with the onset of a tumour.

3.1.2. Tumour environment and calcifications

Tumours are known to induce hypoxia and upregulation of metabolic processes. Changes in metabolic activity lead to an increase of H^+ and CO_2 intracellular concentrations which are released (via different transporters) out of the cells creating an acidic environment [84]. This phenomenon has been observed in breast cancer progression. In fact, in normal breast ducts, the extracellular pH (pHe) and intracellular pH (pHi) are 7.4 and 7.2, respectively, which correspond to a physiological pH.

Conversely, in DCIS, the pHe decreases to 6.8 and 6.7 for invasive stage, whilst the pHi remains stable around 7.2 in both stages. The regulation of tumour pH plays an important role in cell proliferation and cancer progression [85].

Thus, the acidic environment created by tumour can involve different precursors in microcalcifications. In this study, the hypothesis is that different elements found in breast tissue biopsy samples can be associated with cHap but also with other components (e.g. OCP, ACP). Hence, a spectroscopic analysis of minerals other than cHap is appropriate in order to determine the composition of microcalcifications in human tissue samples.

3.2. Spectroscopic analysis

Many studies have previously used FTIR and Raman spectroscopy techniques to readily analyse biological apatite and in particular the carbonated apatite mainly found in biological samples, e.g. bone, dental enamel [36], [86]. For instance, using these complementary techniques, it is possible to assess the contribution of each component of mineral standards (phosphate and carbonate groups) separately. In fact, PO_4^{3-} and CO_3^{2-} ions present both IR- and Raman-active modes [87].

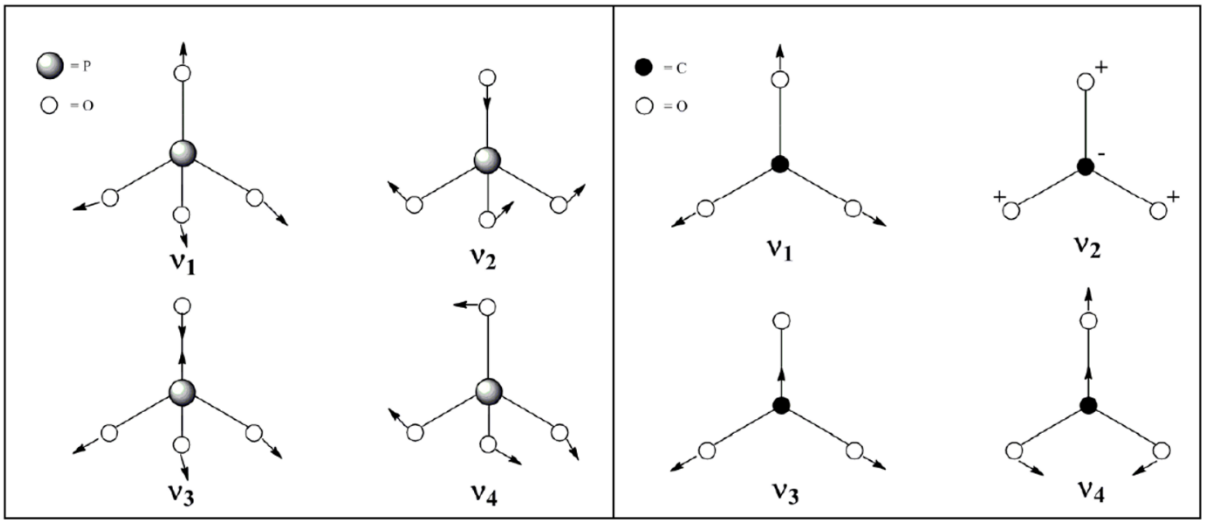

Figure 3.1 Vibrational modes of (left) PO_4^{3-} ion and (right) CO_3^{2-} ion. Modified from [87].

As illustrated in Figure 3.1 (left), phosphate ions have four distinct vibrational modes: ν_1 and ν_3 corresponding to the symmetric and asymmetric stretching, respectively, ν_2 and ν_4 corresponding to the symmetric and asymmetric bending, respectively. Note that stretching is related to a change in bond length whilst bending is related to a change in bond angle [87]. These vibrational modes are active both in Raman and IR spectroscopy.

Carbonate ions (Figure 3.1 right) have also four vibrational modes: ν_1 and ν_3 corresponding to the symmetric and asymmetric stretching, respectively, ν_2 and ν_4 corresponding to the out-of-plane and in-plane bending, respectively. ν_1 is the only Raman-active mode, whilst ν_2, ν_3 and ν_4 are the IR-active modes (mutual exclusion rule) [87].

Based on this knowledge, the starting point of the study was to identify the peaks related to phosphate and carbonate ions and assess their position.

3.2.1. FTIR and Raman spectra of cHap powders

Mineral standards (as presented in Chapter 2, section 2.1.3) were analysed using FTIR and Raman spectroscopy. A number of peaks (PO_4^{3-} and CO_3^{2-} bands) and their positions were assessed based on published tables in the literature in order to interpret data from biopsy samples and in vitro microcalcifications.

3.2.1.1. Raman spectra

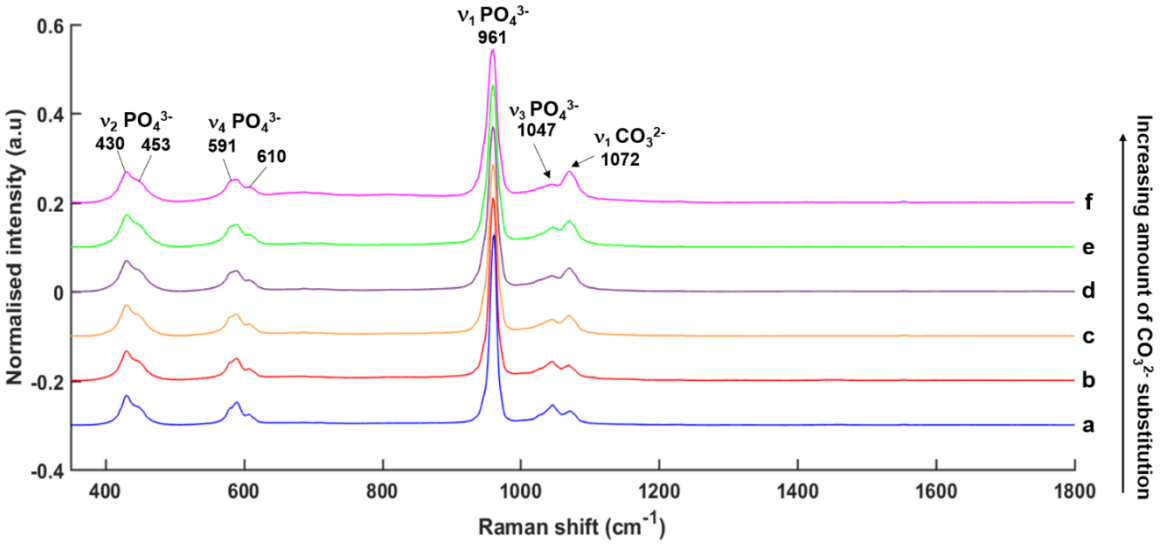

Figure 3.2 Raman spectra from Hap pellets containing an increasing percentage of CO_3^{2-} substitution: (a) 1.24%, (b) 2.92%, (c) 4.43%, (d) 5.24%, (e) 7.52% and (f) 8.12% w/w. The spectra exhibit specific PO_4^{3-} and CO_3^{2-} bands of interest. Each spectrum was obtained as an average of 5 spectra per mineral. Spectra were normalised to the overall intensity in the range 1800-350 cm^{-1}.

Figure 3.2 shows an example of Raman spectra in the fingerprint region from Hap containing different percentage of CO_3^{2-} substitution. Raman spectra exhibit several PO_4^{3-} and CO_3^{2} bands. Based on data from Penel et al., the peak at 1072 cm^{-1} was assigned to the ν_1 CO_3^{2-} band whilst all the other peaks are related to different vibrational modes of the PO_4^{3-} ion [36]. The ν_1 CO_3^{2-} band is well-defined and appears to increase proportionally to the increasing amount of CO_3^{2-} substitution. The peak assignment is reported in Table 3.2.

The PO_4^{3-} band at 961 cm^{-1} is the most known and used in several studies, for instance to determine the crystallinity of Hap or to calculate the amount of carbonate. Penel et al. have highlighted that, based on this peak, it is possible to discriminate between type A and type B CO_3^{2-} ion substitutions [36]. In fact, in type A substitutions, the phosphate peak presents two peaks at 947 and 957 cm^{-1} which is not the case in our cHap powders. Regarding the CO_3^{2-} band, discrimination is also possible with two peaks at around 1103 and 1070 cm^{-1} for type A and B, respectively. Only one peak at 1072 cm^{-1} is apparent in our samples. These results demonstrate that our samples contain only type B CO_3^{2-} ion substitution.

Table 3.2 Assignment of Raman peak positions for PO_4^{3-} and CO_3^{2-} bands for each cHap based on [36].

Peak position (cm^{-1})							Assignment
1.24	2.92	4.43	5.24	7.52	8.12	wt.%	
431	430	430	430	430	430		v_2 PO_4^{3-}
451	451	451	452	452	452		
579	580	580	580	580	580		v_4 PO_4^{3-}
591	590	590	590	590	590		
609	609	610	610	611	611		
961	961	961	960	960	960		v_1 PO_4^{3-}
1024							v_3 PO_4^{3-}
1047	1045	1045	1045	1046	1044		v_1 CO_3^{2-}
1072	1070	1070	1070	1070	1070		

In parallel, pure hydroxyapatite without carbonate substitution was also analysed and compared with cHap in order to distinguish the main changes in the Raman spectra due to carbonation (See Appendix, supplementary data 2, Figure B.1). The comparison between pure Hap and the different cHap spectra shows the same position for all the phosphate peaks. However, an additional peak at 1076 cm^{-1} is observed in pure Hap spectra, which corresponds to ν_3 PO_4^{3-} band. No carbonate bands are apparent in pure Hap spectra.

3.2.1.2. FTIR spectra

The same investigation was performed using FTIR spectroscopy. Figure 3.3 shows an example of FTIR spectra in the fingerprint region from KBr pellets of Hap containing different percentage of CO_3^{2-} substitution.

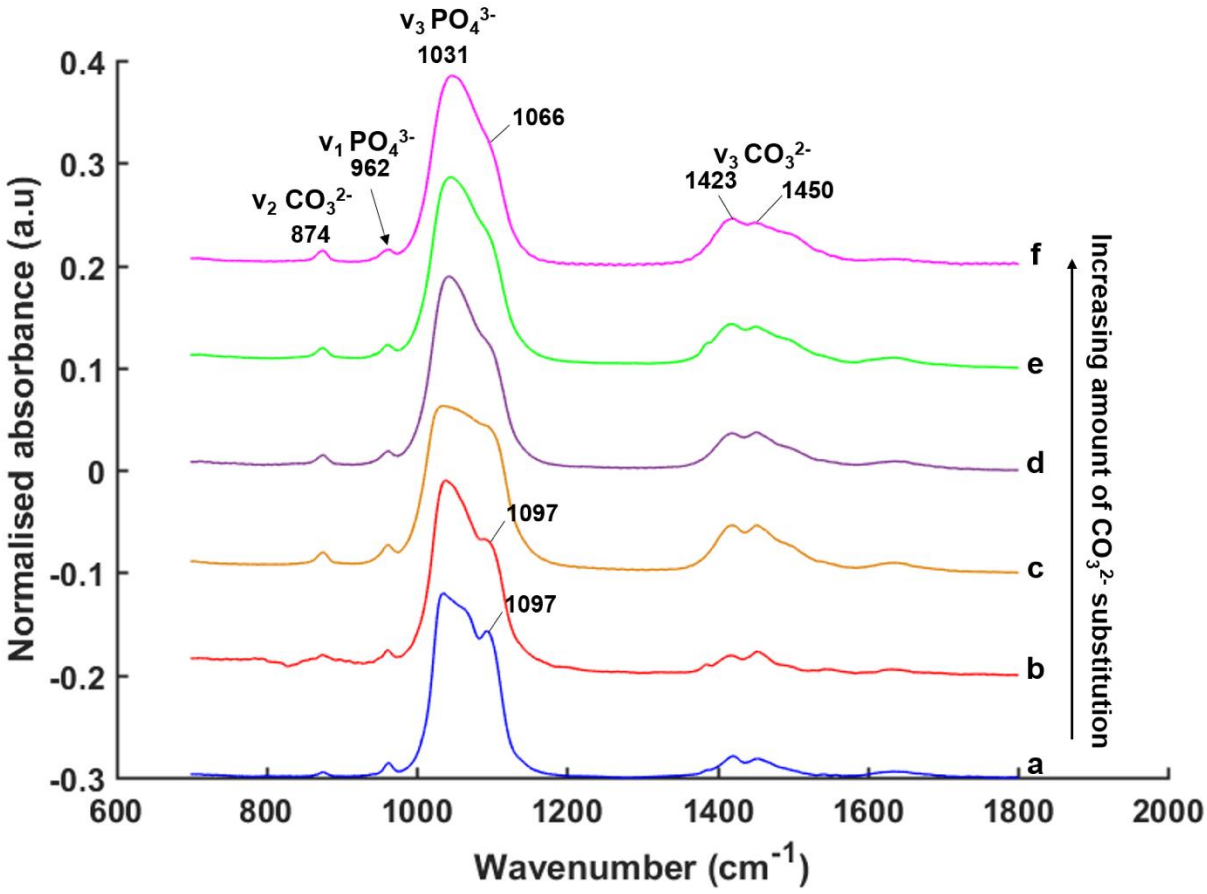

Figure 3.3 FTIR spectra from Hap pellets containing an increasing percentage of CO_3^{2-} substitution: (a) 1.24%, (b) 2.92%, (c) 4.43%, (d) 5.24%, (e) 7.52% and (f) 8.12% w/w. The spectra exhibit specific PO_4^{3-} and CO_3^{2-} bands of interest. Each spectrum was obtained as an average of 5 spectra per mineral. Spectra were normalised to the overall intensity in the range 1800-700 cm^{-1}.

For clarity, spectra were normalised and stacked (See appendix, supplementary data 2, Figure B.2 for the full spectral range). Four specific peaks are well-defined and correspond to ν_1 and ν_3 PO_4^{3-} bands and ν_2 and ν_3 CO_3^{2-} bands. In particular, for the ν_3 PO_4^{3-} band, which is a broad peak, the shape seems to vary with the amount of carbonate. A shoulder at 1097 cm^{-1} appears in the lowest concentrations of carbonate at 1.24 and 2.92 wt.% (a and b, blue and red spectra) and disappears slowly from 4.43 to 8.12 wt.% of CO_3^{2-} substitution (Fig. 3.3c-f). The ν_2 and ν_3 CO_3^{2-} bands are also well-defined and appear to increase proportionally to the increasing amount of CO_3^{2-} substitution.

FTIR spectra exhibit numerous PO_4^{3-} and CO_3^{2-} bands. When comparing with literature, it appears that three peaks correspond to CO_3^{2-} bands at 1450 and 1423 cm^{-1} and one at 874 cm^{-1}. Two peaks at 962 and 1031 cm^{-1} are PO_4^{3-} bands [88], [89]. The assignment for each peak is summarised in Table 3.3.

Table 3.3 Assignment of peak positions for PO_4^{3-} and CO_3^{2-} bands for cHap samples based on the literature, [88]–[90].

Peak position (cm^{-1})							Assignment	Literature
1.24	2.92	4.43	5.24	7.52	8.12	wt.%		
961	961	961	961	961	961		v_1 PO_4^{3-}	[88],[89]
1034	1036	1031	1044	1044	1047		v_3 PO_4^{3-}	[88],[89]
1063								
1094	1091	1097	1094	1095	1096			
1421	1416	1420	1419	1415	1419		v_3 CO_3^{2-}	[88],[90]
1454	1454	1454	1454	1452	1455			
875	875	875	875	874	875		v_2 CO_3^{2-}	[88]

Based on these results, it is also possible to distinguish type A from type B CO_3^{2-} ion substitution. In fact, for type B, two peaks are found between 1450-1456 cm^{-1} and 1422-1427 cm^{-1} for ν_3 CO_3^{2-} and 875 cm^{-1} for ν_2 CO_3^{2-}. For type A substitution, three peaks are found at 1545, 1450-1456 cm^{-1} for ν_3 CO_3^{2-} and 880-881 cm^{-1} for ν_2 CO_3^{2-} [88]. In our cHap standards, only type B CO_3^{2-} ion substitution is found which is in line with the results obtained from Raman spectra. However, further analysis needs to be performed e.g. area under each peak, calculation of carbonate-to-phosphate ratio etc.

3.2.2. Raman and FTIR spectra of other standards

In order to complete the study, additional minerals were analysed using Raman and FTIR spectroscopy. Spectra of ACP, β-TCP and OCP, which are considered potential precursor phases, were recorded. Raman and FTIR spectra are shown in Figure 3.4 and 3.5, showing peak positions and their corresponding assignment to PO_4^{3-} and CO_3^{2-} modes.

Regarding the Raman spectra (Figure 3.4), the peaks correspond to different vibrational modes of the phosphate group. ACP exhibits five peaks:

- ν_1 PO_4^{3-} band at 955 cm^{-1} (with an upshift of 4 cm^{-1} to the peak previously found) [91], [92].
- ν_3 PO_4^{3-} bands at 1034 and 1077 cm^{-1} (instead of a single peak at around 1050 cm^{-1}) [91].
- ν_4 PO_4^{3-} band at 588 cm^{-1} and ν_2 PO_4^{3-} band at 427 cm^{-1} as expected.

Unfortunately, the literature is quite poor and contradictory regarding the Raman analysis of ACP. The shift and additional peaks could be due to the sample preparation, which depends greatly on temperature and preparation time [92].

The spectrum of β-TCP presents nine peaks (1088, 1015, 969, 949, 630, 548, 476, 438 and 407 cm^{-1}) [91], [93] and OCP eight peaks (1077, 1046, 1011, 958, 874, 609, 590, 427 cm^{-1}) [91], [94], [95] corresponding to the different vibrational modes for PO_4^{3-} ion which are expected and in line with other publications.

The FTIR spectra of ACP (Figure 3.5) exhibit four peaks corresponding to PO_4^{3-} and CO_3^{2-} modes: ν_1 PO_4^{3-} band at 1059 cm^{-1} [96], ν_3 CO_3^{2-} bands at 1427 and 1483 cm^{-1}, and ν_2 CO_3^{2-} band at 873 cm^{-1} which seems to arise from type B CO_3^{2-} ion substitution.

The spectrum of β-TCP exhibits seven peaks [91], [97] and OCP five peaks [91], [95] corresponding to as many PO_4^{3-} modes. All peak positions are in line with the literature.

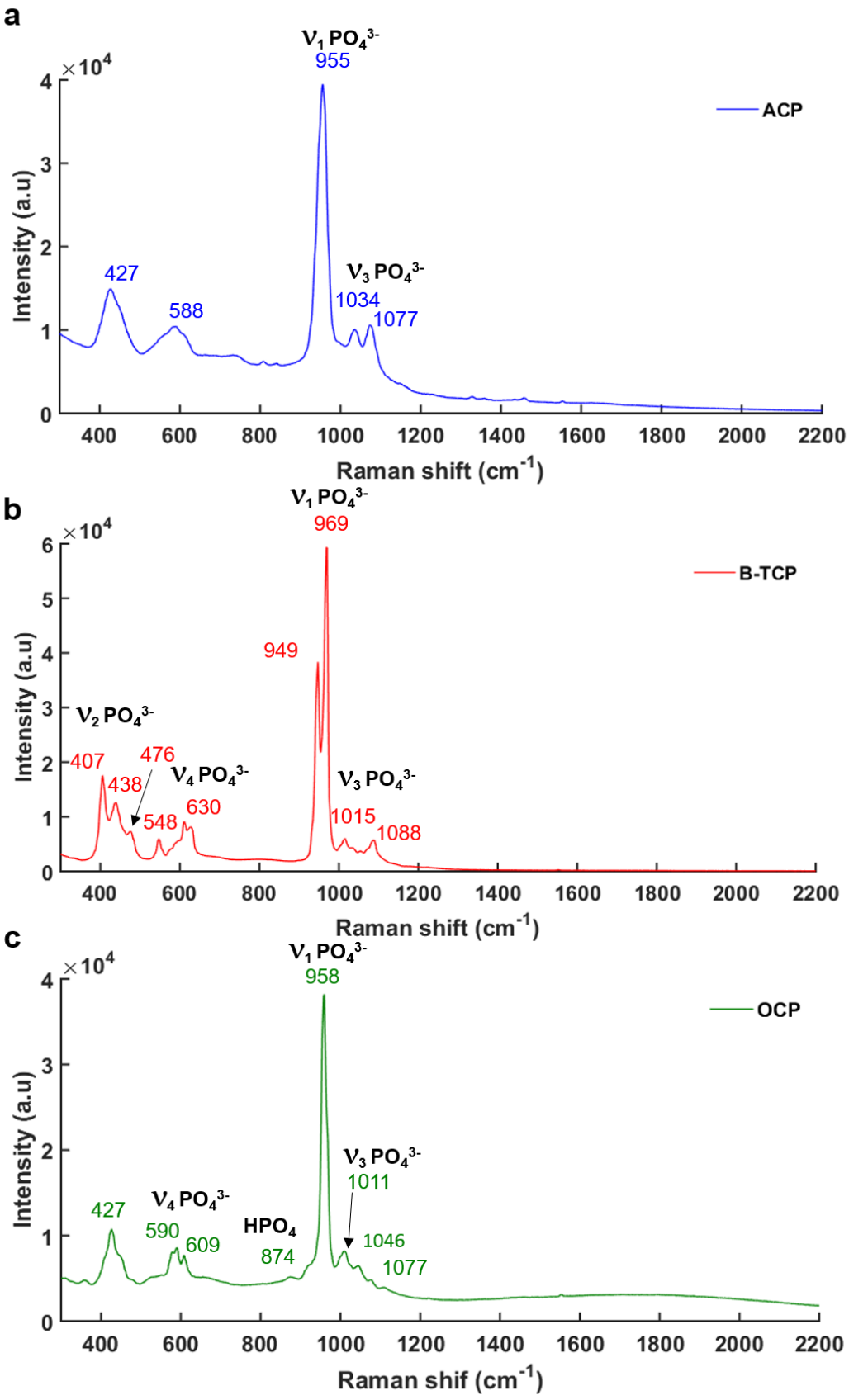

Figure 3.4 Raman spectra of (a) ACP, (b) β-TCP and (c) OCP powders. Average of 5 spectra. Spectra were baseline-corrected to 2200-350 cm^{-1}.

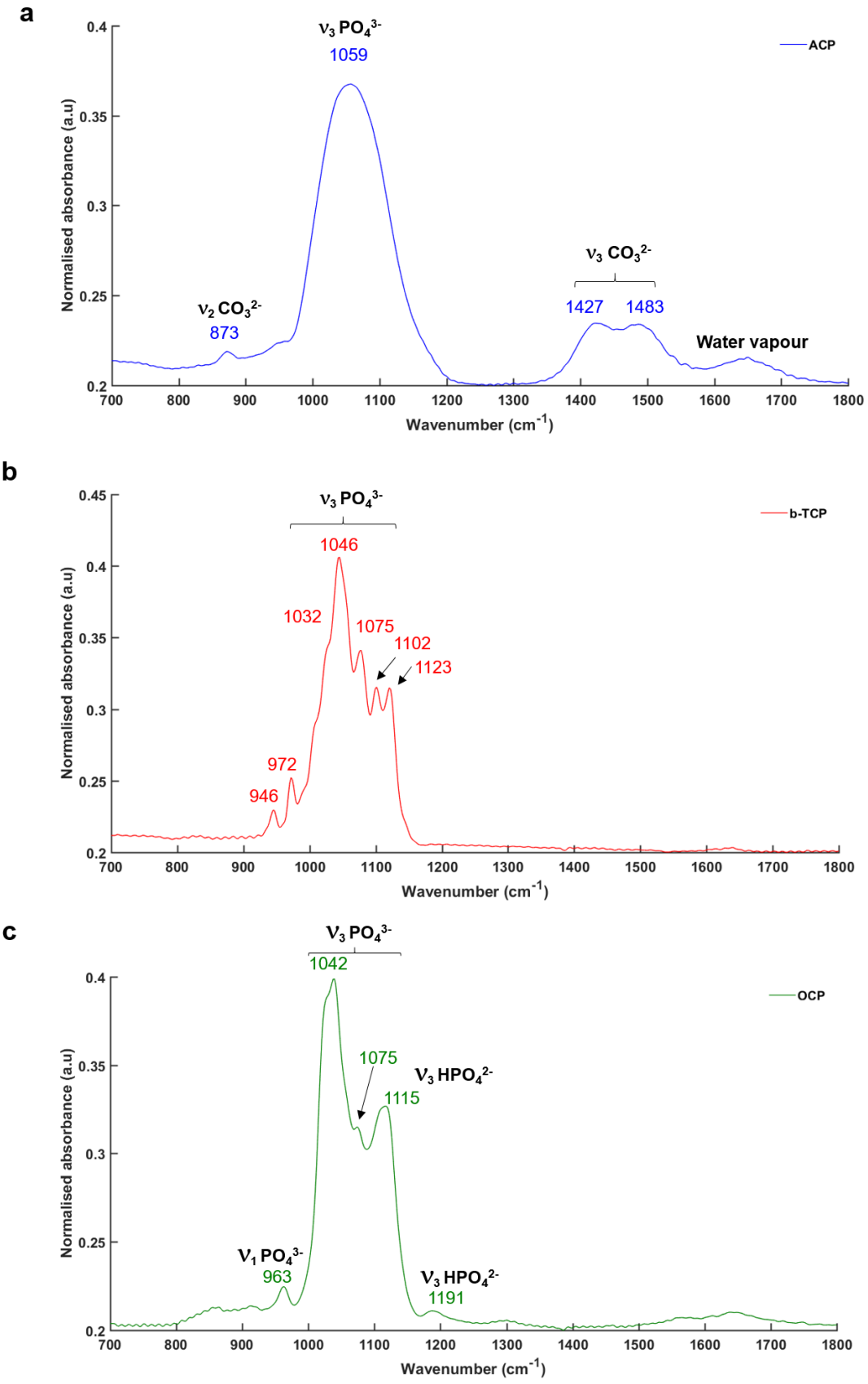

Figure 3.5 FTIR spectra of KBr pellets from (a) ACP, (b) β-TCP and (c) OCP. Average of 5 spectra. Spectra were normalised to 1800-700 cm^{-1}.

3.3. Peak analysis

To analyse the phosphate and carbonate bands of the minerals, a peak decomposition by curve fitting analysis was applied to the spectra. This method allows us to single out overlaid peaks and to extract the area and full width at half maximum (FWHM) for each peak. These data are then used to calculate the carbonate-to-phosphate (C:P) ratio for each sample. A study from Gadaleta et al. suggests using as a reference, the results from the second derivative analysis (for the FTIR data), to enable sub-peak positions to be appropriately identified and correlated with the curve fit analysis [98]. The results from the peak decomposition for each sample's FTIR and Raman spectra are shown in Appendix, supplementary data 2, Figure B.3–B.8.

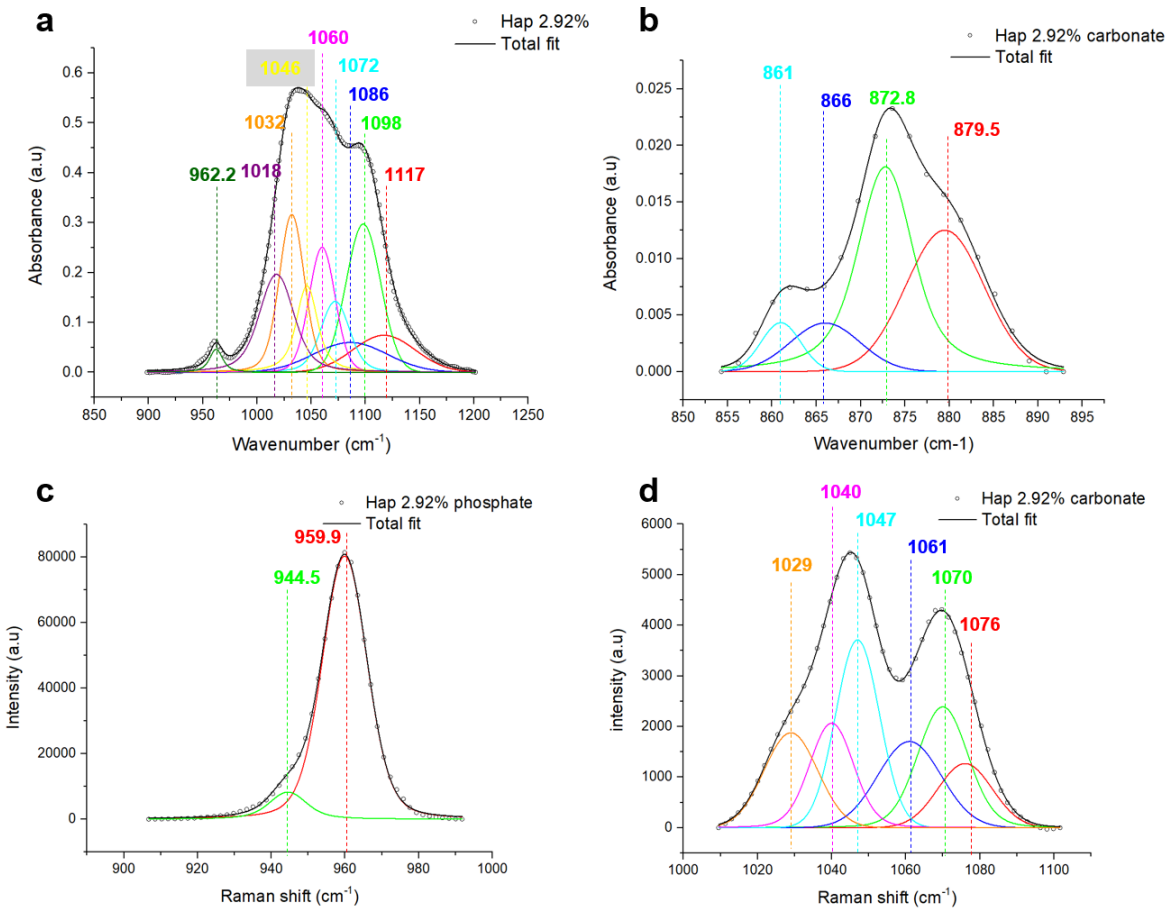

Figure 3.6 Results of curve fit analysis applied to (a, b) FTIR and (c, d) Raman spectra of cHap containing 2.92 wt. % CO_3^{2-} substitution. Spectra were truncated to (a, c) phosphate band (1200-900 cm^{-1}) and (b, d) carbonate band (890-855 cm^{-1}) and baseline-corrected. $R^2 > 0.99$.

Figure 3.6 illustrates the results of peak decomposition applied to FTIR and Raman spectra for each CO_3^{2-} and PO_4^{3-} band separately. The peak decomposition gives information about the sub-bands in FTIR and Raman spectra. All FTIR spectra from cHap pellets present the same profile with nine components (1117, 1098, 1086, 1072, 1060, 1046, 1018, 1032 and 962 cm^{-1}) for PO_4^{3-} except for cHap 5.24% and 8.12% CO_3^{2-}: one additional peak at 1002 cm^{-1} for 5.24% cHap and one missing at 1072 cm^{-1} for 8.12% cHap substitution (see Appendix, supplementary data 2, Figure B.3). Regarding the CO_3^{2-} band, all cHap are well-represented by four components at around 880, 873, 866 and 861 cm^{-1}.

The peak positions and their assignments are summarised in Table 3.4.

Table 3.4 FTIR peak positions and their assignments to the phosphate and the carbonate bands of cHap based on the literature, [86], [88], [89], [98]–[102].

Peak position (cm^{-1})	Assignment	References
861	v_2 CO_3^{2-}, Hap	[102]
866	v_2 CO_3^{2-}, Labile, unstable, non-apatitic	[98],[100]
873	v_2 CO_3^{2-} type B cHap	[98],[100]
879	v_2 CO_3^{2-} type A cHap	[98],[100]
962	v_1 PO_4^{3-}	[88],[89],[98],[99]
998-1002	v_3 PO_4^{3-}	[98]
1018-1020	Nonstoichiometric apatite, type B cHap	[89],[98],[99],[101]
1030-1032	v_3 PO_4^{3-} occurring in stoichiometric apatite	[86],[98]
1044-1045	v_3 PO_4^{3-}	[88]
1063		[89],[99]
1056-1075		[98]
1086		[88]
1098		[98]
1109-1117	v_3 PO_4^{3-} found in mature, poorly crystalline Hap	[98]

All listed peak positions correspond to different vibrational modes of CO_3^{2-} and PO_4^{3-} and are in line with the literature [86], [88], [89], [98]–[102].

To determine the sub-bands in FTIR spectra, the results were combined with those derived from the second derivative spectra. The correlation between the second derivative results (Figure 3.7) and the peak decomposition show a good agreement in terms of number and position of the peaks.

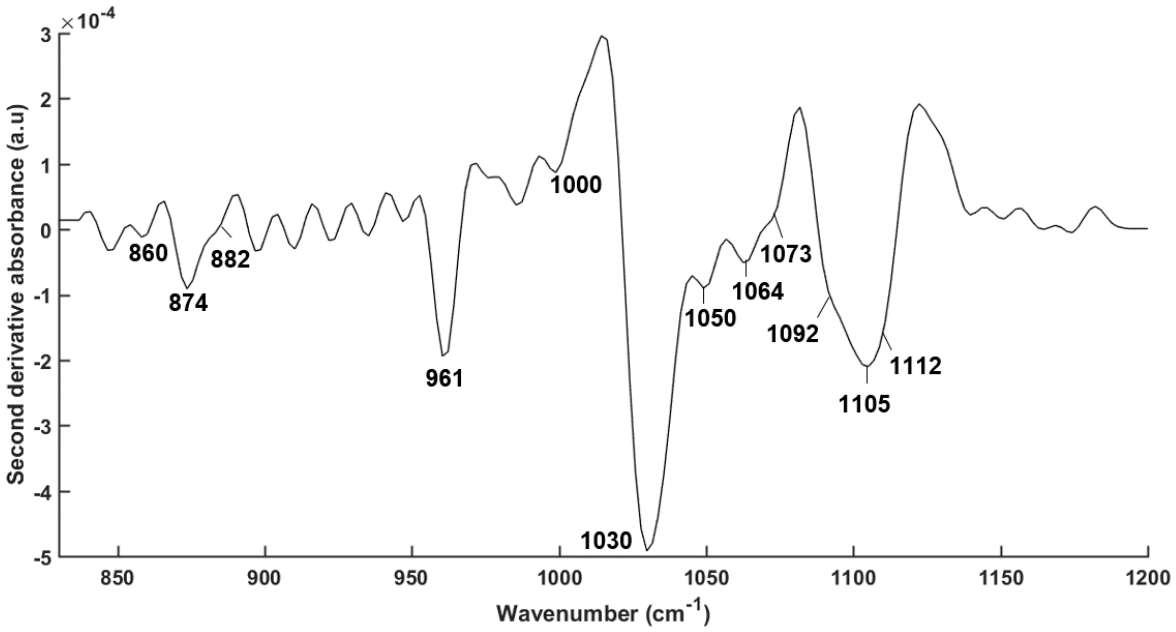

Figure 3.7 Second derivative spectrum of cHap pellet with 2.92 wt. % CO_3^{2-} substitution.

In parallel, a peak decomposition was also performed for the carbonate band at 1500-1400 cm^{-1} in order to select the best carbonate peak for a calibration curve.

As illustrated in Figure 3.8, FTIR spectrum exhibits five components at around 1495, 1466, 1453, 1441 and 1419 cm^{-1} corresponding to a combination of the ν_1 CO_3^{2-} band [88]. All the FTIR spectra exhibit the same five components (data not shown).

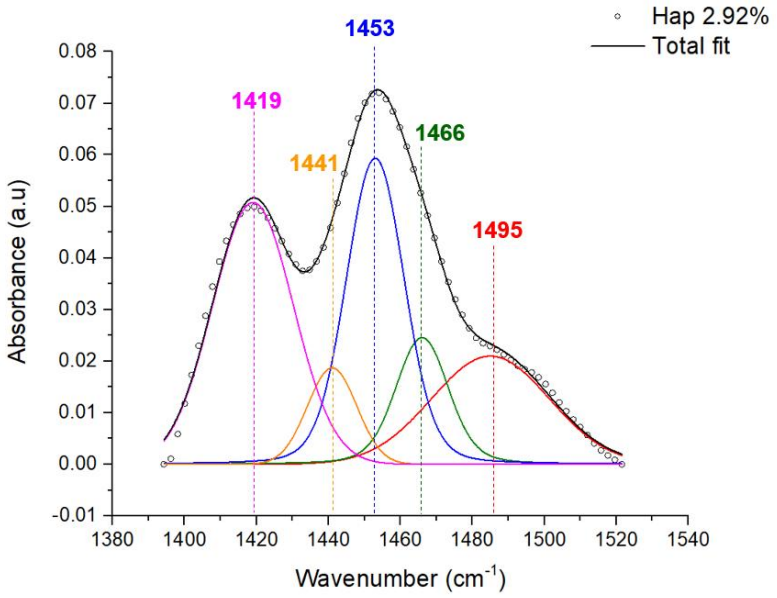

Figure 3.8 Results of a peak decomposition performed on the FTIR spectrum of cHap with 2.92 wt. % CO_3^{2-} substitution. The spectrum was baseline-corrected to 1400-1520 cm^{-1}. $R^2 > 0.99$.

Regarding the Raman spectra, the same analysis was performed and illustrated in Figure 3.6 (see above). cHap spectra exhibit the same profile for PO_4^{3-} and CO_3^{2-} bands. There are two components at around 945 and 960 cm^{-1} for the PO_4^{3-} band. For the CO_3^{2-} band, six components are present for each sample: 1029, 1040, 1047, 1061, 1070, and 1076 cm^{-1}, where 1070 cm-1 corresponds to the ν_1 CO_3^{2-} mode at 1070 cm^{-1} [103]. The peak positions and their assignments are listed in Table 3.5.

Table 3.5 Raman peak shifts and their assignments to the phosphate and carbonate modes of cHap based on the literature, [36], [103].

Peak position (cm^{-1})	Assignment	References
945	v_3 PO_4^{3-}, type A cHap	
960	v_1 PO_4^{3-}	
1029	v_3 PO_4^{3-}	[36],[103]
1040		
1047		
1061		
1070	v_1 CO_3^{2-}	
1076	v_3 PO_4^{3-}	[103]

The area and FWHM of each peak (from FTIR and Raman spectra) are summarised in Appendix, supplementary data 2, Table B.1–1.6.

A peak decomposition analysis was also applied to the spectra of the other minerals including ACP, OCP and β-TCP. Common peaks to cHap were found in these minerals based on both FTIR and Raman data (see Appendix, supplementary data 2, Figure B.5 and B.8).

3.4. Calculation of the C:P ratio

The aim of this study was to derive a calibration curve, based on the results from curve fitting analysis, to assess the carbonate content of microcalcifications in breast tissue biopsy sections. The C:P ratio was calculated based on peak areas for each cHap sample to which a given amount of carbonate substitution (provided by the

manufacturer) was associated. This calculation was performed for both Raman and FTIR spectra in order to validate the method.

3.4.1. Analysis of FTIR spectra from cHap pellets

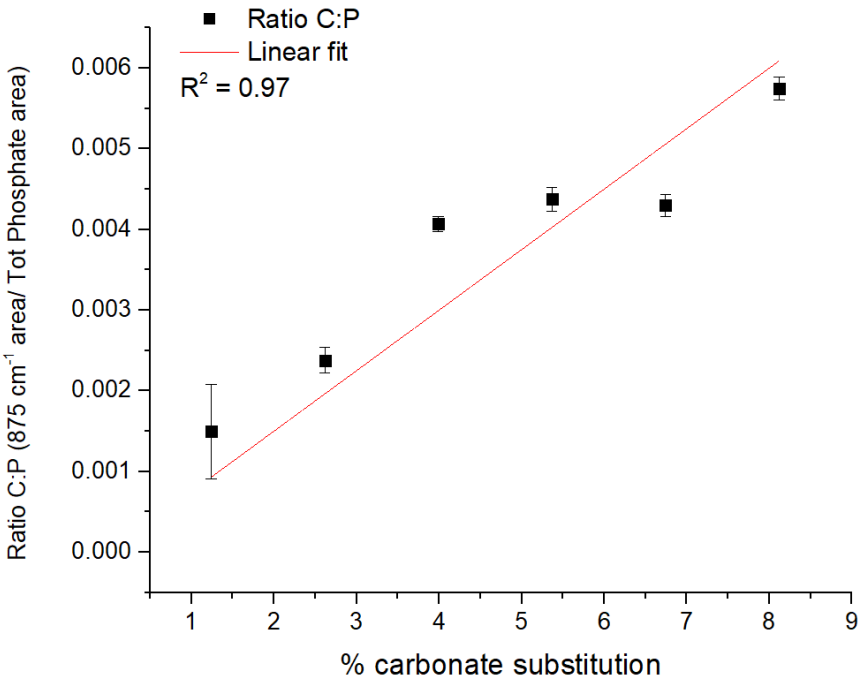

Figure 3.9 Linear regression of the plot of C:P ratio vs. % CO_3^{2-} substitution in cHap pellet samples. Data were obtained from FTIR spectra as the ratio of the peak area at 875 cm^{-1} to the sum of all phosphate peak areas. Two replicates were performed in those experiments. Values are mean ± SD. Regression equation: $y = 7.42 \cdot 10^{-4} x$; $R^2 = 0.97$.

The lack of information regarding the optimal definition of C:P ratio to use for FTIR analysis makes it challenging to extract a calibration curve, and hence different combinations were tested. Firstly, a calibration curve was performed based on the ratio of the 875 cm^{-1} peak area for carbonate peak to the total phosphate peak area. From this calculation, the quantitative relationship between the CO_3^{2-}/PO_4^{3-} peak area ratio and the amount of CO_3^{2-} in each cHap was established by linear regression with a high correlation coefficient ($R^2 = 0.97$) as illustrated in Figure 3.9. Secondly, different C:P ratios were calculated e.g. based on the total CO_3^{2-} peak area to the PO_4^{3-} peak area, or total CO_3^{2-} peak area to 1032 cm^{-1} peak area, however they either give similar

results or do not improve the calibration curve or the correlation coefficient (see Appendix, supplementary data 2, Figure B.9).
The curve fitting results based on carbonate bands at 1456, 1423 and 1408 cm^{-1} were also tested for the calibration curve but they do not change or improve the correlation coefficient (R^2 = 0.92) (see Appendix, supplementary data 2, Figure B.10).

In parallel, an integration method was used and the ratio was calculated from the total area under each phosphate and carbonate peak. This also did not change or improve the calibration curve or the correlation coefficient (R^2 = 0.95) (see Appendix, supplementary data 2, Figure B.11).

3.4.2. Analysis of Raman spectra from cHap pellets

A calibration curve was also derived using the ratio of the peak areas at 1070 and 960 cm^{-1} for CO_3^{2-} to the PO_4^{3-} bands. These peak positions have previously been used in other studies [70], [74], [103], [104].

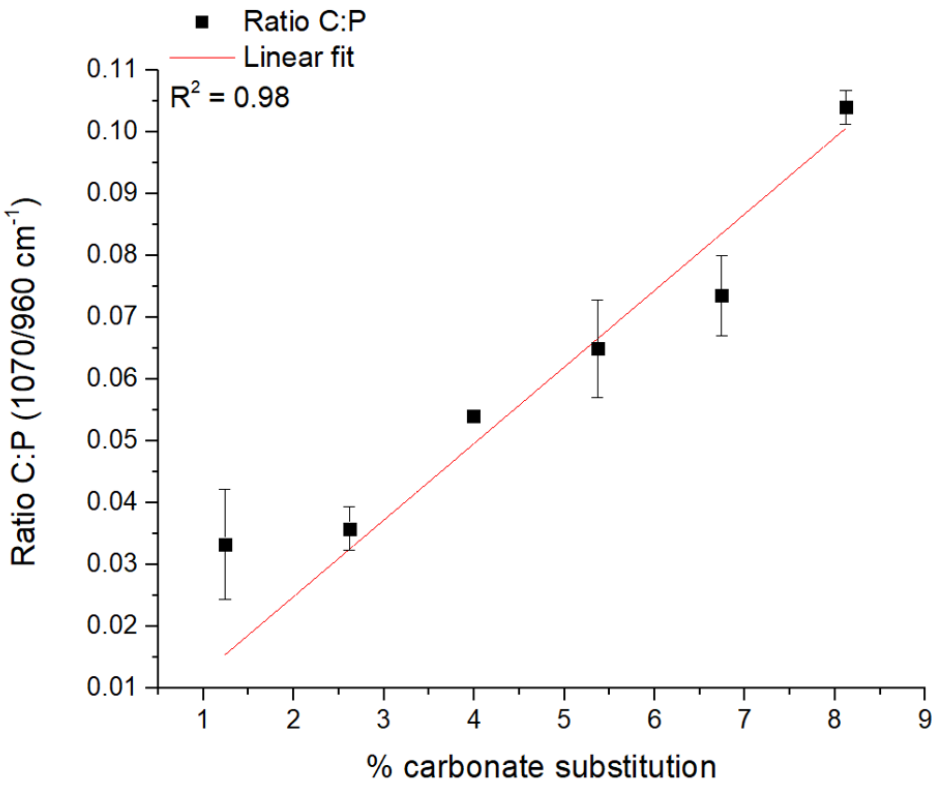

Figure 3.10 Linear regression of the plot of C:P ratio vs. % CO_3^{2-} substitution in cHap pellet samples. Data were obtained from Raman spectra as the ratio of the peak area at 1070 cm^{-1} to 960 cm^{-1}. Two replicates were performed in those experiments. Values are mean ± SD. Regression equation: $y= 1.239 \cdot 10^{-2} x$; $R^2 = 0.98$.

As illustrated in Figure 3.10, there is a linear regression of the plot of C:P ratio vs. amount of carbonate substitution with a high correlation coefficient ($R^2 = 0.98$).

The delicate part of this work using Raman spectra is that the carbonate and phosphate peaks are overlaid and this can lead to a bias in the calibration curve. However, surprisingly the calibration curve gave a good result in this case.

3.5. Discussion

This chapter which is devoted to the analysis of mineral standards confirms the possibility to analyse mineral compounds e.g. cHap, OCP, β-TCP and ACP using vibrational spectroscopy. Moreover, the analysis of minerals other than cHap, which is usually analysed in most studies, reveals that they exhibit similar features to cHap in both Raman and FTIR spectra. These results are crucial information for the rest of this study and can be translated to the analysis of biological samples and

microcalcifications. This study also highlights specific peaks of phosphate and carbonate (960 and 1070 cm^{-1}, respectively) [103] found in cHap Raman spectra. For cHap FTIR spectra, specific peaks are observed at 1030 cm^{-1} for phosphate and 875, 1408, 1423, 1456 cm^{-1} for type B carbonate ion substitution [88]. The cHap samples seem to contain type B CO_3^{2-} substitution, which matches the information given by the manufacturer. The choice of using B type in this study is in line with the literature. In fact, for instance, dental enamel presents 90% type B CO_3^{2-} substitution whilst only 10% represents type A CO_3^{2-} substitution [36] and the same results are found in bone mineral [100]. In breast microcalcifications, to date it has been demonstrated the presence of type B CO_3^{2-} substitution only. However, the literature is sometimes contradictory: according to Ren et al., the carbonate peaks at 880, 1413 and 1450 cm^{-1} are not characteristic of carbonated apatite. The presence of a sub-band at 880 cm^{-1} could be the result of carbonate absorption at the surface of Hap crystal rather than in the lattice [88]. However, several studies are based on these peaks for assignment and validation of the method [100], [102].

The next step of this study was to determine the sub-bands contained in Raman and FTIR spectra in order to single out overlaid peaks e.g. at 1070 cm^{-1} for carbonate.

The peak decomposition is a method commonly used in several studies of mineralisation [70] and mineral analysis [100] to decompose different regions in the spectra. Regarding the FTIR spectra, the samples present different profiles and can have additional or different components that can be assessed with second derivative analysis; however, even the second derivative spectra exhibit interferences and noise. Different elements can explain the noise and interferences. To avoid scattering artefacts in the FTIR spectra, a sample preparation using KBr pellets was necessary but not perfect, as pellets may differ in thickness, homogeneity and surface flatness. Moreover, the spectral limit at 700 cm^{-1} due to the MCT detector in the FTIR system can affect the spectral band shape in this region. Despite these limitations, the obtained calibration curves show a good linear regression between the different C:P ratios and the amount of carbonate substitution (R^2 = 0.97 and 0.98 for FTIR and Raman data, respectively). The peak decomposition analysis seems to be more reproducible for Raman data than FTIR data: Raman spectra present the same number of components for carbonate and phosphate bands and similar peak positions. In Raman spectroscopy, no specific sample preparation is needed and the powders are directly analysed without any artefact in the spectra.

However, in parallel to this method, a PLS model will be applied to the spectra from biopsy samples to assess the amount of carbonate in each microcalcification. An integration method based on the total area under the phosphate and carbonate peaks would be easier and faster to calculate; however, for comparison with Raman data, it is not possible to apply it because the carbonate and phosphate peaks are overlaid. All in all, peak decomposition appears the most accurate method to analyse the spectra in terms of microcalcification composition.

Chapter 4 : Investigation of the chemical composition of microcalcifications in breast cancer

4.1. Introduction

Previous analyses of breast tissue sections using Raman and IR spectroscopies suggest that the grade of pathology is correlated to the chemical composition of microcalcifications, in particular the carbonate content in the Hap lattice or the protein level inside the microcalcification [59], [105].

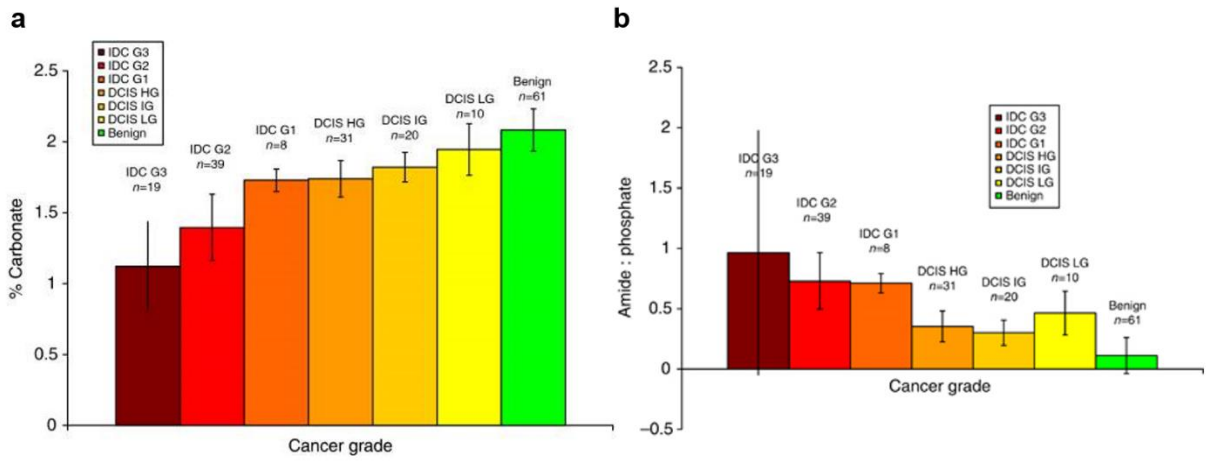

Figure 4.1 Different breast lesions (Benign, *in situ* (low, intermediate and high grades) and invasive cancer grades 1, 2, 3) classified according to (a) the amount of CO_3^{2-} and (b) the protein levels into breast microcalcifications assessed by FTIR spectroscopy. From R. Baker, 2010.

Baker et al. have previously shown that in benign lesions, microcalcifications from breast tissues have a higher concentration of carbonate ion substitution than malignant lesions (see Figure 4.1a). Besides, protein level measured by calculating the amide-to-phosphate peak ratio increases going from benign to invasive lesions [59]. The same results have been found by Haka et al. by calculating the peak height of CO_3^{2-} stretching at 1070 cm^{-1} and the FWHM of the PO_4^{3-} peak at 960 cm^{-1} for each stage of breast cancer. They concluded that the CO_3^{2-} peak is broader in benign lesions and it is not linearly correlated with the broadening of the PO_4^{3-} peak, which means that different impurities were added in Hap crystal and these seem to be

associated with proteins. They concluded that the protein level is higher in malignant lesions [105].

However, several questions remain to be addressed: why is the Hap crystal carbonate-substituted specifically in benign lesions? Is the crystal disorder created by impurities only due to proteins and specifically in malignant lesions? Could the pH variation at different stages (as discussed in Chapter 3, section 3.1.2) play a role in Hap crystal formation and are its precursors involved?

To answer these questions, a comparison between microcalcification features was made between frozen and paraffinised tissue sections for different stages of breast pathology.

4.2. Chemical and spatial information on microcalcifications found in frozen breast tissues

4.2.1. FTIR analysis

FTIR spectroscopy-derived information were obtained for microcalcifications using the Agilent system with two different detectors, as described in Chapter 2, section 2.2.2. One approach was to record FTIR images and the second one was to record single FTIR spectra.

As expected from the literature and shown in Figure 4.2, FTIR spectra of microcalcifications present structured phosphate and carbonate bands. FTIR images were recorded in the spectral range 3800-900 cm^{-1} which includes the CO_3^{2-} peaks at around 1420 and 1450 cm^{-1} and the PO_4^{3-} peak at around 1030 cm^{-1} (Figure 4.2a). Single point measurements were recorded in the spectral range 3800-800 cm^{-1} which also allows the detection of the CO_3^{2-} peak at around 875 cm^{-1} (Figure 4.2b). There is a difference in the shape of the phosphate peak (1200-900 cm^{-1}) between the mean spectrum from single point measurement (Figure 4.2b) and mean spectrum extracted from the FTIR image (Figure 4.2a). In fact, the mean spectrum from the single point measurement is an average of the entire microcalcification whereas the mean spectrum extracted from the FTIR image corresponds to a small area within the microcalcification.

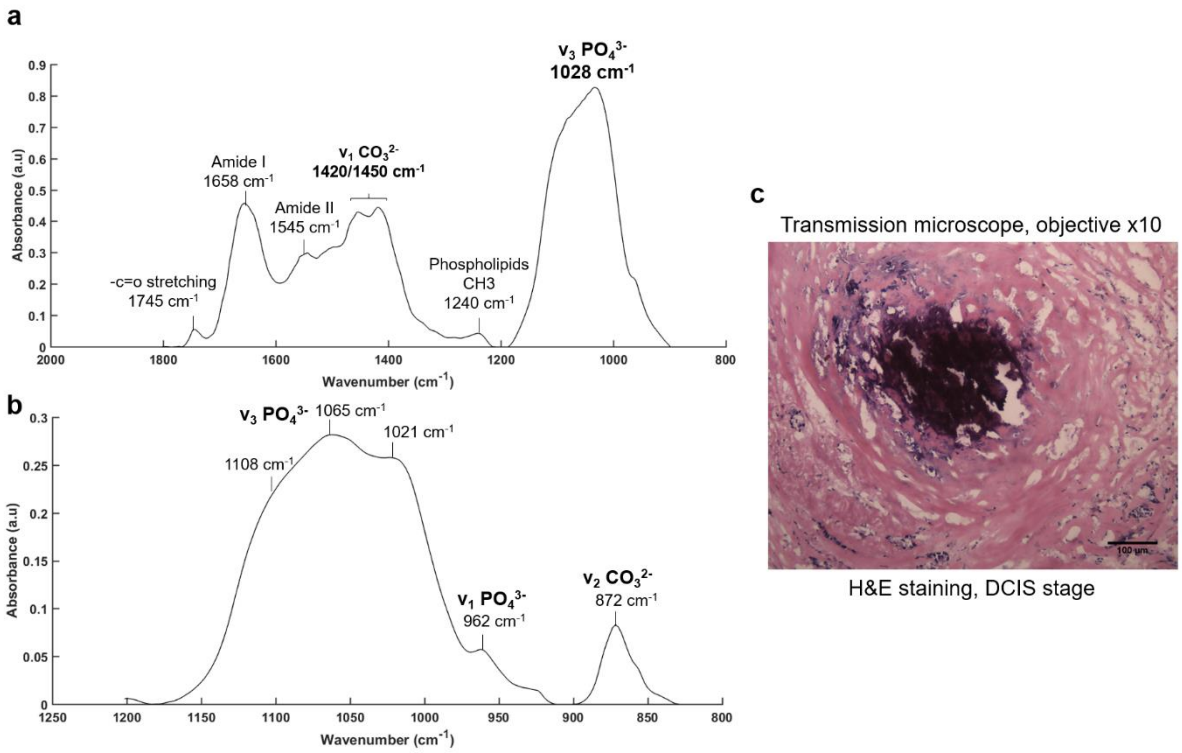

Figure 4.2 FTIR spectra of a microcalcification found in DCIS tissue obtained using (a) an FTIR image in the range 1800 to 900 cm^{-1} and (b) a single point measurement in the range 1200-830 cm^{-1}. (c) Image of the H&E stained breast tissue taken with a transmission microscope, x10 objective.

These data are rich in information but have also several disadvantages. The critical aspect of the single point measurements is that, for frozen tissues, the contribution from water vapour is very important at short wavelengths (protein or lipid peaks) and also in the carbonate region (at around 1420-1450 cm^{-1}). The second aspect is that, in order to take a measurement, a large area is only selected manually with the Agilent system and it is impossible to use a specific spatial resolution. The advantage of this measurement over that conducted with the imaging system is that the carbonate peak at 875 cm^{-1} can be measured. In fact, with the FTIR FPA imaging system, it is impossible to record a spectrum below 900 cm^{-1} due to the limit imposed by the detector sensitivity; on the other hand, the imaging mode allows a selection of a specific spatial resolution (i.e. 5.5 μm^2 pixel size) on the contrary to the single point measurement and the carbonate peak in the 1400 cm^{-1} region is measurable. However, when tissue sections are embedded in paraffin, the carbonate peaks at 1420-1450 cm^{-1} are often overlaid with the CH_3 vibration of paraffin which makes this region non-exploitable. For these type of samples, correlative analysis using both single point measurements and FTIR images is useful.

Another advantage of using the FTIR imaging system is that FTIR images give information about the spatial distribution of the microcalcifications within the tissue as shown in Figure 4.3.

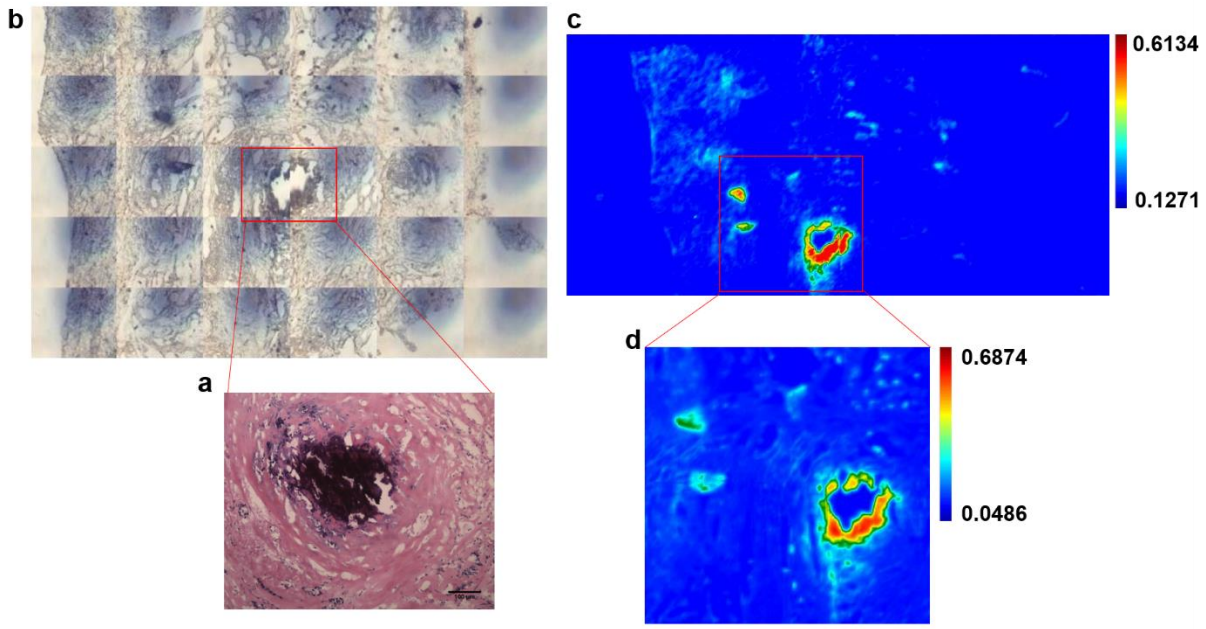

Figure 4.3 Visible and micro-transmission FTIR images of a DCIS breast cancer biopsy. (a) Histological section stained with H&E and imaged with a transmission microscope, x10 objective. (b) White light image acquired with an Agilent FTIR microscope. The images were recorded in the range 1800 to 900 cm^{-1} and show the distribution of the phosphate peak intensity at 1020 cm^{-1} obtained using (c) 4x objective and (d) 15x objective.

Figure 4.3 illustrates the good agreement in the apparent microcalcification observed in a histological section with H&E staining, a white light image and FTIR images based on the phosphate peak intensity at 1020 cm^{-1}. All these micrographs exhibit the same morphological features. In the FTIR images, the microcalcification is represented in false colours, where red corresponds to high intensity at 1020 cm^{-1} and blue to low intensity. Thus, FTIR images allow the identification of microcalcifications in non-stained (label-free) tissue sections and can be used as a guide for localised micro-Raman analysis. These measurements were performed for each sample and different stages of breast cancer as shown in Figure 4.4.

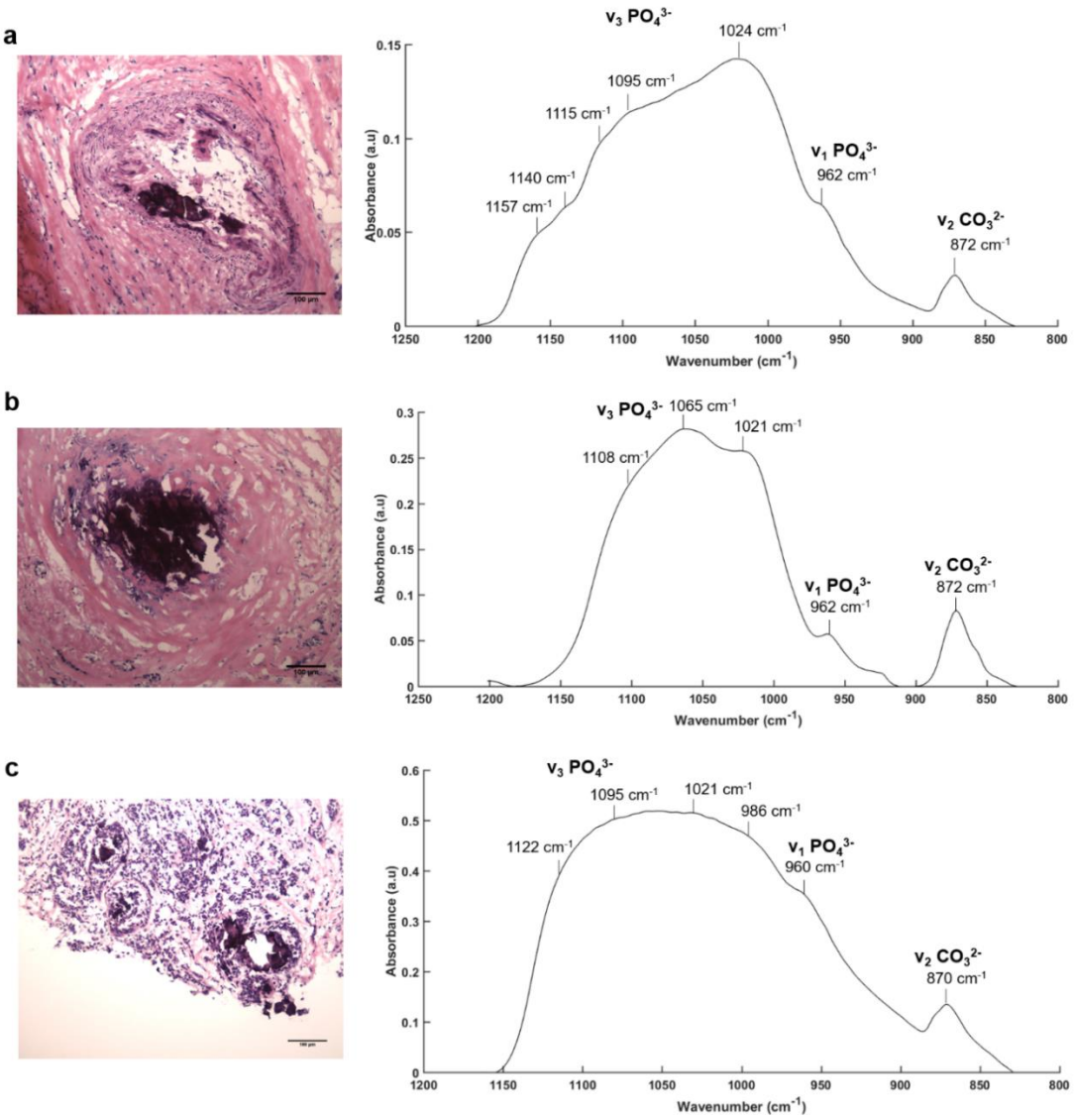

Figure 4.4 Histological sections with H&E staining and corresponding FTIR spectra for three breast lesions: (a) Benign, (b) DCIS low grade and (c) IDC grade 2. An average of 10 spectra (single point measurements) were taken from microcalcifications in the range 1200-830 cm^{-1}.

A comparison of spectra extracted from benign, DCIS low grade and IDC grade 2 shows similar characteristics for phosphate and carbonate bands (see also Appendix, supplementary data 3, Figure C.1 showing spectra extracted from micro-FTIR images). Figure 4.4 shows that the phosphate peaks found for these species are numerous and are not simply related to a particular stage of pathology. In Figure 4.4a, the phosphate band (1200-900 cm^{-1}) is defined by six sub-bands at 962, 1024, 1095, 1115, 1140, and 1157 cm^{-1} corresponding to ν_1,ν_3 PO_4^{3-} bands and HPO_4^{2-} containing apatite, whilst in Figure 4.4b, the phosphate peak shape is more defined with a shoulder at 1021 cm^{-1} (non-stoichiometric apatite) and three peaks at 962,1065, and

1108 cm^{-1} (ν_1 and ν_3 PO_4^{3-} bands). The phosphate band in Figure 4.4c is broader than the other peaks (Figure 4.4a and b) and its shape looks similar to those found in ACP mineral standard (see Chapter 3). Several sub-bands are present such as 960, 1024, 1095, 1115, 1140, and 1157 cm^{-1} for the ν_1, ν_3 PO_4^{3-} bands and HPO_4^{2-} containing apatite. All spectra exhibit the same carbonate peak at 872 cm^{-1} (± 2 cm^{-1}) corresponding to ν_2 CO_3^{2-}, which is less prominent than the phosphate peak (1200-900 cm^{-1}).

In parallel, to get complementary information about the composition of microcalcifications, Raman analysis was performed for these breast tissue sections.

4.2.2. Raman analysis

An example of Raman data of a breast sample for a particular stage of DCIS is illustrated in Figure 4.5.

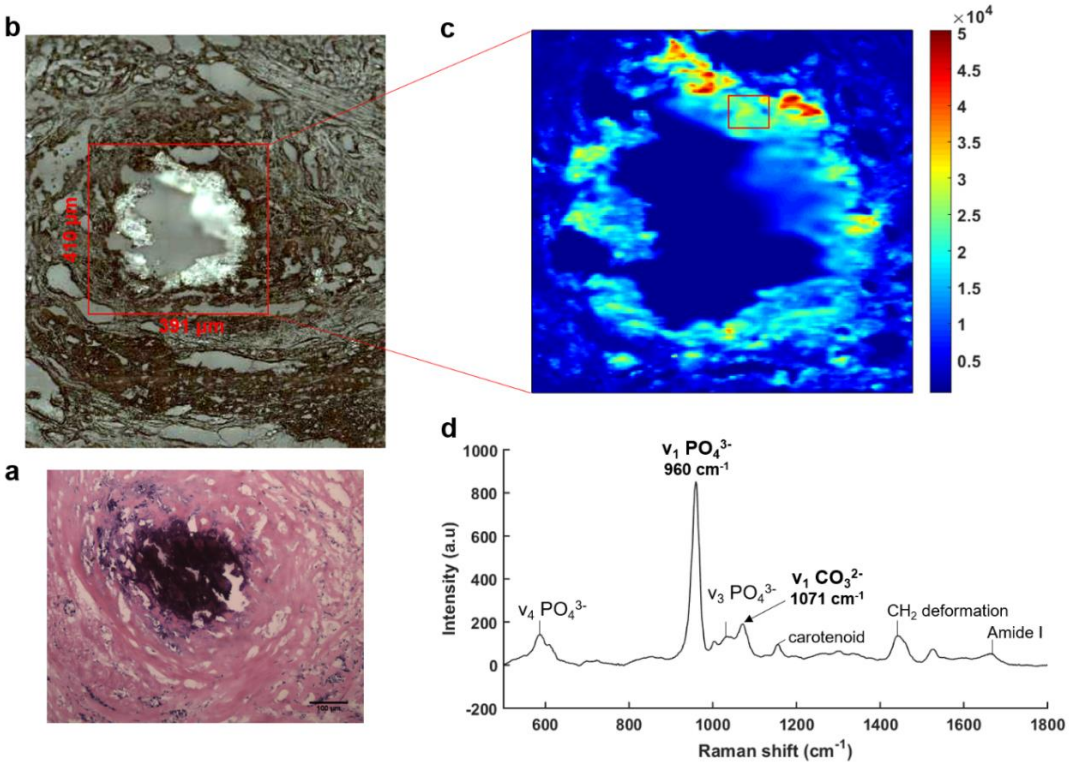

Figure 4.5 Visible images and Raman map of a breast DCIS biopsy sample. (a) Histological section stained with H&E and imaged with a transmission microscope, x10 objective. The red box denotes a 391 x 410 μm^2 area where a Raman map was measured. (b) White light image acquired with a Renishaw Raman microscope. (c) Raman map showing the distribution of the phosphate peak intensity at 960 cm^{-1} obtained using a 50x objective. (d) Average of 10 Raman spectra extracted from the middle region of the microcalcification (c).

Figure 4.5a displays a histological section with H&E staining, where the microcalcification appears in dark purple and the surrounding tissue in pink whereas the white light image taken from a Renishaw microscope (Figure 4.5b) shows a bright white microcalcification. Figure 4.5c illustrates the Raman map which refers to the phosphate peak intensity at 960 cm^{-1}. The microcalcification is represented by the red-to-green regions in the false colour image. The mean spectrum in Figure 4.5d (extracted from the red box in Figure 4.5c) exhibits several peaks of interest. In particular, three phosphate peaks at 583, 960 and 1032 cm^{-1} and one carbonate peak at 1071 cm^{-1} are noted, which correspond to the cHap crystal in microcalcifications.

Other elements are present such as proteins and lipids: 1662 cm^{-1} Amide I (proteins), 1440 cm^{-1} CH_2 deformation (lipids and proteins), 1157 and 1526 cm^{-1} carotenoids (absent in normal tissue) [106]. Based on the spatial resolution of around 1 µm and the ability to extract pure calcification spectra from the middle of the microcalcification, i.e. with apparently no tissue included, it is possible to conclude that there is not only pure cHap crystal but also a mix of proteins and lipids.

To gain a better understanding of the spatial distribution of these species, a PCA was applied to each Raman map. An example of PCA results showing the first nine PC scores and loadings are presented in Figure 4.6. In this example, the microcalcification was found in DCIS with a low grade (Figure 4.6a). As illustrated in Figure 4.6b, the PC1 score denotes the microcalcification (yellow) with a corresponding phosphate peak in the PC1 loading (Figure 4.6c). PC2 and PC3 scores denote the surrounding tissue (yellow) with a strong contribution of proteins and lipids in the corresponding PC loadings. The remaining PC loadings are less defined in terms of spatial distribution and have a lower signal-to-noise ratio which should not be used for the discrimination between microcalcifications and surrounding tissue. For clarity, the first three PC loadings and their peak assignment have been reported in Figure 4.7. The PC1 loading (Figure 4.7a) shows a strong contribution of phosphate and carbonate peaks at 960 and 1071 cm^{-1} for cHap, as well as lipid and protein contributions at 1442 cm^{-1} and carotenoids at 1157 and 1527 cm^{-1} [107], [108]. They appear to be located in the region of the microcalcification (yellow, Figure 4.6b). However, PC2 loading (Figure 4.7b and c), associated to the surrounding tissue, show a strong contribution of collagen (proline and hydroxyproline: 875 and 854 cm^{-1}), lipids (1447, 1300 and 1437 cm^{-1}), proteins (Amide I at 1667 cm^{-1}) and carotenoids (1157 and 1527 cm^{-1}) [107], [108].The PC3 loading exhibits a weak contribution of a phosphate mineral at 968 cm^{-1} surrounding the Hap crystal (in orange, Figure 4.6b) and carotenoids (1157 and 1527 cm^{-1}) but also collagen at 873 and 938 cm^{-1} in the surrounding tissue area [106], [107]. The phosphate species found at 968 cm^{-1} could correspond to Mg-substituted whitlockite (or β-TCMP), as suggested by Scimeca et al. [42]. These results are in line with the literature. According to several studies, carotenoids are expressed to prevent breast cancer and play a role in the immune system as antioxidants and anti-proliferative agents [108], [109].

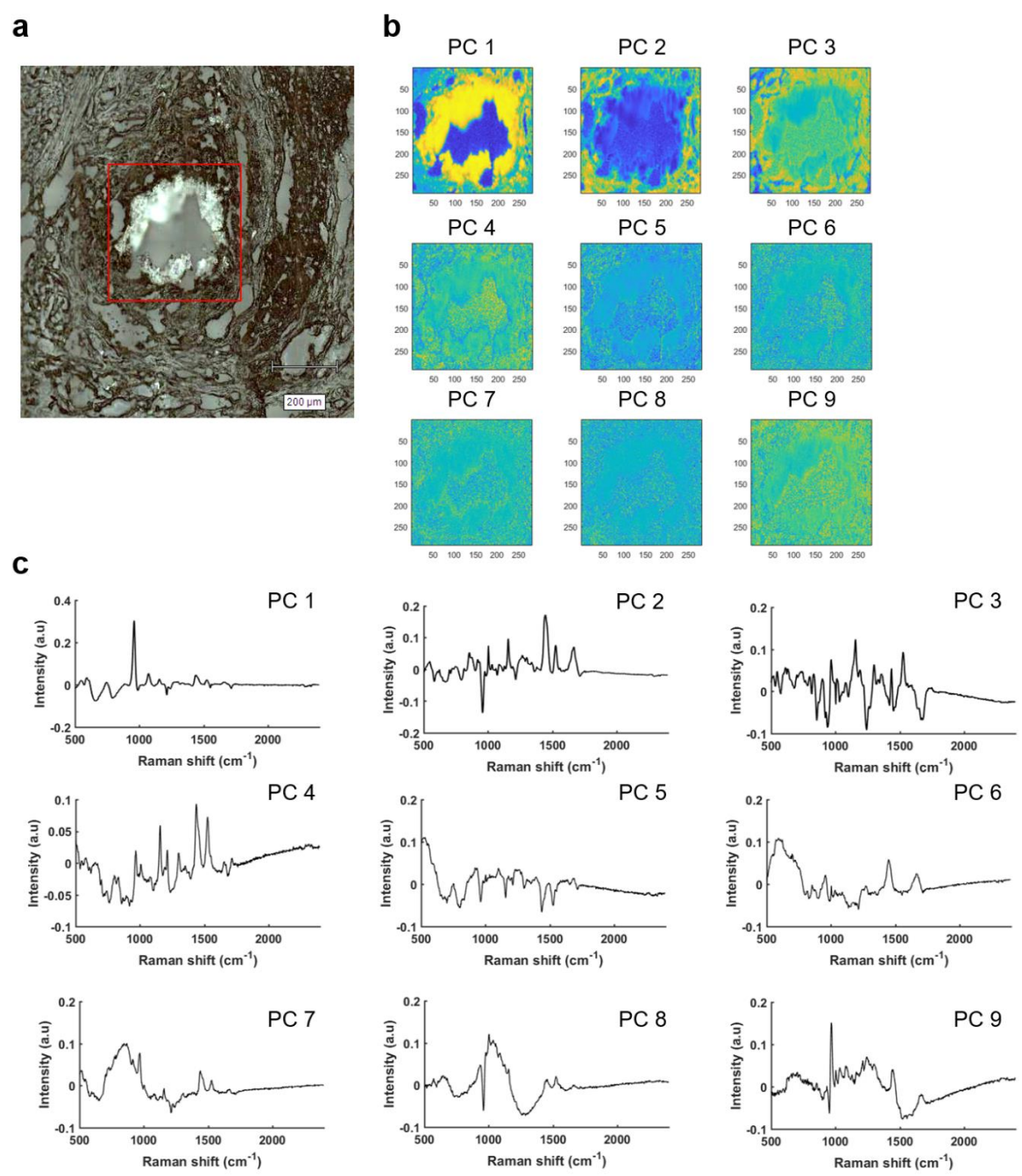

Figure 4.6 (a) Visible image of a breast DCIS (low grade) tissue section showing a microcalcification. The red box denotes a region where a Raman map was acquired. PCA was performed on the Raman map: (b) the first nine PC scores and (c) corresponding PC loadings.

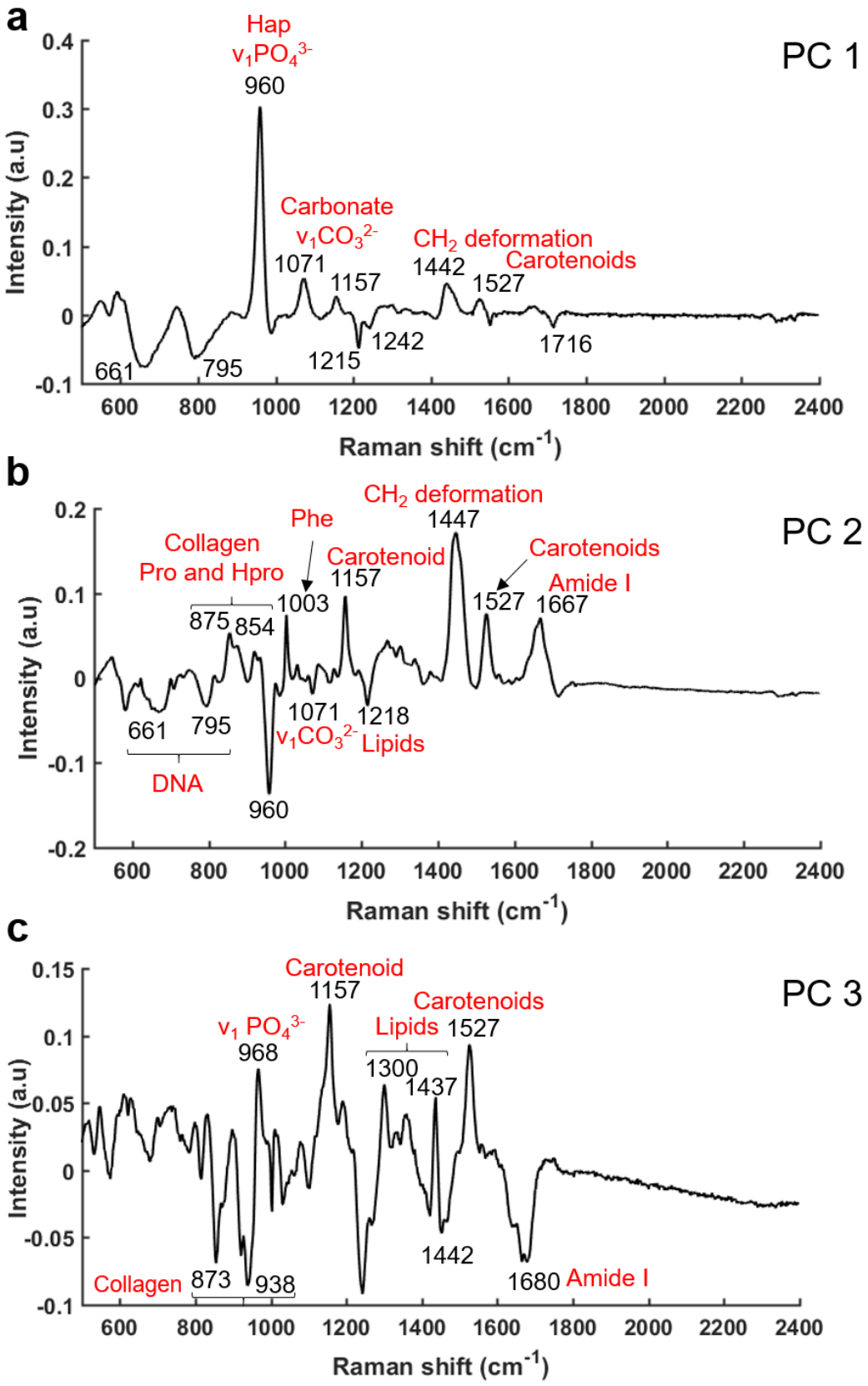

Figure 4.7 Loadings for (a) PC1, (b) PC2 and (c) PC3 showing the peak assignment. Pro: Proline, Hpro: Hydroxyproline, and Phe: Phenylalanine.

For a comparison with the FTIR spectra (see above, Figure 4.4), Raman spectra were recorded from adjacent sections of benign, DCIS low grade and IDC grade 2 samples and illustrated in Figure 4.8. It shows similar characteristics between each other, in particular for phosphate and carbonate peaks at 960 and 1071 cm^{-1}, respectively. Moreover, proteins (1256 and 1657 cm^{-1}), lipids (1442 and 1300 cm^{-1}) and carotenoids at 1125 and 1154 cm^{-1} are also well represented for each cancer type [107], [108].

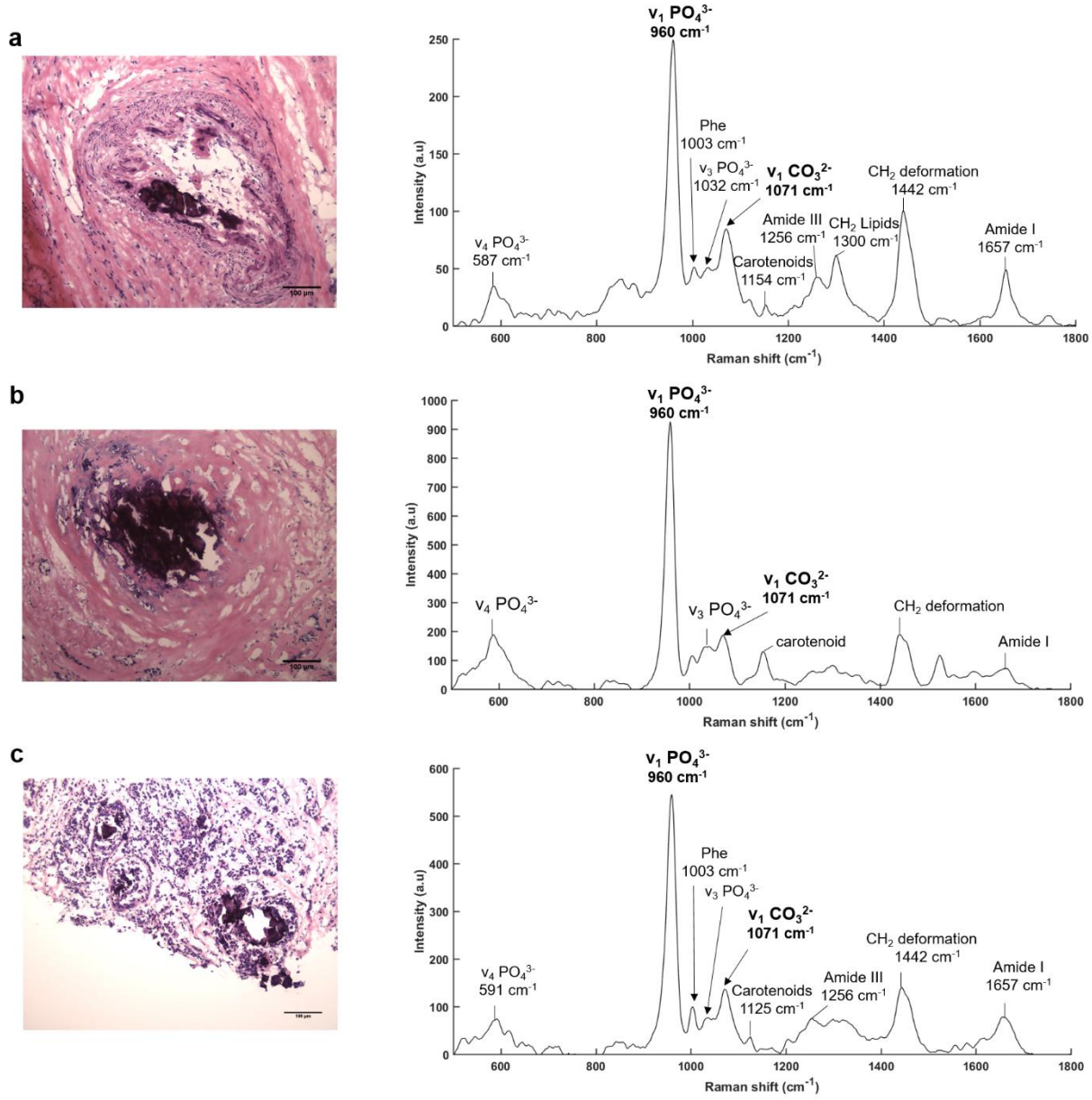

Figure 4.8 Histological sections with H&E staining and comparison of Raman spectra of three breast frozen lesions: (a) Benign, (b) DCIS low grade and (c) IDC grade 2. An average of ten spectra were taken from microcalcifications and baseline correction was performed in the range 1800-500 cm^{-1}. Phe: phenylalanine.

For frozen tissue sections, FTIR and Raman spectra are well defined by several components such as lipids, proteins, or cHap. However, access to fresh or frozen tissue is sometimes difficult and a series of samples which are formalin-fixed paraffin-preserved (FFPP) provided by hospitals archives is often convenient. Unfortunately, paraffin has a strong contribution in the Raman spectra (1063, 1130, 1296 and 1436 cm^{-1}) [110] and FTIR spectra (1377, 1466, 2850, 2922, 2958 cm^{-1}) [110] and interferes with specific features of microcalcifications, especially phosphate and carbonate bands. A possibility in the analysis of FFPP tissue sections is to remove paraffin from the samples. However, one question remains: does the de-paraffinisation process damage or affect the microcalcification integrity? Therefore, breast tissue sections embedded in paraffin for the FTIR analysis and de-paraffinised tissue sections for Raman analysis were analysed and the results shown in the following sections.

4.3. Chemical and spatial information of microcalcifications found in breast tissues embedded in paraffin

A batch of breast tissue sections was analysed using complementary methods. As described in Chapter 2, section 2.1.2, one breast section embedded in paraffin and mounted on BaF_2 was used for the FTIR analysis and an adjacent breast section was mounted on stainless steel and de-paraffinised (as described in section 2.3.2.2) prior to the Raman analysis.

4.3.1. FTIR analysis of paraffinised sections

Breast tissue sections embedded in paraffin were analysed using the FTIR imaging system and single point measurements. An example is illustrated in Figure 4.9.

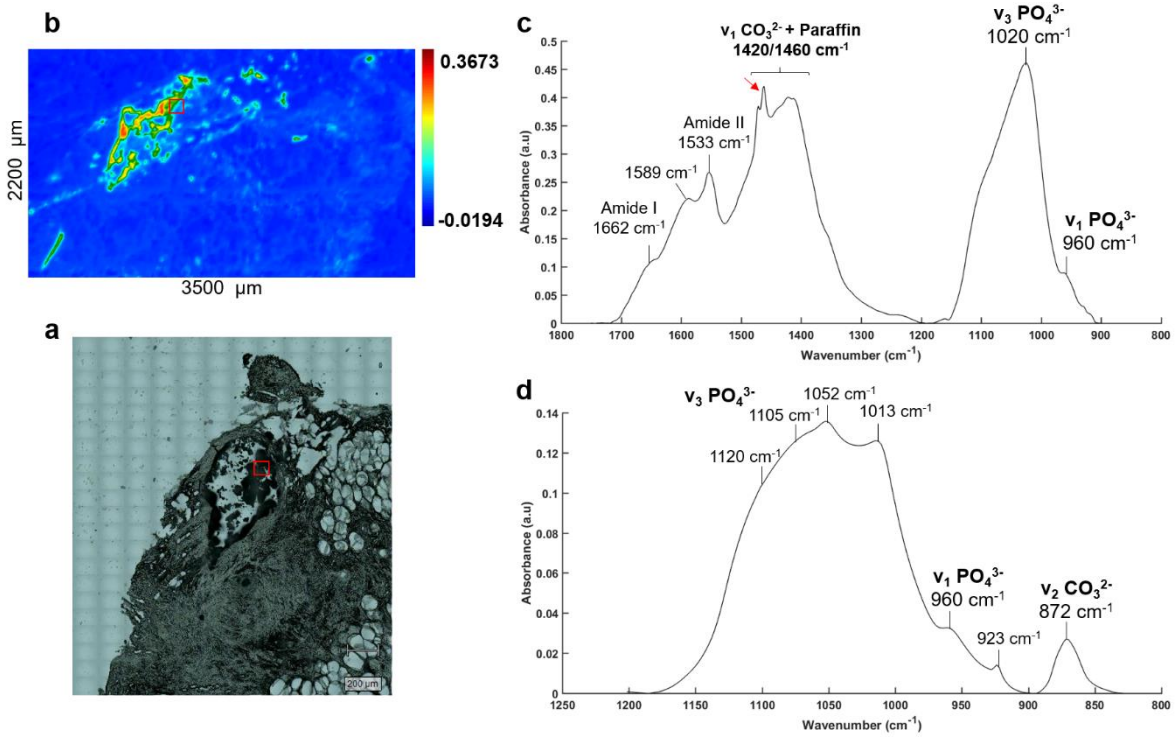

Figure 4.9 Visible and micro-transmission FTIR images of a breast DCIS (grade 3) section. (a) White light image acquired with a Renishaw microscope, x15 objective. (b) FTIR image showing the distribution of the phosphate peak intensity at 1020 cm^{-1} obtained using a 15x objective. (c) Mean IR spectrum extracted from the FTIR image (red box in b) truncated to the range 1800-900 cm^{-1} and (d) mean IR spectrum from single point measurements (red box in a) truncated to 1200-830 cm^{-1}.

As discussed in relation to Figure 4.2, the shape of the phosphate peak is different between the mean spectrum from single point measurement (Figure 4.9d) and the mean spectrum extracted from the FTIR image (Figure 4.9c). The spectra are not from the same location within the microcalcification, as they measured at different times on different instruments.

The FTIR spectra (Figure 4.9c-d) appear to exhibit the same characteristics as those from the frozen tissue. The phosphate peak is apparent between 1200 and 900 cm^{-1} and carbonate peaks are observed at 872, 1420 and 1462 cm^{-1}. Unfortunately, the peak of carbonate at 1462 cm^{-1} (red arrow in Figure 4.9c) is overlaid to the CH_2 scissoring of paraffin [110], which affects the peak decomposition analysis in this region (1400-1500 cm^{-1}). However, the single point spectra between 900 and 800 cm^{-1} are still exploitable.

4.3.2. Raman analysis of de-paraffinised sections

As discussed previously, the effect of de-paraffinisation on breast cancer microcalcification analysis was investigated using Raman microspectroscopy and an example is illustrated in Figure 4.10.

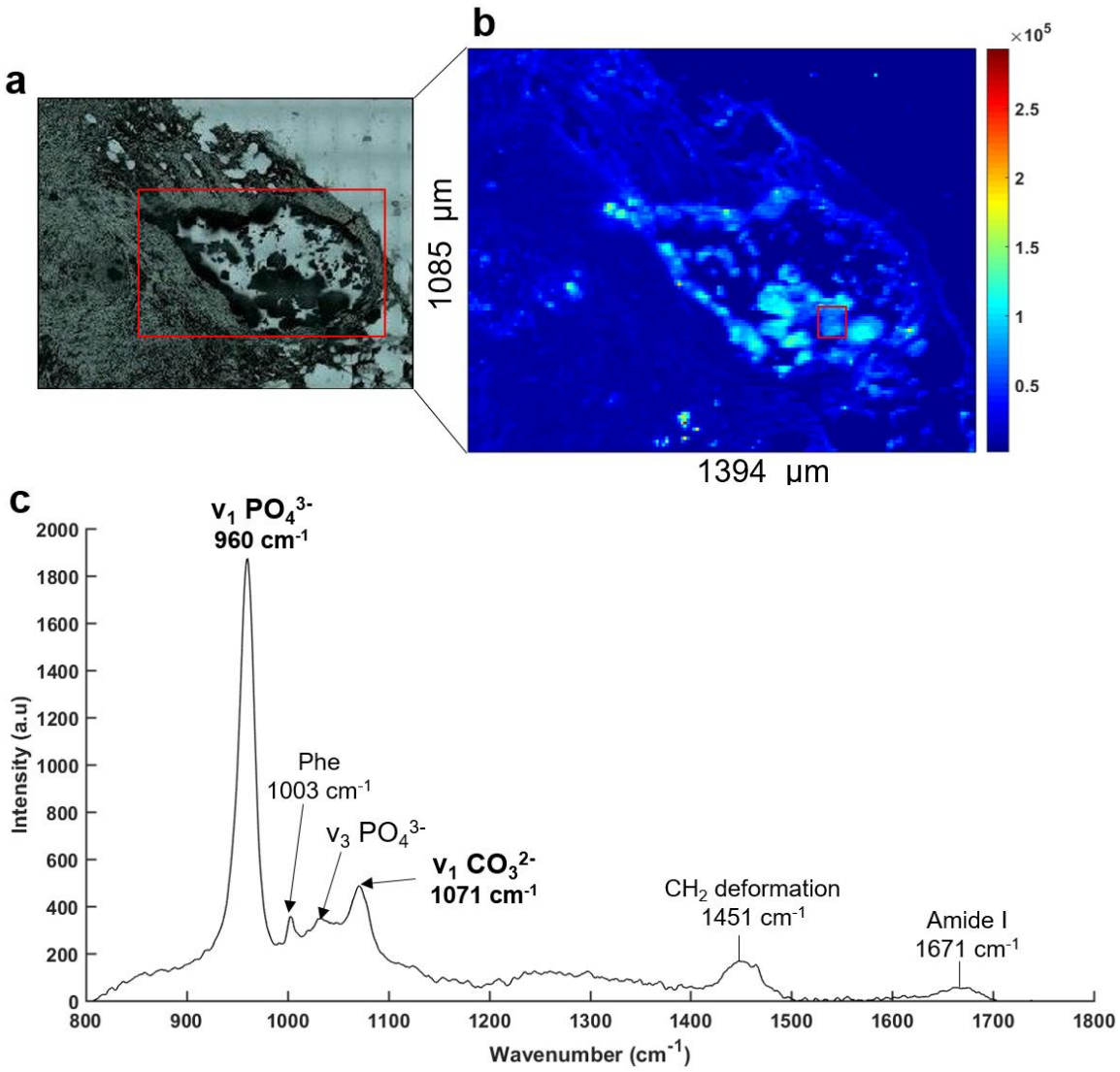

Figure 4.10 Visible image and Raman map of a breast DCIS (grade 3) section. (a) White light image acquired with a Renishaw microscope. (b) Raman map showing the distribution of the phosphate peak intensity at 960 cm^{-1} obtained using a 50x objective. (c) Average of ten Raman spectra extracted from a region of the microcalcification (red box in b).

The visible image (Figure 4.10a) shows a large microcalcification in black and the area of the micro-Raman acquisition (red box). The Raman map, which is based on the phosphate peak intensity at 960 cm^{-1} (Figure 4.10b), shows the microcalcification in false colour cyan. A mean Raman spectrum extracted from this map (Figure 4.10c) exhibits the same features as those of frozen tissue. Phosphate and carbonate peaks are observed at 960 and 1071 cm^{-1} for $\nu_1\, PO_4^{3-}$ and $\nu_1\, CO_3^{2-}$ bands, respectively, as well as proteins and lipids at 1671 and 1451 cm^{-1} [107], [108], which suggest that this microcalcification contains a mix of cHap, proteins and lipids.

In a similar way as previously done for frozen tissue sections, a PCA was performed for each Raman map and results are shown for breast tissue with DCIS grade 3 in Figure 4.11a. The PC scores and loadings are presented in Figure 4.11b and c. As illustrated in Figure 4.11b, the PC1 score map denotes the microcalcification (yellow) with an important phosphate and carbonate contribution in PC1 loading (Figure 4.11c). The PC2 score map denotes the surrounding tissue (orange) with a strong contribution of proteins and lipids in PC2 loading. The other PC loadings are associated with the background. For clarity, the first two PC loadings and their peak assignments are reported in Figure 4.12. PC1 loading, associated to the microcalcification (Figure 4.12a), shows a strong contribution of phosphate and carbonate peaks at 960 and 1072 cm^{-1} for cHap, as well as a lipid contribution at 1295 cm^{-1} and proteins (1172 cm^{-1} for tryptophan and Phenylalanine and 1257 cm^{-1} for Amide III). Less collagen (854, 875, 936, and 1003 cm^{-1}) and proteins (Amide I at 1678 cm^{-1} and CH_2 deformation at 1449 cm^{-1}) are present in this area. However, PC2 loading (Figure 4.12b), associated to the surrounding tissue, shows a strong contribution of collagen (Proline and Hydroxyproline: 875, 936 and 854 cm^{-1}), lipids (1295 and 1450 cm^{-1}), proteins (1450, Amide III at 1235 and 1268 cm^{-1}, Amide I at 1674 cm^{-1}) and also Hap (960 cm^{-1}) [107].

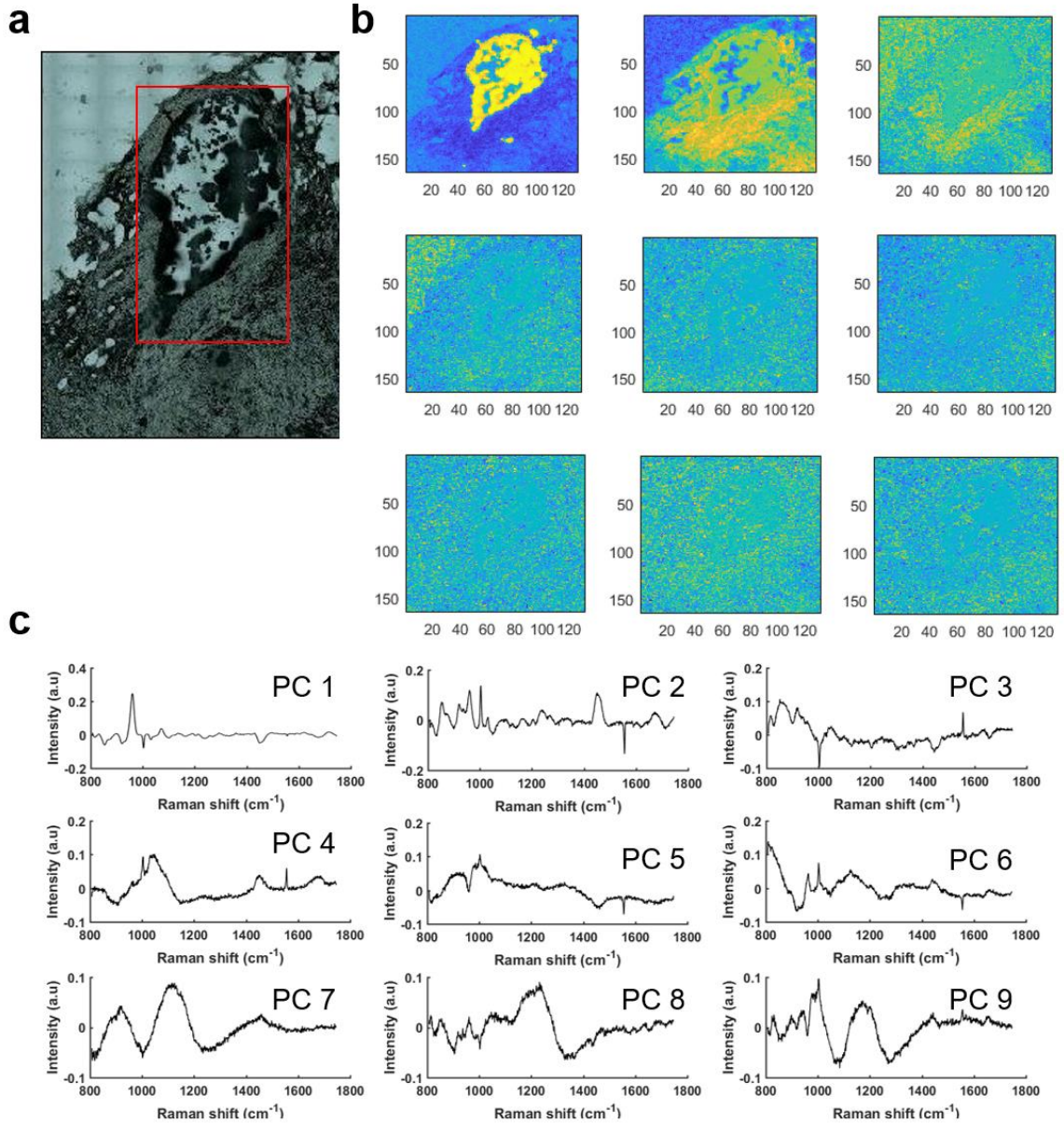

Figure 4.11 (a) Visible image of breast DCIS (grade 3) tissue showing a microcalcification. The red box denotes a region where a micro-Raman map was acquired. PCA was performed: (b) the first nine PC scores and (c) corresponding PC loadings.

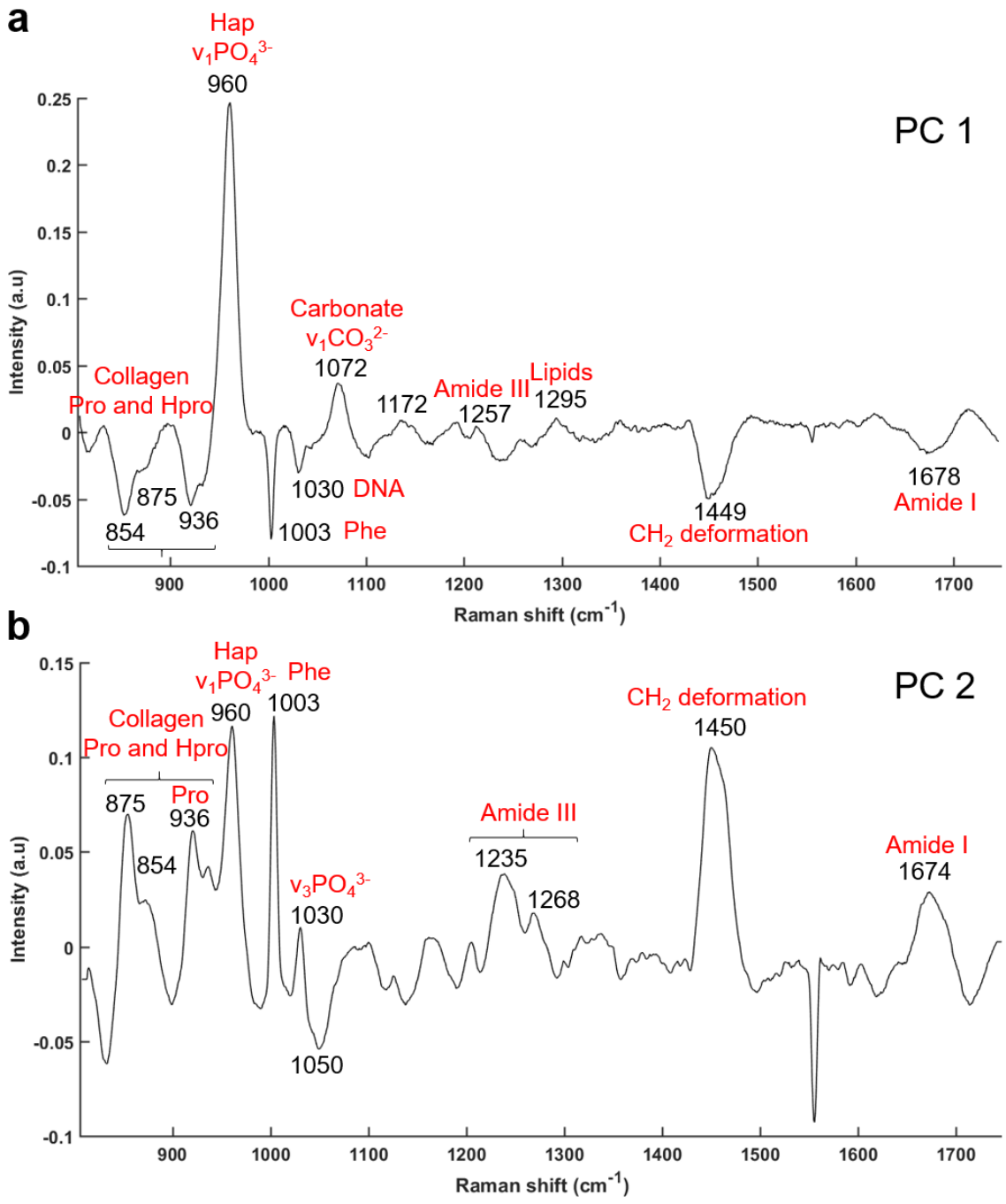

Figure 4.12 (a) PC1 and (b) PC2 loadings showing the peak assignments for different contributions in Raman spectra. Pro: Proline, Hpro: Hydroxyproline, and Phe: Phenylalanine.

Ó'Faoláin et al. have previously compared fresh, frozen and FFPP tissue sections using Raman microspectroscopy and concluded that the freezing or fixing process can have an impact on the protein and lipid intensity or their peak positions [110]. A shift in peak positions corresponding to CH_2 deformation and Amide I is observed between frozen tissue (1442 and 1657 cm^{-1}, Figure 4.8) and de-paraffinised tissue (1451 and 1671 cm^{-1}, Figure 4.10). However, the de-paraffinisation process does not appear to affect the chemical composition of Hap crystals, which are still well-represented by the phosphate and carbonate bands at the same positions as in frozen tissue. Further analysis will clarify this effect as well as the presence of other minerals in the microcalcifications.

4.4. Peak analysis

A mineral peak decomposition by curve fit analysis was performed for all datasets (FTIR and Raman spectra; frozen, paraffinised and de-parafinised tissues).

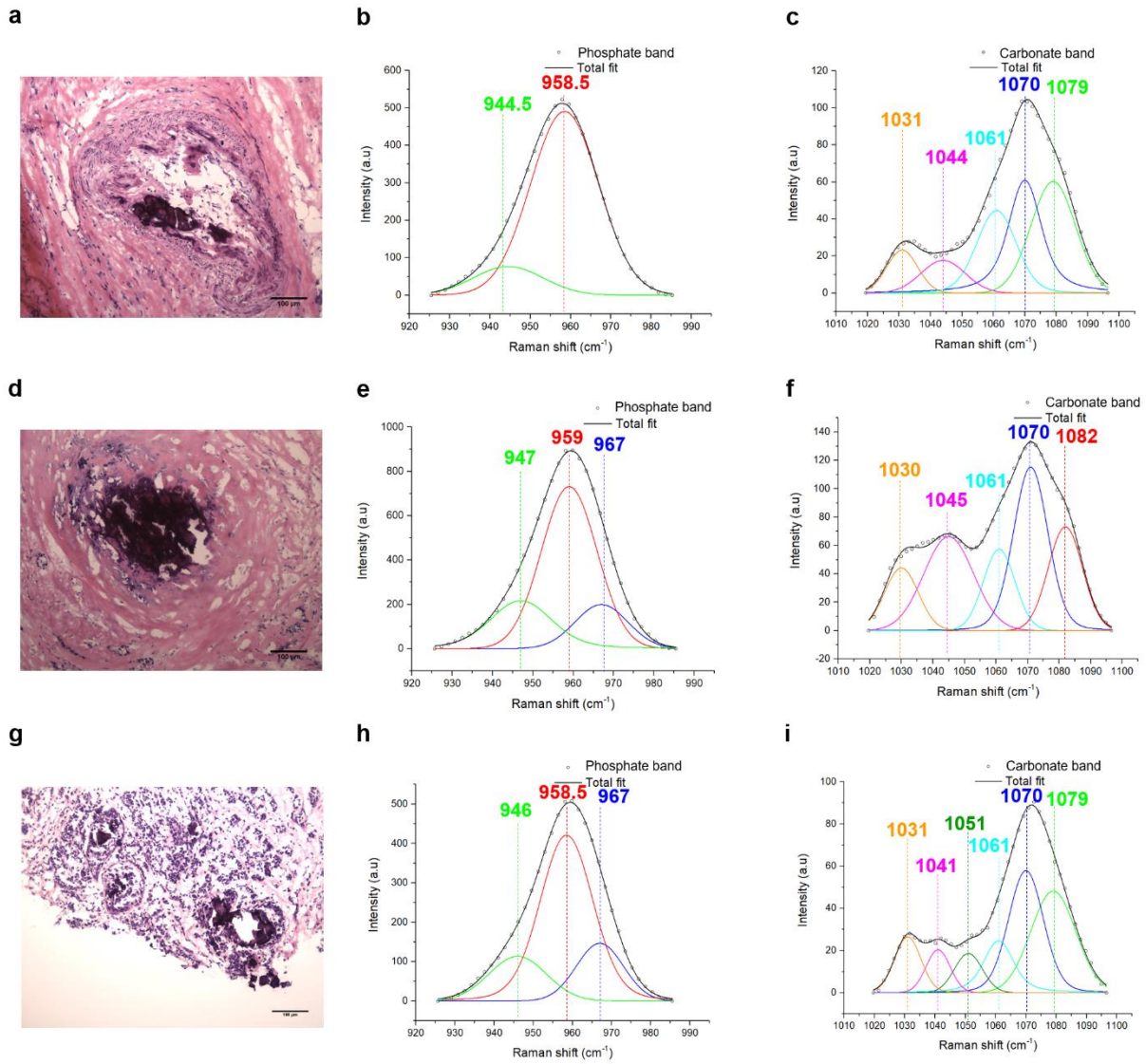

Figure 4.13 Results from curve fit analysis applied to Raman spectra. Histological sections with H&E staining and comparison of Raman spectra of frozen tissues with three breast lesions: (a) Benign, (d) DCIS low grade and (g) IDC grade 2. Spectra were truncated to the phosphate band at 990-930 cm^{-1} (b, e and h) and to the carbonate band at 1100-1020 cm^{-1} (c, f and i) and baseline corrected. For each fit, the regression is very good ($R^2 > 0.99$).

The results shown in Figure 4.13 for Raman spectra of frozen samples have been found to be very similar to those from de-paraffinised samples, in terms of peak positions and number of sub-bands (see Appendix, supplementary data 3, Figure C.2). The decomposed peaks illustrated in Figure 4.13 are associated with different vibrational modes of phosphate and carbonate ions (as described in Chapter 3) and are in line with several characteristics of the mineral standards analysed previously. For instance, the phosphate peaks at 945-947, 959 and 967 cm^{-1} correspond to the ν_1 PO_4^{3-} mode (Figure 4.13 b, e and h). In Figure 4.13 c, f and i, the peak positions at 1031, 1041-1045, 1051, 1061, 1079 cm^{-1} are assigned to the ν_3 PO_4^{3-} mode [36], [91], [103]. The carbonate peaks at 1070 and 1082 cm^{-1} are associated with the ν_1 CO_3^{2-} mode [36], [91], [103]. The main carbonate peak at 1070 cm^{-1} is overlaid with the phosphate band and therefore it is challenging to determine the C:P ratio for each microcalcification. These results seem to indicate the presence of cHap in our microcalcifications, however the case is more complex. In fact, as described in Chapter 3, it is hard to discriminate cHap from ACP or β-TCP for example, due to a similar peak decomposition profile (similar sub-bands). For instance, Figure 4.13e and h show the same peaks at around 946, 959 and 967 cm^{-1} which may indicate the presence of β-TCP. However, the carbonate peak at 1070 cm^{-1} also suggests the presence of cHap. Here, microcalcifications from DCIS and IDC lesions could be a mixture of cHap and β-TCP. In contrast, the microcalcification within the benign lesion illustrated in Figure 4.13b and c is made of cHap only, with two peaks for phosphate band at 945 and 960 cm^{-1} and 1070 cm^{-1} for carbonate band. Nevertheless, it is impossible to assign a specific composition to microcalcifications for a specific stage of the pathology. Figure 4.13 illustrates the heterogeneity between microcalcifications. A curve fit analysis was also performed for other benign lesions (Appendix, supplementary data 3, Figure C.3) that exhibit an additional peak at 968 cm^{-1} without any carbonate bands, which is not the case in Figure 4.13b and c. This suggests that it could be possible to find β-TCP as a precursor of Hap, but not for all benign lesions.

The same analysis was performed for the FTIR data and results are illustrated in Figure 4.14.

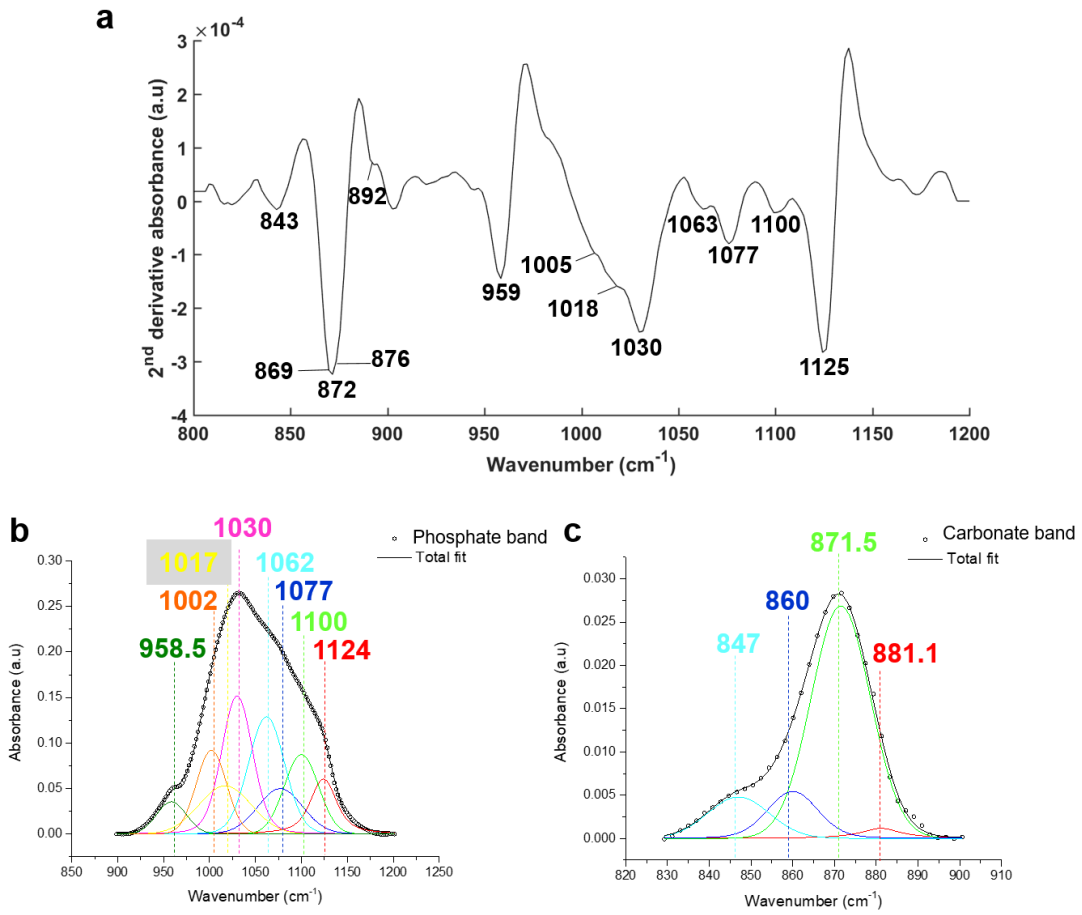

Figure 4.14 Results from curve fit analysis of FTIR spectra from paraffinised breast tissue (benign lesion). (a) Second derivative spectrum between 1200 and 830 cm^{-1}. Curve fit analysis was performed on spectra truncated to (b) the phosphate band at 1200-900 cm^{-1} and (c) the carbonate band at 890-830 cm^{-1} and baseline corrected. For each case, the regression is very good ($R^2 > 0.99$).

The results shown in Figure 4.14 are representative of results for all the FTIR spectra for the single point measurement from frozen and paraffinised samples where the number of sub-bands is the same for the phosphate and carbonate bands (see Appendix, supplementary data 3, Figure C.4). However, a shift in a sub-band is noted from 959 cm^{-1} (paraffinised tissue) to 967 cm^{-1} (frozen tissue) for the ν_1 PO_4^{3-} band, which is still unclear (Appendix, supplementary data 3, Figure C.4). Figure 4.14a shows the sub-peak positions that were used in the peak decomposition analysis (Figure 4.14b and c). The phosphate peak is well represented by eight components: 1124 cm^{-1} corresponding to poorly crystalline Hap; 1100, 1077, 1030 and 1002 cm^{-1} for the ν_3 PO_4^{3-} mode; 1017 cm^{-1} for non-stoichiometric apatite; and 959 cm^{-1} for the ν_1 PO_4^{3-} mode [88], [89], [98]. For several DCIS and invasive breast lesions, additional

peaks are found at 1150-1160 cm^{-1} which are due to the HPO_4^{2-} ion in acidic environment [86], [99]. This tends to correlate with the pH changes observed during cancer progression, with a more acidic environment in advanced stages [84], [85]. In Figure 4.14c, even if a peak shift is noticed between second derivative spectrum and the curve fit analysis, the carbonate band is defined by four components: 881 cm^{-1} for the ν_3 CO_3^{2-} mode; 872 cm^{-1} for the ν_2 CO_3^{2-} mode; 860 cm^{-1} corresponding to the ν_2 CO_3^{2-} mode, unstable and non-apatitic; and 847 cm^{-1} for the ν_4 CO_3^{2-} mode [98], [100], [111]. This denotes the same spectral characteristics as the mineral standards used for reference. FTIR spectroscopy is more challenging with materials that include crystals due to scattering. In addition, the limit of detection of carbonate peak in long wavenumbers and the weakness of the signal in this region are such that errors can arise during data processing. However, the comparison between microcalcifications and mineral standards can give some useful information.

By comparing the sub-band positions from the curve fit analysis between standard minerals and breast tissue sections in the total dataset (frozen and de-paraffinised tissues), out of 49 microcalcifications analysed by Raman microspectroscopy, 20 seem to be made of cHap only, 10 present the same patterns for cHap and β-TCP, 6 are a combination of cHap and ACP, 6 may be made of β-TCP only, 2 present the same patterns for ACP, 4 microcalcifications show the same peak positions as cHap, ACP and β-TCP, and 1 seems to be a combination of cHap and OCP (see Appendix, supplementary data 3, Table C.1).

Similarly, out of 48 microcalcifications analysed by FTIR spectroscopy (frozen and paraffinised tissues), 20 exhibit the same peak positions as a combination of cHap and ACP, 13 seem to be made of cHap only, 7 show the same patterns as cHap and β-TCP, 2 are made exclusively of OCP, 3 of a combination of cHap, β-TCP and ACP, 2 microcalcifications is β-TCP only, and 1 microcalcification shows the same peak positions as cHap and OCP (see Appendix, supplementary data 3, Table C.1).

Based only on the peak positions it is challenging to determine the chemical composition of breast microcalcifications and their predictions could be different from FTIR and Raman spectra when the microcalcifications are comparable (Appendix, supplementary data 3, Table C.1). For instance, regarding the FTIR spectra, ACP and cHap present the similar spectral characteristics which tend to challenge the

discrimination between the two minerals (e.g. B9 to B11, and I1 for paraffinised/de-paraffinised sections, Table A2.1). The only difference is that the phosphate peak at around 1030 cm^{-1} found for ACP is broader than that of cHap (Appendix, supplementary data, Table C.1). The same issue was encountered for OCP mineral predicted in D4 microcalcification (paraffinised/de-paraffinised sections, Table A2.1) for the FTIR spectra and only cHap seems to be present in Raman spectra.

To have a precise idea of the microcalcification composition, all these data need to be investigated in detail for carbonate amount of each microcalcification or evaluation of mineral composition.

4.5. Estimation of carbonate and other components content in microcalcifications

4.5.1. Calculation of the C:P ratio

Using the calibration curve illustrated in Chapter 3, the C:P ratio was calculated using the area under each peak obtained from the curve fit analysis. The C:P ratio was calculated by using carbonate peak at 1070 cm^{-1} and phosphate peak at 960 cm^{-1} for Raman spectra, whereas the carbonate peak at 875 cm^{-1} and the total phosphate peak area are used for the FTIR spectra. The results are listed in Table 4.1 and 4.2 for frozen and paraffinised/ de-paraffinised samples, respectively. For clarity, microcalcifications are numerated by their breast lesions, e.g. B for benign, D for DCIS, and I for invasive cancer. When the same microcalcification is analysed by IR and Raman spectroscopy (same area), a double red arrow is added in the table.

Table 4.1 Carbonate amount estimated in frozen breast tissue microcalcifications by curve fit analysis performed on Raman and FTIR spectra for three breast lesions: B: Benign, D: DCIS, and I: invasive cancer. Double red arrows are added to notify that the same microcalcifications were analysed by Raman and FTIR spectroscopy. If the double red arrows are missing, the microcalcifications analysed by Raman and IR spectroscopy are different.

Frozen tissue sections										
FTIR analysis						Raman analysis				
	Total carbonate (875cm^{-1} peak area)	Total phosphate (Total peak area)	Ratio C:P (875 cm^{-1} /Tot P area)	% carbonate substitution estimated			Total carbonate (1070 cm^{-1} peak area)	Total phosphate (960 cm^{-1} peak area)	Ratio C:P (1070/960 cm^{-1})	% carbonate substitution estimated
B1	0.27	22.31	0.012	**16.28**	↔	**B1**	490.64	4359.74	0.113	**9.08**
B2	-	-	-	-		**B2**	1023.48	10454.22	0.098	**7.90**
D1	-	-	-	-		**D1**	1257.88	5982.50	0.210	**16.97**
D2	0.12	22.86	0.005	**7.04**	↔	**D2**	1353.86	9040.08	0.150	**12.09**
D3	0.38	26.74	0.014	**18.96**	↔	**D3**	1657.52	12631.45	0.131	**10.59**
I1	0.21	39.43	0.005	**6.96**	↔	**I1**	367.72	8623.04	0.04	**3.44**
I2	0.29	27.18	0.0107	**14.33**	↔	**I2**	652.38	6129.78	0.106	**8.59**
I3	-	-	-	-		**I3**	1565.53	14205.24	0.110	**8.89**
I4	-	-	-	-		**I4**	1436.93	5784.38	0.248	**20.05**
I5	-	-	-	-		**I5**	768.88	8563.10	0.090	**7.25**
I6	-	-	-	-		**I6**	869.36	9890.12	0.088	**7.09**
I7	-	-	-	-		**I7**	740.16	6544.16	0.113	**9.13**
I8	0.10	37.50	0.003	**3.59**	↔	**I8**	248.5	6544.16	0.038	**3.07**
I9	-	-	-	-		**I9**	-	-	-	-
I10	-	-	-	-		**I10**	-	-	-	-
I11	-	-	-	-		**I11**	561.71	5506.88	0.102	**8.23**
I12	0.86	97.04	0.0088	**11.76**		**I12**	1875.98	14893.19	0.126	**10.17**
I13	-	-	-	-		**I13**	1287.86	10041.60	0.128	**10.35**
I14	-	-	-	-		**I14**	807.37	6275.76	0.129	**10.38**
I15	0.38	43.40	0.0087	**11.63**	↔	**I15**	1738.85	20774.70	0.084	**6.76**
I16	0.66	55.49	0.012	**15.95**		**I16**	-	-	-	-
I17	-	-	-	-		**I17**	495.46	4762.68	0.104	**8.40**
I18	-	-	-	-		**I18**	-	-	-	-
I19	1.37	105.76	0.013	**17.23**	↔	**I19**	883.67	7576.41	0.117	**9.41**
I20	1.15	80.55	0.0143	**19.04**	↔	**I20**	730.64	9697.16	0.075	**6.08**
I21	-	-	-	-		**I21**	723.51	10505.49	0.069	**5.56**

Table 4.2 Carbonate amount estimated in paraffinised and de-paraffinised breast tissue microcalcifications by curve fit analysis performed on Raman and FTIR spectra for three breast lesions: B: Benign, D: DCIS, and I: invasive cancer. Double red arrows are added to notify that the same microcalcifications were analysed by Raman and FTIR spectroscopy. If the double red arrows are missing, the microcalcifications analysed by Raman and IR spectroscopy are different.

Paraffinised and de-paraffinised tissue sections										
FTIR analysis						Raman analysis				
	Total carbonate (875cm^{-1} peak area)	Total phosphate (Total peak area)	Ratio C:P (875 cm^{-1} /Tot P area)	% carbonate substitution estimated			Total carbonate (1070 cm^{-1} peak area)	Total phosphate (960 cm^{-1} peak area)	Ratio C:P (1070/960 cm^{-1})	% carbonate substitution estimated
B1	0.48	32.39	0.015	**19.90**	↔	**B1**	2615.67	38733.77	0.068	**5.45**
B2	0.22	17.32	0.013	**17.03**	↔	**B2**	-	-	-	-
B3	0.06	6.27	0.010	**13.53**		**B3**	3055.80	38452.57	0.079	**6.41**
B4	-	-	-	-		**B4**	4327.52	33953.07	0.127	**10.29**
B5	-	-	-	-		**B5**	2466.93	45750.05	0.054	**4.35**
B6	0.35	35.34	0.0098	**13.22**		**B6**	4394.55	44256.69	0.099	**8.01**
B7	0.09	10.45	0.008	**11.28**		**B7**	-	-	-	-
B8	-	-	-	-		**B8**	-	-	-	-
B9	0.20	23.25	0.009	**11.85**	↔	**B9**	3597.75	50487.64	0.071	**5.75**
B10	0.37	26.39	0.014	**18.81**	↔	**B10**	3858.69	64964.23	0.059	**4.79**
B11	0.22	10.49	0.021	**28.82**	↔	**B11**	3734.14	64750.07	0.058	**4.65**
B12	1.62	137.21	0.012	**15.88**	↔	**B12**	1856.54	15104.43	0.123	**9.92**
B13	0.86	99.51	0.009	**11.72**		**B13**	-	-	-	-
B14	1.32	37.88	0.035	**46.89**		**B14**	2080.64	23516.26	0.088	**7.14**
B15	-	-	-	-		**B15**	2257.92	22096.28	0.102	**8.25**
B16	-	-	-	-		**B16**	3292.57	40588.47	0.081	**6.55**
B17	0.17	19.92	0.0083	**11.26**		**B17**	-	-	-	-
B18	0.52	76.17	0.0068	**9.22**	↔	**B18**	1779.16	6414.62	0.277	**22.39**
B19	0.16	22.162	0.0072	**9.74**		**B19**	2436.29	8020.58	0.304	**24.52**
D1	0.36	27.61	0.013	**17.52**	↔	**D1**	1226.72	38256.77	0.032	**2.59**
D2	1.09	99.95	0.0109	**14.70**	↔	**D2**	-	-	-	-
D3	0.06	5.61	0.0114	**15.39**	↔	**D3**	-	-	-	-
D4	0.10	18.55	0.005	**6.91**	↔	**D4**	2458.45	31041.62	0.079	**6.39**
D5	0.06	49.11	0.0012	**1.61**		**D5**	-	-	-	-
D6	0.17	54.13	0.0031	**4.12**		**D6**	-	-	-	-
D7	0.19	58.59	0.0033	**4.47**		**D7**	2218.34	4429.96	0.501	**40.42**
D8	0.40	93.06	0.004	**5.85**		**D8**	1574.42	4435.99	0.355	**28.65**
D9	0.15	72.12	0.002	**2.83**		**D9**	-	-	-	-
D10	0.10	48.13	0.0022	**2.94**		**D10**	-	-	-	-
I1	0.34	33.32	0.010	**13.87**	↔	**I1**	1833.66	25648.58	0.071	**5.77**
I2	0.17	33.81	0.005	**6.84**		**I2**	-	-	-	-

The common range of carbonate ion substitution found in biological samples is around 2-8 wt.% [112] with, for instance, around 6 wt.% for bone and 5 wt.% for dentine [38]. In the present case, whether frozen or paraffinised tissues, some samples show a very high carbonate content, e.g. 47 or 29 wt.%, (Table 4.2, microcalcifications B11 and B14) in microcalcifications analysed from FTIR spectra. The amount of carbonate calculated is often more than 10 wt.% for a several samples (Tables 4.1 and 4.2). Different combinations of ratios were calculated (875 cm^{-1} CO_3^{2-} peak to total PO_4^{3-} band area; total CO_3^{2-} band to 1032 cm^{-1} PO_4^{3-} peak area; or total CO_3^{2-} band to total PO_4^{3-} band area) and that does not change significantly the calculated content of carbonate in each microcalcification (data not shown).

Regarding the Raman spectra, the amount of carbonate per microcalcification seems to be lower than that determined from IR and often less than 10 wt.% (except for I4 with 20 wt.% in Table 4.1; B18, B19, D7 and D8 with 22, 25, and 40, and 29 wt.%, respectively, in Table 4.2), which is much more realistic physiologically. When a comparison could be made between FTIR and Raman spectra, the determination of the carbonate concentration is lower using Raman spectra (e.g. in Table 4.1, I20 contains 19 wt.% carbonate for IR and only 6 wt.% for Raman). Different combinations of ratios were also tested for the Raman data but they did not improve the results any further. In the case of the highest concentrations of carbonate found for a few samples (e.g. in Table 4.1 for Raman spectra from de-paraffinised tissue sections), microcalcification D7 is around 40 wt.% for FTIR spectra from paraffinised tissue sections, B14 is around 47 wt.%. - their peak decomposition analysis shows common sub-bands with cHap, β-TCP and ACP which could affect the calculation and could explain their high concentrations due to the contribution of several minerals (e.g. ACP contains also carbonate ions and their proportion is unknown). The Hap crystal could also be substituted by other elements, such as Na and Al [41], or the carbonate ion substitution is not only type B but also a mix of A and B which can affect the C:P ratio. Moreover, for some microcalcifications, the signal was too weak or too noisy to enable the carbonate band to be decomposed and, as a consequence, another method needs to be applied in order to validate the previous results.

4.5.2. Prediction of microcalcification composition

A PLS model which is a supervised method was applied to predict the amount of carbonate in microcalcifications. Results are summarised in Table 4.3. The model was performed with Raman spectra for microcalcifications from frozen sections (Table 4.3a) and de-paraffinised tissues (Table 4.3). As it is observed, the amount of carbonate for both sets of samples is in a reasonable range of 5.7 to 10.3 wt.% and 5.8 to 9.6 wt.% for microcalcifications from frozen sections and de-paraffinised sections, respectively. These ranges are roughly similar in both cases. The PLS method seems to improve the prediction of carbonate amount. In fact, only one microcalcification has a high carbonate concentration (Table 4.3, B1 with 9.43 wt.% for frozen sections), which is better than calculations from curve fit analysis. As concluded previously, other compounds or other substitutions can interfere in the C:P ratio. All carbonate amounts in microcalcifications are roughly the same for frozen or de-paraffinised tissue sections.

Unfortunately, due to the small number of microcalcifications, a correlation between the percentage of carbonate ion substitution and the degree of pathology is not possible here. The PLS method was also applied for the FTIR spectra but, as expected, it gave very high amount of carbonate substitution which does not seem to be realistic. The PLS model is based on specific features of cHap (phosphate and carbonate bands) and, in the case of the FTIR data, other factors could interfere in the prediction in terms of spectral features from protein and phosphate contribution of nucleic material (DNA).

Table 4.3 Comparison of a PLS model and curve fit analysis for the carbonate amount prediction in frozen and de-paraffinised breast tissue microcalcifications. Analysis was performed on Raman spectra for three breast lesions: B: Benign, D: DCIS, and I: invasive cancer. Double red arrows are added to notify that the same microcalcifications were analysed for both methods. If the double red arrows are missing, the microcalcifications analysed by Raman and IR spectroscopy are different.

Frozen tissue sections			
	% Carbonate substitution predicted		
	PLS model		Curve fit analysis
B1	9.43	↔	9.08
B2	6.54	↔	7.90
D1	8.83	↔	16.97
D2	8.71	↔	12.09
D3	8.05	↔	10.59
D4	6.63		-
D5	9.32		-
D6	10.33		-
I1	5.87	↔	3.44
I2	7.2	↔	8.59
I3	6.78	↔	8.89
I4	6.24	↔	20.05
I5	6.64	↔	7.25
I6	6.73	↔	7.09
I7	9.27	↔	9.13
I8	7.63	↔	3.07
I9	8.5		-
I10	7.67		-
I11	6.24	↔	8.23
I12	5.72	↔	10.17
I13	5.72	↔	10.35
I14	7.29	↔	10.38
I15	6.81	↔	6.76
I16	-		-
I17	6.25	↔	8.40
I18	6.75		-
I19	6.13	↔	9.41
I20	6.05	↔	6.08
I21	6.78		5.56
I22	8.68		-

De-paraffinised tissue sections			
	% Carbonate substitution predicted		
	PLS model		Curve fit analysis
B1	6.16	↔	5.45
B2	-		-
B3	-		6.41
B4	6.44	↔	10.29
B5	-		4.35
B6	-		8.01
B7	6.01		-
B8	-		-
B9	9.56	↔	5.75
B10	5.86	↔	4.79
B11	7.75	↔	4.65
B12	6.45	↔	9.92
B13	-		-
B14	6.82	↔	7.14
B15	6.99	↔	8.25
B16	7.74	↔	6.55
B17	-		-
B18	7.02	↔	22.39
B19	8.01	↔	24.52
B20	7.67	↔	-
B21	6.67	↔	-
B22	7.33	↔	-
D1	7.67	↔	2.59
D2	7.33	↔	-
D3	6.29	↔	-
D4	-		6.39
D5	6.13		-
D6	-		-
D7	-		40.42
D8	6.38	↔	28.65
D9	7.93		-
D10	-		-
I1	7.69	↔	5.77
I2	7.69		-

4.6. Discussion

The opportunity to have access to frozen tissue sections enabled a validation to be made for the composition of microcalcifications using vibrational spectroscopy. Even though the frozen and de-paraffinised sections were not the same for each sample, the de-paraffinisation process did not seem to affect the spectral signatures of the microcalcifications. In fact, for Raman spectra, the phosphate peak is always located at 960 cm^{-1} and the carbonate peak at 1070 cm^{-1}, as it was for frozen sections and mineral standards (Chapter 3). This study has shown the heterogeneity in terms of proteins, lipids and carbonate content of microcalcifications between different samples from the same stage of pathology. In fact, some microcalcifications reveal the presence of carotenoids which have antioxidant and anti-proliferative effects [108], [109]. Due to the small number of samples, it is not possible to generalise the results according to a specific stage of pathology, and a larger number set for a specific type of sample (frozen sections or de-paraffinised sections) is necessary. Kunitake et al. have suggested that the collagen network is embedded or in contact with the surface of the microcalcification and plays a role to protect the surrounding tissue from the inflammatory process enhanced by microcalcification itself [113]. Second Harmonic Generation (SHG) or polarised FTIR spectroscopy could be effectively applied to localise and bring new information about the organisation of collagen fibres around microcalcifications in breast sections for different stages of disease and different shapes of microcalcifications. A correlation could be done between the Raman maps, FTIR and SHG images. In our samples, it was found that a large majority of microcalcifications contain carbonate ion substitutions in the Hap lattice. As discussed previously, the carbonate content increases in benign lesions [59] which is expected in our study but, considering the difficulties of evaluating the carbonate content, e.g. by curve fitting analysis, integration method or PLS model, and also the small number of samples, it is not possible to make definitive conclusions. Nevertheless, the PLS method applied to Raman spectra provides a realistic amount of carbonate ion substitution in microcalcifications which is in the same range for both types of sections (frozen or de-paraffinised) and is promising for further analysis.

The other challenging point is the use of FTIR spectroscopy and imaging with scattering due to the Hap crystal or cHap pellets which can add a bias in the calculation

of carbonate content. However, this study supports the hypothesis of intermediate mineral phases in microcalcifications. In addition, other elements substituted such as Mg, Na or Al could also affect the C:P ratio. These elements have been highlighted in breast microcalcifications using X-ray diffraction [41], [113]. In fact, it has been demonstrated that magnesium-substituted whitlockite (or β-TMCP) is increased in DCIS and invasive breast lesions based on changes observed for the Hap crystal [114]. X-ray techniques could offer a good complementary approach for exploring the elemental composition of microcalcifications. A study using micro-CT scan and X-ray fluorescence has shown the feasibility to localise quickly the microcalcifications in block breast sections and histological sections [115]. The combination of all these techniques (vibrational spectroscopy, X-ray diffraction etc.) can contribute to improve the knowledge about microcalcifications. Nevertheless, due to the heterogeneity of microcalcifications in terms of size and morphology [32], [35], [113] (as discussed in Chapter 1) or the small number of different compounds, their analyses remain challenging. Another approach seems to be necessary such as the study of *in vitro* microcalcifications. By using a cellular model of mineralisation, it may be possible to assess the progression of microcalcifications day by day and have a follow-up of their maturation process.

Chapter 5 : Assessment of breast cancer cell mineralisation using vibrational spectroscopy

5.1. Introduction

Many studies have investigated spectroscopy to probe the physiological and pathological mineralisation using different cell lines [104], [116], [117], but not a single one has yet focused on *in vitro* mechanisms of breast microcalcifications. The first *in vitro* model of mammary cell mineralisation was developed in 2012 by a team at the RSCI led by Dr Morgan using different breast cancer cell lines in order to study the molecular mechanisms involved in breast microcalcifications [118], [119]. To simplify the process, osteogenic agents are added to induce cell mineralisation, where β-glycerophosphate (βG) is a source of inorganic phosphate (Pi) for cells, ascorbic acid (AA) promotes collagen production and Dexamethasone (Dex) induces osteoblastic differentiation [120] which promote Hap formation and propagation in the ECM. Their first experiments used a murine mammary 4T1 cell line [118]. As illustrated in Figure 5.1a-c, mineralisation was followed at day 4 to 28 after induction. The mineralisation was assessed using Alizarin red (AR) staining (Figure 5.1a), which is commonly used to visualise rich calcium deposits [121], and validated by a calcium assay through an elevated calcium level in these calcifications (Figure 5.1b). The mineralisation was also studied by Raman micro-spectroscopy after 28 days of mineralisation using the phosphate peak at 960 cm^{-1} specific to Hap (Figure 5.1c). The formation of calcium deposits was induced by an osteogenic cocktail (OC) added in a regular medium, which contains a combination of βG and AA. In addition, they found that the microcalcification formation was dependent of the alkaline phosphatase (ALP) activity to produce inorganic phosphate (Pi), essential for Hap crystal formation [118]. Their results were promising and the protocol of mineralisation was applied to a human mammary MDA-MB-231 cell line [119]. In a manner similar to their previous study, cell mineralisation was assessed using AR staining and calcium assay after 28 days. In contrast to the murine cell line, MDA-MB-231 cells required an OC supplemented with Dexamethasone (Dex) to induce calcium deposits (Figure 5.1d and e). These experiments shown the ability of mineralisation of a human breast cancer cell line. This model is an opportunity to investigate molecular mechanisms involved in the

mineralisation process to understand the occurrence of microcalcifications in mammary gland.

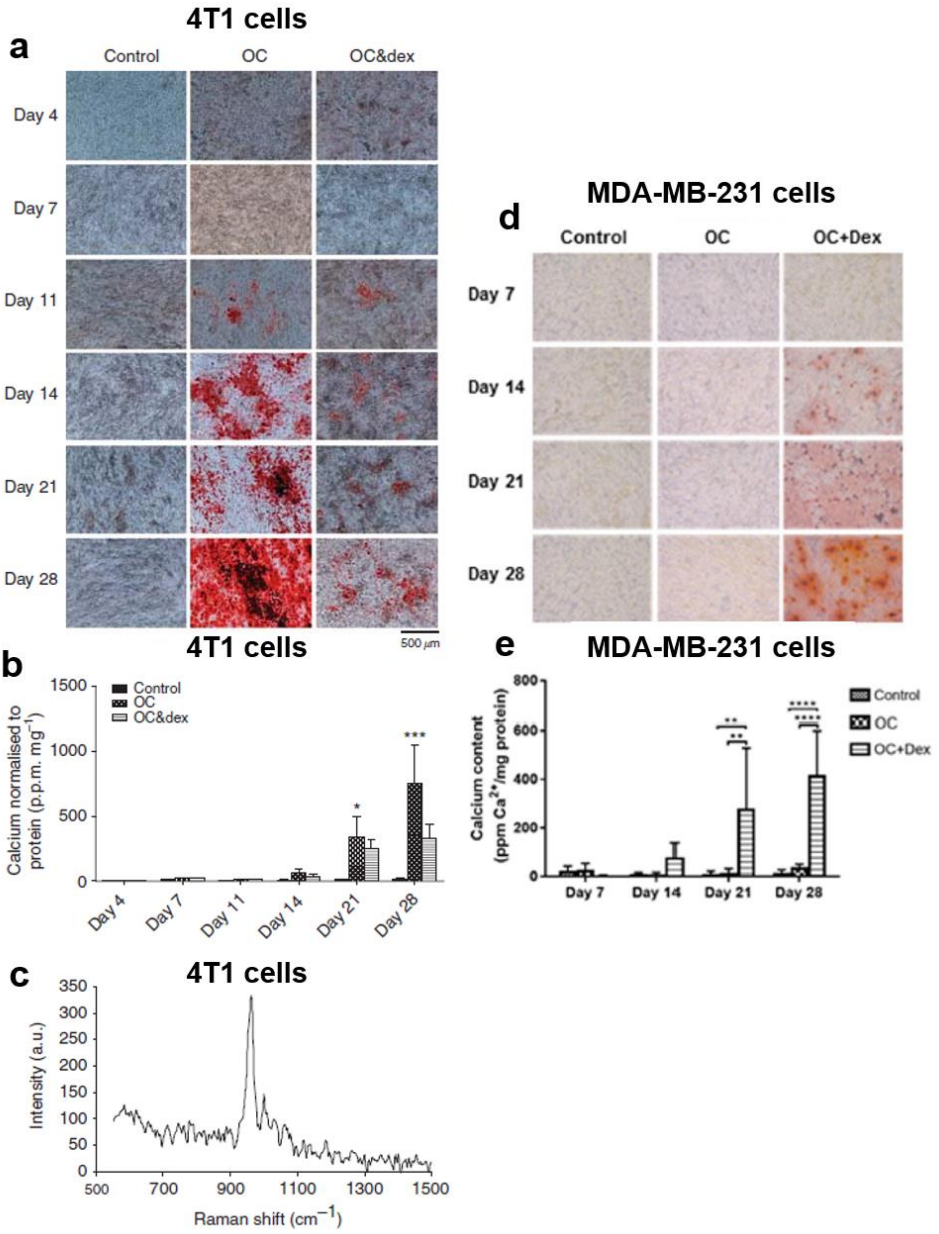

Figure 5.1 Assessment of mineralisation of MDA-MB-231 cell line using an osteogenic cocktail (OC) made of ascorbic acid, β-glycerophosphate and Dexamethasone (Dex). The mineralisation was followed at day 7 to 28 for (a) 4T1 cells and (d) MDA-MB-231 cells using Alizarin red staining at x100 magnification. (b, e) The calcium level was determined using the o-cresolphthalein calcium assay and normalised to protein. (c) Raman spectrum of calcium deposits found in 4T1 cells after 28 days of mineralisation. Adapted from [119], [120].

The collaboration with Dr Morgan was conducted as part of the EU Marie Curie Mid-TECH project and the aim of our study was to explore the calcium deposits in this MDA-MB-231 mammary cell model to evaluate their composition over time by using vibrational spectroscopy. Thus, this model allowed us to follow the maturation process and then to correlate specific spectral features of microcalcifications to our breast biopsies at different stages of the disease.

5.2. Time-course of the mineralisation

In our study, two different pathways were evaluated, i.e. cells grown by adding inorganic phosphate (Pi) and Dex or by using an OC (βG + AA+ Dex) in their culture media as described in Chapter 2, section 2.3.6.

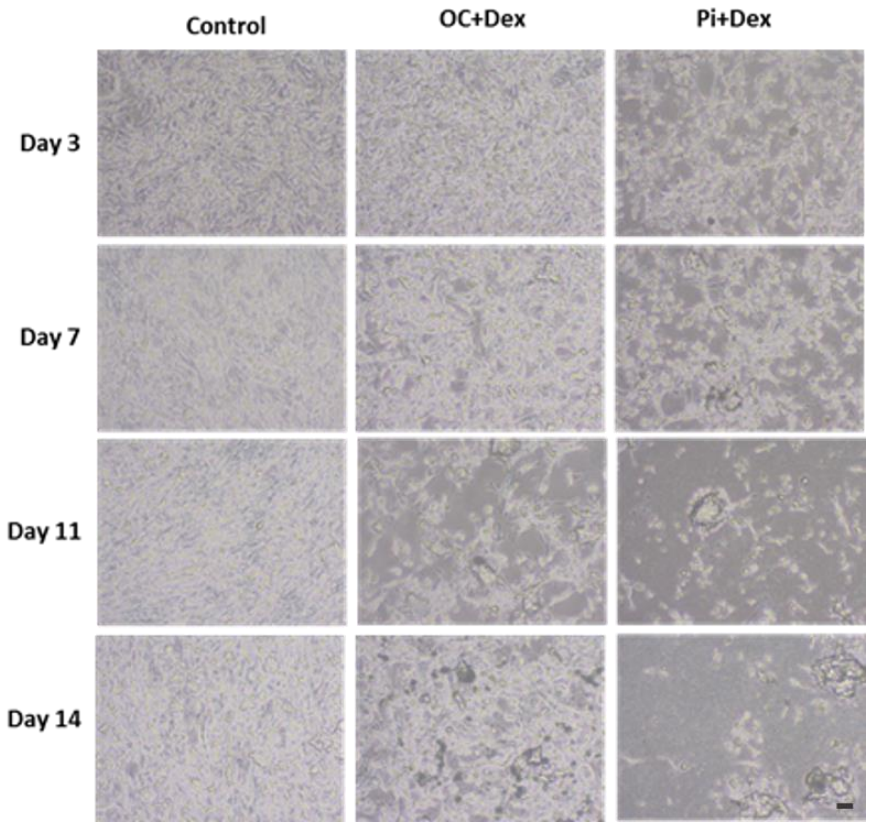

Figure 5.2 Representative images of MDA-MB-231 cells growing at different time point of mineralisation (Day 3, 7, 11 and 14). Cells grown on BaF_2 substrate in control medium (regular medium), OC (osteogenic cocktail: βG + Ascorbic acid + Dexamethasone) and Pi + Dexamethasone medium. (n=3). X100 magnification, scale bar represents 50 μm. Figure provided by S. O'Grady from the RSCI.

Figure 5.2 illustrates cells growing on BaF_2 substrate for each condition up to 14 days. This figure shows that cells treated with Pi for 11 and 14 days are more aggregated than cells at day 3 or the control group. This was not found to be the case when cells are grown on plastic within 6-well plates. Moreover, it is not possible to grow cells beyond 14 days when they are treated with Pi without damaging the BaF_2 substrate. Both these factors are not a good combination for cell survival.
However, besides these points, for our study it was possible to follow and assess the mineralisation at different time points using Raman micro-spectroscopy.

5.2.1. Spectral characteristics

As illustrated in Figure 5.3a, cells treated with Pi present the onset of mineralisation only three days after their treatment (blue spectrum) compared to the control and cells treated with OC+Dex (or βG) (red and green spectra). In fact, the Raman spectrum of cells treated with Pi (blue spectrum) exhibits a distinct peak at 960 cm^{-1} corresponding to the ν_1 PO_4^{3-} mode of Hap. For all conditions, we found spectral features related to proteins (Amide I and III) and lipids at 1656, 1338, 1300, 1257 and 1447 cm^{-1}, but also collagen with hydroxyproline and proline signals at around 853, 875 and 935 cm^{-1}.
Regarding the cells treated with βG, the mineralisation process begins at day 11 (Figure 5.3b, green spectrum) and the spectrum shows a peak shifted to 956 cm^{-1} compared to the spectrum from cells treated with Pi at 959 cm^{-1} (blue spectrum). A phosphate peak at 587 cm^{-1} corresponding to the ν_4 PO_4^{3-} mode [70] is apparent in the spectrum of cells treated with Pi at day 3 (blue spectrum, Figure 5.3a). At day 11, this peak is present in spectra of cells treated with Pi and βG at 587 and 584 cm^{-1}, respectively (blue and green spectra, Figure 5.3b). When cells are treated with βG, a shift is observed for both ν_1 PO_4^{3-} and ν_4 PO_4^{3-} bands. This suggests the presence of another mineral phase in the *in vitro* microcalcifications. It is also noted that there are several peaks, as previously, corresponding to proteins and lipids but weaker when cells are treated with βG than control cells. For further information, spectra from cells at day 7 and 14 are illustrated in Appendix, supplementary data 4, Figure D.1. No phosphate peak at day 7 for cells with βG is noted. At day 14, the peaks for lipids and proteins are weaker for cells treated with Pi and βG than those from the control group.

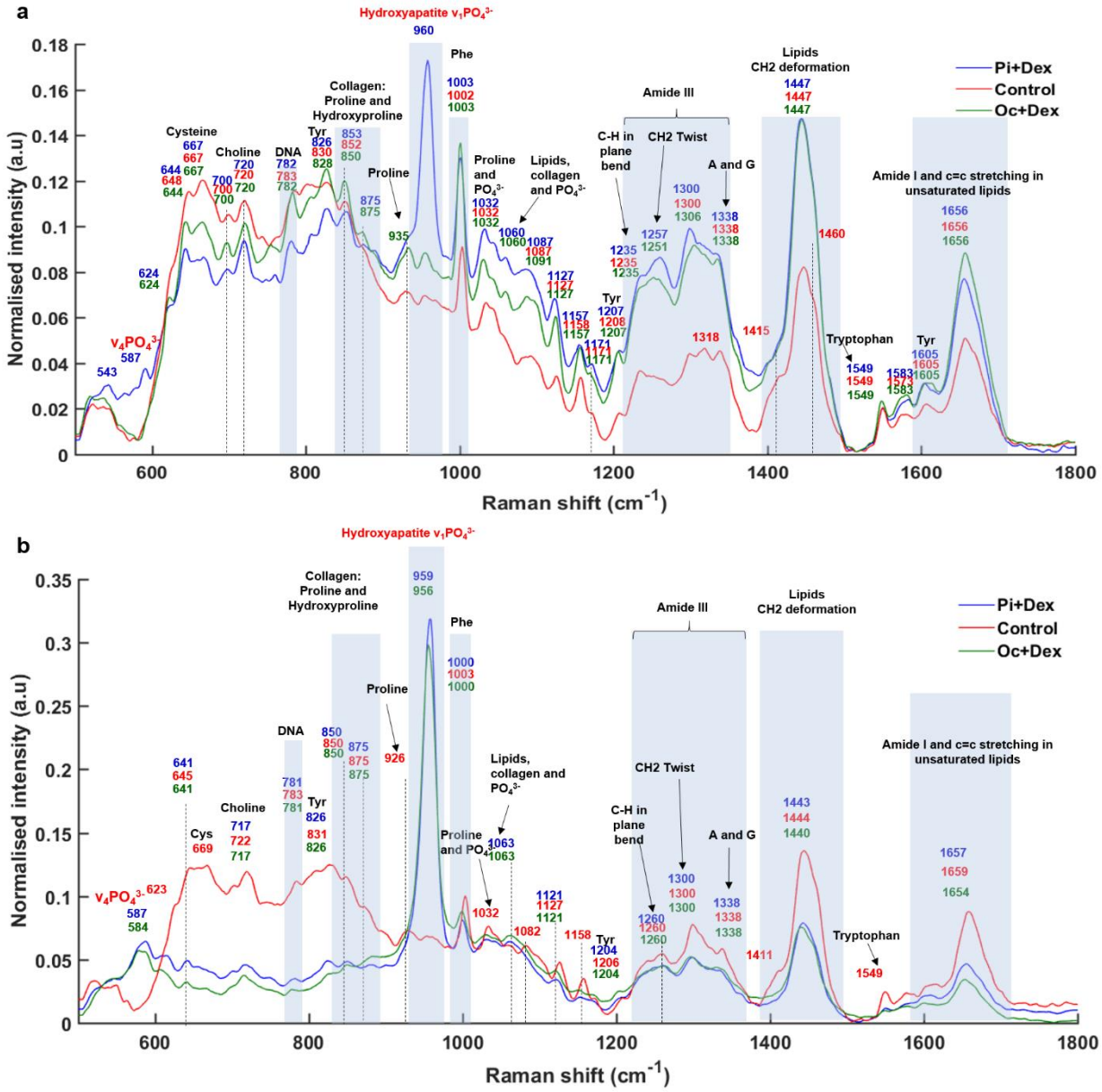

Figure 5.3 Raman spectra acquired from breast cancer cells after 3 days (a) and 11 days (b) of mineralisation. Pi: inorganic phosphate, OC: osteogenic cocktail, Dex: Dexamethasone, Phe: Phenylalanine, Cys: Cysteine, Tyr: Tyrosine. Cells were treated with Pi+Dex and OC+Dex (βG). Non-treated cells are considered as control. Each spectrum is an average of 40 spectra for each condition.

5.2.2. Principal Component Analysis

To understand the chemical changes underlying the mineralisation process, a PCA was performed on the spectra extracted from breast cancer cells for each condition (Figure 5.4): control (red dots), cells treated with βG (green dots) and Pi (blue dots).

This allows a follow-up of the mineralisation process at day 3, 7, 11 and 14. Figure 5.4 illustrates PCA score plots and corresponding PC loadings.

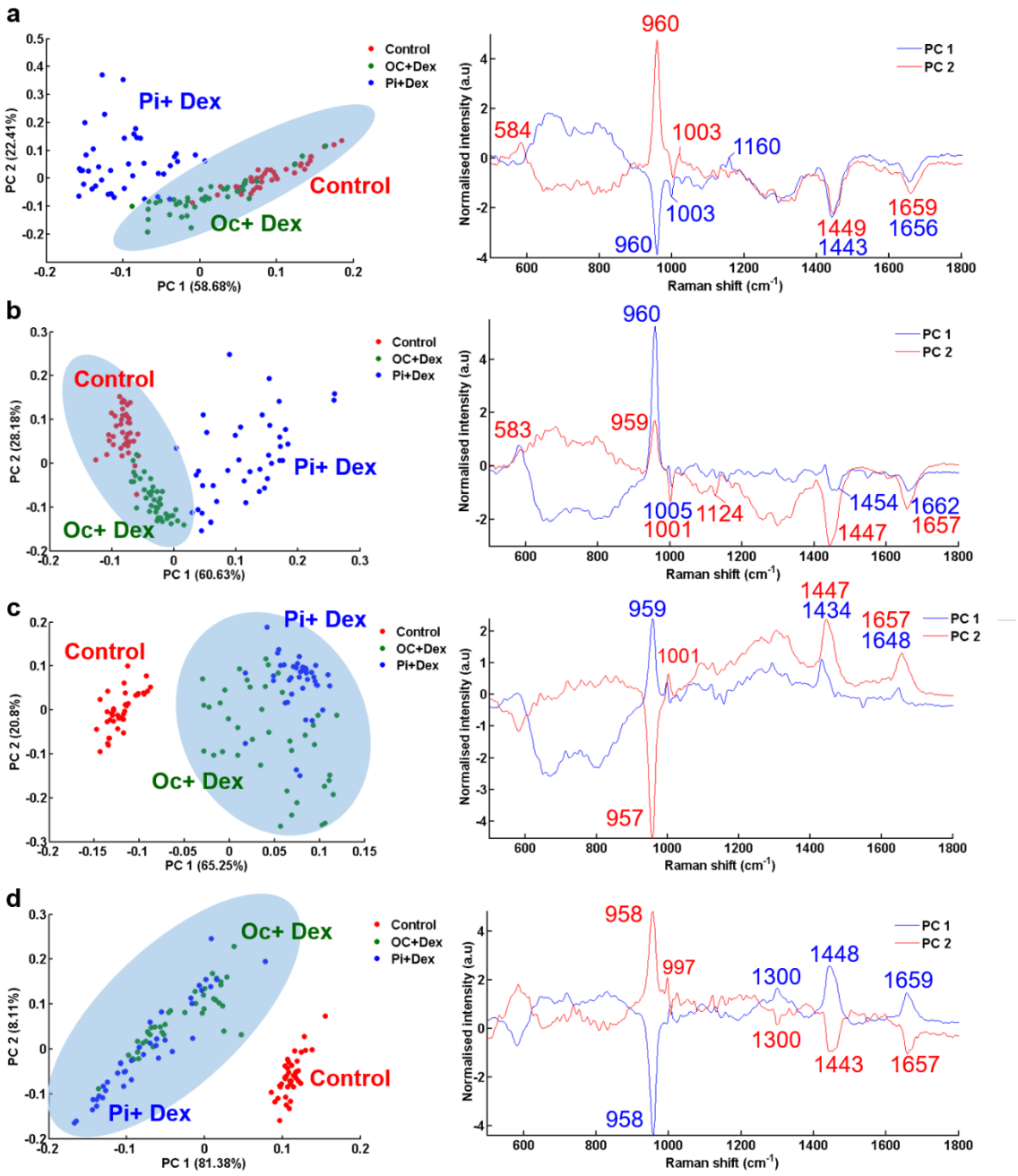

Figure 5.4 Principal Component Analysis (PCA) applied to 40 Raman spectra collected from breast cancer cells after 3 days (a), 7 days (b), 11 days (c) and 14 days (d) of mineralisation and for each condition (control in red, cells treated with βG (OC+Dex) in green and Pi+Dex in blue). PC1 and PC2 loadings are shown in blue and red, respectively.

At day 3 and 7 (Figure 5.4a and b), the cells treated with βG and control cells appear to belong to the same cluster (blue ellipse). PC 1 and 2 represent 58.68% and 22.41%

at day 3 and 60.63% and 28.18% at day 7 of the entire variance in the dataset. As expected, cells treated with Pi (blue dots) induce a faster mineralisation (day 3, Figure 5.4a) compared to the cells treated with βG which occurs only at day 11 (Figure 5.4c). Moreover, calcium deposits from Pi culture medium exhibit more phosphate and less proteins than control group (Figure 5.4b and c, PC1 and 2 loadings). At day 11 and 14 (Figure 5.4c and d), clusters are inverted and control cells are in a different group than cells treated with Pi and βG (blue ellipse). PC1 and 2 represent 65.25% and 20.8% at day 11 and 81.38% and 8.11% at day 14 of the entire variance in the dataset. As discussed above, cells treated with βG have started their mineralisation and present a phosphate peak at 957 cm^{-1}. In parallel, there is an important level of phosphate and less of proteins than the control group in their calcium deposits. However, at day 11, calcium deposits from both the culture media present an unexpected increase of protein level (Figure 5.4c and d, PC1 and 2 loadings).

In order to have a follow-up of the mineralisation process, PCA was also performed for each day and condition together. PCA score plots as well as PC 1 and 2 loadings and PC1 and 3 loadings are illustrated in Figure 5.5.

For PCA with PC scores 1 and 2, which represent 57.48% and 27.13% of the entire variance in the dataset (Figure 5.5a), two clusters are distinct:

- Control cells (all days) and cells treated with βG at day 3 and 7 (blue crescent-shaped).
- Cells treated with Pi (all days) and cells treated with βG at day 11 and 14 (blue ellipse).

PC 1 and 2 loadings show that calcium deposits from Pi and βG culture medium for day 11 and 14 have a high level of phosphate and less proteins than the control group.

For PCA with PC scores 1 and 3, which represent 57.48% and 6.30% of the entire variance in the dataset (Figure 5.5b), three clusters are distinct:

- Control cells (all days) and cells treated with βG for day 3 and 7 (blue ellipse 1).
- Cells treated with Pi (all days except for day 14) and cells treated with βG for day 11 (blue ellipse 2).
- All cells treated with osteogenic agents at day 14 (blue ellipse 3).

PC 1 and 3 loadings show similar results. There is an increase in phosphate content (peak at 958 cm^{-1}) and less lipids and proteins (1448 and 1656 cm^{-1}) as the mineralisation evolves compared to control and both Pi and βG culture media.

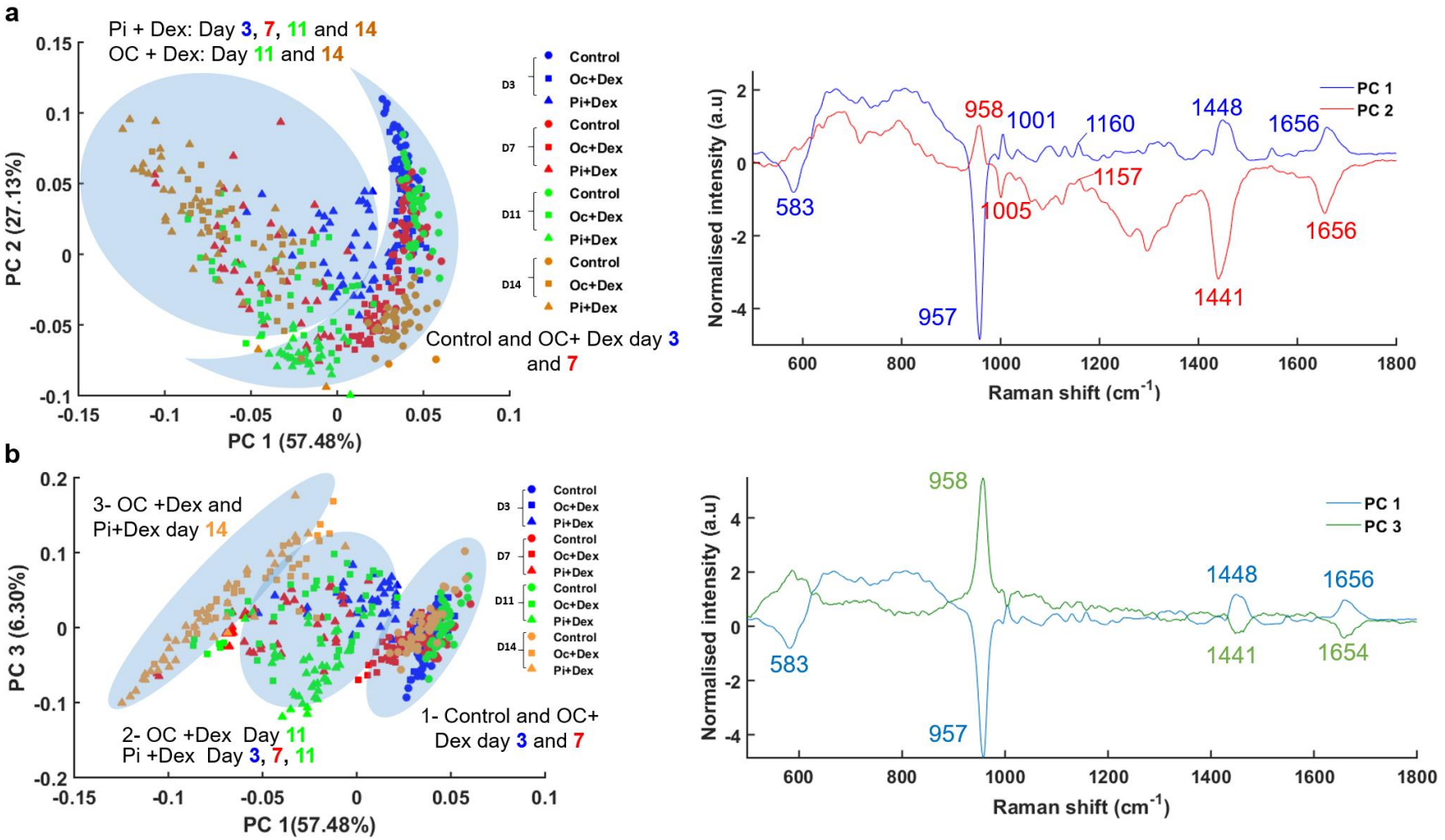

Figure 5.5 PCA plots from 40 Raman spectra acquired from breast cancer cells 3 days (blue), 7 days (red), 11 days (green) and 14 days (orange) of mineralisation and for each condition (control in dot, cells treated with βG (OC+Dex) in square and Pi in triangle). (a) PC 1 and 2 score plots and their loadings (blue and red) and (b) PC 1 and 3 score plots and their loadings (blue and green).

5.2.3. Spatial distribution of calcium deposits

PCA was applied to the Raman maps in order to localise different sites of mineralisation. Results at days 11 and 14 for cells treated with Pi and βG are illustrated in Figures 5.6 to 5.13.

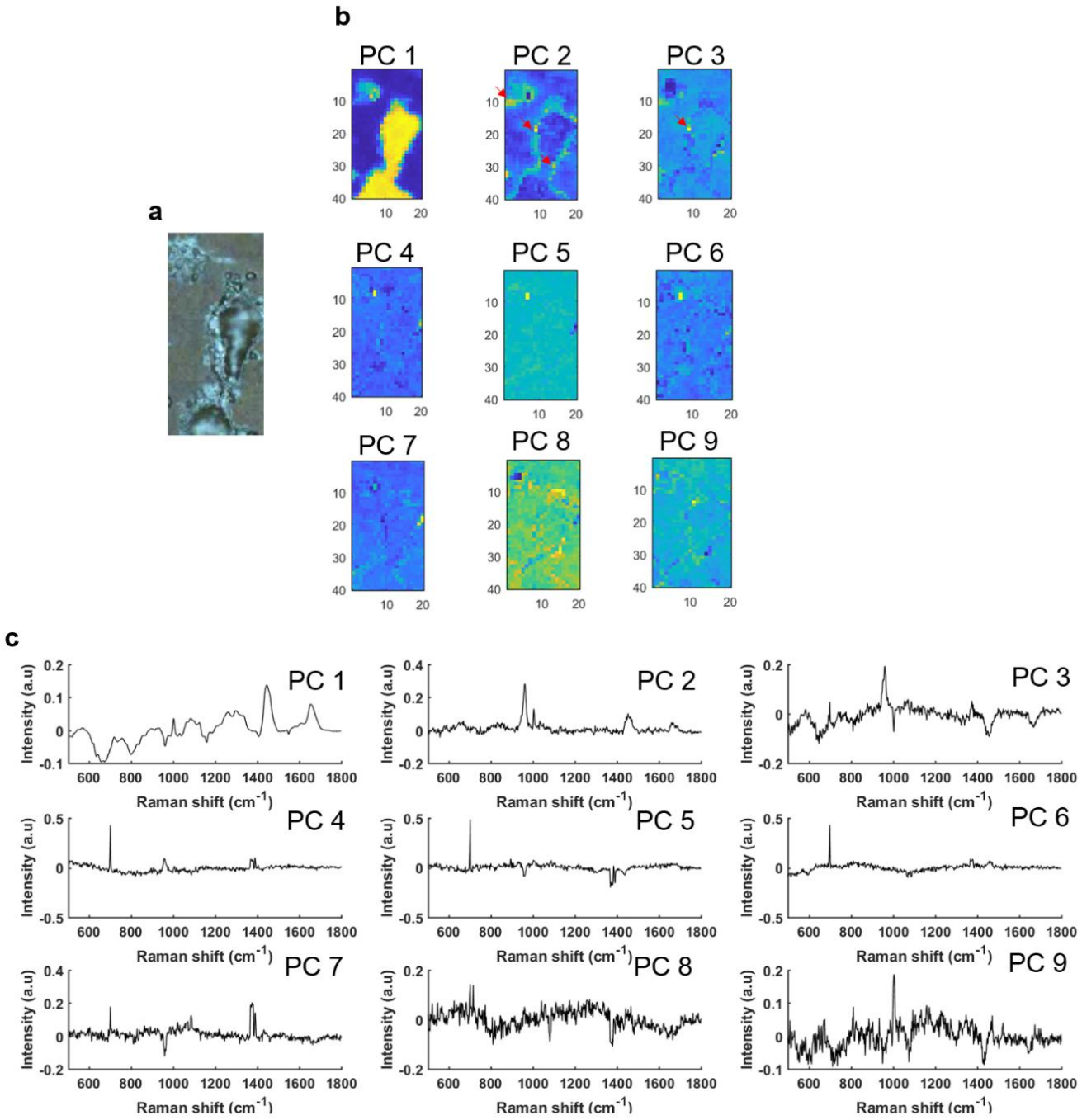

Figure 5.6 PCA performed on a Raman map collected from breast cancer cells treated with Pi after 11 days of mineralisation. (a) White light image of breast cancer cells, (b) the first nine PC scores, and (c) corresponding PC loadings.

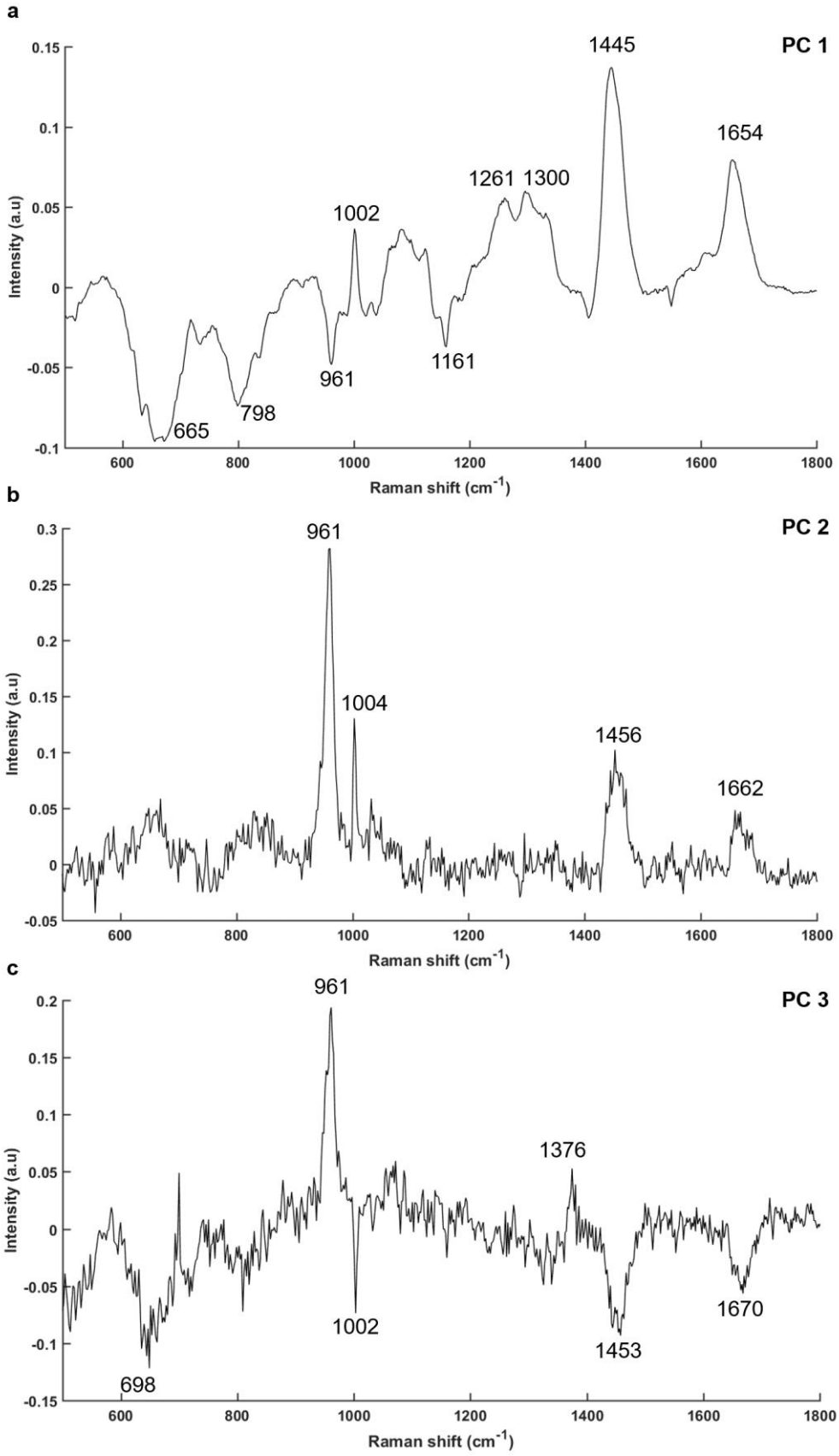

Figure 5.7 Loadings for (a) PC1, (b) PC2 and (c) PC3 showing peak positions for different contributions in Raman spectra for breast cancer cells treated with Pi after 11 days of mineralisation.

Figure 5.6 illustrates the PCA scores and loadings for cells with Pi in the medium after 11 days of mineralisation and, for clarity, Figure 5.7 shows PC1, 2 and 3 loadings and their peak assignments. PC1 loading shows that cells contain a combination of proteins and lipids (1654, 1445, 1300, 1621 cm^{-1} for Amide I, CH_2 deformation and Amide III) [106], [108], [122] and carotenoids at 1157 cm^{-1}. Their co-localisation is represented by yellow colour in the PC1 score (Figure 5.6b). In orange, DNA signal is well-represented by peaks at 665 and 798 cm^{-1} [106], [107]. PC2 exhibits a combination of phosphate, lipid and protein peaks and they are represented by yellow spots (red arrows, Figure 5.6b), whereas PC3 loading is mainly due to calcium deposits (peak at 959 cm^{-1}) represented by a yellow spot (red arrow, Figure 5.6b).

In the same way, for cells growing in the Pi medium after 14 days of mineralisation (Figure 5.8 and 5.9), the main components are defined by PC 1, 2 and 3. The PC1 score represents the nucleus of cells (yellow and orange, Figure 5.8b) whilst the PC2 score is defined by the calcium deposits with several small yellow spots (red arrows, Figure 5.8b). The PC3 represents the cytoplasm of cells (Figure 5.8b, in yellow and orange). As previously, PC 1, 2 and 3 loadings and their peak assignments are shown individually for clarity in Figure 5.9. In the PC1 loading, the nucleus is rich is DNA (Figure 5.8b, PC1 score, in orange) with peaks at 677 and 794 cm^{-1} [106], [107]. This area is also rich in lipids and proteins (1654, 1445, 1333 and 1303 cm^{-1} for Amide I, CH_2 deformation and Amide III, respectively) [106], [108], [122] and identified by yellow colour (Figure 5.8a, PC1 score). The PC2 loading shows a high phosphate peak for Hap at 959 cm^{-1} corresponding to calcium deposits in small spots (Figure 5.8b, red arrows) without proteins or lipids (Figure 5.9b).

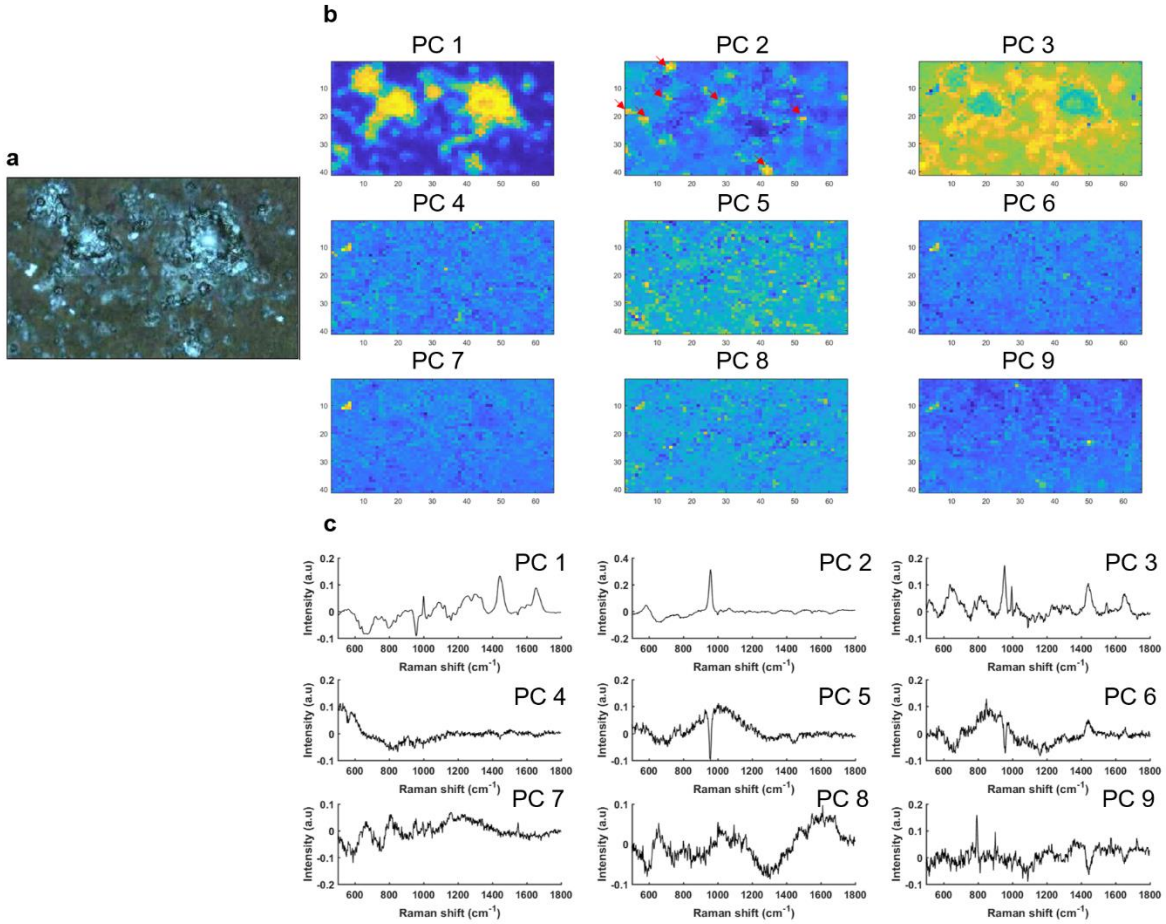

Figure 5.8 PCA performed on a Raman map collected from breast cancer cells treated with Pi after 14 days of mineralisation. (a) White light image of breast cancer cells, (b) the first nine PC scores, and (c) corresponding PC loadings.

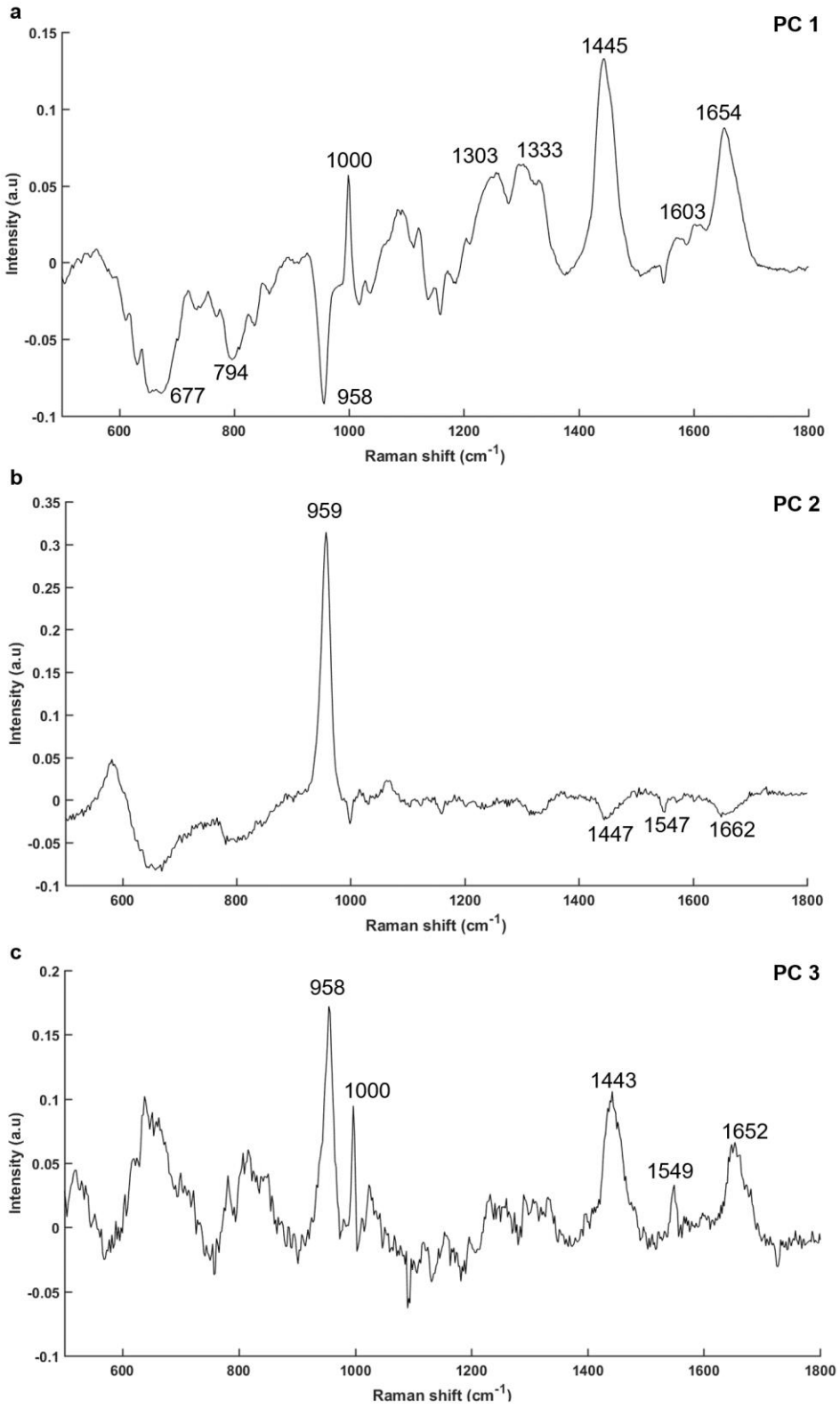

Figure 5.9 Loadings for (a) PC1 (b) PC2 and (c) PC3 showing peak positions for different contributions in Raman spectra for breast cancer cells treated with Pi after 14 days of mineralisation.

The same analysis was performed on Raman maps from cells treated with βG, and similar results are found after 11 and 14 days after of mineralisation. PC scores and their loadings at day 11 and 14 are shown in Figure 5.10 to 5.13.

At days 11 and 14, for PC1 loading, DNA is defined by peaks at 655/671 cm^{-1} and 796/798 cm^{-1} (Figures 5.11a and 5.13a), which is represented in orange by PC1 score (Figures 5.10b and 5.12b).

At day 11 and 14, calcium deposits and cytoplasm are well-defined separately. In Figure 5.11b, at day 11 PC2 loading is described by a combination of proteins and lipids in the cytoplasm of cells at 1443 and 1658 cm^{-1} (yellow and orange in PC2 score Figure 5.10b), whereas at day 14 the cytoplasm is represented by the PC3 loading (PC3 score, in yellow, Figure 5.12b).

The calcium deposits are represented in yellow spots by PC3 score for day 11 and PC2 score for day 14 (red arrows, Figures 5.10b and 5.12b). These microcalcifications exhibit a strong phosphate peak at 958 and 957 cm^{-1} without any proteins or lipids (PC2 and 3 loadings, Figure 5.11b and Figure 5.13c).

However, by comparing phosphate peak positions, a shift is noticed between both conditions (Pi and βG treatment). In fact, when cells are treated with Pi, the phosphate peak is around 959-961 cm^{-1} while when cells are treated with βG it is around 957-958 cm^{-1} at day 11 and 14 of mineralisation, which is in line with the previous results and suggests the possibility of the presence of another mineral [116].

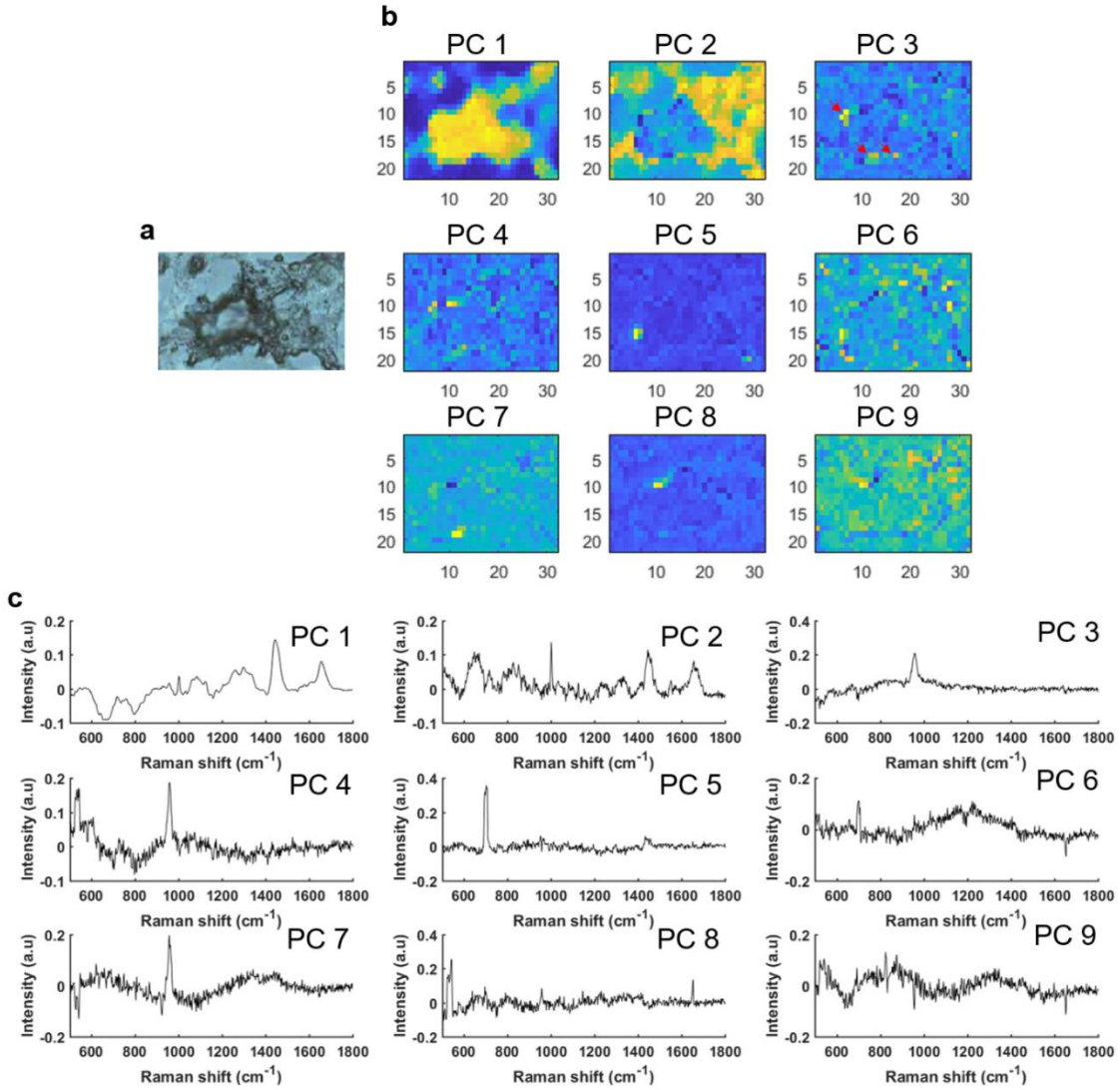

Figure 5.10 PCA performed on a Raman map collected from breast cancer cells treated with βG after 11 days of mineralisation. (a) White light image of breast cancer cells, (b) the first nine PC scores, and (c) corresponding PC loadings.

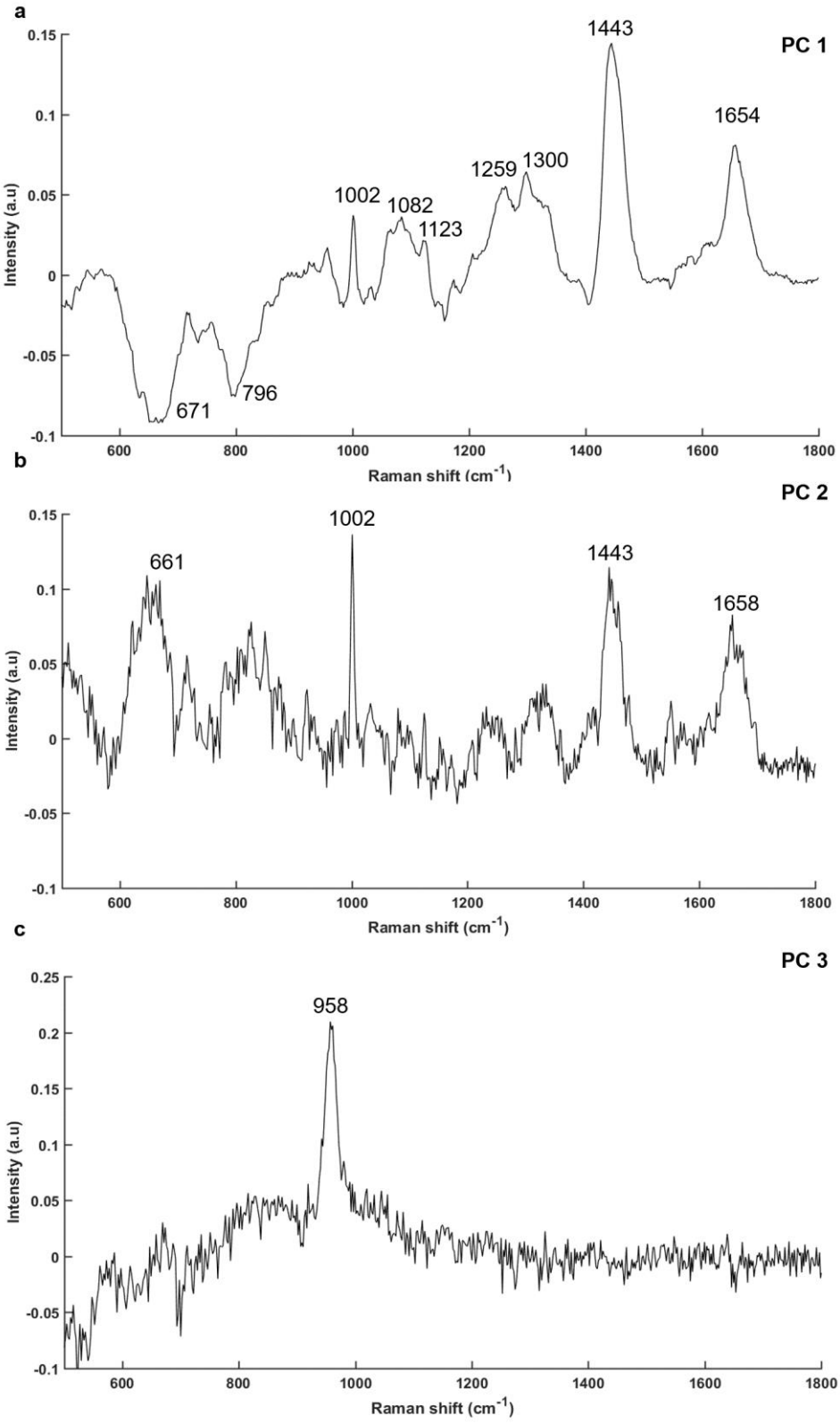

Figure 5.11 Loadings for (a) PC1, (b) PC2 and (c) PC3 showing peak positions for different contributions in Raman spectra for breast cancer cells treated with βG after 11 days of mineralisation.

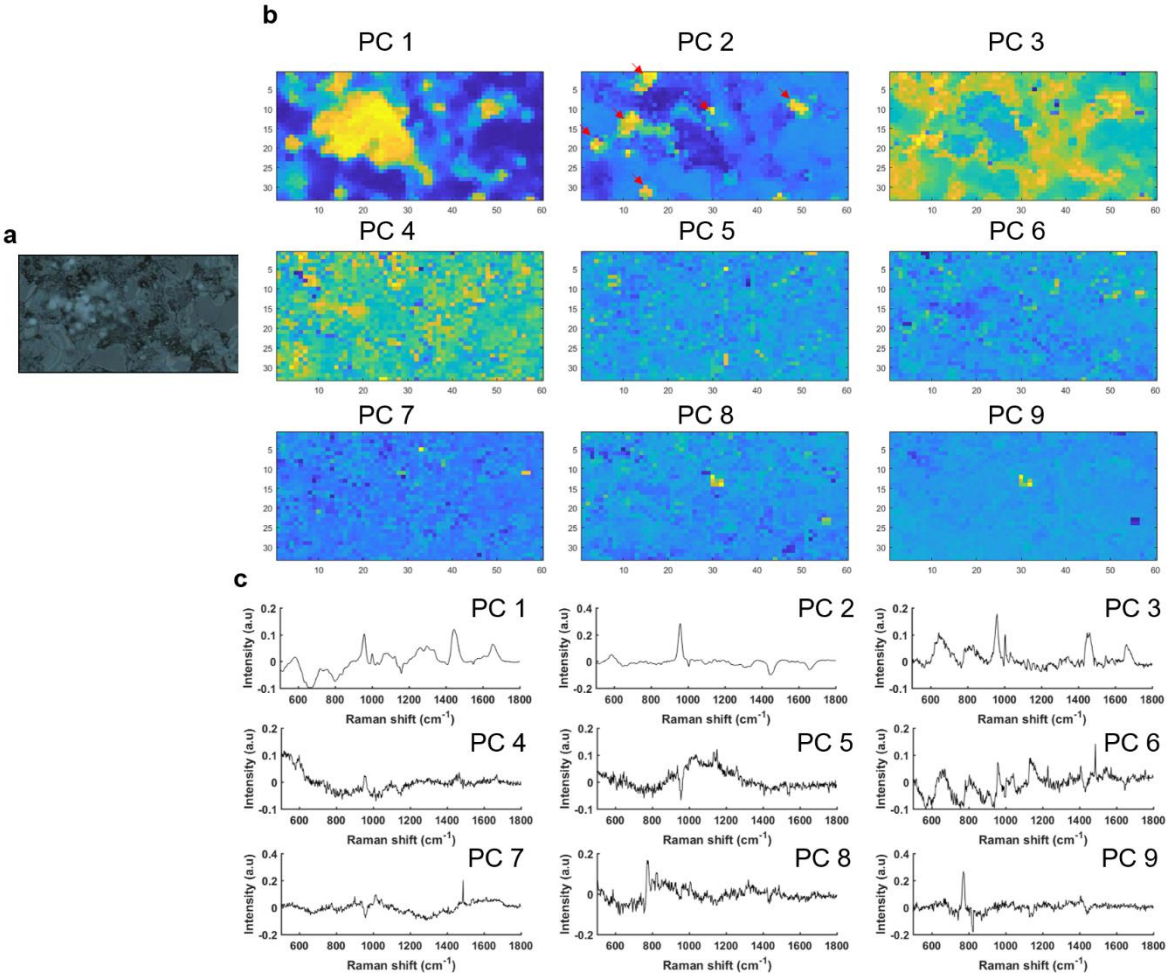

Figure 5.12 PCA performed on a Raman map collected from breast cancer cells treated with βG after 14 days of mineralisation. (a) White light image of breast cancer cells, (b) the first nine PC scores, and (c) corresponding PC loadings.

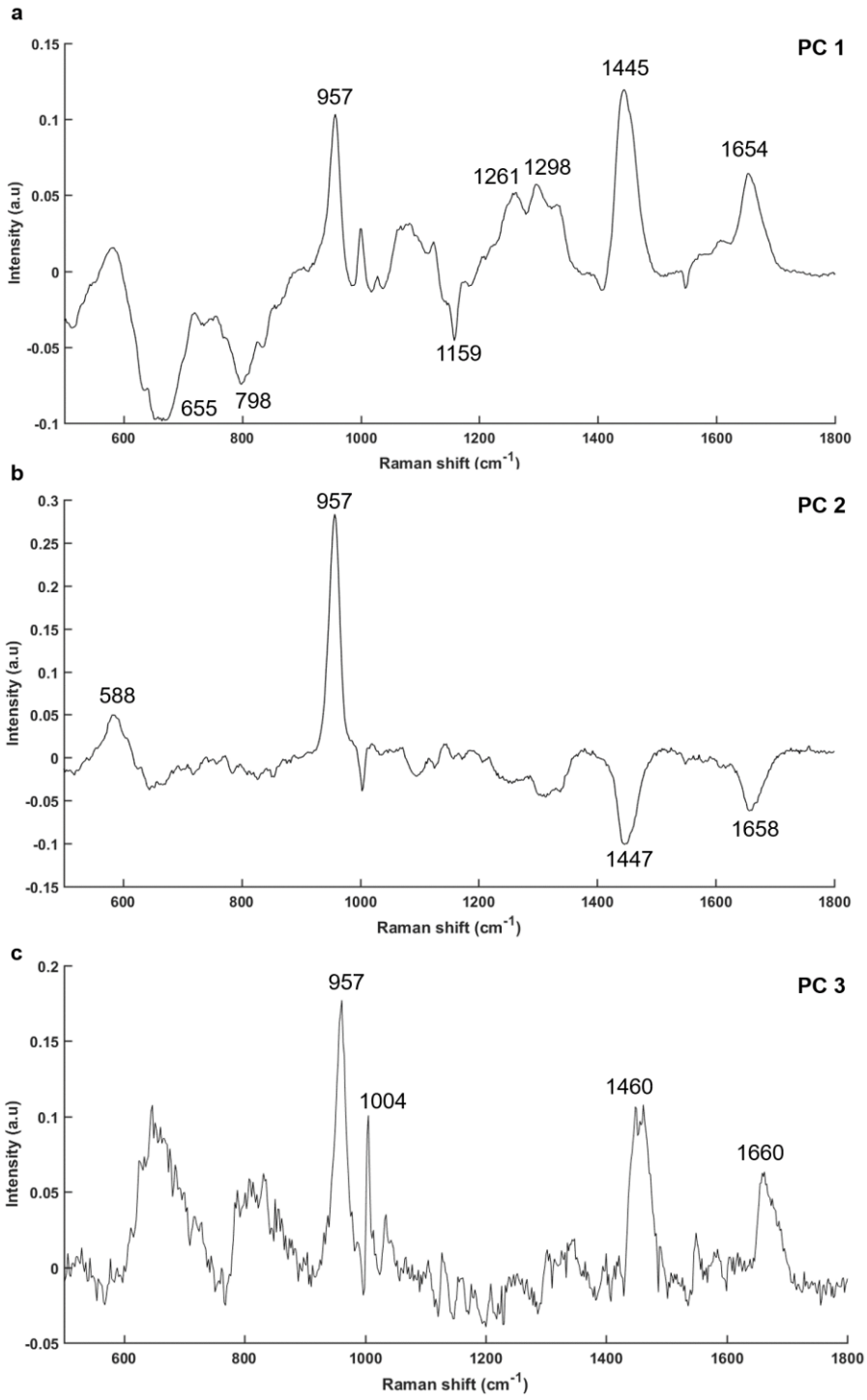

Figure 5.13 Loadings for (a) PC1, (b) PC2 and (c) PC3 showing peak positions for different contributions in Raman spectra for breast cancer cells treated with βG after 14 days of mineralisation.

As discussed in Figures 5.4 and 5.7, cells treated with Pi at day 11 exhibit calcium deposits with a combination of proteins and lipids, which is not the case at day 14, where only a phosphate peak is observed. The calcium deposits from cells growing with βG at day 11 and 14 do not have proteins or lipids and the phosphate peaks are

shifted compared to cells treated with Pi. This suggests different mechanisms of mineralisation. Moreover, these microcalcifications seem to be outside the cells for cells treated with Pi and βG, however further investigations are needed using higher spatial resolution.

In this context, few samples containing cells treated with Pi and βG after day 11 of mineralisation were sent to Synchrotron Australia and Synchrotron Soleil in France for tests. Tobin et al. have used macro-attenuated total reflection Fourier Transform infrared (ATR-FTIR) spectroscopy. This technique is based on the absorption of an evanescent field generated by the reflection of IR light at the interface between an ATR crystal and the biological sample [123], [124]. In our case, a spatial resolution of 0.5 μm and 2 μm was applied which is higher than that of our system in transmission mode. An example is illustrated in Appendix, supplementary data 4, Figure D.2 showing an external calcium deposits with a strong phosphate region in the cells (red areas, white arrows) for both conditions, Pi and βG treatments, which is more evident using FTIR spectroscopic imaging (Appendix, supplementary data 4, Figure D.3) with a 3 μm spatial resolution. In addition, Kansiz et al. have applied optical photothermal infrared (O-PTIR) spectroscopy on few samples. In this technique, a mid-IR laser induces photothermal effect into the biological sample surface, which is detected by a visible laser thus providing enhanced spatial resolution [125]. An example is shown in Appendix, supplementary data 4, Figure D.4 and the spatial resolution used in this test was 0.4 μm, which is the same as that of ATR-FTIR spectroscopic imaging but without the disadvantage of damaging the sample by contact with the crystal. The results show several small spots (red arrows) with a high phosphate intensity, which correspond to calcium deposits by cells. These results seem promising and further investigations are necessary with several replicates for reproducibility.

5.3. Analysis of mineralisation

5.3.1. Peak analysis

A peak decomposition by curve fit analysis was performed for all Raman and IR spectra, including each day and condition. Figure 5.14 illustrates the results of a peak decomposition applied to Raman spectra for each ν_1 PO_4^{3-} band between 985 and 915 cm^{-1} for cells treated with Pi (day 3 to 14) and cells with βG (day 11 and 14).
For cells treated with Pi, the phosphate band exhibits four components at 967, 958, 950 and 943.5 cm^{-1} which corresponds to ν_1 PO_4^{3-} and ν_3 PO_4^{3-} bands. For information, regarding the other replicates, the phosphate peak at 959 cm^{-1} is shifted to 959.7 cm^{-1}.
The presence of all these peaks in the phosphate band is in line with previous results and could be related to a combination of cHap and OCP minerals (OCP is defined by three peaks at 968, 960 and 945 cm^{-1} as described in Chapter 3). The peak at 936 cm^{-1} found at day 3 could be due to proline, which corresponds to the α-helix of collagen [107], [126] and this is in line with the observation done in Figure 5.3a.
For the cells treated with βG, the components are 966, 956, 950 and 942 cm^{-1} which could be a combination of β-TCP and cHap or ACP (β-TCP is defined by 966 and 957 cm^{-1} and ACP by 958 and 945 cm^{-1}, see Chapter 3). In fact, the presence of the shifted phosphate peak at 956 cm^{-1} supports this hypothesis.

In parallel, a curve fit analysis was also performed on the ν_1 CO_3^{2-} band between 1095 and 1020 cm^{-1}, when it was possible due to weak signals, and illustrated in Appendix, supplementary data 4, Figure D.5. A small peak at 1070 cm^{-1}, resulting from the curve fit analysis suggests the presence of small amount of carbonate ion substitution in the samples. The same analysis has been done for each replicate and are reproducible (data not shown). These results enable to calculate the C:P ratio or the crystallinity of Hap, even give complementary information about the quantity of different precursors in the samples.

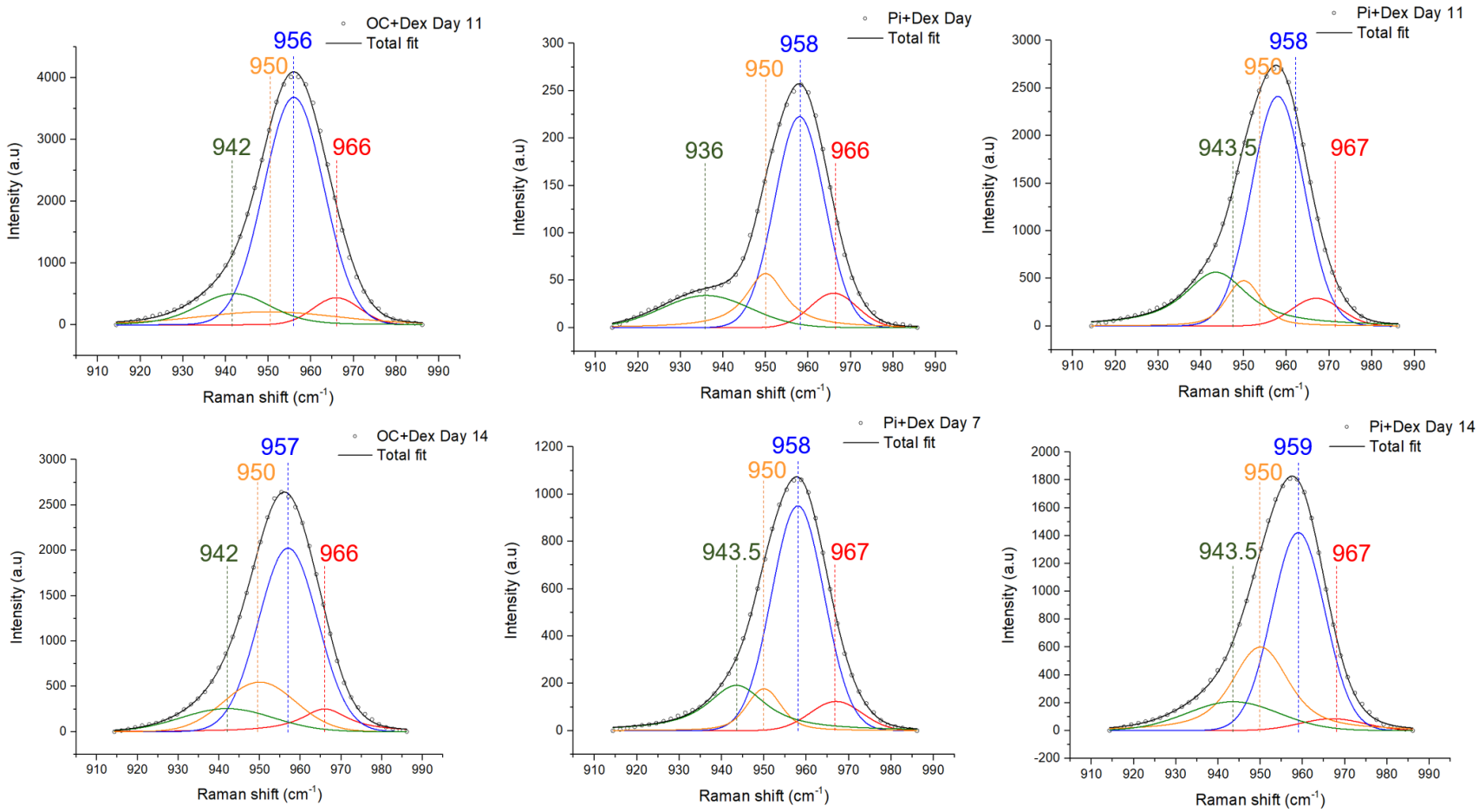

Figure 5.14 Results from curve fit analysis of Raman spectra from cells treated with Pi + Dex at 3, 7, 11 and 14 days of mineralisation and OC+Dex (βG) at 11 and 14 days of mineralisation. Spectra were truncated to the phosphate band at 985-915 cm^{-1} and baseline-corrected. For each case, $R^2 > 0.99$.

5.3.2. Carbonate-to-phosphate ratio

The C:P ratio was calculated using the results from curve fit analysis and based on the ratio between carbonate peak at 1070 cm^{-1} and phosphate peak at 960 cm^{-1} using the areas under each peak. By comparing the ratio with that found in the calibration standards as outlined in Chapter 3, we determined the amount of carbonate ion substitution from Raman spectra of cells treated with Pi or βG at day 3, 7, 11 and 14 of mineralisation. The ratio and the amount of carbonate estimated for each sample are listed in Appendix, supplementary data 4, Table D.1.

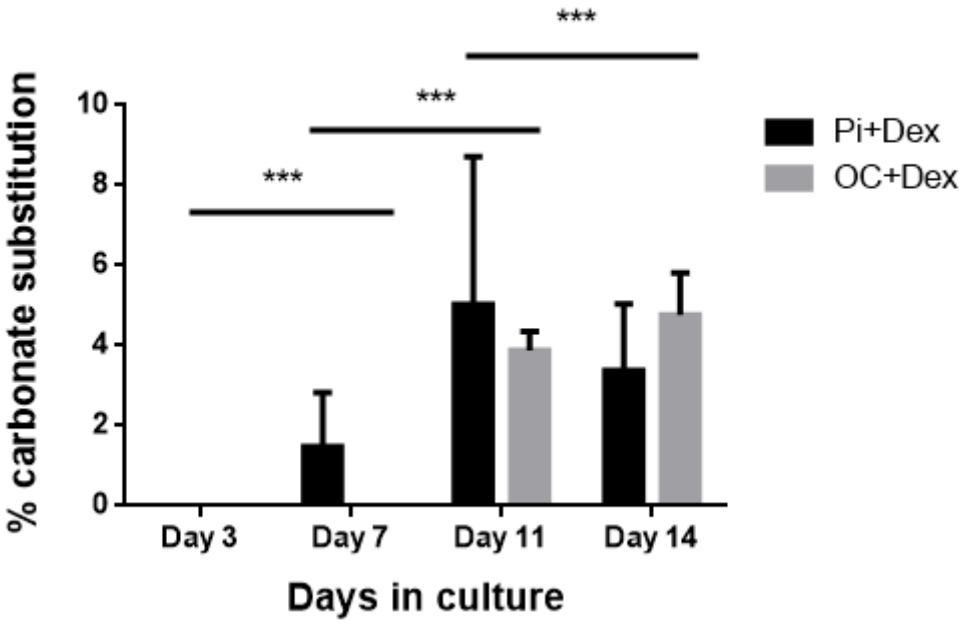

Figure 5.15 C:P ratio based on the area under the carbonate peak at 1070 cm^{-1} and phosphate peak at 960 cm^{-1} for the different treatments (OC+Dex and Pi+Dex) and different days of mineralisation. Data are presented as a mean ± SD. Two-way ANOVA test was performed, P=0.0005***.

Figure 5.15 shows an increase of carbonate content in Hap lattice for cells treated with βG during the mineralisation process. In fact, the carbonate content of cells after 11 days was found to be around 3.5 wt.% and rose to 4.7 wt.% after 14 days. While the mineralisation of cells treated with Pi starts after 3 days of initiation, the incorporation of carbonate into the Hap crystal (at least to greater levels than the detection limit) appears after 7 days of mineralisation varying between 1.8 and 2.7 wt.% and increases up between 2 to 9.5 wt.% at day 11. It seems to decrease after 14 days with 2.3 to 5 wt.% (the carbonate content for each replicate is listed in Appendix, supplementary 4,

Table D.1). The variations of carbonate content in microcalcifications observed between the three replicates may be due to the curve fit analysis, the spectral quality or the differences in cHap crystal growth. By getting information of the crystal size for both conditions, it should allow to highlight different processes of Hap crystal growth.

5.3.3. Hap crystallinity

Several studies suggest that the crystallinity or the size of Hap crystal can be related to the inverse of the full width at half maximum (FWHM) of the peak at 960 cm^{-1} for ν_1 PO_4^{3-} mode [70], [126]. Based on the results obtained from this curve fit analysis, the inverse of the FWHM of phosphate peak was calculated and the results are summarised in Figure 5.16.

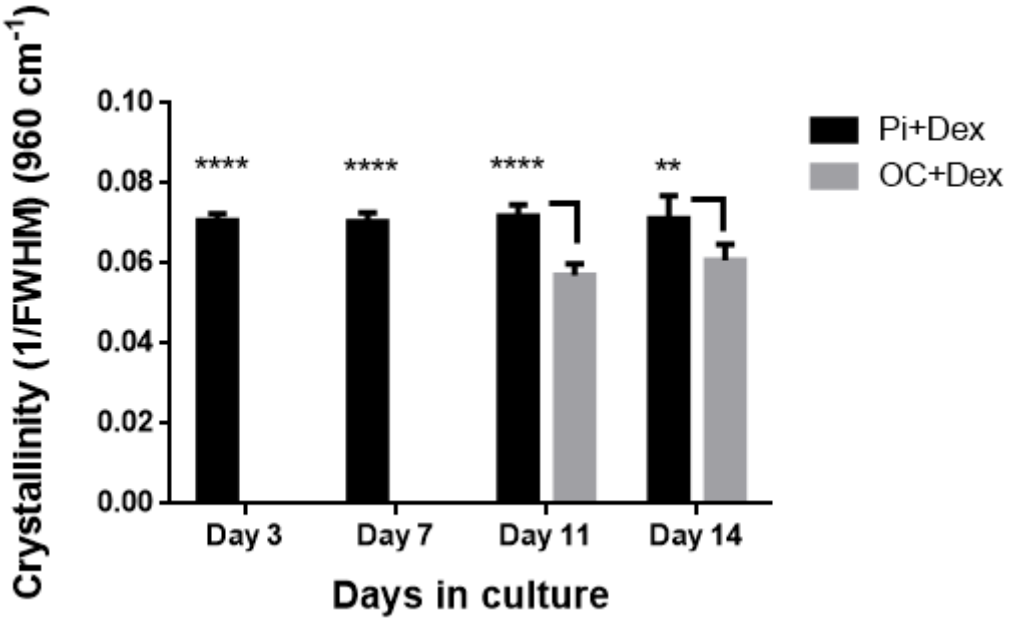

Figure 5.16 Hap crystallinity based on the inverse of the FWHM of peak at 960 cm^{-1} after 3, 7 11 and 14 days of mineralisation and for both treatments Pi and βG. Data are presented as a mean ± SD. Two-way ANOVA test was performed, P< 0.0001**** and P< 0.0001**.

The maturation of Hap crystal in Pi condition is faster than βG condition, which is not surprising considering the mechanism of phosphate uptake by cells. As discussed in Chapter 1, βG must be hydrolysed by the ALP enzyme to release a free phosphate at the surface of the cell. Then, phosphate is absorbed by the cell via transporter

channels. In case of a medium supplemented with Pi, this one is directly absorbed by the cell to induce microcalcifications. In this context, Figure 5.16 shows a stable size of Hap for days 3 to 14 of mineralisation when cells are treated with Pi. Cells treated with βG developed a smaller crystal than Pi condition.

Legeros at al. have suggested that the incorporation of ion substitution such as Mg^{2+} or CO_3^{2-} ions in the Hap lattice could reduce the stability of the crystal and induce a higher solubility [80]. Figure 5.15 shows that calcium deposits released from cells treated with βG have more CO_3^{2-} incorporated in their Hap lattice, which is in line with their lower crystal size (Figure 5.16) than that from cells treated with Pi.

5.3.4. Other mineral phases

Microcalcifications are mainly described and classified by their mineral content such as calcium oxalate and Hap. However, the presence of mineral precursors has been investigated in several studies during bone formation, osteoblast differentiation or mineralisation of jaw periosteal cells [69], [70], [127]. The following results are focusing on the intermediate species present in our samples, based on the peak decomposition analysis in Figure 5.14. The results are summarised in Figure 5.17.

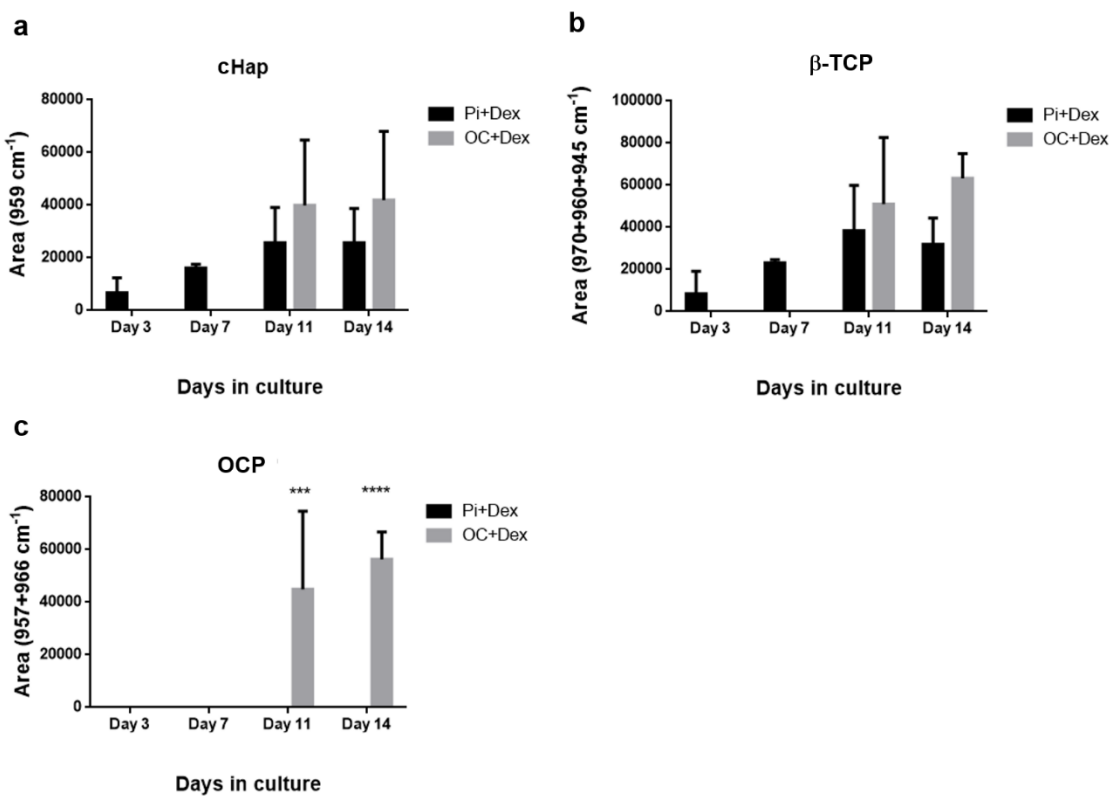

Figure 5.17 Involvement of different calcium phosphate phases in breast cancer cell mineralisation. (a) cHap, (b) β-TCP, and (c) OCP. Data are presented as a mean ± SD. Two-way ANOVA test was performed, P = 0.0215*, P = 0.0004*** and P < 0.0001****.

In βG culture medium, the calcium deposits appear to be made of cHap, OCP and β-TCP at day 11 and 14. For cells treated with Pi, cHap and β-TCP, the deposits are present in the microcalcifications at day 3 to 14. Moreover, no OCP deposits are found in these microcalcifications, which is the opposite of those found in βG culture medium. Hap and ACP minerals are not easy to discriminate due to the same spectral features. Moreover, other approaches such as X-ray diffraction should allow us to determine the elemental composition and whether the β-TCP is magnesium-substituted as it is found in other calcifications [41], [42]. These results reveal that calcium deposits are different in both culture media. Calcium deposits are more stable in terms of crystallinity, carbonate incorporation, and occur faster for a medium supplemented with Pi than βG culture medium.

Further analyses are necessary to understand the full process of microcalcification maturation and to investigate if a particular phosphate species could be a predictive factor for potential malignancy in breast. In this context, it is possible to correlate these results with those obtained from breast tissue sections, and to compare them in terms of spectral characteristics and peak decomposition.

5.4. Exploring the relationship between breast cancer cell mineralisation and different stages of the disease

A comparison was performed between Raman spectra recorded for breast cancer cells and breast tissue sections. The results are illustrated in Figure 5.18.

Several spectral features are similar between breast tissues and breast cancer cells in terms of $\nu_4\,PO_4^{3-}$, $\nu_1\,PO_4^{3-}$ bands and $\nu_1\,CO_3^{2-}$ bands for phosphate and carbonate corresponding to cHap of microcalcifications but also lipids and proteins with CH_2 deformation and Amide I, respectively. In contrast to breast cancer cells, carotenoids are found in breast tissue for benign and DCIS lesions. A double peak is noted for CH_2 deformation from DCIS and invasive lesions. The first peak at 1442/1444 cm^{-1} corresponds to a combination of proteins, fatty acids and cholesterol and the second peak at 1456/1459 cm^{-1} (Figure 5.18, red arrows) corresponds to the deoxyribose in DNA [106], [122].

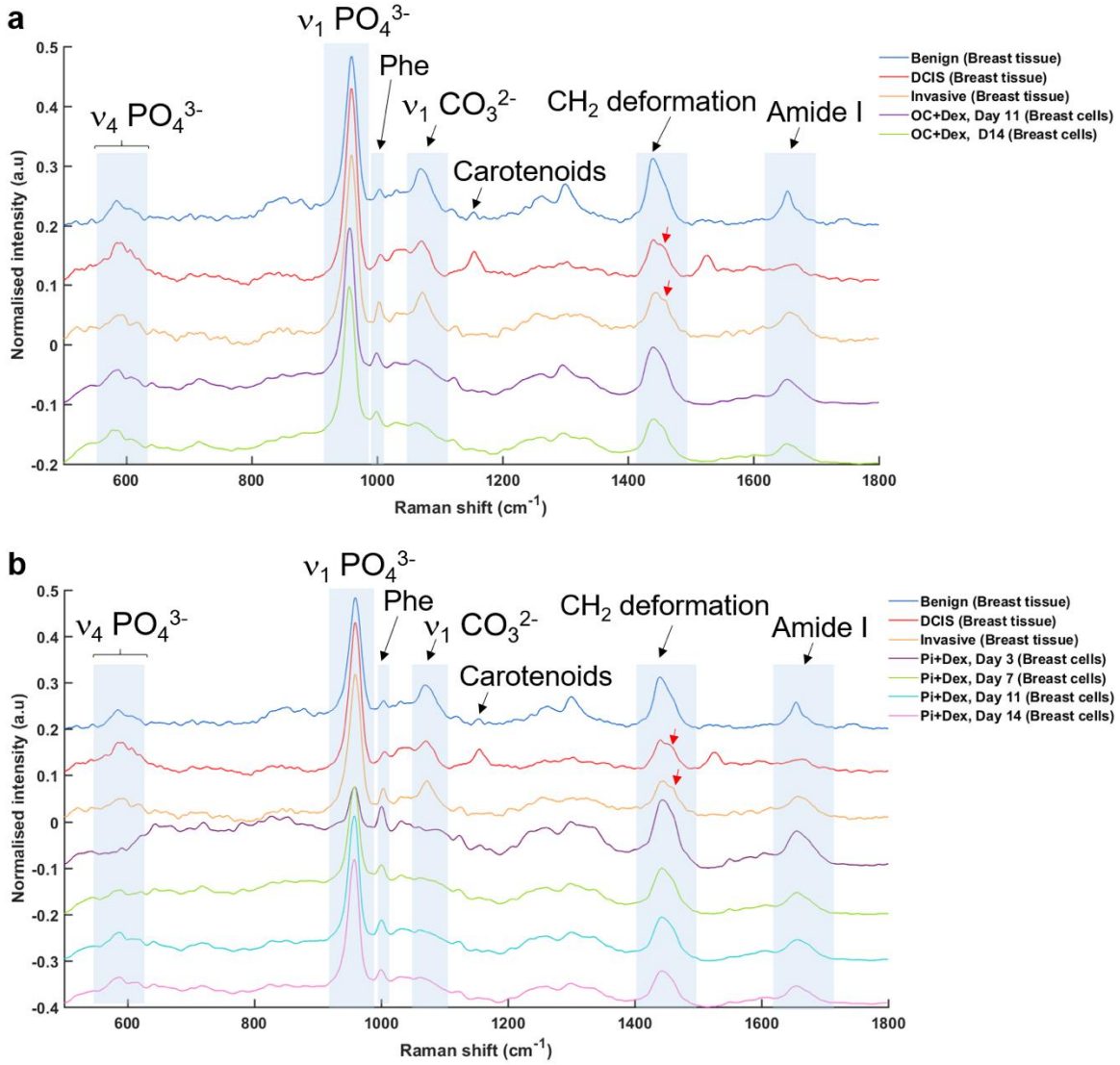

Figure 5.18 Average Raman spectra recorded from microcalcifications in benign, DCSI and invasive breast sections and compared with *in vitro* microcalcifications from breast cancer cells treated with (a) OC + Dex at day 11 and 14 of mineralisation and (b) Pi + Dex at day 7, 11 and 14 of mineralisation. Phe: phenylalanine, OC: osteogenic cocktail and Dex: dexamethasone.

Similar spectral characteristics are found in breast cancer cells and breast tissue spectra in terms of phosphate peak positions but also lipids and proteins. Same results are found when a comparison is made between curve fit analysis of phosphate and carbonate bands from breast cancer cells and breast tissues (see Figure 4.14, Chapter 4 and Figure 5.14). The positions and number of sub-bands for phosphate and carbonate bands are quite similar. The results suggest that different phosphate species and not only Hap are involved in the mineralisation process, and the *in vitro* model could be used for their identification.

5.5. Discussion

Raman micro-spectroscopy reveals a phosphate peak at 956/960 cm^{-1} suggesting the production of phosphate species by cells to induce mineralisation. This study shows that a faster mineralisation is induced (at day 3) when the cell medium is supplemented in Pi rather than βG (day 11). This also shows the ability of this technique to follow the mineralisation process as suggested by several studies [69], [70], [74]. In fact, PCA allows a discrimination of two pathways of mineralisation with two different clusters at day 3 and 7 between control group and cells treated with βG *vs.* cells treated with Pi. This model highlights a shift of the phosphate peak position at 956 cm^{-1} from cells treated with βG suggesting the presence of intermediate phosphate species such as β-TCP or OCP [116]. Moreover, spectra of cells treated with Pi exhibit a stable Hap crystal compared to those from cells supplemented in βG. In fact, Gosling et al. using crystallographic analysis have observed changes in crystal formation in microcalcifications from breast cancer tissues due to variations in cell microenvironment [128]. For instance, in benign lesions with a neutral pH, ACP is a precursor and a high carbonate level is found in mature Hap crystal, whilst the pH is more acidic for invasive lesions, OCP precursor is involved and a lower carbonate content is observed in Hap lattice [128]. However, our findings suggest that β-TCP may play a role as precursor of Hap formation, suggesting that the process may be more complex than previously thought.

In parallel, the proof-of-concept studies using macro-ATR [123] or O-PTIR [125] which have enhanced spatial resolution (0.5 μm) show promising results for locating crystal deposits in breast cancer cells and need to be investigated.

Zoladek et al. have demonstrated the potential of Raman micro-spectroscopy for a real-time study of apoptosis process in MDA-MB-231 cells. A chamber was incorporated into the microscope to reproduce physiological conditions of culture (37°C and 5% CO_2) to keep cells alive [129]. A similar setup could be used to follow in real-time the mineralisation process.

The FTIR analysis of the *in vitro* mineralisation was challenging due to a strong scattering background in the spectra. A Mie scattering correction was applied using the Kohler's method [75] to correct the baseline in the spectra. Unfortunately, the results were not as expected. In fact, it was difficult to obtain a coherent discrimination

between groups of cells treated with different osteogenic agents from the control group. The difficulty in the discrimination could be due to a strong contribution of nucleic acids, which could also be associated to the phosphate band between 1200-900 cm^{-1}. They can interfere in the calculation of C:P ratios.

Even if our findings show similar spectral characteristics of mineralisation between breast cancer cells and breast tissue sections, our mineralisation model is based on a 2D cell culture, but to recreate the occurrence of microcalcifications in mammary glands two main points need to be discussed. Firstly, the use of osteogenic agents to induce mineralisation is directed by an upregulation of ALP activity but there is no evidence of mineralisation for *in vivo* breast cells in contact with osteogenic agents. The second point is that cells are grown on plastic plate in 2D, which does not directly replicate in vivo conditions. In this context, Vidavsky et al. have developed a 3D model by creating breast cell spheroids containing microcalcifications (see Chapter 1, section 1.4.4) by adding calcium and magnesium at similar concentration as blood levels [43]. The idea could be to perform the analysis of spheroid sections using Raman and FTIR micro-spectroscopy.

Chapter 6 : Identification of breast microcalcifications using quantum cascade laser source and upconversion detection

6.1. Introduction

Vibrational spectroscopy associated with bright light sources, e.g. synchrotron radiation, supercontinuum (SC) light or quantum cascade laser (QCL) sources, have emerged over the past decades. Their purpose is to provide a rapid and highly sensitive approach to gain chemical information in biomedical studies.

A synchrotron is a source of electromagnetic radiation. This radiation is produced when electrons moving around a large ring are accelerated at close to the speed of light. This source is characterised by high brightness and covers a broad range of wavelengths from IR to the X-ray regime. Its brightness is due to the high concentration of the light over a small area, which is reflected in an improvement of the signal-to-noise ratio (SNR) when deployed in chemical imaging studies [130]. Synchrotron IR micro-spectroscopy has been validated and used in various biomedical studies including tissue sections [131], fixed or living cells [132], [133], but dedicated large-scale facilities are needed for these applications.

Another type of high brightness light source is the supercontinuum (SC) laser, which converts laser light into a broad light spectrum [134]. This phenomenon is apparent when the laser light is pulsed through a nonlinear optical fibre [134]. SC light can cover from ultraviolet to IR range [134]. Borondics et al. have performed a comparison between SC and synchrotron radiations and demonstrated the superior SNR achieved by the SC source in the measurement of liver tissue section [135]. The first application using SC source on biological tissues was made by Petersen et al. showing the feasibility of imaging colon tissue sections in the fingerprint region at selected wavelengths between 5.7 and 7.3 μm (1754 and 1370 cm^{-1}). More investigations are necessary but the advantage is that the technology could be easily used in the lab and combined with a micro-FTIR system with a better potential than Globar thermal or synchrotron sources [136].

In parallel, the past few years have seen several demonstrations of mid-IR imaging using QCL sources and applied in several studies, especially in bowel diseases [137],

[138] but also breast cancer [139], [140]. These applications have been made on tissue microarrays (TMA) of breast tissue sections [139], [140]. For instance, Mittal et al. have combined four tuneable QCL sources in their setup in order to cover the fingerprint region from 1940 to 770 cm^{-1} (5.2 to 13 μm) [140]. TMA have also been analysed using commercial micro-FTIR systems with a thermal source and the images have been compared to those recorded with the QCL sources. Full spectral range (1940-770 cm^{-1}) (Figure 6.1a) and a selection of twelve wavelengths (Figure 6.1b) have been recorded in the fingerprint region. Their home-built setup allowed the analysis of 101 TMA cores of 1 mm diameter in only 8 h, while 50 days are necessary for the commercial micro-FTIR system and for obtaining data with an adequate SNR (average of 32 scans).

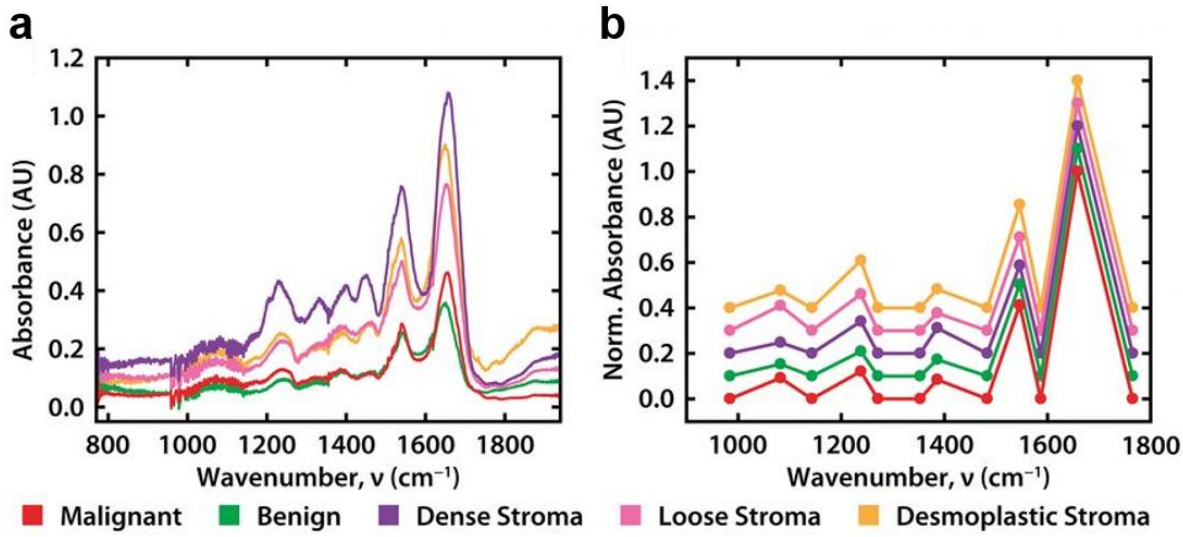

Figure 6.1 Spectra of five tissue types recorded from a TMA of breast tissue. (a) Point spectra at 1 cm^{-1} resolution. (b) Normalised and baseline corrected spectra of twelve selected wavelengths of interest. Figure from [140].

S. Mittal et al. have demonstrated a good potential for breast cancer analysis by differentiating tissue subtypes (malignant, benign …). However, the QCL source coupled to a micro-FTIR system in the long wavelength region has not been applied for the study of breast microcalcifications. In this context, Tseng et al. have developed a QCL source coupled to an upconversion microscopy system using raster scanning for analysing breast tissue sections. The QCL source covers long wavelengths from 9.4 to 12 μm (1060 to 830 cm^{-1}) in order to get spectral information on the ν_3 PO_4^{3-}, ν_1 PO_4^{3-} and ν_2 CO_3^{2-} bands at 1030, 960 and 875 cm^{-1}, respectively [98]. This source

was coupled to an upconversion system using a silicon detector for improving the sensitivity [73]. In this setup, a long wavenumber infrared (LWIR) QCL is shone onto a sample, then combined with a near infrared (NIR) beam and finally focused onto a silver gallium sulphide ($AgGaS_2$) nonlinear crystal. The mixed signal is upconverted into a NIR signal (e.g. 1020 cm^{-1} to 958.8 nm) and detected via a silicon detector (more details about the instrumentation are reported in Chapter 2, section 2.2.3).

A collaboration was conducted during this PhD as part of the Mid-TECH project with Prof. Pederson and Prof. Tidemand-Lichtenberg at the Technical University of Denmark. The aim of our study was to test the LWIR QCL source and upconversion imaging technology to enable a rapid and precise identification of microcalcifications' composition in breast tissue, with the potential for a cost-effective instrument as a clinical tool.

6.2. Analysis of Hap pellets

In order to assess the spectral quality and peak shapes and positions for phosphate and carbonate bands in upconverted spectra, an analysis was performed with KBr pellets of Hap with different amounts of carbonate substitution. An example is illustrated in Figure 6.2 showing spectra from pellets with Hap containing 2.92 and 7.52 wt.% carbonate substitution measured at a single point with both IR systems. The FTIR spectra (Figure 6.2a) show a good agreement with the upconverted spectra (Figure 6.2b) in terms of peak positions for phosphate and carbonate ions.

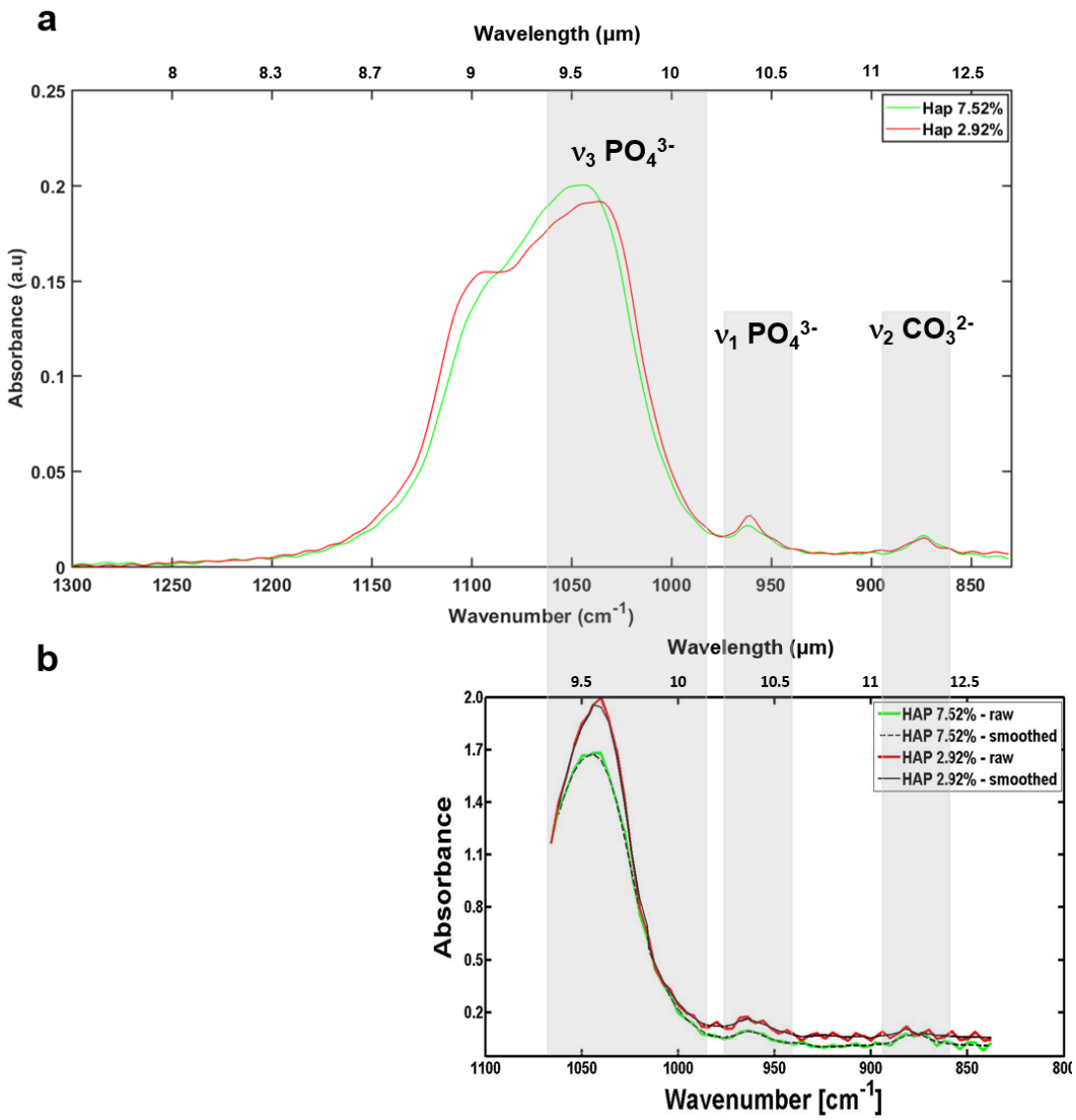

Figure 6.2 Spectra recorded from Hap pellets with 2.92 wt.% (red) and 7.52 wt.% (green) carbonate substitution using (a) a micro-FTIR Agilent system in the spectral range from 1300 to 830 cm^{-1} and (d) an upconversion system from 1060 to 830 cm^{-1} with 4 cm^{-1} step.

In the FTIR spectra, the ν_3 PO_4^{3-} band is a broad peak between 1200 and 1000 cm^{-1}, whilst the ν_1 PO_4^{3-} band is a small peak at 962-958 cm^{-1} and the ν_2 CO_3^{2-} band is also a small signal at 875 cm^{-1} [98], [100]. Similar peaks are also found in the upconverted spectra with a maximum at 1044, 964 and 875 cm^{-1}. Unfortunately, the ν_3 PO_4^{3-} band, which is a broad peak, is not entirely covered by the QCL laser.

6.3. Analysis of breast tissue sections

After validating the agreement between phosphate and carbonate peak positions in Hap pellets, the upconversion system was used to analyse breast tissue sections. A comparison was performed with the commercial Agilent FTIR imaging system and illustrated below.

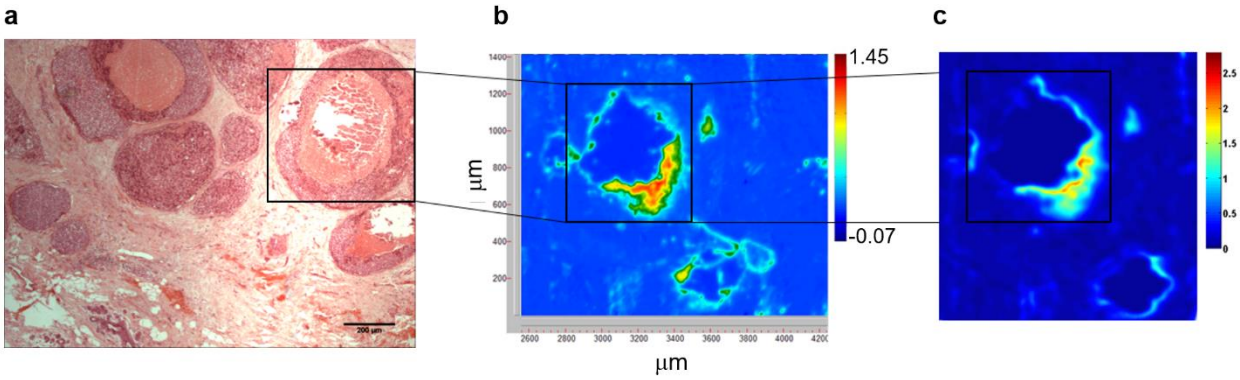

Figure 6.3 Comparison between the micro-FTIR imaging system and upconversion system. (a) Histological section of breast tissue section (DCIS stage) and H&E stained. (b) FTIR absorption image referring to the phosphate peak intensity at 1020 cm^{-1} recorded with the Agilent imaging system with an 15x objective and 5.5 µm x 5.5 µm pixel size. (c) Upconversion absorption image of the phosphate peak intensity 1020 cm^{-1} corresponding to the upconverted signal at 958.8 nm and 1.8 µm x 1.8 µm pixel size, [141].

Figure 6.3a shows a histological section of breast tissue biopsy stained with H&E, whereby the black box denotes a microcalcification area analysed using the FTIR imaging system (Figure 6.3b) and upconversion system (Figure 6.3c). In this figure, the FTIR image was measured at the phosphate peak intensity corresponding to 1020 cm^{-1} while the upconversion system converted the LWIR signal at 1020 cm^{-1} to NIR at 958.8 nm. All these micrographs exhibit the same morphological features and the microcalcification is represented by the red-to-green regions in the false colour image. The absorbance in the microcalcification area (black box) measured with the upconversion system is higher than in the FTIR image, owing to the more intense laser source having less likelihood of saturation of peaks (as seen in FTIR) used in the former system resulting in a higher SNR [142]. Moreover, this microcalcification area is approximately 0.5 mm^2 in size. The acquisition time for this area is around 5 min for

the full spectral range 3900-800 cm^{-1}, a single image with 64 scans and a spectral resolution of 4 cm^{-1} using the FTIR system, whilst this area was measured at 1020 cm^{-1} in 30 s using the upconversion system. Nevertheless, the acquisition time for the upconversion system depends on the number of wavelengths selected and the speed of the xy translation stage (scanning speed of 5 mm/s in x-direction and 10 μm in y-direction) [141], [143].

In our study, only few wavelengths are required to discriminate microcalcifications from tissue, based on the phosphate and carbonate peaks. The second derivative was calculated for the spectral range 1200-830 cm^{-1} to gain relevant information in this region and allow selecting wavelengths of interest for QCL analysis. A series of upconverted images taken from breast tissue sections are illustrated in Figure 6.4. In this figure, the second derivative spectrum evidences several peaks at 1032, 1020 and 985 cm^{-1} for ν_3 PO_4^{3-} band [98], 959 and 930 for ν_1 PO_4^{3-} band [91], and 875 cm^{-1} for ν_2 CO_3^{2-} band [98], [100] (Figure 6.4a). These peak positions were used to obtain the multispectral upconversion images shown in Figure 6.4b, and random peaks were added to cover a maximum of the phosphate region (1040-930 cm^{-1}). There is a good discrimination between the microcalcification (red box) and the surrounding tissue. A decrease in phosphate signal between 1040 and 930 cm^{-1} can also be seen. The carbonate peak is detected with a low signal at 875 cm^{-1} in the microcalcification (red arrows) which correlates with the second derivative spectrum illustrated above and the mean spectrum in single point measured in the same microcalcification (see Appendix, supplementary data 5, Figure E.1).

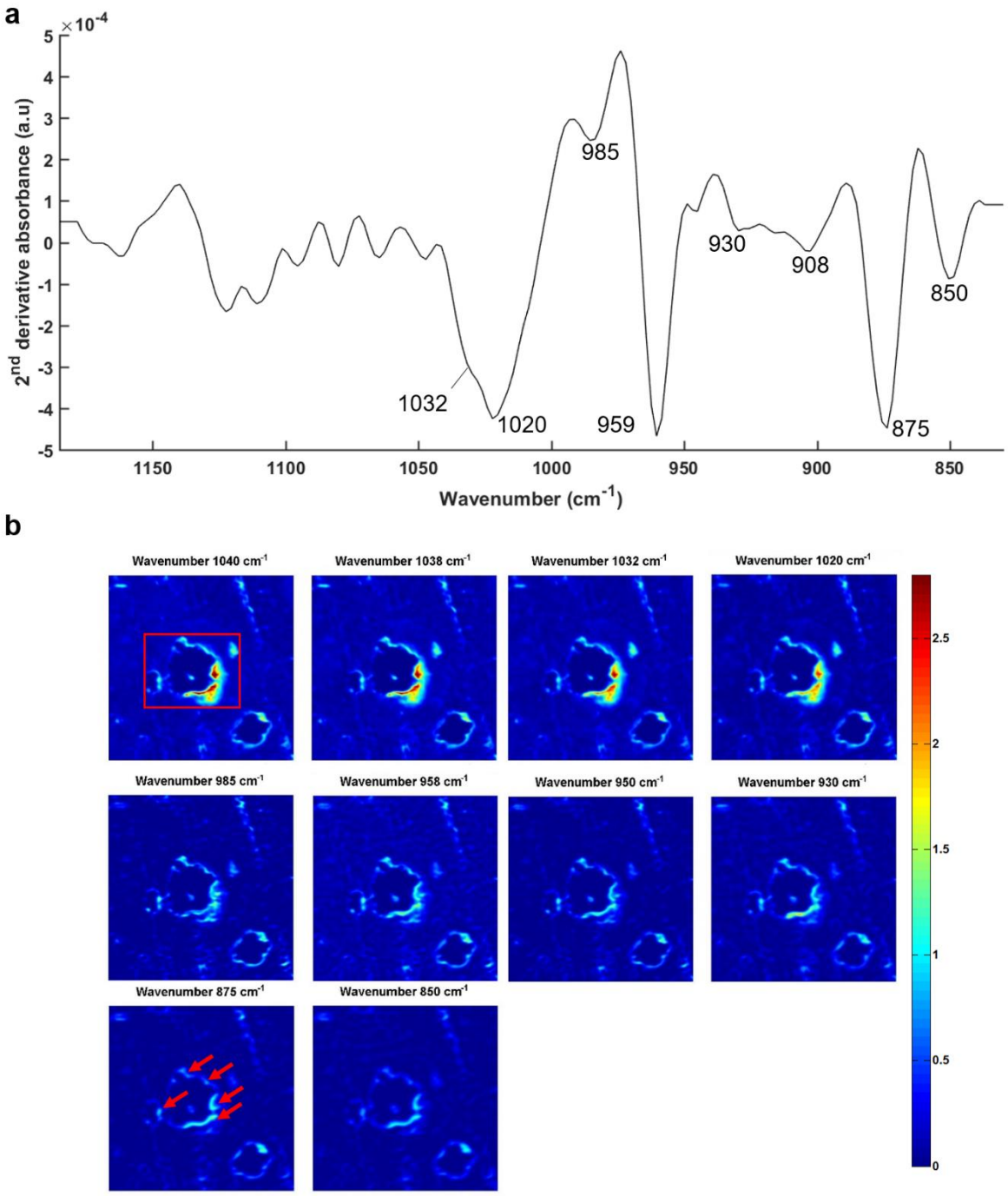

Figure 6.4 (a) Second derivative spectrum of a microcalcification extracted from a breast tissue section (DCIS stage). (b) Series of upconversion images obtained at 1040, 1038, 1032, 1020, 985, 958, 950, 930, 875 and 850 cm^{-1} with 1.8 μm x 1.8 μm pixel size. Red arrows show carbonate signals in microcalcification area.

To demonstrate the potential of the upconversion system, a comparison was made between five spectra extracted from the FTIR image and from the upconverted images at twelve different wavelengths (Figure 6.5).

In both cases, spectra were extracted from microcalcification and surrounding tissue (dashed black box, Figure 6.5a). A comparison between the full FTIR spectrum (in blue) and the upconverted absorbance for each wavelength (red circles) is plotted in a graph for the microcalcification area (Figure 6.5b) and the surrounding tissue (Figure 6.5c). In the area of microcalcification, ν_3 and ν_1 PO_4^{3-} bands are both present, whereas the surrounding tissue does not exhibit specific features for Hap. Due to the limit of the FPA detector in the micro-FTIR imaging system, spectra become noisy below 900 cm^{-1} (LWIR region) and the spectral signatures are not considered reliable for the ν_2 CO_3^{2-} band, however in the upconverted absorption spectrum there seems to be present a small signal at 875 cm^{-1}. Overall, there is a good match between the two techniques for the microcalcification area.

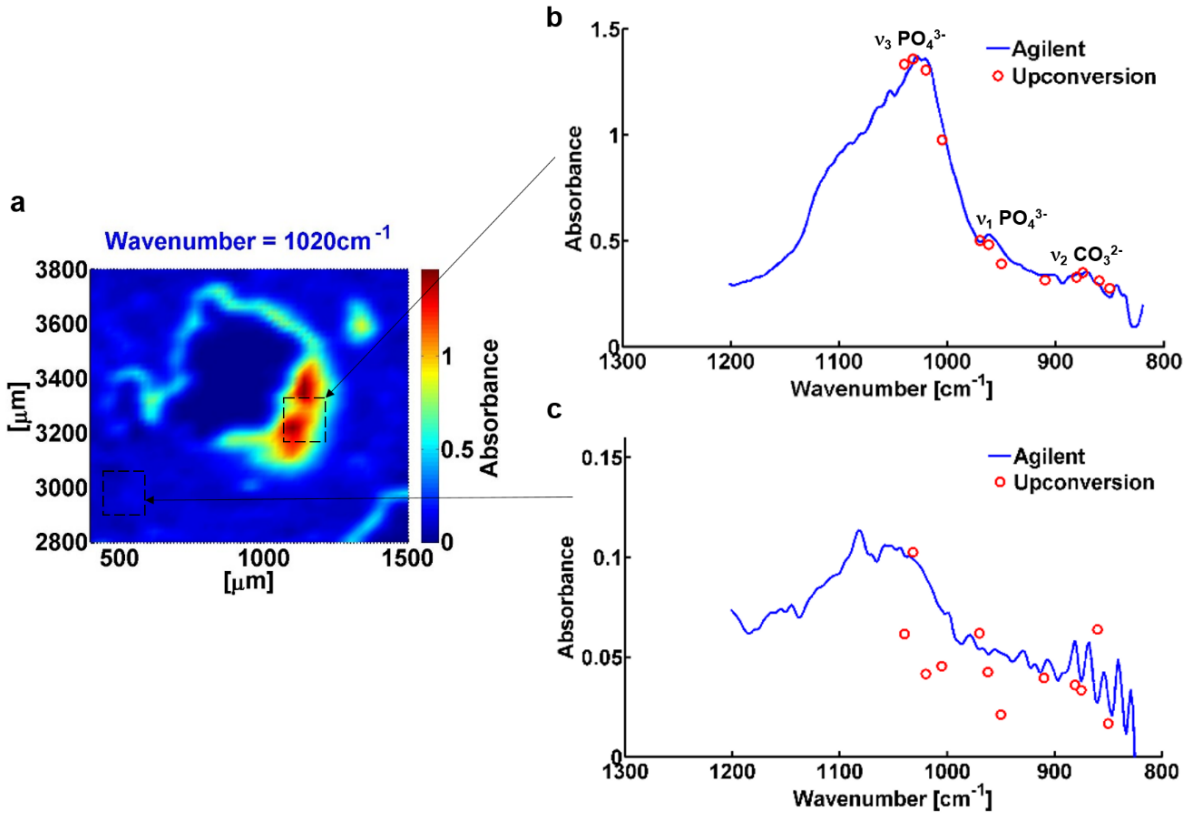

Figure 6.5 Illustration of an (a) upconverted image of microcalcification from breast tissue section obtained at 1020 cm^{-1} (958.8 nm). Spectra extracted from (b) microcalcification area (dashed black box) and (c) surrounding tissue (dashed black box) in the spectral range between 1200-800 cm^{-1} for the FTIR image (blue spectrum) and at 1040,1032,1020, 1005, 970, 962, 950, 910, 881, 875, 860 and 850 cm^{-1} for the upconverted images (red circles), [141].

Another example of comparison between H&E staining, FTIR and upconverted images of breast sections is illustrated in Appendix, supplementary data 5, Figure E.2. It shows a good agreement in terms of spatial distribution of microcalcifications in the breast tissue. In the same manner as above, several wavelengths were selected from the second derivative spectrum and recorded using the upconversion system (see Appendix, supplementary data 5, Figure E.3). As previously, a decrease in phosphate signal is observed in the range between 1040 and 930 cm^{-1} and a very low signal at 875 cm^{-1} is detected for carbonate band, which is in line with the FTIR spectrum (not shown). In parallel, a comparison between FTIR spectra extracted from three different areas in microcalcifications (Appendix, supplementary data 5, Figure E.4) shows a good match between phosphate and carbonate peaks. Nevertheless, the upconverted spectra evidence a higher absorbance than FTIR spectra (as expected and already discussed in Figure 6.3) and the images have higher spatial resolution (See Figure 6.3) [142].

6.4. Discussion

These results demonstrate the potential of upconversion imaging to detect microcalcifications in breast tissue sections. The limit at 900 cm^{-1} in the FTIR imaging system due to the MCT-FPA detector means that we were unable to record the carbonate peak at 875 cm^{-1}. The use of an LWIR tuneable laser source (9.4 to 12 μm) enabled us to explore the carbonate peak distribution in the upconverted images. The results show a good agreement in terms of spectral features of microcalcifications between the commercial FTIR imaging system and the upconversion system. The latter setup allows fast acquisition (30 s/upconverted image) for recording of one specific wavelength but the inconvenience of this technique is the scanning speed [141]. In fact, the acquisition time depends on the speed of scanning, which is 5 mm/s in x-direction and 10 μm/s in y-direction, but also on the number of wavelengths selected [141]. However, the QCL source coupled to an upconversion detection offers several advantages. In fact, silicon detectors do not require liquid nitrogen cooling compared to MCT detectors, and the QCL is more intense than Globar thermal source. Moreover, silicon detectors are cheaper, have a higher sensitivity and a lower noise than MCT-FPA detectors.

The main inconvenience from QCLs is the need for a series of QCL sources to cover a suitable range of wavelengths of interest, which is very expensive [64], [142]. In 2014, one system (Spero® QCL system) was commercialised (Daylight solution®), limited to a spectral range of 1800-900 cm^{-1} but customisable to 2300-830 cm^{-1}, and with a pixel size varying from 1.4 x 1.4 μm to 4.3 x 4.3 μm (see Figure 6.6) [144]. Since then, several studies have emerged using this device on colon tissue sections [138], [145] and renal fibrosis [146].

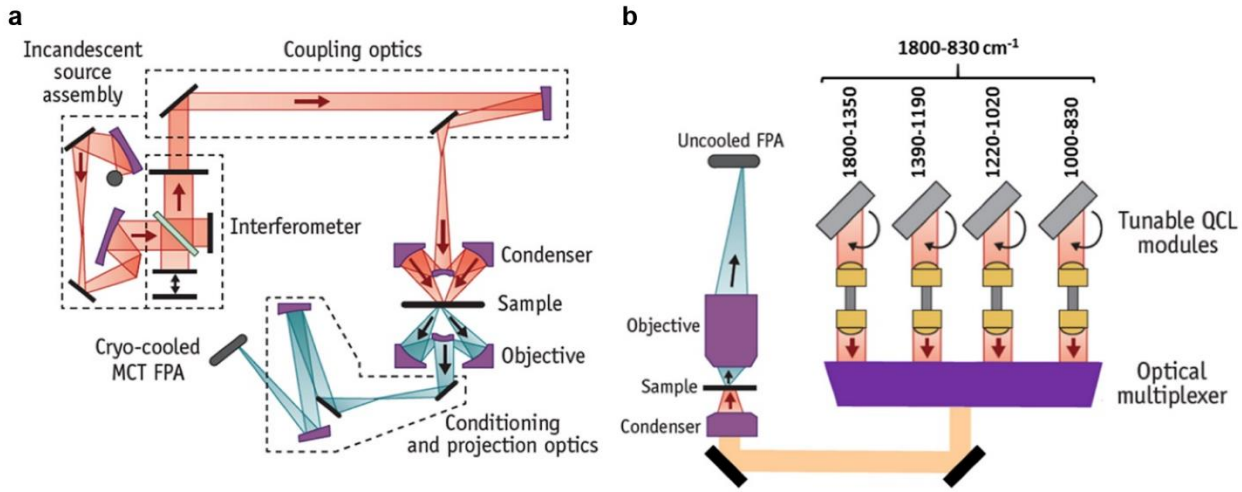

Figure 6.6 Illustration of (a) a micro-FTIR imaging system with a liquid nitrogen-cooled MCT-FPA detector and (b) Spero system using four QCL sources coupled to a microscope unit and uncooled FPA detector (Daylight solutions®), [144].

For the next experiments, an improvement is necessary regarding the microscope stage in term of scanning speed. Based on the Spero® system (Figure 6.6), additional QCL sources could be added to cover the LWIR regime for the entire ν_3 PO_4^{3-} band (1200-900 cm^{-1} or 8.3 to 11.1 μm) or to cover the ν_3 CO_3^{2-} band in the short wavelength region (1500-1400 cm^{-1} or 6.7 to 7.1 μm). In fact, this region could bring complementary information in the case of frozen sections, where there is no interference from paraffin on the carbonate peaks.

The advantage of silicon detectors is that they are cheaper and more compact than MCT detectors in a microscope system. All these new IR sources added in a compact system offer a large range of possibilities such as improvement of data quality and faster acquisition time, which is beneficial for clinical applications.

Chapter 7 : General discussion

The main purpose of this work was to understand the composition of microcalcifications expressed in breast cancer using vibrational spectroscopy using different approaches, e.g. mineral standards, microcalcifications in breast tissue sections, and *in vitro* mineralisation. For the first time, this study demonstrated the potential of the vibrational spectroscopy to follow the mineralisation over time via a unique 2D model of breast cancer cell mineralisation. In parallel, the use of an innovative setup, mixing a bright source in the long wave regime and a simple detection based on silicon detectors, gives new perspectives for analysing breast microcalcifications. All these techniques allowed to understand the maturation process for microcalcifications and evidenced for the first time that different phosphate species were involved during the Hap crystal formation in breast cancer.

7.1. Potential understanding of mineralisation process

The analysis of breast tissue sections and the mineralisation of the breast cancer cells evidence the same spectral features in terms of phosphate and carbonate bands compared to the mineral standards. Even though the frozen and de-paraffinised sections were not the same sample or same section, the de-paraffinisation process did not seem to affect the spectral signatures of the microcalcifications. The study reveals specific peaks of phosphate and carbonate bands at 960 and 1070 cm^{-1}, respectively found in Raman spectra. For FTIR spectra, specific peaks are observed at 1030 cm^{-1} for phosphate and 875, 1408, 1423, 1456 cm^{-1} for type B carbonate ion substitution. Our study does not show the presence of type A carbonate substitution in Raman and FTIR spectra (1106 and 881 cm^{-1}, respectively) of the calcium deposits.

Previously, it has been demonstrated that the carbonate content is higher in benign lesions [59], which was also expected in our study. However, considering the difficulties of evaluating the carbonate content e.g. by curve fitting analysis, integration method or PLS model, and also the small number of samples, it is not possible to make definitive conclusions. In fact, the evaluation of carbonate content in these microcalcifications suggests a high range of carbonate ion substitutions. However,

different artefacts could interfere in the calculation. Not only that, with advances in spatial resolutions and analysis methods it is now clear that microcalcifications are incredibly heterogeneous in nature, potentially including various mineral phases.

The analysis of other mineral standards than cHap (e.g. OCP, ACP, and β-TCP) has shown similar spectral features to those found in breast microcalcifications. For instance, ACP presents the same phosphate peak at 959 cm^{-1} in Raman spectra as cHap with a more significant broadening. Moreover, even if the literature suggests that type B carbonate ion substitution is mainly found in biological samples, this does not rule out the presence of type A carbonate substitutions in breast microcalcifications; as it was suggested by Gosling et al. [128]. All these elements could interfere in the calculation of different C:P ratios and the calibration curve.

Using all the literature available, Gosling et al. have proposed a hypothetic model of microcalcification formation in mammary gland, which occurs in benign, DCIS, and invasive stage of breast cancer (Figure 7.1) [128], which tends to support our hypothesis for the presence of different precursors in breast microcalcifications.

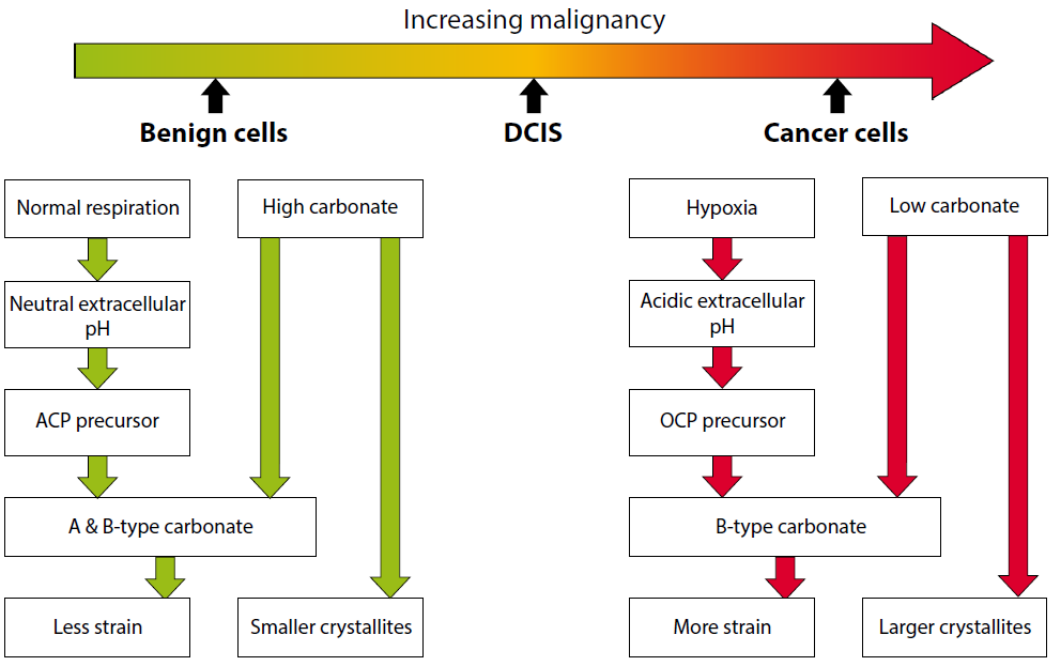

Figure 7.1 Schematic representation of the hypothetic microcalcification formation in the breast from benign to DCIS and invasive cancer stages. From S. Gosling, 2019.

Baker et al. have demonstrated that a higher carbonate concentration is observed in benign lesions compared to malignant lesions [59]. The incorporation of carbonate ions in the lattice induces changes in the crystal shape and size [147]. In fact, the Hap crystal size is smaller in case of benign lesions when compared to the crystallites found in malignant lesions [128]. Moreover, Gosling et al. have suggested that the ratio of type A to type B carbonate substitutions is likely to relate to the stage of pathology. Both types A and B are in the lattice of Hap crystal in benign lesions, whereas the level of type B substitution increases and the level of type A substitution decreases in case of malignant lesions [128]. However, in this work as outlined above, no type A Hap was seen in the 18 benign calcifications measured here.

The pH changes in the cell microenvironment have already been demonstrated during breast cancer progression [85], and an acidic pH is found for a late stage of breast cancer. One of the consequences of these biological changes is that they can affect the Hap crystal structure and crystallinity but also its formation and the recruitment of different cHap mineral precursors.

The analysis of the *in vitro* mineralisation of breast cancer cells by Raman micro-spectroscopy tends also to validate this hypothesis. This study has shown the ability of this technique to follow the mineralisation process as suggested by several studies [129], [148], [149]. A faster mineralisation is induced (at day 3) when the cell medium is supplemented in Pi rather than βG (day 11), providing free phosphate ions to the cells rather than needing to synthesise it from a precursor. By utilising PCA it was possible to clearly determine two pathways of mineralisation with two different clusters at day 3 and 7 between control group and cells treated with βG *vs.* cells treated with Pi. This model highlights a shift of the phosphate peak position at 956 cm^{-1} and a width slightly higher from cells treated with βG suggesting the presence of intermediate phosphate species such as OCP [116]. Moreover, information extracted from spectra of cells treated with Pi exhibit a stable Hap crystal compared to those from cells supplemented in βG. However, according to Gosling et al., the crystallographic analysis highlights changes in crystal formation in microcalcifications from breast cancer tissues due to variations in cell microenvironment [128]. For instance, in benign lesions with a neutral pH, ACP is a precursor and a high carbonate level is found in

mature Hap crystal, whilst the pH is more acidic for invasive lesions, OCP precursor is involved and a lower carbonate content is observed in Hap lattice [128]. In this cellular model, the culture medium has a pH of 7.4 maintained by bicarbonate ions buffer. However, during the cell growth, cells release metabolites which can change the pH and become more acidic, until the medium was replaced after three days. This could play a role in the specific mineralisation process modelled here.

In parallel, our curve fit analysis in the phosphate regions suggests also the presence of β-TCP, which may play a role as precursor of Hap formation and suggesting that the process may be more complex than previously thought. In fact, calcium phosphate species are important elements in the body in normal physiological conditions e.g. bone formation, mineral balance etc. [150]. Among these species, cHap is the result of a final solid mineral phase of mineralisation [81]. The application of new techniques such as vibrational spectroscopy or X-ray diffraction (XRD) evidences that the mineralisation process involves several mineral precursors including OCP, ACP and DCPD for the formation of a mature Hap crystal [151].

Pathological calcifications are more complex, still misunderstood, and the involvement of precursor phases is different according to their location in the body. For instance, the XRD analysis has revealed cHap, OCP, DCPD and β-TCMP in dental calculus, whereas cHap, OCP, ACP and β-TCMP are found in calcified soft tissues (lung, heart …) [80]. Recently, the presence of β-TCMP has also been demonstrated in breast microcalcifications [42], [114].

In order to understand the mineralisation process, synthetic systems have been investigated using mineral standards. Their synthesis is made in a supervised environment, by controlling the concentration of each element (ratios of phosphate, calcium, magnesium, carbonate …) but also the temperature and the medium's pH for each reaction [80], [148]. In this context, it was possible to get a schematic representation of the transformation of different calcium phosphate species into another (Figure 7.2).

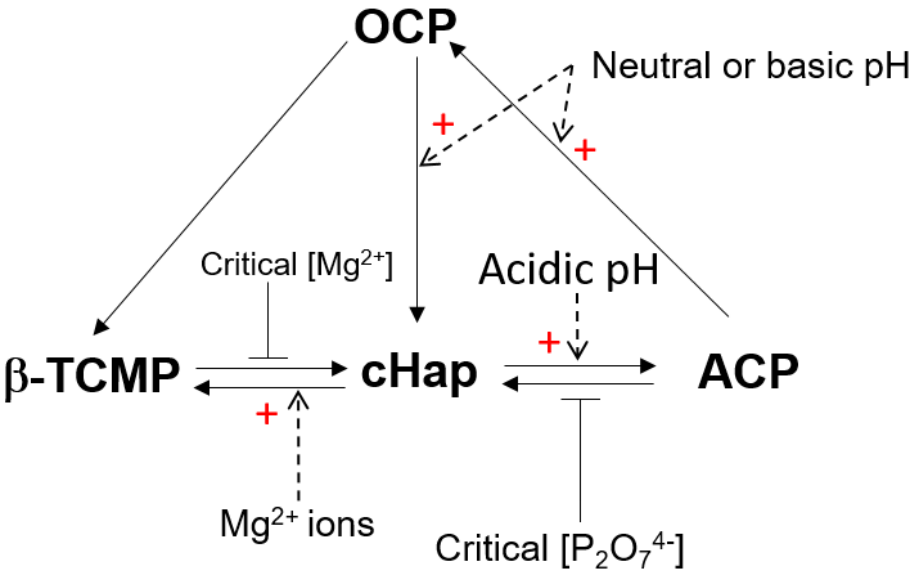

Figure 7.2 Schematic diagram of calcium phosphate species transformation in synthetic system. The pH, Mg^{2+} and $P_2O_7^{4-}$ concentrations, phosphate and carbonate amounts were precisely calculated and controlled. Each red cross denotes that a reaction is enhanced by a specific factor (e.g. ions, pH …). β-TCMP: Magnesium-substituted tricalcium phopshate Mg^{2+}: Magnesium ion, $P_2O_7^{4-}$: Pyrophosphate ion. Adapted from [80].

Legeros et al. have summarised different pathways for the transformation of cHap, ACP, OCP and β-TCMP (Mg-substituted tricalcium phosphate) [80]. Hap is the most stable form of phosphate species in neutral or basic conditions [81] and is formed from different precursors and by different reactions of hydrolysis or precipitation [80]. Lotsari et al. have suggested that ACP has a contribution in the cHap formation during bone formation [152]. In fact, ACP could spontaneously be transformed into Hap in physiological conditions [81]. In parallel, a medium rich in CO_3^{2-} induces the hydrolysis of ACP into cHap, but this reaction is inhibited in presence of an excess of pyrophosphate ($P_2O_7^{4-}$ ions) or Mg^{2+} ions [80]. Suzuki et al. have also suggested the importance of OCP during bone formation [151]. At neutral pH, OCP can transform into cHap by hydrolysis with a high concentration of carbonate and this reaction is irreversible [80], [151]. On the other hand, an acidic environment and a very low concentration of carbonate induce the OCP [80].

In a synthetic environment, the formation of Hap crystal from β-TCP depends on the pH of the medium, but this reaction is inhibited in presence of a high concentration of Mg^{2+} at room temperature [81]. The presence of β-TCP is more controversial due to

the fact that this pure form is not found in physiological conditions, although only Mg^{2+} substituted β-TCP (β-TCMP) is found [153]. The potential presence of β-TCP based on our curve fit model is in line with the study led by Scimeca et al. [42]. It is possible to distinguish by X-ray diffraction (XRD) β-TCP from β-TCMP by a shift in the XRD peaks because Mg^{2+} replaces Ca^{2+}. For the FTIR spectroscopy, in both cases, spectra exhibit spectral features of β-TCP [154]. Until now, there is no data available based on the discrimination between both standards using Raman micro-spectroscopy.

The type of phosphate precursors at different stages of breast cancer depends on its microenvironment. For instance, neutral pH and high carbonate level are found in benign lesions, which combine all factors to convert ACP to cHap (as described above in synthetic environment) [80], [81]. According to Gosling et al., the hydrolysis of ACP, rich in carbonate, is a good candidate to facilitate the incorporation of carbonate ion substitutions in Hap lattice. On the contrary, OCP is favoured in acidic environment to facilitate the cHap formation [80], which is the case in malignant lesions.

However, at the end of this thesis, it is impossible to determine if all these reactions from a mineral to another happen in biological tissues but a majority of them are certainly present in pathological mineralisation [40], [80]–[82].

7.2. New spectroscopic tools for the breast microcalcification analysis

Over the past decades IR spectroscopy associated with bright light sources, e.g. synchrotron radiation, supercontinuum (SC) light or quantum cascade laser (QCL), sources have emerged and their purpose is to provide a rapid and highly sensitive approach to gain chemical information in biomedical studies. A collaboration with Prof. Petersen and Prof. Tidemand-Lichtenberg from DTU gave us the opportunity to have access to their unique upconversion technologies coupling a commercially available LWIR QCL source with a upconversion system. The use of novel IR spectroscopic technologies based on QCL sources and upconversion detectors can be an important approach to gain enhanced spectral information from selecting a specific wavelength, for instance around 875 cm^{-1} (11.4 µm) corresponding to the carbonate peak, which

is difficult to achieve with our MCT-FPA FTIR system. These results demonstrate the potential of upconversion imaging to detect microcalcifications in breast tissue sections. Moreover, it is particularly effective for performing rapid spectral imaging at discrete wavelengths. This technology can potentially be translated into rapid biopsy screening for breast cancer in a clinical setting as a complement to other procedures. Vibrational spectroscopy could be used in the breast screening routine recommended by the NHS. The mammographic images would give information about the spatial distribution and the size of the microcalcifications. In complement, the vibrational spectroscopic analysis would bring all the chemical information. Ideally, by combining these techniques, a system of bare code could be design where a chemical property is related to a shape and size of microcalcification or a stage of breast cancer. All these new technologies (IR sources and detectors) can be combined in a compact and relatively cheap system (£30k-50k), which offers a large range of possibilities such as improvement of data quality and faster acquisition time.

7.3. Future work

This work can be extended in terms of biological samples but also the mineral standards for the analysis of breast microcalcifications:

- The size of cohort samples.

  By increasing the number of samples, it opens possibilities to find other minerals than cHap but also increases the reproducibility of the findings in such a heterogeneous population of samples.
- Refine the calibration curve.

  An increase of samples with different amount of carbonate ion substituted in Hap powders, for instance between 0.5 and 6 wt.% of carbonate content usually found in biological samples [38], is necessary to be more accurate in the estimate of carbonate content in biopsy samples.
- Different type of cHap standards could be used such as type A or a combination of type A and B in Hap lattice [100].

  Even if the literature suggests that type B carbonate ion substitutions are the main type of substitution found in biological samples, exploring type A

carbonate ion substitutions gives opportunities to find them in breast microcalcifications [128].

- Finding a supplier for dicalcium phosphate dihydrate (DCDP) standard, which is also considered as a cHap precursor phase [80], [151], could be useful for comparison with biological microcalcifications.
  In fact, at low pH and high concentration of CO_3^{2-}, DCPD could also be transformed into cHap [80].

The mineralisation in different contexts has been analysed by several approaches (listed below), which can lead us to apply them in the microcalcification study:

- Techniques based on X-ray (XRD, X-ray fluorescence (XRF)…) could give the elemental composition of microcalcifications [114], [115].
  For instance, the analysis by XRD of a small number of microcalcifications has shown the presence of β-TCMP in small concentrations, which provides promising results [42], [114] and could be useful to identify other mineral phases in breast microcalcifications.
- Stimulated Raman Scattering (SRS) to image, with high resolution and speed, the spatial distribution of carbonate and phosphate in microcalcifications [155].
- Raman micro-spectroscopy of live cells, in real-time, to assess cell mineralisation day by day [129].
- As discussed in Chapter 5, a 3D model based on breast cell spheroids containing microcalcifications as a new *in vitro* model [43].

The relationship between the microcalcification and its microenvironment is still not fully understood. Nevertheless, Morgan et al. have shown that the Hap crystal enhances the mitogenesis and, as a consequence, the cell proliferation and the production of matrix metalloproteinases (MMPs) [44]. Their upregulation can lead to a collagen degradation, which induces ECM remodelling and migration of epithelial cells, and an epithelial organisation in breast tissue [149], [156]. In this context, an exploration of the architecture of collagen fibres by multiphoton microscopy such as SHG could be helpful for locating collagen networks surrounding the microcalcifications [113].

7.4. Conclusion

This work aimed to untangle the different mineral phases found in breast microcalcifications. Vibrational spectroscopy has shown its potential for the investigation of microcalcifications by giving information about their chemical composition and their spatial distribution in breast tissues. This work also contributes to understanding the mineralisation process in pathological conditions.

Therefore, further detailed study of microcalcifications associated with breast cancers is important both for an understanding of the disease progression from a diagnostic and prognostic perspective but also for the development of a potential therapeutic agent to protect against the remodelling.

Appendix

A. Appendix - Supplementary Data 1

Figure A.1 Patient consent form given by the RD&E Tissue Bank to patients prior to collect samples for the study.

CONSENT STATEMENTS	**Please Circle**
I confirm that I have had opportunity to consider the information, ask questions and have had these questions answered satisfactorily.	**YES / NO**
I agree to donate samples and data available during my routine clinical care to the RD&E Tissue Bank and I give permission for NHS staff to obtain information from my medical record for the purposes of research.	**YES / NO**
I understand that my samples and hospital data will be stored securely at the Royal Devon & Exeter NHS Foundation Trust Tissue Bank in Exeter.	**YES / NO**
I understand that genetic material may be extracted from my samples and used for future research into the causes of disease.	**YES / NO**
I understand that my agreement is voluntary and that I am free to withdraw my samples and associated data any time without giving any reason and without my medical care or legal rights being affected.	**YES / NO**
I understand that with the agreement of a steering committee the tissue bank will provide my anonymised data and samples to researchers for the purpose of understanding disease and improving healthcare.	**YES / NO**
OPTIONAL STATEMENTS	
I give permission for researchers to feedback information to my referring hospital doctor that might be relevant to: a) my current condition b) other conditions that might affect me but have not yet been identified c) conditions that might affect my family in the future	 **YES / NO** **YES / NO** **YES / NO**

Donor Name: ……..

Date …..... Signature ……

Consented by …… Date …… Signature ……

Collaborating Clinician Name: ……..

This is a copy of the consent form that you signed when you agreed to join the RD&E Tissue Bank. The Donor Code on the top right hand side of the consent form is the anonymous code that we will use to identify you. If, in the future you would like to withdraw your samples from the RD&E tissue bank and make any other changes to your consent please telephone us at RD&E Tissue Bank on 01392 408178 quoting this donor code and your first and last initial.

If you would like to have a say in which studies have access to the RD&E tissue bank you may peruse current requests for samples and research reports at https://crf.exeter.ac.uk/web/content/bhybk

Figure A.2 Breast tissue donation form summarising clinical information about biopsy samples completed by RD&E Tissue Bank. WLE: wide local excision

BREAST TISSUE
DONATION FORM

RELEVANT CLINICAL INFORMATION

Date of Surgery Tissue Donation: …./…./20….

Site: Right / Left BMI:

Breast biopsy sample obtained? Yes / No

Surgical procedure Undertaken: WLE / Mastectomy

Additional Procedures: SNB / Axillary Clearance / None / Other

Diagnosis type: Screening / symptomatic

ER Status: Positive / Negative Intensity: Weak / Mod / Strong Percentage:

Her2 Status: Positive / Negative

Family History: Yes / No Relationship: Age at diagnosis:

Menopausal status: Pre / Peri / Post

HRT use: Yes / No Age commenced: How many years:

Current/Previous Breast Ca treatment: Yes / No Type:

Presence or absence of Metastases: Yes / No Site:

B. Appendix - Supplementary Data 2

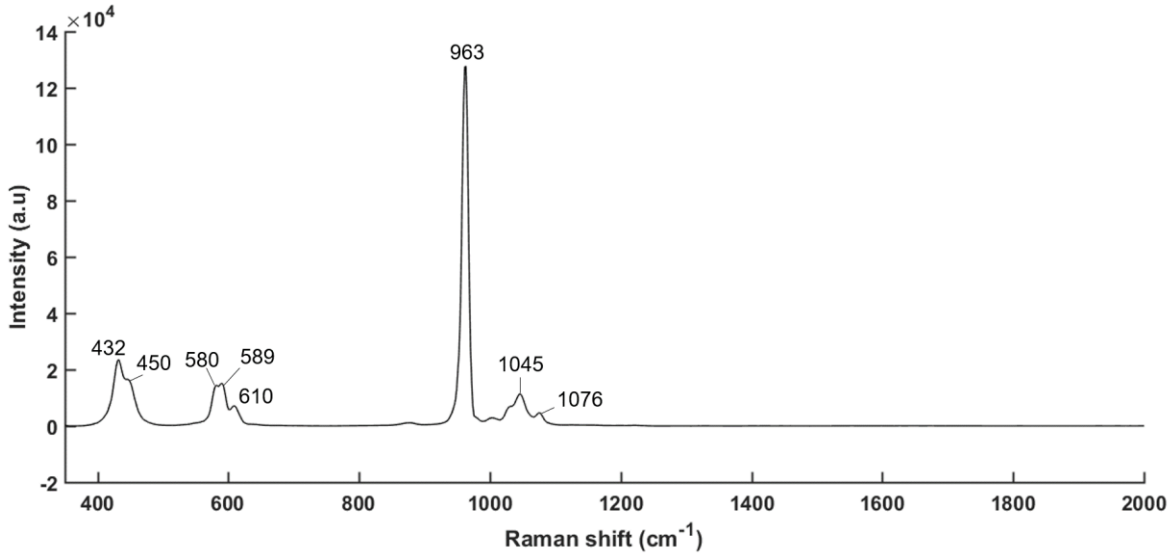

Figure B.1 Average of 5 Raman spectra from pure Hap powder from Sigma Aldrich. Spectrum was baseline corrected to 2000-350 cm^{-1}.

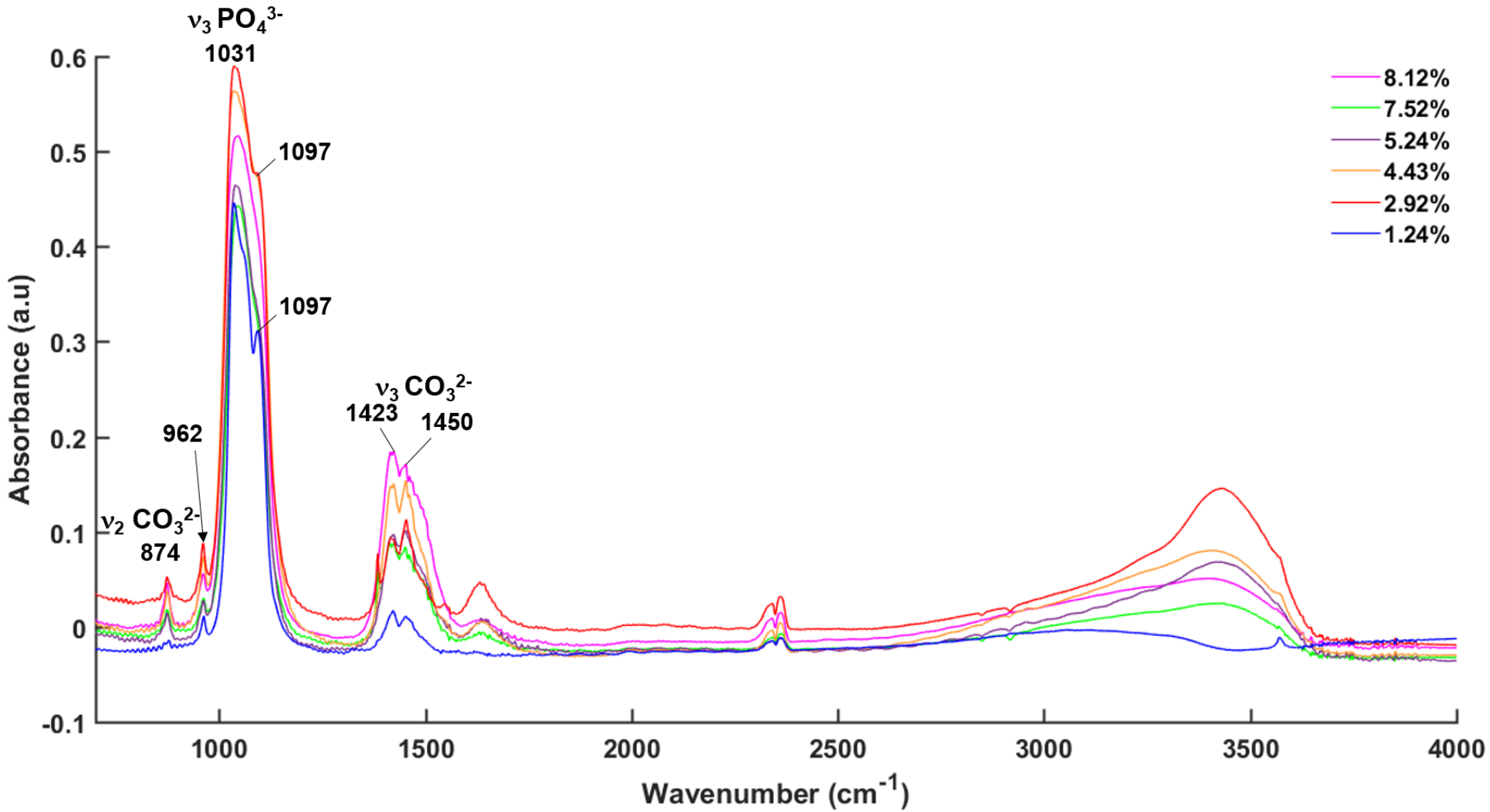

Figure B.2 Average of five raw FTIR spectra from cHap pellets recorded to the spectral range between 4000 and 700 cm^{-1}.

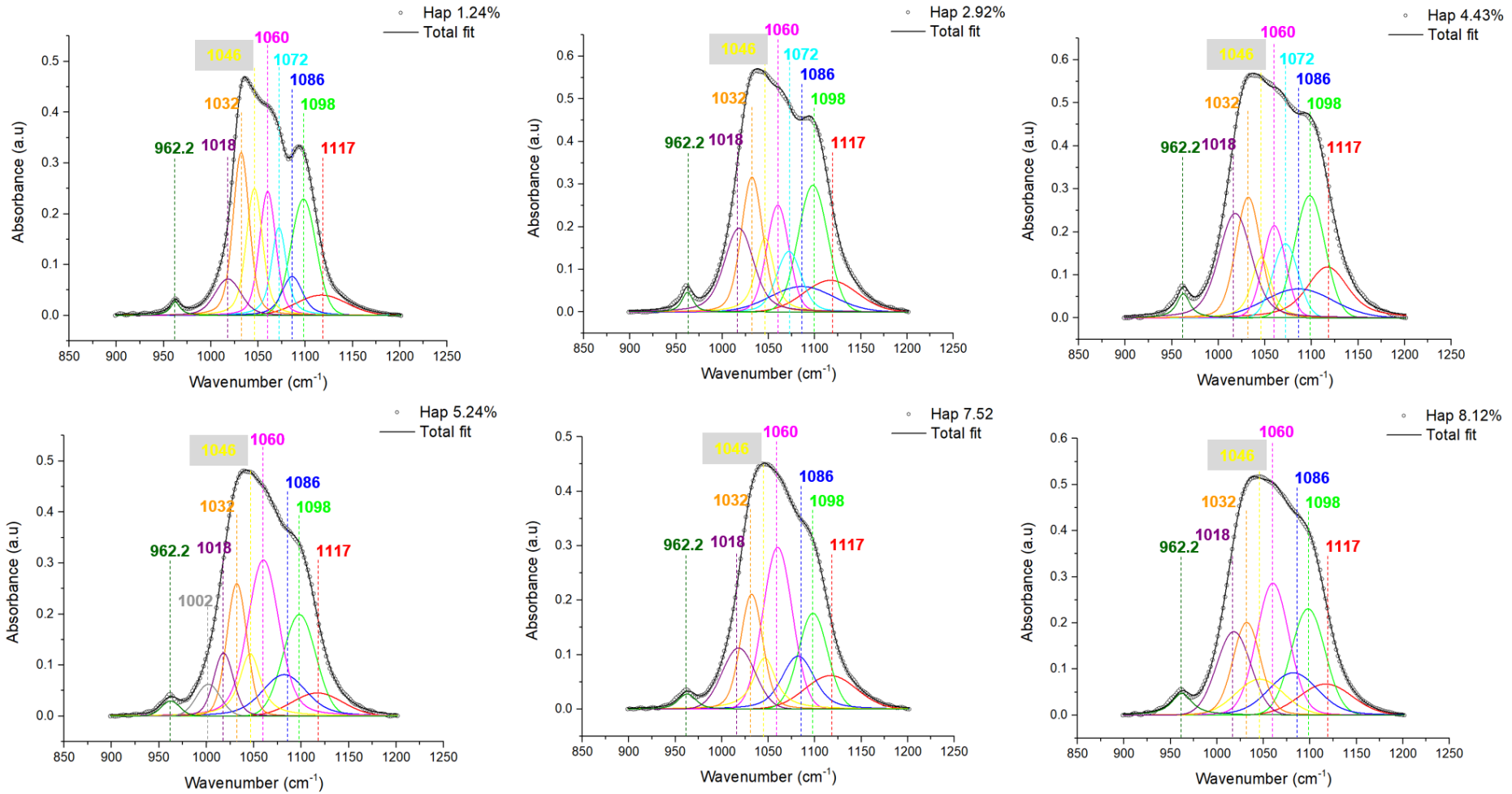

Figure B.3 Results of Gaussian and Lorentzian peak decomposition applied to the FTIR spectra of carbonated Hap compounds in the spectral range 1200-900 cm^{-1} corresponding to the phosphate region. $R^2 > 0.99$.

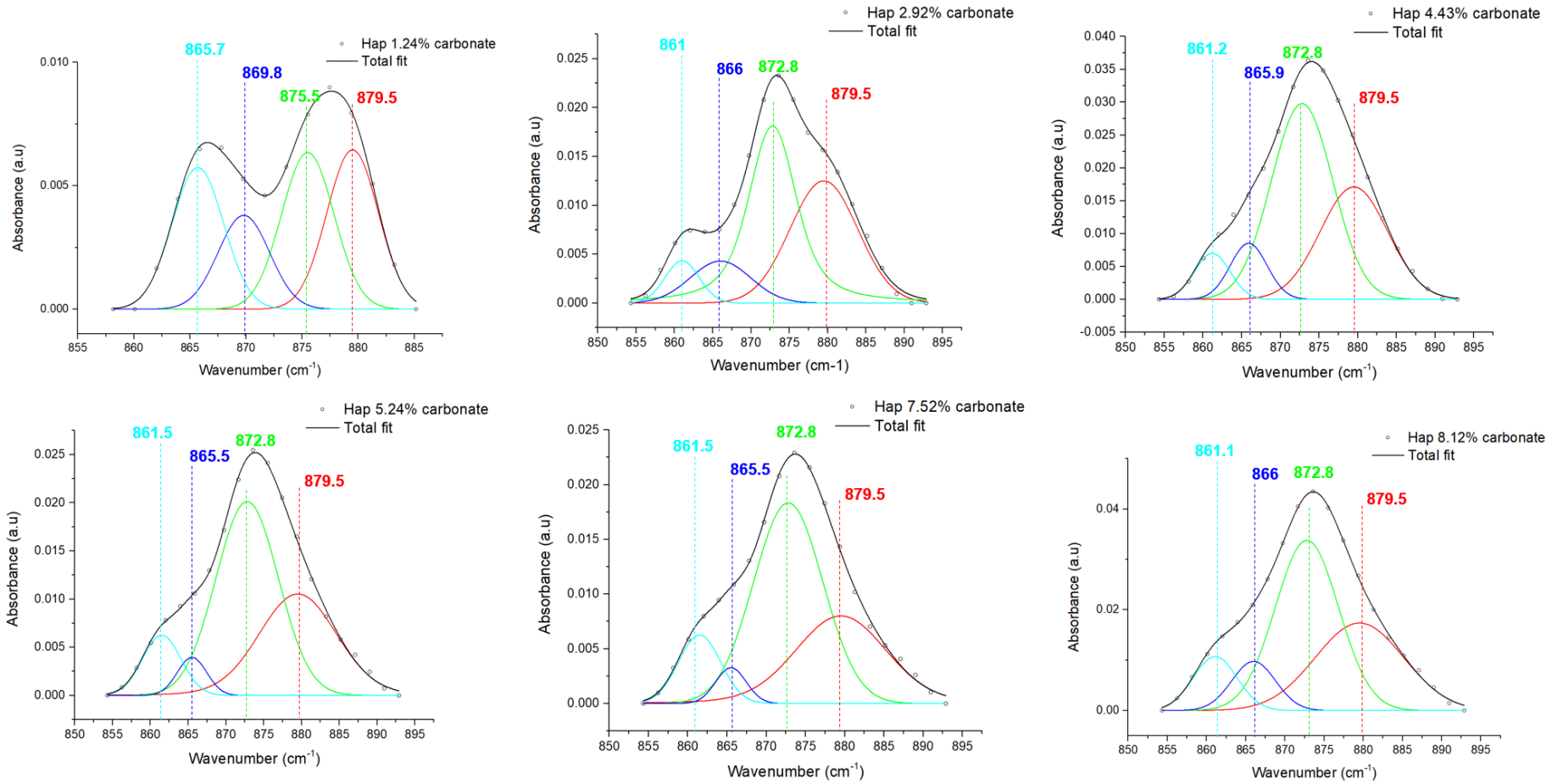

Figure B.4 Results of Gaussian and Lorentzian peak decomposition applied to the FTIR spectra of carbonated Hap compounds in the spectral range 890-830 cm^{-1} corresponding to the carbonate region. $R^2 > 0.99$.

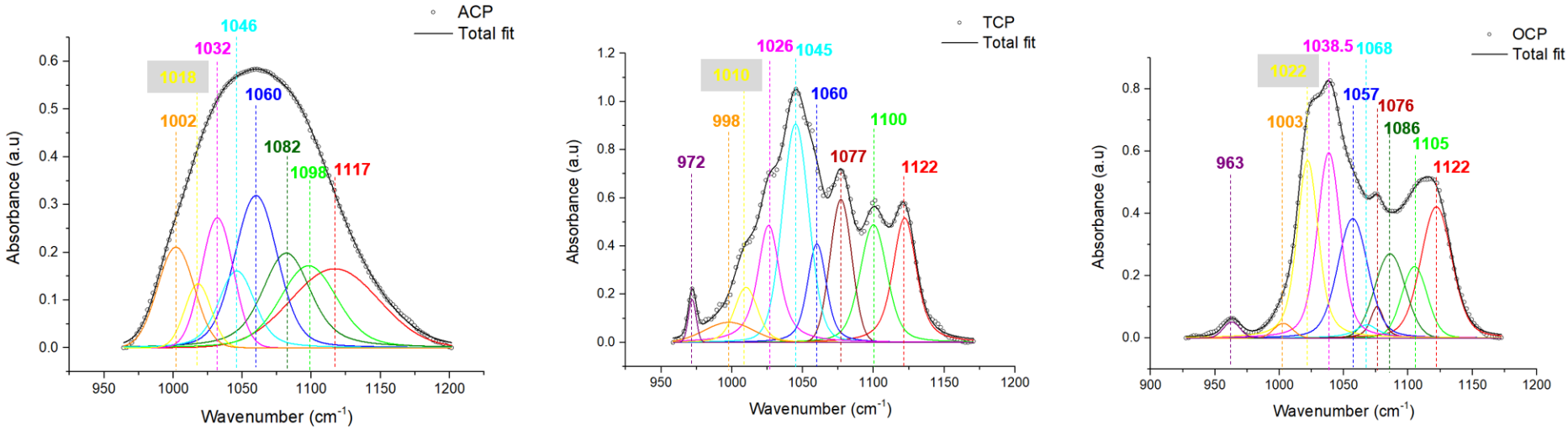

Figure B.5 Results of Gaussian and Lorentzian peak decomposition applied to the FTIR spectra of ACP, β-TCP and OCP compounds in the spectral range 1200-900 cm^{-1} corresponding to the phosphate region. $R^2 > 0.99$.

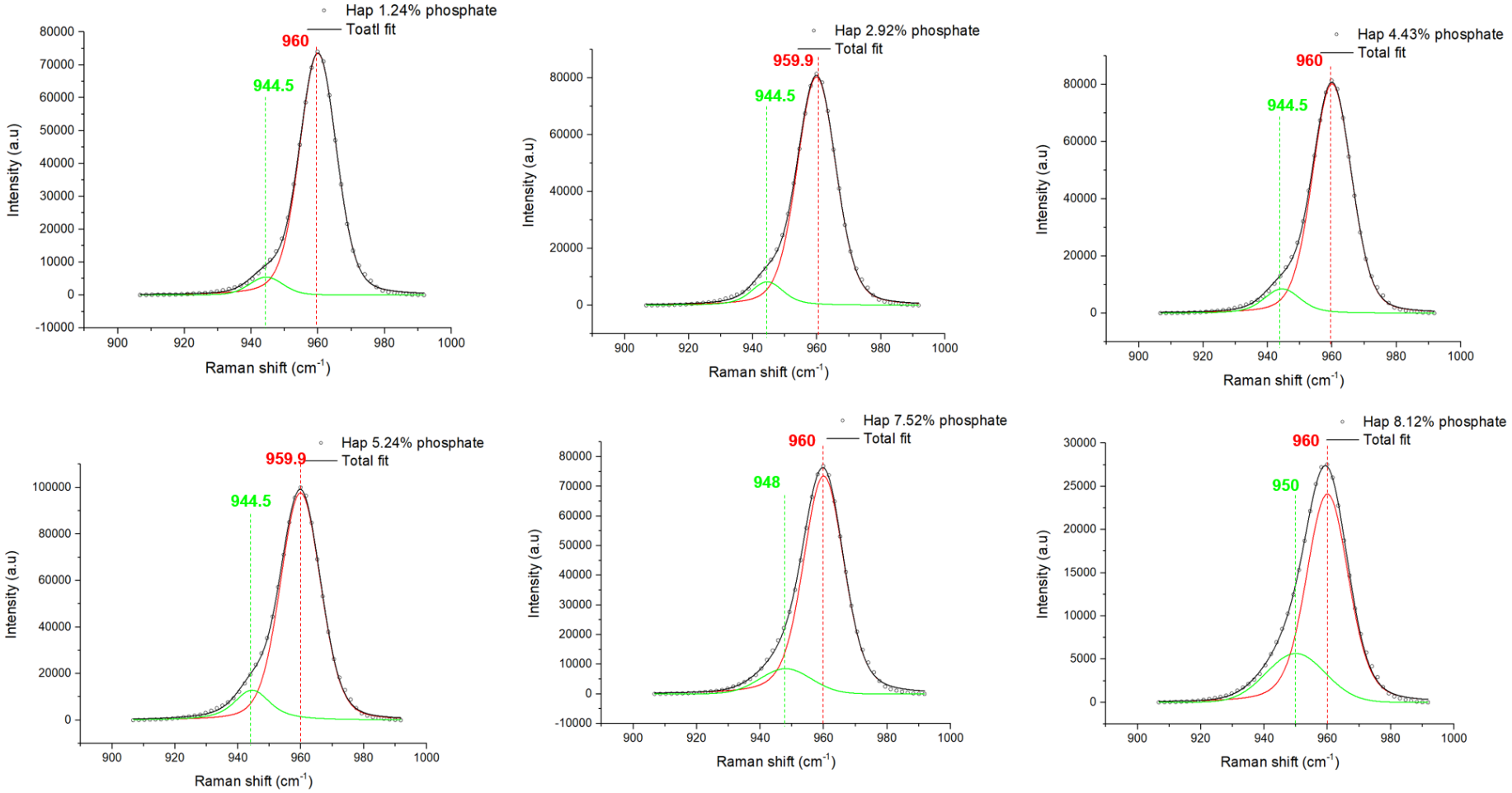

Figure B.6 Results of Gaussian and Lorentzian peak decomposition applied to the Raman spectra of carbonated Hap compounds in the spectral range 1000-900 cm^{-1} corresponding to the phosphate region. $R^2 > 0.99$.

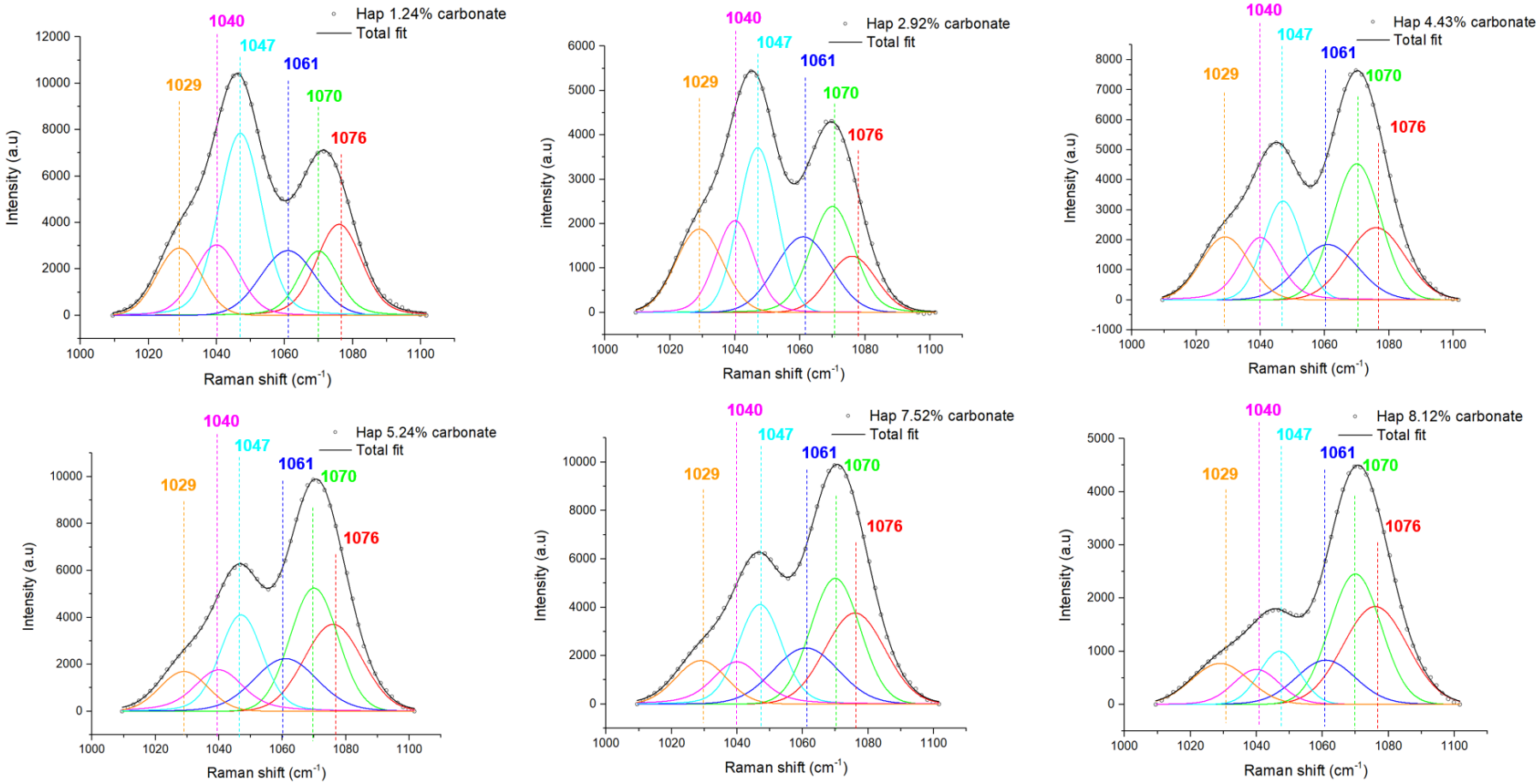

Figure B.7 Results of Gaussian and Lorentzian peak decomposition applied to the FTIR spectra of carbonated Hap compounds in the spectral range 1100-1010 cm^{-1} corresponding to the phosphate region. $R^2 > 0.99$.

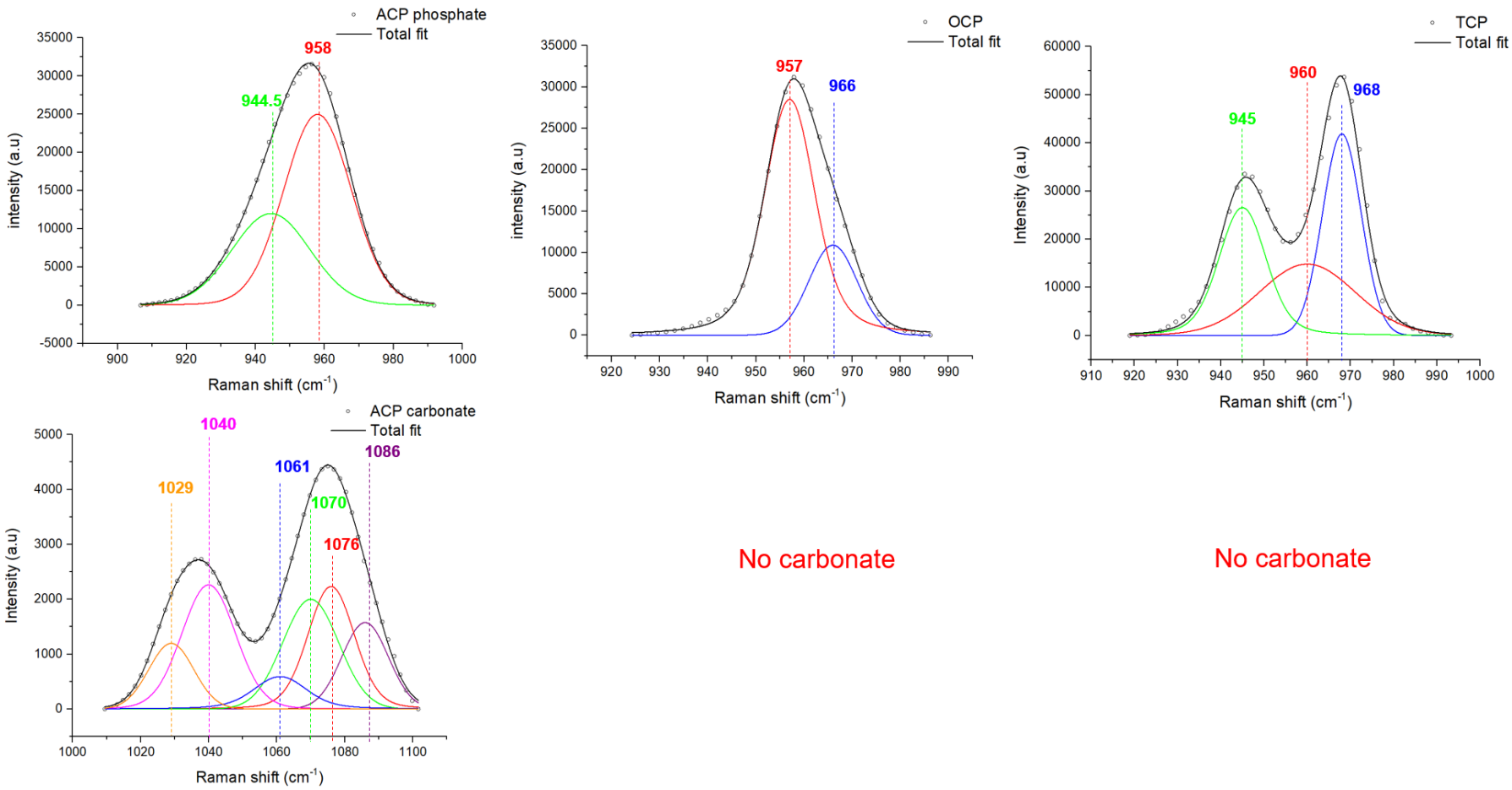

Figure B.8 Results of Gaussian and Lorentzian peak decomposition applied to the Raman spectra of ACP, β-TCP and OCP compounds in the spectral range 1000-1010 cm^{-1} corresponding to the phosphate region. $R^2 > 0.99$.

Table B.1 Wavenumbers of FTIR peaks of ACP, β-TCP and OCP and their assignment based on the peak decomposition and the literature, [86], [88], [89], [91], [94], [98], [99], [101].

Assignment	ACP	β-TCP	OCP	References
v_1 PO_4^{3-}			963	[91],[94]
		972		[91]
v_3 PO_4^{3-}	1002	998	1003	[89],[98],[99],[101]
Nonstoichiometric apatite	1018	1018	1022	[91], [94]
v_3 PO_4^{3-}	1032	1026		[86], [98]
	1046	1045		[88], [91]
	1060	1060		[89], [99]
			1068	[98]
		1077	1076	[89], [91],[98]
	1082		1086	[88]
	1098	1100	1105	[91], [94]
v_3 PO_4^{3-} in acidic phosphate environment (HPO_4^{2-})	1117	1122	1122	[98]

Table B.2 Raman shifts of ACP, β-TCP and OCP peaks and their assignments based on the peak decomposition and the literature [36], [103].

Assignment	ACP	β-TCP	OCP	References
v_1 PO_4^{3-}	945		945	[36],[103]
	958	957	960	[36],[103]
		966	968	[103]
v_3 PO_4^{3-}	1029			[36],[103]
	1040			[36],[103]
	1061			[36],[103]
v_1 CO_3^{2-}	1076			[103]
v_3 PO_4^{3-}	1086			[103]

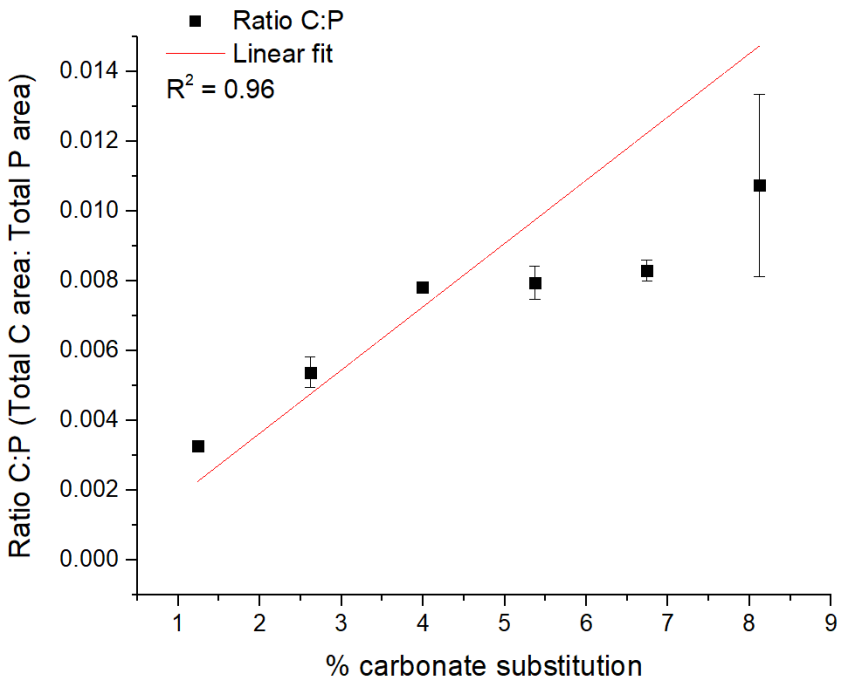

Figure B.9 Linear regression of the plot of C:P ratio vs. % CO_3^{2-} substitution in cHap pellet samples. Data were obtained from FTIR spectra as the ratio of the total carbonate to phosphate peak areas. Two replicates were performed in those experiments. Values are mean ± SD. Regression equation: y= $1.82 \cdot 10^{-3}$ x; R^2 = 0.96.

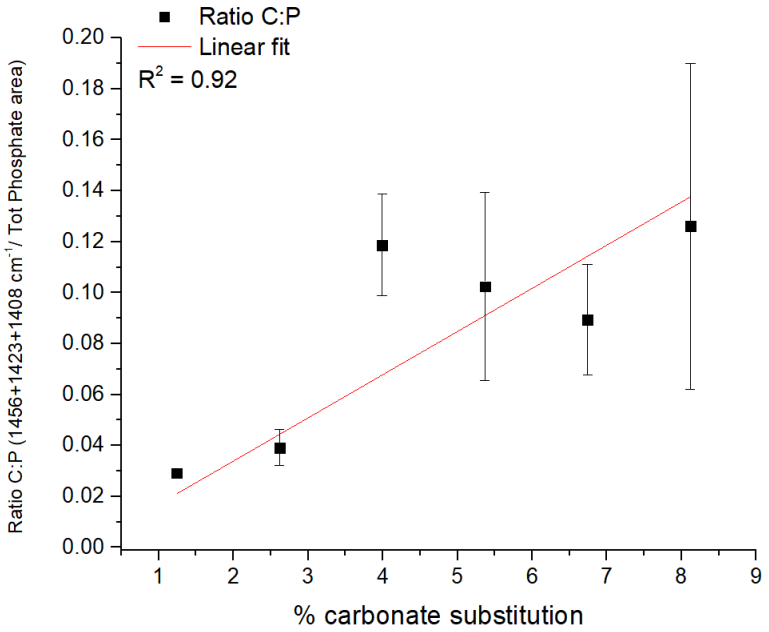

Figure B.10 Linear regression between the ratio C:P vs. % of CO_3^{2-} substitution in cHap pellet samples. Data were obtained from FTIR spectra as the ratio of the total carbonate to phosphate peak areas. Two replicates were performed in those experiments. Values are mean ±SD. Regression equation y= $1.70 \cdot 10^{-2}$ x; R^2= 0.92.

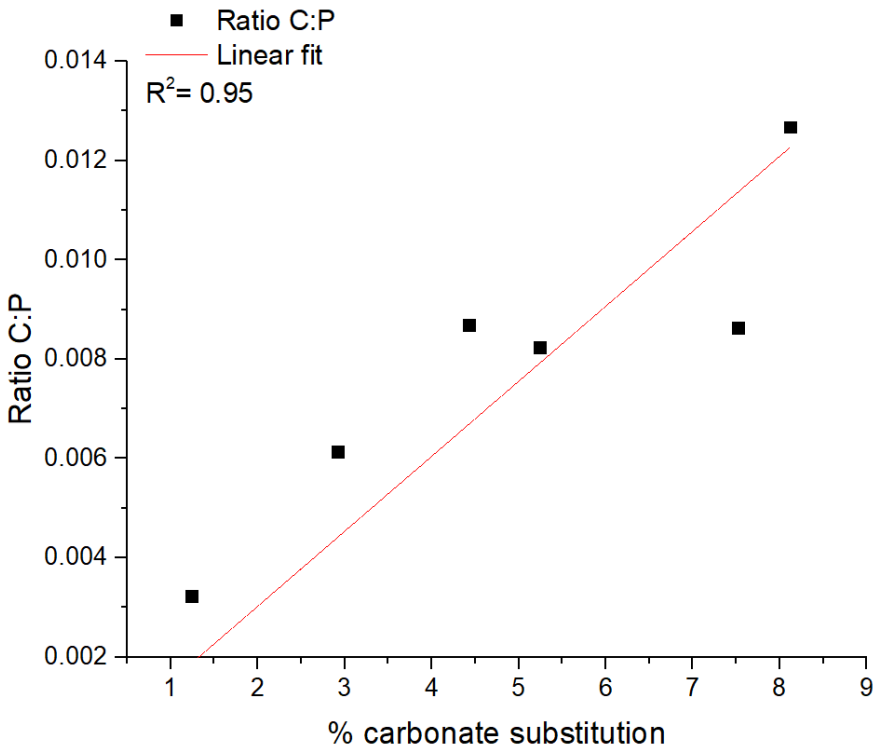

Figure B.11 Linear regression between the ratio C:P vs. % of CO_3^{2-} substitution in cHap pellet samples. Data were obtained from FTIR spectra as the ratio of the total carbonate to phosphate peak areas. Two replicates were performed in those experiments. One replicate has been performed. Values are mean ±SD. Regression equation $y= 1.51 \cdot 10^{-3} x$; $R^2= 0.95$.

Table B.3 Peak areas for the subbands of FTIR spectra from cHap pellets based on the peak decomposition analysis.

Area															
cHap	1117 cm^{-1}	1098 cm^{-1}	1086 cm^{-1}	1072 cm^{-1}	1060 cm^{-1}	1046 cm^{-1}	1032 cm^{-1}	1018 cm^{-1}	1002 cm^{-1}	962 cm^{-1}	879 cm^{-1}	875 cm^{-1}	869 cm^{-1}	866 cm^{-1}	861 cm^{-1}
1.24	2.68	7.75	2.57	4.28	5.97	6.38	7.91	2.80		0.52	0.04	0.04	0.02	0.03	
2.92	5.35	11.90	5.10	5.30	7.88	5.54	10.06	9.24		0.94	0.14	0.18		0.04	0.02
4.43	8.26	11.58	6.20	5.87	6.83	4.64	10.11	12.25		1.47	0.19	0.30		0.05	0.04
5.24	3.03	8.61	5.48		14.23	4.70	7.22	3.48	1.98	0.76	0.14	0.21		0.02	0.04
7.52	4.27	6.89	5.02		11.79	4.01	6.85	4.96		0.83	0.12	0.20		0.02	0.04
8.12	4.81	10.53	6.62		12.95	5.04	7.95	8.33		1.95	0.25	0.34		0.07	0.08
FWHM															
cHap	1117 cm^{-1}	1098 cm^{-1}	1086 cm^{-1}	1072 cm^{-1}	1060 cm^{-1}	1046 cm^{-1}	1032 cm^{-1}	1018 cm^{-1}	1002 cm^{-1}	962 cm^{-1}	879 cm^{-1}	875 cm^{-1}	869 cm^{-1}	866 cm^{-1}	861 cm^{-1}
1.24	63.00	31.20	25.78	18.75	20.43	20.34	20.29	32.65		12.51	5.41	5.51	5.40	5.42	
2.92	67.87	37.60	80.24	31.40	28.31	23.19	27.20	37.46		14.42	10.42	7.37		9.24	5.26
4.43	52.35	38.31	86.33	31.97	28.96	24.42	31.23	41.27		17.09	10.26	9.36		5.61	5.42
5.24	62.80	40.64	54.74		38.88	26.12	24.93	24.35	29.84	22.97	12.08	9.72		4.59	6.02
7.52	65.08	36.80	40.98		37.22	28.43	28.04	41.55		22.85	13.65	10.41		4.58	6.36
8.12	66.95	42.85	62.26		41.07	60.48	34.99	43.18		26.61	13.27	9.52		6.59	6.63

Table B.4 FWHMs for the subbands of FTIR spectra from ACP, β-TCP and OCP pellets based on the peak decomposition analysis.

Area													
	1122 cm^{-1}	1105 cm^{-1}	1086 cm^{-1}	1076 cm^{-1}	1068 cm^{-1}	1060 cm^{-1}	1045 cm^{-1}	1038 cm^{-1}	1032 cm^{-1}	1022 cm^{-1}	1002 cm^{-1}	972 cm^{-1}	963 cm^{-1}
ACP	13.27	9.92	10.63			13.49	6.11		7.87	3.21	7.00		
β-TCP	13.32	13.20		11.37		8.20	22.54			12.51	5.38	3.61	1.22
OCP	14.11	5.95	8.02	1.67	1.40	12.41		15.51		14.15	0.85		0.83
FWHM													
	1122 cm^{-1}	1105 cm^{-1}	1086 cm^{-1}	1076 cm^{-1}	1068 cm^{-1}	1060 cm^{-1}	1045 cm^{-1}	1038 cm^{-1}	1032 cm^{-1}	1022 cm^{-1}	1002 cm^{-1}	972 cm^{-1}	963 cm^{-1}
ACP	75.21	48.61	41.26			36.59	30.72		27.17	22.53	31.20		
β-TCP	19.51	22.36		18.01		15.72	21.93			18.29	19.36	40.68	6.45
OCP	28.50	23.30	27.86	12.17	21.01	27.61		21.20		19.42	17.04		15.26421

Table B.5 Peak areas for the subbands of Raman spectra from cHap pellets based on the peak decomposition analysis.

Area									
cHap	**1076 cm^{-1}**	**1070 cm^{-1}**	**1061 cm^{-1}**	**1047 cm^{-1}**	**1040 cm^{-1}**	**1029 cm^{-1}**	**960 cm^{-1}**	**945 cm^{-1}**	**950 cm^{-1}**
1.24	71147.97	44446.22	56472.25	133294.8	52819.75	47093.68	1124370	73371.58	
2.92	23366.81	42837.6	36598.17	54930.98	32443.12	33969.93	1341210	128262.3	
4.43	54449.58	83944.08	42386.05	49680.4	36721.21	39484.87	1326540	139933.8	
5.24	84524.34	99289.54	58788.07	74597.57	41657.15	32101.11	1698250	241841.6	
7.52	86067.77	98553.9	58426.83	72847.89	38702.99	34510.94	1326580		171291.1
8.12	44967.73	47668.99	19322.91	15219.94	12024.7	16797.52	450147.36		131714.3

FWHM									
cHap	**1076 cm^{-1}**	**1070 cm^{-1}**	**1061 cm^{-1}**	**1047 cm^{-1}**	**1040 cm^{-1}**	**1029 cm^{-1}**	**960 cm^{-1}**	**945 cm^{-1}**	**950 cm^{-1}**
1.24	15.64	13.58	18.99	14.87	15.45	15.28	13.10	11.81	
2.92	17.31	15.97	20.17	13.90	13.99	17.02	14.35	12.00	
4.43	21.25	17.39	21.61	14.18	14.65	17.66	14.30	13.28	
5.24	21.45	17.77	23.49	15.85	18.24	17.81	15.08	13.47	
7.52	21.49	17.80	23.33	15.71	17.58	18.06	15.10		18.92
8.12	22.95	18.25	21.17	14.33	16.41	20.46	15.70		21.88

Table B.6 FWHMs for the subbands of Raman spectra from ACP, β-TCP and OCP pellets based on the peak decomposition analysis.

Area									
	1086 cm^{-1}	**1076 cm^{-1}**	**1070 cm^{-1}**	**1061 cm^{-1}**	**1040 cm^{-1}**	**1029 cm^{-1}**	**966 cm^{-1}**	**957 cm^{-1}**	**945 cm^{-1}**
ACP	26914.48	41034.85	41252.26	13334.47	46316.45	19758.43		628968.7	345579.3
β-TCP							471103.98	426182.5	401812.6
OCP							136339.13	436795.8	

FWHM									
	1086 cm^{-1}	**1076 cm^{-1}**	**1070 cm^{-1}**	**1061 cm^{-1}**	**1040 cm^{-1}**	**1029 cm^{-1}**	**966 cm^{-1}**	**957 cm^{-1}**	**945 cm^{-1}**
ACP	16.04	16.15	19.38	18.37	18.67	15.51		23.10	26.67
β-TCP							10.57	26.25	12.90
OCP	11.77	12.41					11.77	12.41	

C. Appendix - Supplementary Data 3

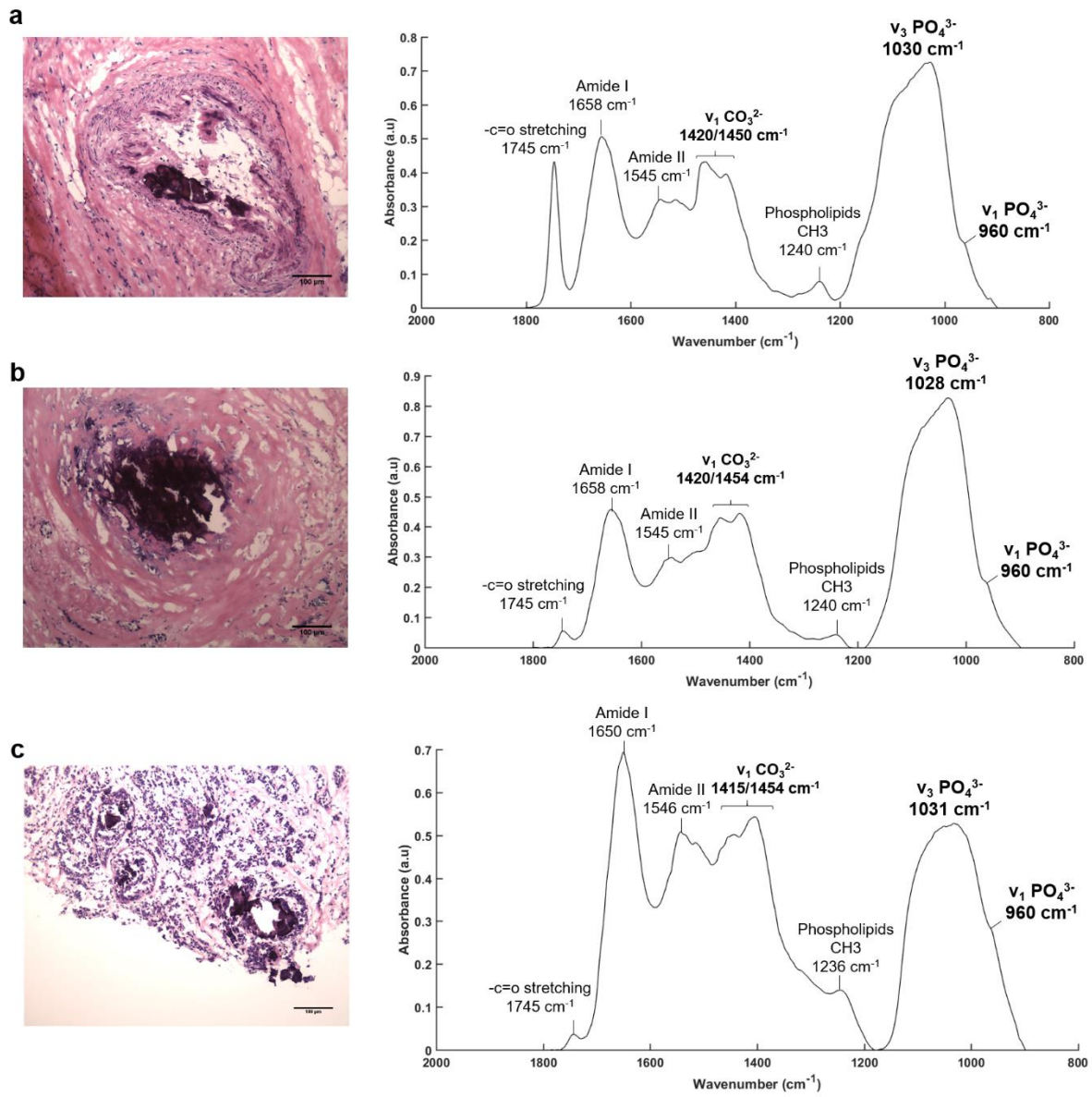

Figure C.1 Histological sections with H&E staining and corresponding FTIR spectra at three stages of breast cancer: (a) Benign, (b) DCIS low grade and (c) IDC grade 2. An average of 10 spectra were extracted from FTIR images of microcalcifications in the range 1800-900 cm^{-1}.

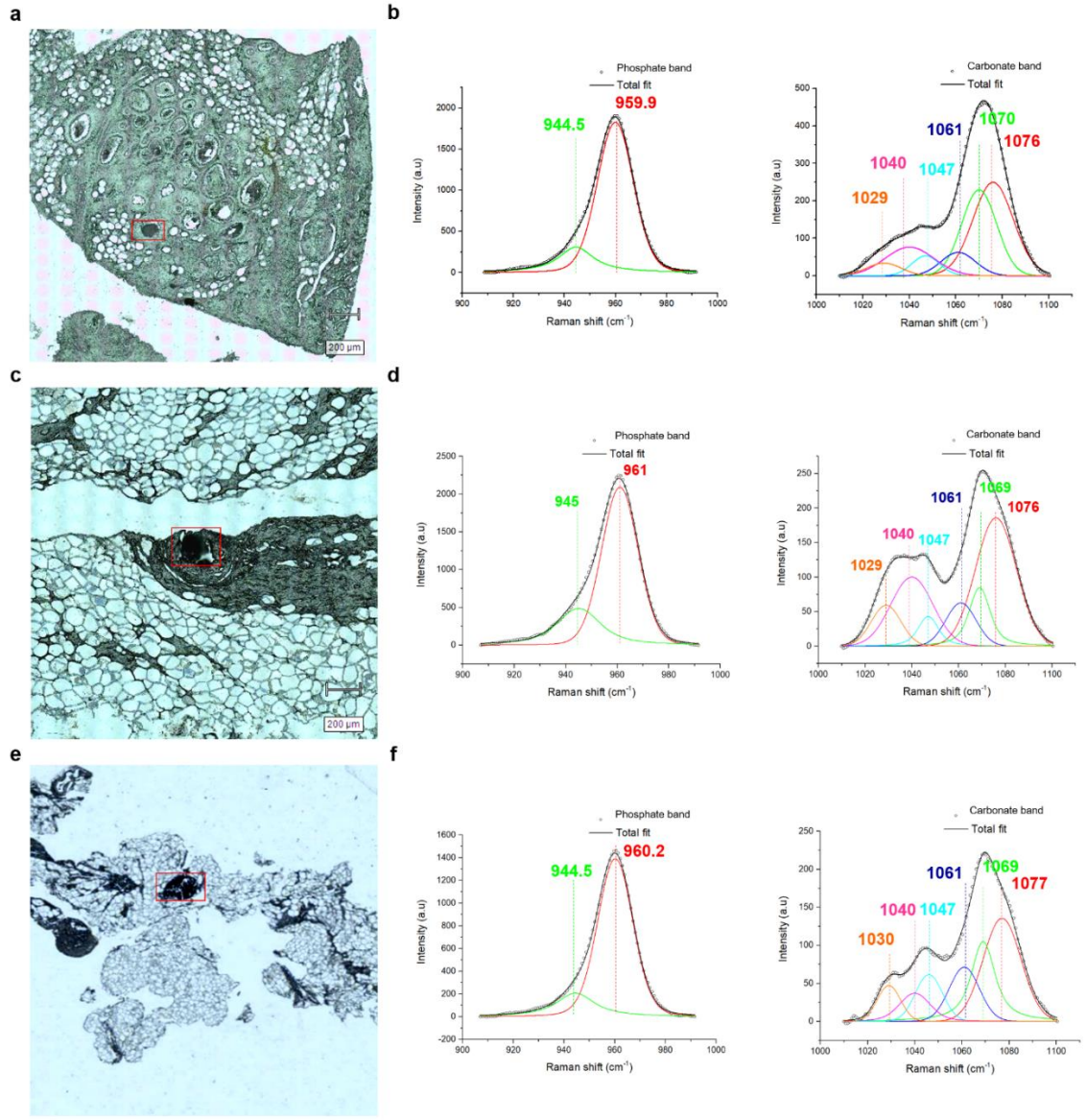

Figure C.2 Results from curve fit analysis applied to Raman spectra. Histological sections with H&E staining and comparison of Raman spectra of de-paraffinised tissues of three breast lesions: (a) Benign, (c) DCIS low grade and (e) IDC grade 2. (b,d, and f) Spectra were truncated to the phosphate band at 990-930 cm^{-1} and to the carbonate band at 1100-1020 cm^{-1} and baseline corrected. For each fit, the regression is very good ($R^2 > 0.99$).

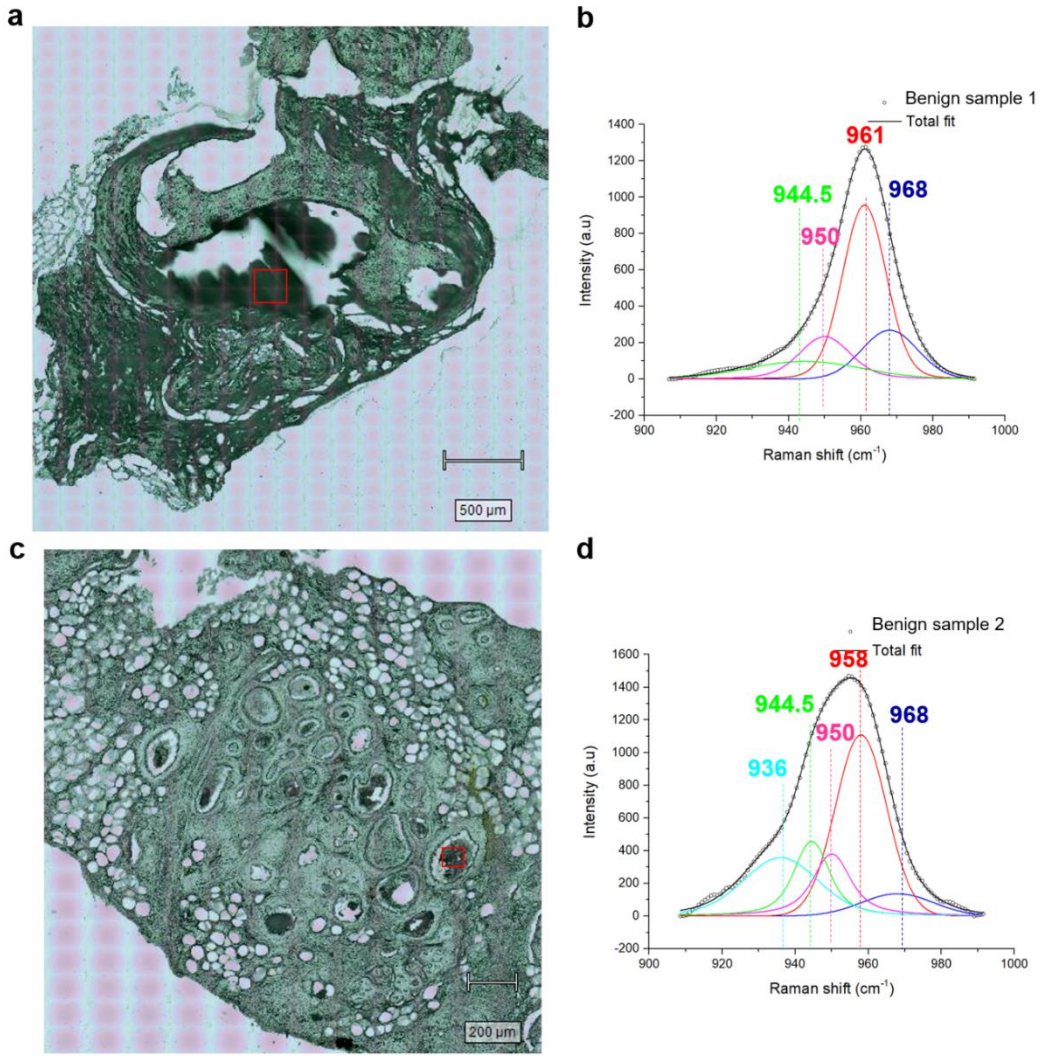

Figure C.3 Results from curve fit analysis applied to the Raman spectra. (a and c) Visible images of de-paraffinised breast tissue sections (benign stage). Red boxes denote the regions where Raman maps were acquired. (b and d) Spectra were truncated to the phosphate band at 990-930 cm^{-1} and baseline corrected.

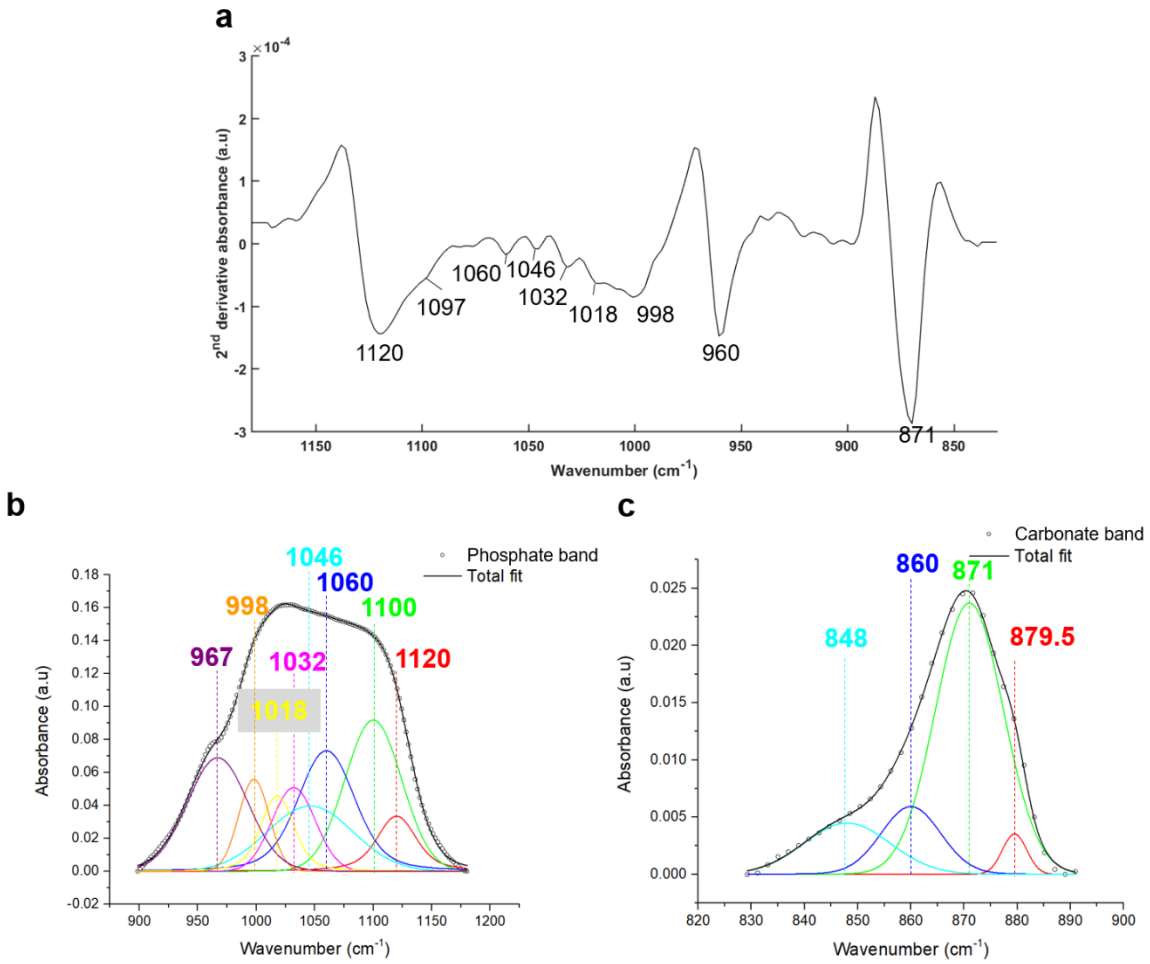

Figure C.4 Results from curve fit analysis of FTIR spectra from frozen breast tissue (benign lesion). (a) Second derivative spectrum between 1200 and 830 cm^{-1}. Curve fit analysis was performed on spectra truncated to (b) the phosphate band at 1200-900 cm^{-1} and (c) the carbonate band at 890-830 cm^{-1} and baseline corrected. For each case, the regression is very good ($R^2 > 0.99$).

Table C.1 Predicted phosphate species in frozen and paraffinised/de-paraffinised breast tissue microcalcifications using sub-peak positions obtained by curve fit analysis performed on Raman and FTIR spectra for three breast lesions: B: Benign, D: DCIS, and I: invasive cancer. Double red arrows are added to notify that the same microcalcifications were analysed by Raman and FTIR spectroscopy.

Paraffinised and de-paraffinised tissue sections				
FTIR analysis			Raman analysis	
B1	cHap (Type A?)	↔	**B1**	cHap
B2	cHap	↔	**B2**	β-TCP
B3	cHap		**B3**	cHap
B4	OCP		**B4**	cHap
B5	cHap		**B5**	cHap
B6	cHap		**B6**	cHap
B7	cHap		**B7**	β-TCP
B8	cHap		**B8**	-
B9	cHap + ACP	↔	**B9**	cHap
B10	cHap + ACP	↔	**B10**	cHap
B11	cHap + ACP	↔	**B11**	cHap
B12	cHap + ACP	↔	**B12**	cHap + β-TCP
B13	cHap + ACP		**B13**	-
B14	cHap + ACP + β-TCP		**B14**	cHap + ACP + β-TCP
B15	cHap + ACP + β-TCP		**B15**	cHap + ACP + β-TCP
B16	cHap + ACP + β-TCP		**B16**	cHap + ACP + β-TCP
B17	cHap + ACP		**B17**	-
B18	cHap + ACP	↔	**B18**	cHap + ACP + β-TCP
B19	cHap + ACP		**B19**	β-TCP
D1	cHap + ACP	↔	**D1**	cHap
D2	cHap + ACP	↔	**D2**	cHap
D3	β-TCP	↔	**D3**	β-TCP
D4	cHap + OCP	↔	**D4**	cHap
D5	cHap		**D5**	-
D6	cHap		**D6**	-
D7	cHap + ACP		**D7**	cHap + ACP + β-TCP
D8	cHap + ACP		**D8**	cHap + ACP + β-TCP
D9	cHap + ACP		**D9**	-
D10	cHap + ACP		**D10**	-
I1	cHap + ACP	↔	**I1**	cHap
I2	cHap + β-TCP		**I2**	cHap low carb

Frozen tissue sections				
FTIR analysis			Raman analysis	
B1	cHap + ACP	↔	**B1**	cHap +ACP
B2	-		**B2**	cHap
D1	OCP	↔	**D1**	cHap + OCP or cHap +ACP
D2	cHap + ACP	↔	**D2**	cHap + β-TCP
D3	cHap + β-TCP	↔	**D3**	cHap + β-TCP
I1	cHap	↔	**I1**	cHap
I2	cHap + ACP	↔	**I2**	ACP
I3	cHap or β-TCP	↔	**I3**	cHap High carb
I4	cHap or β-TCP	↔	**I4**	cHap + β-TCP
I5	-		**I5**	cHap
I6	-		**I6**	cHap
I7	-		**I7**	cHap +ACP
I8	cHap + β-TCP	↔	**I8**	cHap + β-TCP
I9	cHap + β-TCP	↔	**I9**	cHap + β-TCP
I10	-		**I10**	cHap + β-TCP
I11	cHap + β-TCP	↔	**I11**	cHap
I12	cHap		**I12**	cHap +ACP
I13	-		**I13**	cHap +ACP
I14	-		**I14**	cHap +ACP
I15	cHap	↔	**I15**	cHap
I16	cHap		**I16**	-
I17	β-TCP		**I17**	ACP
I18	-		**I18**	cHap +ACP
I19	cHap + ACP	↔	**I19**	cHap + β-TCP
I20	cHap + ACP	↔	**I20**	cHap + β-TCP
I21	-		**I21**	cHap + β-TCP

D. Appendix - Supplementary Data 4

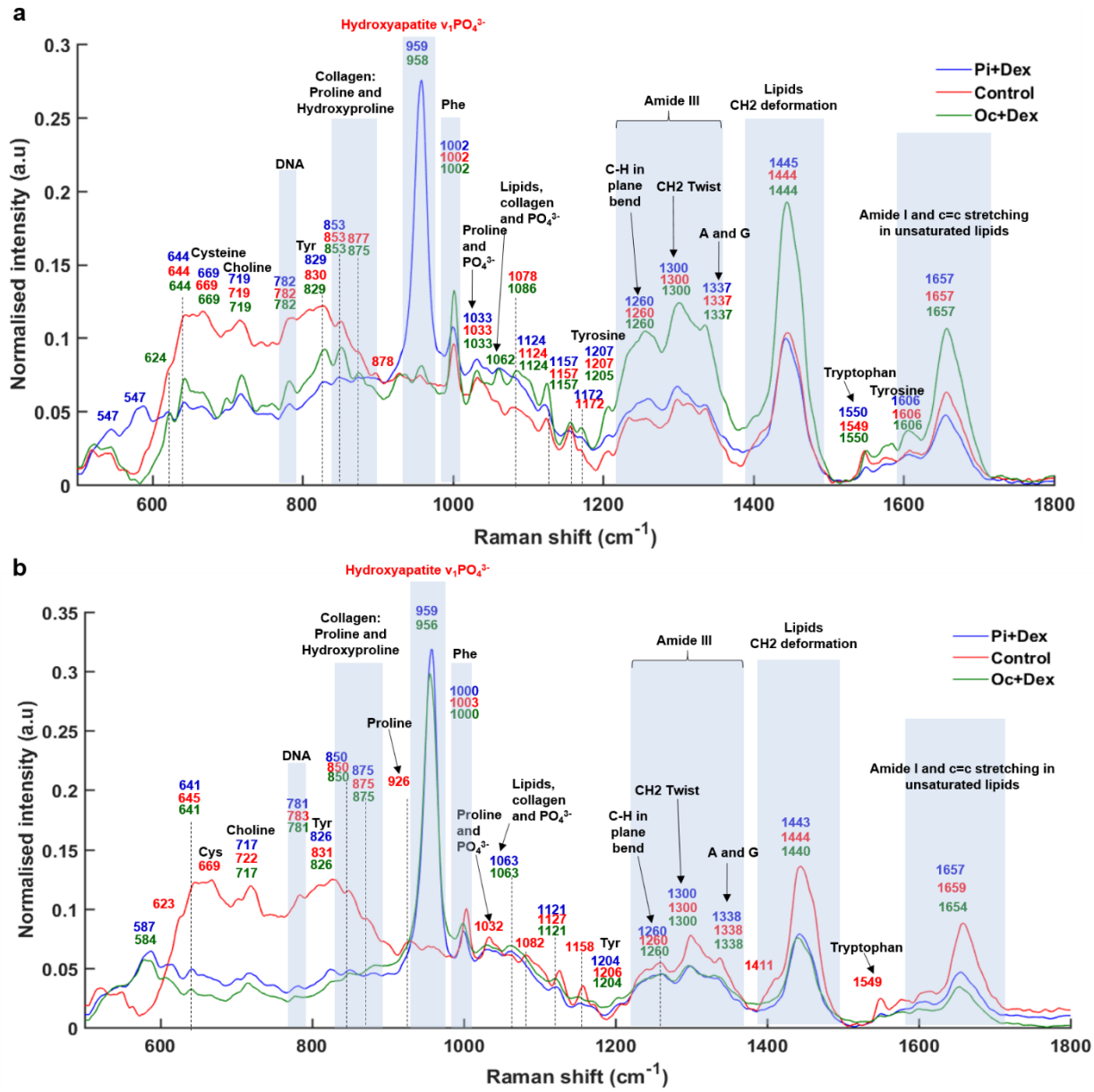

Figure D.1 Mean Raman spectra collected from breast cancer cells after 7 days (a) and 14 days (b) of mineralisation. Pi: inorganic phosphate, OC: osteogenic cocktail, Dex: Dexamethasone, Phe: Phenylalanine, Cys: Cysteine, Tyr: Tyrosine. Cells were treated with Pi+Dex and OC+Dex (βG). Non-treated cells are considered as control. A mean of 40 spectra were performed for each condition.

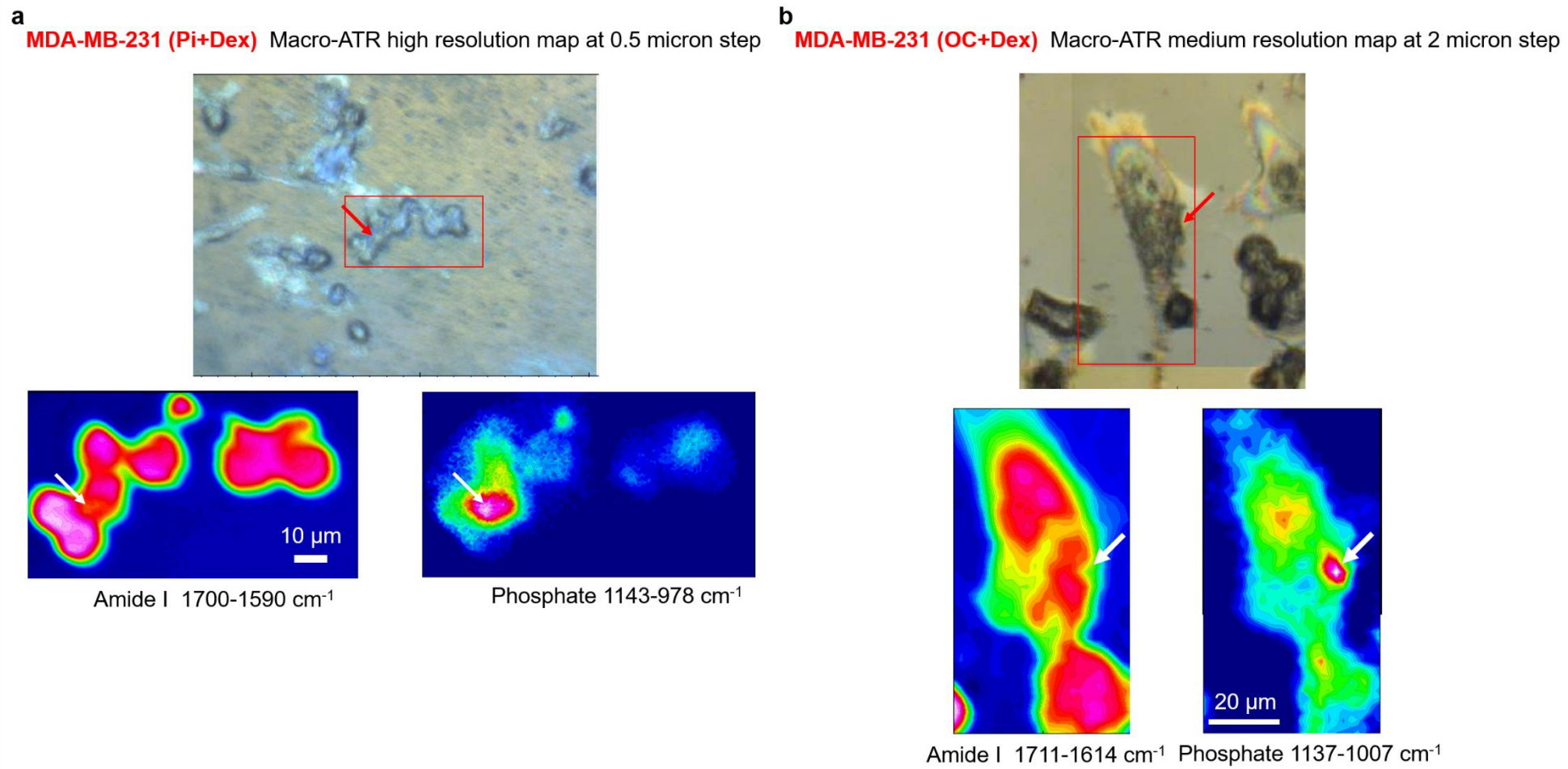

Figure D.2 ATR-FTIR spectroscopy analysis of breast cancer cells treated with (a) Pi+Dex and (b) OC + Dex. For both conditions, FTIR images are based on the Amide I and phosphate peak intensities. Red and white arrows correspond to the location of high phosphate intensity found in calcium deposits. Figure provided by M. Tobin and J. Vongsvivut from Australian synchrotron.

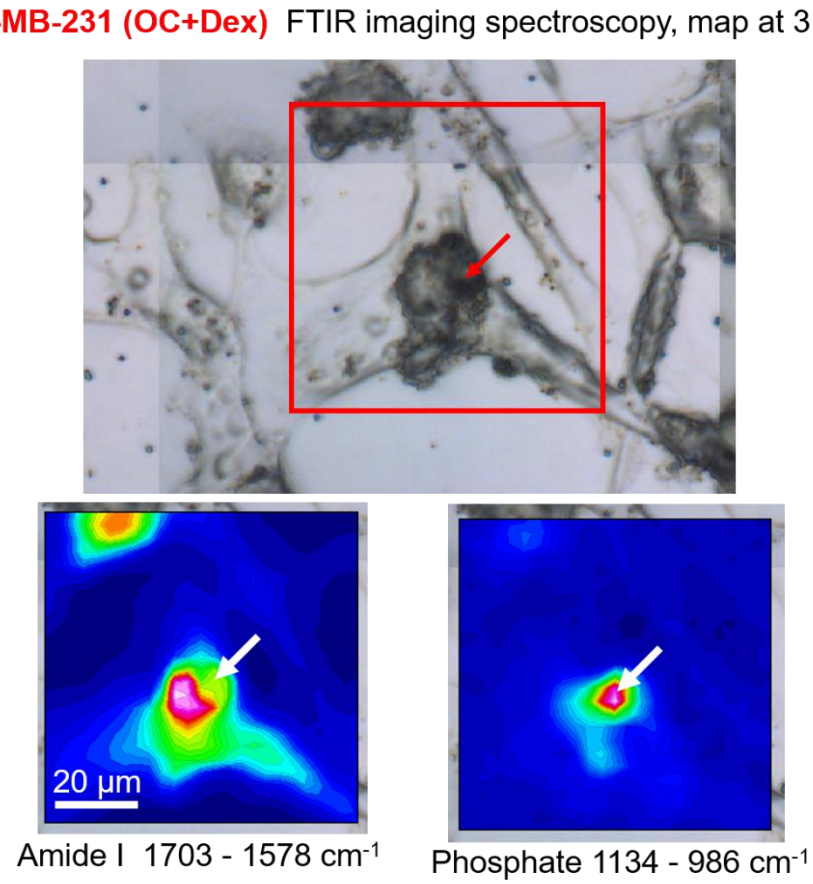

Figure D.3 FTIR imaging spectroscopy analysis of breast cancer cells treated with OC + Dex. FTIR images are based on the Amide I and phosphate peak intensities. Red and white arrows correspond to the location of high phosphate intensity found in calcium deposits. Figure provided by M. Tobin and J. Vongsvivut from Australian synchrotron.

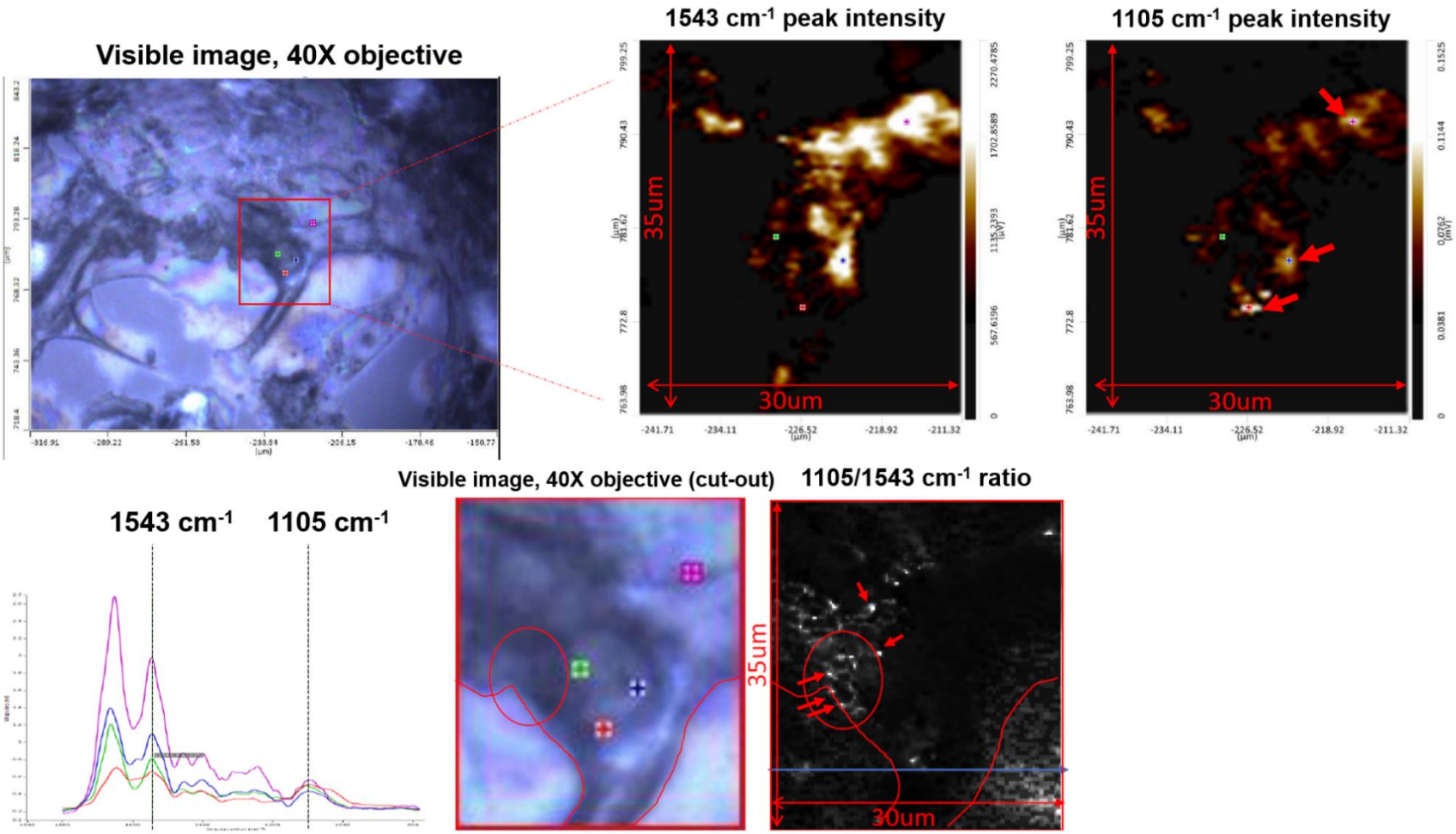

Figure D.4 O-PTIR spectroscopy analysis of breast cancer cells treated with OC + Dex after 11 days of mineralisation. Images are based on the Amide I, phosphate peak intensities, and the ratio protein-to-phosphate ratio. Red arrows correspond to the location of high phosphate intensity found in calcium deposits. Figure provided by J. Nallala (Exeter) and M. Kansiz, from Photothermal spectroscopy corp. at the Synchrotron Soleil, France.

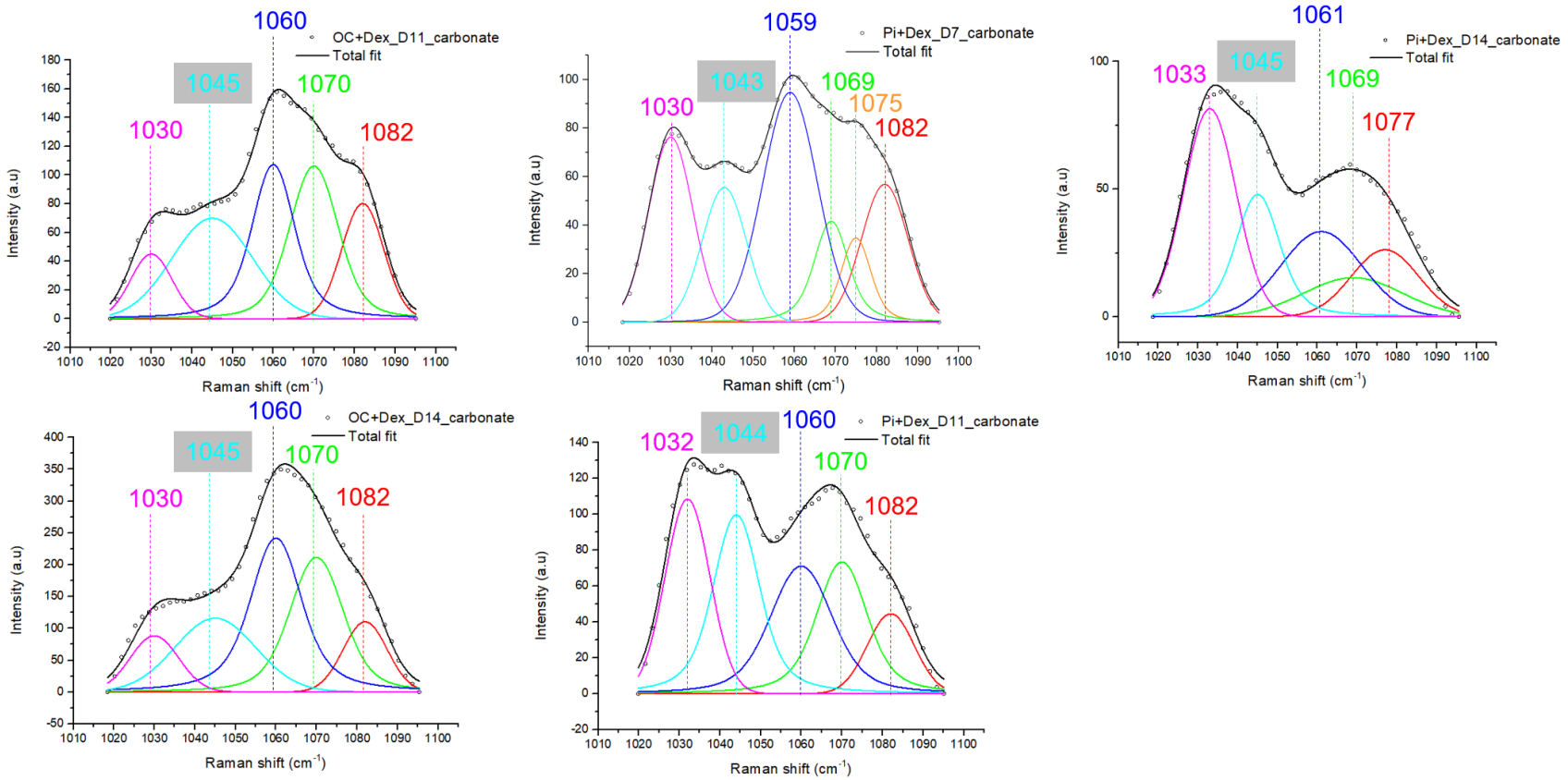

Figure D.5 Results from curve fit analysis of Raman spectra for cells treated with Pi + Dex at day 7, 11 and 14 and OC+Dex (βG) at day 11 and 14. Spectra were truncated to the carbonate band to 1095-1020 cm^{-1} and baseline-corrected. For each case, $R^2 > 0.99$.

Table D.1 Calculation of Carbonate-to-phosphate ratio and carbonate amount in breast cancer cells after 3, 7, 11 and 14 days of mineralisation for each replicate after Pi and βG treatments. Calculation based on the areas under each component calculated by curve fit analysis.

replicate 1	Pi+Dex				OC+Dex			
	D3	D7	D11	D14	D3	D7	D11	D14
Total carbonate area (1070 cm^{-1})		532.1874	1381.29	476.6257			1783.378	4026.754
Total phosphate area (960 cm^{-1})	13326.36	16161.71	28703.09	14921.99			39086.05	55181.12
Ratio C:P (1070/960 cm^{-1})		0.032929	0.048123	0.031941			0.045627	0.072973
% carbonate substitution estimated Linear fit equation: y=0.01239x		2.6577	3.884052	2.57798			3.682564	5.889701

replicate 2	Pi+Dex				OC+Dex			
	D3	D7	D11	D14	D3	D7	D11	D14
Total carbonate area (1070 cm^{-1})			1250.643	2629.599			678.4038	2777.681
Total phosphate area (960 cm^{-1})	3726.509	17527.5	11027.32	40120.58			15462.33	58759.18
Ratio C:P (1070/960 cm^{-1})			0.113413	0.065542			0.043875	0.047272
% carbonate substitution estimated Linear fit equation: y=0.01239x			9.15361	5.289943			3.541132	3.815358

replicate 3	Pi+Dex				OC+Dex			
	D3	D7	D11	D14	D3	D7	D11	D14
Total carbonate area (1070 cm^{-1})		325.0166	953.0748	628.1136			3570.488	2113.542
Total phosphate area (960 cm^{-1})	3270.777	14810.43	37381.06	22319.61			65119.22	37010.3
Ratio C:P (1070/960 cm^{-1})		0.021945	0.025496	0.028142			0.05483	0.057107
% carbonate substitution estimated Linear fit equation: y=0.01239x		1.771196	2.057804	2.271331			4.425345	4.609108

E. Appendix - Supplementary Data 5

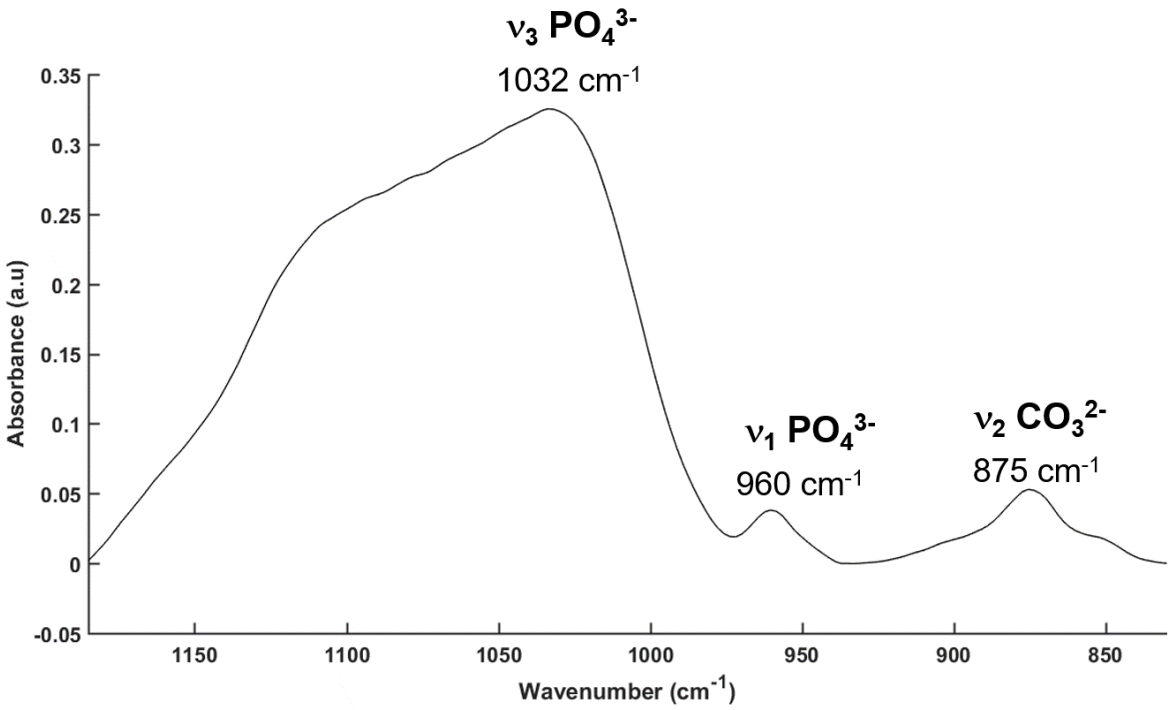

Figure E.1 FTIR spectrum in single point measured from a microcalcification in breast tissue section (DCIS stage) in the spectral range 1200-830 cm^{-1} including phosphate and carbonate regions. An x15 objective and spectral resolution of 4 cm^{-1} were used in this measurement.

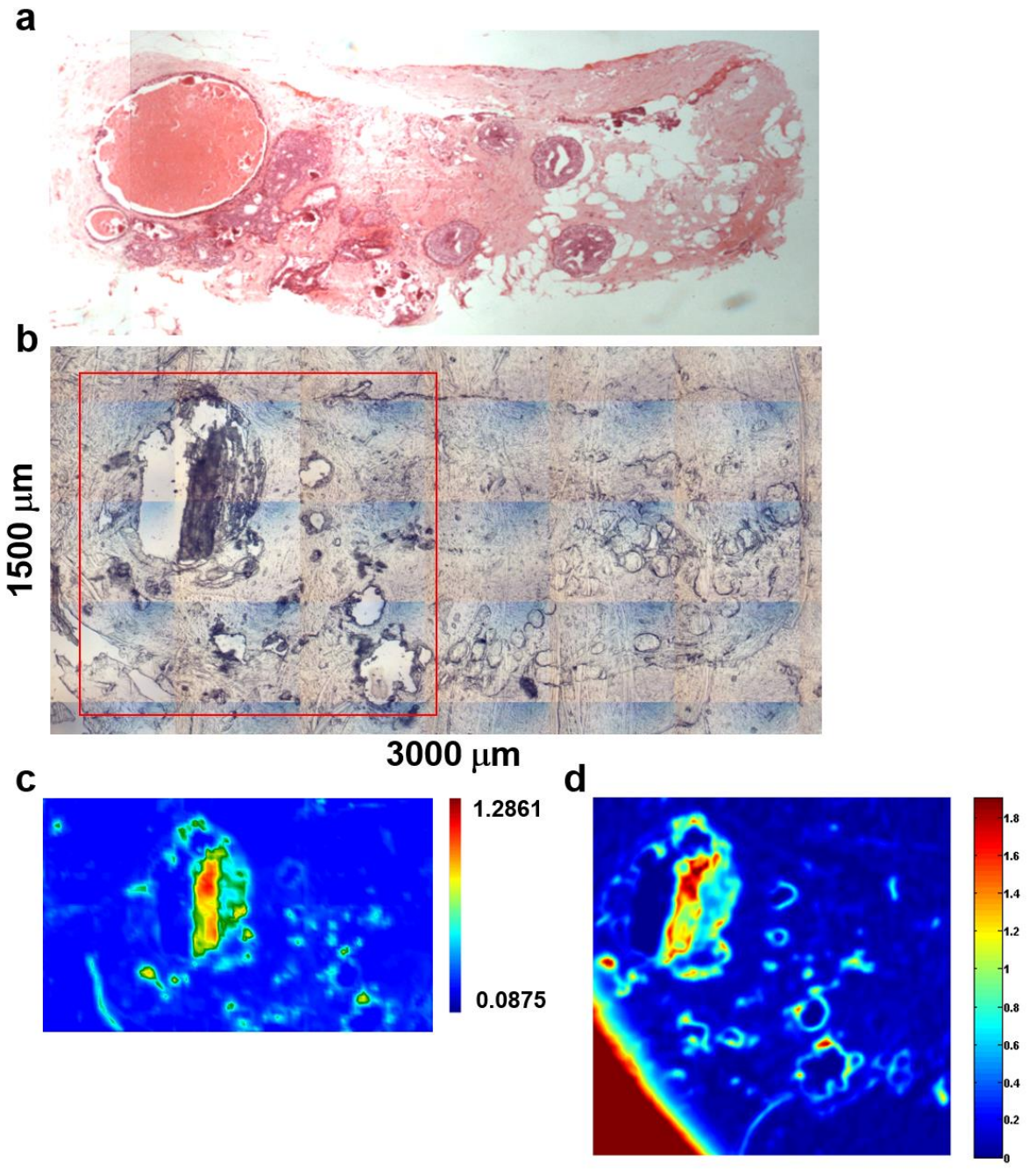

Figure E.2 Comparison between the micro-FTIR imaging system and upconversion system. (a) Histological section of breast tissue section (DCIS stage) and H&E stained. (b) White light image of a breast tissue section without staining mounted onto BaF_2. (c) FTIR absorbance image referring to the phosphate peak intensity at 1020 cm^{-1} recorded on the spectral range 3900-900 cm^{-1} with the Agilent imaging system with an x15 objective and 5.5 μm^2 pixel size. (c) Upconversion absorbance image at the phosphate peak intensity 1020 cm^{-1} corresponding to the upconverted signal at 958.8 nm.

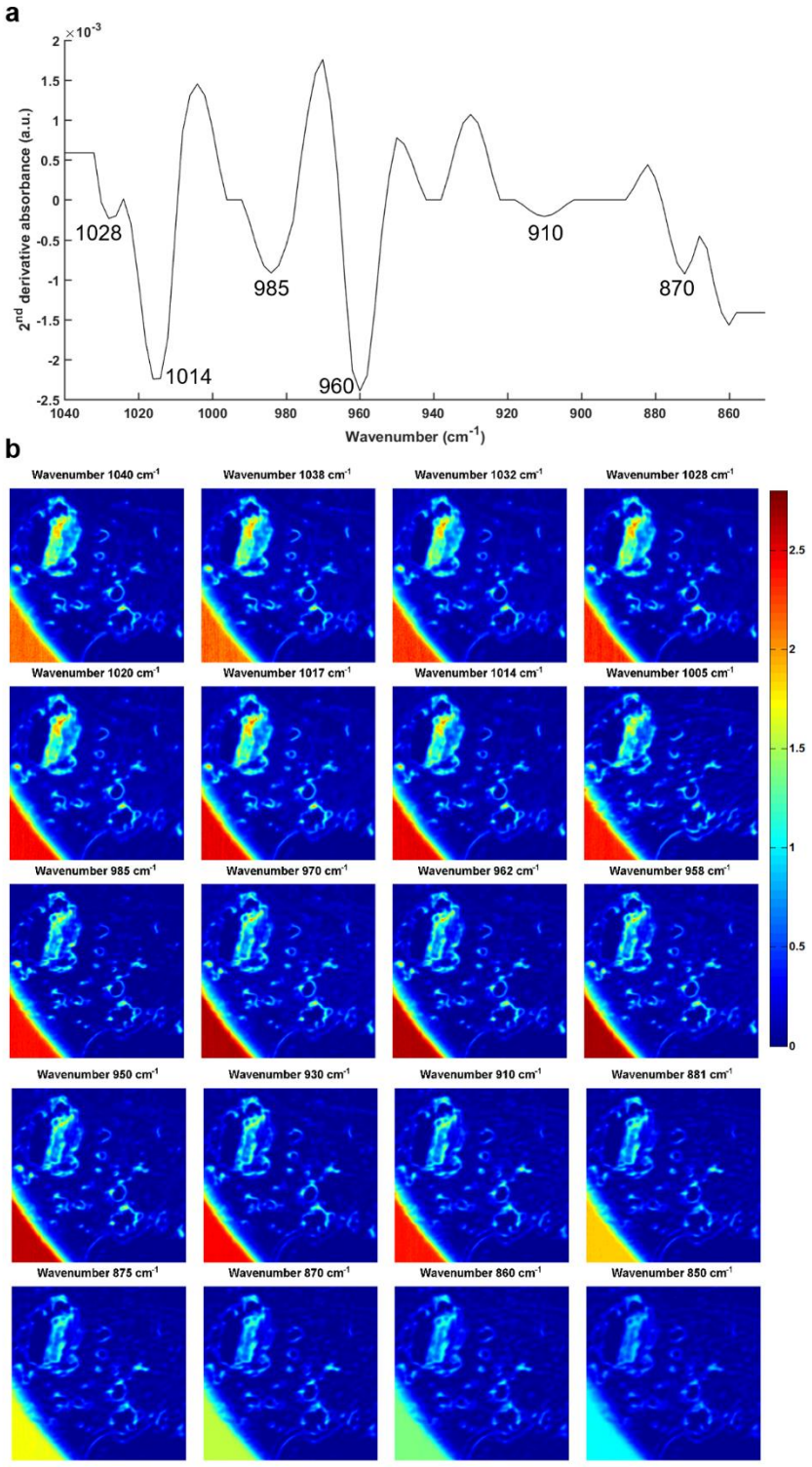

Figure E.3 (a) Second derivative spectrum of a microcalcification extracted from breast tissue section (DCIS stage). (b) Multispectral upconversion images obtained at 1040, 1038, 1032, 1028, 1020, 1017, 1014, 1005, 985, 970, 962, 958, 950, 930, 910, 875, 870, 860 and 850 cm^{-1}.

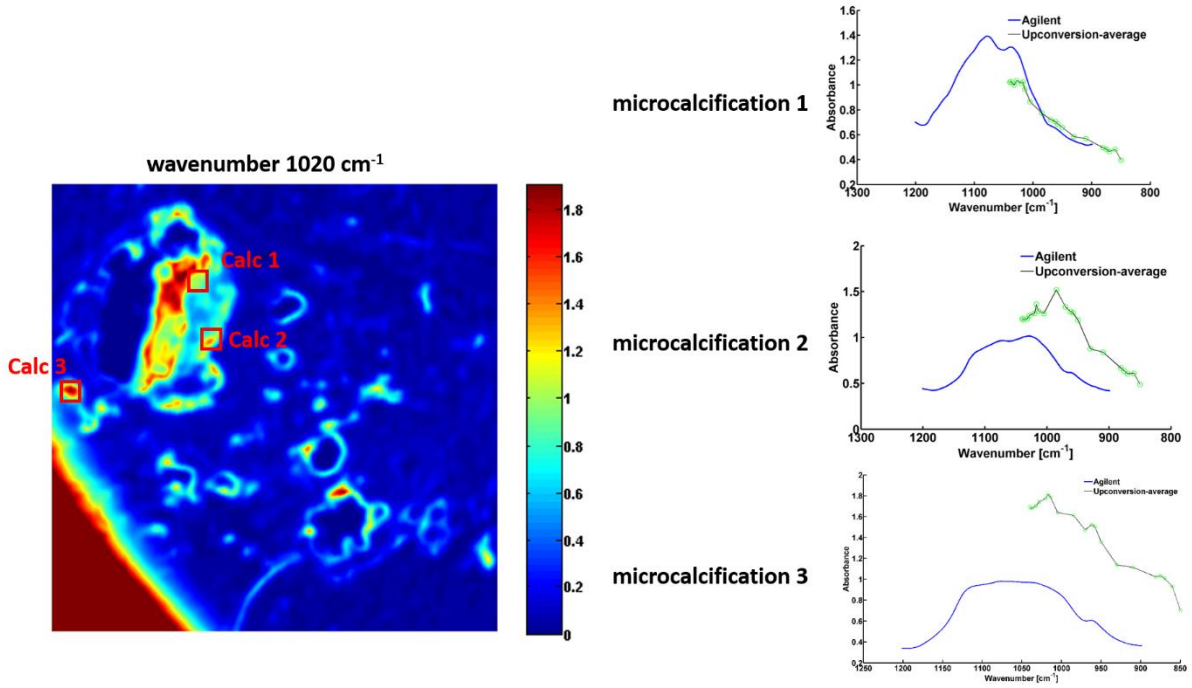

Figure E.4 Upconverted image of a microcalcification from breast tissue section obtained at 1020 cm^{-1}. Spectra recorded from three microcalcification areas (red squares) in the spectral range between 1200-900 cm^{-1} for the FTIR image (blue spectrum) and at 1040, 1038, 1032, 1028, 1020, 1017, 1014, 1005, 985, 970, 962, 958, 950, 930, 910, 875, 870, 860 and 850 cm^{-1} for the upconverted image (green spectrum).

F. Contributions

a. Papers

- S. Gosling, R. Scott, C. Greenwood, **P. Bouzy**, J. Nallala, I. D. Lyburn, N. Stone, K. Rogers,
  "Calcification Microstructure Reflects Breast Tissue Microenvironment," Journal of Mammary Gland Biology and Neoplasia 24(4):333–342, 2019. https://doi.org/10.1007/s10911-019-09441-3

- Y.-P. Tseng, **P. Bouzy**, C. Pedersen, N. Stone, P. Tidemand-Lichtenberg, "Upconversion raster scanning microscope for long-wavelength infrared imaging of breast cancer microcalcifications," Biomedical Optics Express 9/10, 4979 (2018). https://doi.org/10.1364/boe.9.004979

- Y.-P. Tseng, **P. Bouzy**, N. Stone, C. Pedersen, P. Tidemand-Lichtenberg, "Long wavelength identification of microcalcifications in breast cancer tissue using a quantum cascade laser and upconversion detection," Biomedical Vibrational Spectroscopy 2018: Advances in Research and Industry, 12, SPIE, San Francisco, 2018. http://dx.doi.org/10.1117/12.2290928

- C. Scotté, H. B. de Aguiar, D. Marguet, E. M. Green, **P. Bouzy**, S. Vergnole, C. P. Winlove, N. Stone, Hervé Rigneault,
  "Assessment of Compressive Raman versus Hyperspectral Raman for Microcalcification Chemical Imaging," Analytical chemistry, 90, 12, 7197-7203, 2018. https://doi.org/10.1021/acs.analchem.7b05303

b. Conferences

- Clircon17, Manchester, UK, 2-5 April 2017.

P. Bouzy, F. Palombo and N. Stone
"Spectroscopic tools for evaluating the content of carbonate substitution of Hydroxyapatite found in breast microcalcifications", Poster presentation (P39).

- Cleo Europe-EQEC, Conference on Lasers and Electro-Optics/Europe and the European Quantum Electronics Conference, Munich, Germany, 25-29 June 2017.

P. Bouzy, F. Palombo and N. Stone
"Spectroscopic tools for the elucidation of disease specific changes in breast cancer", Poster presentation (JSIII-P.4).

- OSA: High-brightness Sources and Light-driven Interactions Congress (MICS), Strasbourg, France, 26–28 March 2018.

P. Bouzy, Y-P. Tseng, C. Pedersen, P. Tidemand-Lichtenberg, F. Palombo, and N. Stone, "Advances in Mid-Infrared Spectroscopic Imaging for Analysis of Breast Cancer Associated Microcalcifications," Oral presentation (MT3C.8).

- 10th conference SPEC 2018, Glasgow, Scotland, 10-15 June 2018.

P. Bouzy, S. O'Grady, B. Gardner, A. Kohler, J. Solheim, F. Palombo, M. P. Morgan and N. Stone, "Assessment of Breast Cancer Cell Mineralisation Using Vibrational Spectroscopy", Oral presentation.

P. Bouzy, Y-P. Tseng, C. Pedersen, P. Tidemand-Lichtenberg, H. Madupali, M. M. J. Tecklenburg, F. Palombo, and N. Stone, "Novel Spectroscopic Tools for Analysis of Breast Cancer associated Microcalcifications," Poster presentation (78).

- San Antonio Breast Cancer Symposium (SABCS), San Antonio, USA, Dec. 2018.

P. Bouzy, S. O'Grady, F. Palombo, M. Morgan and N. Stone, "Exploring the relationship between an in vitro model of breast cancer cell mineralization and the cancer grade specific composition of ex vivo microcalcifications", Poster presentation (P06-01-03).

c. Summer schools as part of the Mid-TECH project

- Berlin, Germany, 29 February – 6 March 2016.

Purpose: Basics of physics of mid-IR light sources and mid-IR detection, Physics of key applications, limitations and options in mid-IR instrumentation, work on and solve real problems in these areas, both in a group and as individuals.

- Fredensborg, Denmark, 15-21 August 2016.

The course will cover entrepreneurship, linking technological inventions and applications to commercialisation. Prior to the Summer School, the PhD students will individually prepare a mid-IR case (a 1-page description of a mid-IR invention or application).

- Lake Windermere, UK, 4-7 July 2017.

Purpose: Fundamental spectroscopy with cutting edge clinical practice
Fundamentals of Infrared Spectroscopy, Spontaneous Raman Spectroscopy, Non-linear Raman Spectroscopy, experimental design, clinical problem solving sessions, spectrometer design, clinical perspectives, spectral Interpretation and chemometric analysis.

- Lund, Sweden, 18-21 June 2018.

Purpose: Basics of Molecular spectroscopy. Mini Mid-TECH seminars to provide a bird’s view of your ESR projects and new opportunities in the scientific field

References

[1] L. C. Collins and S. J. Schnitt, *Breast. 2012. Histology for pathologist, 4th edition, Stacey E. Mills pp.66-81.* 2012.

[2] R. A. Jesinger, “Breast anatomy for the interventionalist,” *Tech. Vasc. Interv. Radiol.*, vol. 17, no. 1, pp. 3–9, 2014.

[3] A. Waugh and A. Grant, *Anatomy and histology in Health and Illness. pp. 438-458.* 2002.

[4] R. D. Cardiff, P. M. Treuting, and H. J. Thompson, *23. Mammary Gland pp. 485-508*. Elsevier Inc., 2018.

[5] A. Stevens and J. Lowe, *Mammary gland. Histology. pp. 364-368*. 1992.

[6] R. L. Siegel, K. D. Miller, and A. Jemal, “Cancer statistics, 2018: Cancer Statistics, 2018,” *CA. Cancer J. Clin.*, vol. 68, no. 1, pp. 7–30, 2018.

[7] “www.cancerresearchuk.org,” *Breast cancer statistics*. .

[8] D. Hanahan and R. A. Weinberg, “Hallmarks of cancer: The next generation,” *Cell*, vol. 144, no. 5, pp. 646–674, 2011.

[9] H. J.Burstein, “Ductal carcinoma in situ of the breast,” *N. Engl. J. Med.*, 2004.

[10] T. Vargo-Gogola and J. M. Rosen, “Modelling breast cancer: One size does not fit all,” *Nat. Rev. Cancer*, vol. 7, no. 9, pp. 659–672, 2007.

[11] G. K. Malhotra, X. Zhao, H. Band, and V. Band, “Histological, molecular and functional subtypes of breast cancers,” *Cancer Biol. Ther.*, vol. 10, no. 10, pp. 955–960, 2010.

[12] D. C. Allred, “Ductal carcinoma in situ: Terminology, classification, and natural history,” *J. Natl. Cancer Inst. - Monogr.*, no. 41, pp. 134–138, 2010.

[13] H. Y. Wen and E. Brogi, “Lobular Carcinoma In Situ,” *Surg. Pathol. Clin.*, vol. 11, no. 1, pp. 123–145, 2018.

[14] C. W. Elston and I. O. Ellis, “Pathological prognostic factors in breast cancer: experience from a large study with long-term follow-up,” *Histopathology*, vol. 19, pp. 403–410, 1991.

[15] S.B. Edge, D.R. Byrd and C. Compton, *AJCC Cancer staging manual*, 7th Edition. Springer US, 2009.

[16] A. M. Kabel, “Tumor markers of breast cancer: New prospectives,” *J. Oncol. Sci.*, vol. 3, no. 1, pp. 5–11, 2017.

[17] M. T. Weigel and M. Dowsett, “Current and emerging biomarkers in breast cancer: Prognosis and prediction,” *Endocr. Relat. Cancer*, vol. 17, no. 4, pp. 245–262, 2010.

[18] S. M. Fragomeni, A. Sciallis, and J. S. Jeruss, “Molecular Subtypes and Local-Regional Control of Breast Cancer,” *Surg. Oncol. Clin. N. Am.*, vol. 27, no. 1, pp. 95–120, 2018.

[19] D. J. Slamon, G. M. Clark, S. G. Wong, W. J. Levin, A. Ullrich, and W. L. Mcguire, “Correlation Amplification,” *Science (80-.).*, vol. 235, no. 4785, pp. 177–182, 1987.

[20] P. Eroles, A. Bosch, J. Alejandro Pérez-Fidalgo, and A. Lluch, “Molecular biology in breast cancer: Intrinsic subtypes and signaling pathways,” *Cancer Treat. Rev.*, vol. 38, no. 6, pp. 698–707, 2012.

[21] B. Dai, X., Li, T., Bai, Z., Yang, Y., Xiuxia, L., Zhan, J., and Shi, “Breast cancer intrinsic subtype classification, clinical use and future trends,” *Am. J. Cancer Res.*, vol. 5, no. 10, pp. 2929–2943, 2015.

[22] Z. Kleibl and V. N. Kristensen, “Women at high risk of breast cancer: Molecular characteristics, clinical presentation and management,” *Breast*, vol. 28, pp. 136–144, 2016.

[23] R. A. Oldenburg, H. Meijers-Heijboer, C. J. Cornelisse, and P. Devilee, “Genetic susceptibility for breast cancer: How many more genes to be found?,” *Crit. Rev. Oncol. Hematol.*, vol. 63, no. 2, pp. 125–149, 2007.

[24] S. Obenauer, K. P. Hermann, and E. Grabbe, “Applications and literature review of the BI-RADS classification,” *Eur. Radiol.*, vol. 15, no. 5, pp. 1027–1036, 2005.

[25] T. Sharma, J. A. Radosevich, G. Pachori, and C. C. Mandal, “A Molecular View of Pathological Microcalcification in Breast Cancer,” *J. Mammary Gland Biol. Neoplasia*, vol. 21, no. 1–2, pp. 25–40, 2016.

[26] L. Tabár, B. Vitak, H. Chen, S. W. Duffy, M. Yen, C. Chiang, U. B. Krusemo, T. Tot, and R. A. Smith, “The Swedish Two-County Trial Twenty Years Later,” *Radiol. Clin. North Am.*, vol. 38, no. 4, pp. 625–651, 2000.

[27] L. W. Bassett and S. Lee-Felker, *Breast imaging screening and diagnosis*, Fifth Edit. Elsevier Inc., 2017.

[28] R. F. Cox and M. P. Morgan, “Microcalcifications in breast cancer: Lessons from physiological mineralization,” *Bone*, vol. 53, no. 2, pp. 437–450, 2013.

[29] M. Le Gal and G. Chavanne and D. Pellier, “Diagnostic value of clustered

microcalcifications discovered by mammography (apropos of 227 cases with histological verification and without a palpable breast tumor," *Bull Cancer*, vol. 71, no. 1, pp. 57–64, 1984.

[30] A. A. Rao, J. Feneis, C. Lalonde, and H. Ojeda-Fournier, "A pictorial review of changes in the BI-RADS fifth edition," *Radiographics*, vol. 36, no. 3, pp. 623–639, 2016.

[31] I. Cheikhrouhou, "Description et classification des masses mammaires pour le diagnostic du cancer du sein," University of Evry-Val d'Essonne, 2012.

[32] R. A. S. L. Tabar, H. T. Chen, M. F. A. Yen, T. Tot, T. Tung, L. chen, S. W. Duffy, "Mammographic tumor features can predict long-term outcomes reliably in women with 1-14-mm invasive breast carcinoma: Suggestions for the reconsideration of current therapeutic practice and the TNM classification system," *Cancer*, vol. 101, no. 8, pp. 1745–1759, 2004.

[33] P. L. Arancibia Hernández, T. Taub Estrada, A. López Pizarro, M. L. Díaz Cisternas, and C. Sáez Tapia, "Breast calcifications: Description and classification according to BI-RADS 5th edition," *Rev. Chil. Radiol.*, vol. 22, no. 2, pp. 80–91, 2016.

[34] L. Wilkinson, V. Thomas, and N. Sharma, "Microcalcification on mammography: Approaches to interpretation and biopsy," *Br. J. Radiol.*, vol. 90, no. 1069, 2017.

[35] J. F. L. Frappart, M. Boudeulle, j. Boumendil, H. C. Lin, I. Martinon, C. Palayer, Y. Mallet-Guy, D. Raudrant, A. Bremond, Y. Rochet, "Structure and composition of microcalcifications in benign and malignant lesions of the breast: study by light microscopy, transmission and scanning electron microscopy, microprobe analysis, and X-ray diffraction.," *Hum. Pathol.*, vol. 15, no. 9, pp. 880–889, 1984.

[36] G. Penel, G. Leroy, C. Rey, and E. Bres, "MicroRaman spectral study of the PO4and CO3vibrational modes in synthetic and biological apatites," *Calcif. Tissue Int.*, vol. 63, no. 6, pp. 475–481, 1998.

[37] M. M. Kerssens, P. Matousek, K. Rogers, and N. Stone, "Towards a safe non-invasive method for evaluating the carbonate substitution levels of hydroxyapatite (HAP) in micro-calcifications found in breast tissue," *Analyst*, vol. 135, no. 12, pp. 3156–3161, 2010.

[38] C. Combes, S. Cazalbou, and C. Rey, "Apatite biominerals," *Minerals*, vol. 6, no. 2, pp. 1–25, 2016.

[39] T. Kubota, A. Nakamura, K. Toyoura, and K. Matsunaga, "The effect of chemical

potential on the thermodynamic stability of carbonate ions in hydroxyapatite," *Acta Biomater.*, vol. 10, no. 8, pp. 3716–3722, 2014.

[40] I. Cacciotti, "Cationic and anionic substitutions in Hydroxyapatite," in *Handbook of Bioceramics and Biocomposites*, 2016, pp. 146–188.

[41] R. Scott, C. Kendall, N. Stone, and K. Rogers, "Elemental vs. phase composition of breast calcifications," *Sci. Rep.*, vol. 7, no. 1, 2017.

[42] M. Scimeca, E. Giannini, C. Antonacci, C. A. Pistolese, L. G. Spagnoli, and E. Bonanno, "Microcalcifications in breast cancer: An active phenomenon mediated by epithelial cells with mesenchymal characteristics," *BMC Cancer*, vol. 14, no. 1, pp. 1–10, 2014.

[43] N. Vidavsky, J.M.R. Kunitake, A. E. Chiou, P. A. Northrup, T. J. Porri, L. Ling, C. Fischbach, and L. A. Estroff, "Studying biomineralization pathways in a 3D culture model of breast cancer microcalcifications," *Biomaterials*, vol. 179, pp. 71–82, 2018.

[44] M. P. Morgan, M. M. Cooke, P. A. Christopherson, P. R. Westfall, and G. M. McCarthy, "Calcium hydroxyapatite promotes mitogenesis and matrix metalloproteinase expression in human breast cancer cell lines," *Mol. Carcinog.*, vol. 32, no. 3, pp. 111–117, 2001.

[45] M. M. Cooke, G. M. McCarthy, J. D. Sallis, and M. P. Morgan, "Phosphocitrate inhibits calcium hydroxyapatite induced mitogenesis and upregulation of matrix metalloproteinase-1, interleukin-1β and cyclooxygenase-2 mRNA in human breast cancer cell lines," *Breast Cancer Res. Treat.*, vol. 79, no. 2, pp. 253–263, 2003.

[46] J. H. Suh, J. M. Gardner, K. H. Kee, S. Shen, A. G. Ayala, and J. Y. Ro, "Calcifications in prostate and ejaculatory system: a study on 298 consecutive whole mount sections of prostate from radical prostatectomy or cystoprostatectomy specimens," *Ann. Diagn. Pathol.*, vol. 12, no. 3, pp. 165–170, 2008.

[47] A. N. Khan, H. H. Al-Jahdali, C. M. Allen, K. L. Irion, S. Al Ghanem, and S. S. Koteyar, "The calcified lung nodule: What does it mean," *Ann. Thorac. Med.*, vol. 5, no. 2, pp. 67–79, 2010.

[48] R. D. Monk and D. A. Bushinsky, "Nephrolithiasis and Nephrocalcinosis," *Compr. Clin. Nephrol.*, pp. 687–701, 2010.

[49] M. Richard, "Independent review of National Screeining Programmes in

England," 2019.

[50] "www.knowyourlemons.com." .

[51] NHS Breast screening programme, "Clinical guidance for breast cancer screening assessment."

[52] I. O. Ellis, S. Humphreys, M. Michell, S. E. Pinder, C. A. Wells, and H. D. Zakhour, "Guidelines for breast needle core biopsy handling and reporting in breast screening assessment," *J. Clin. Pathol.*, vol. 57, no. 9, pp. 897–902, 2004.

[53] R. Sathyavathi, A. Saha, J. S. Soares, N. Spegazzini, S. McGee, R. R. Dasari, M. Fitzmaurice, and I. Barman, "Raman spectroscopic sensing of carbonate intercalation in breast microcalcifications at stereotactic biopsy," *Sci. Rep.*, vol. 5, no. April, pp. 1–12, 2015.

[54] Z. S. Lima, M. R. Ebadi, G. Amjad, and L. Younesi, "Application of imaging technologies in breast cancer detection: A review article," *Open Access Maced. J. Med. Sci.*, vol. 7, no. 5, pp. 838–848, 2019.

[55] S. Radhakrishna, S., Agarwal, S., Parikh P. M., Kaur, K., Panwar , S., Sharma, S., Dey , A., Saxena, K. K., Chandra , M., and Sud, "Role of magnetic resonance imaging in breast cancer management," *South Asian J. cancer*, vol. 7, no. 2, pp. 69–71, 2018.

[56] R. Guo, G. Lu, B. Qin, and B. Fei, "Ultrasound Imaging Technologies for Breast Cancer Detection and Management: A Review," *Ultrasound Med. Biol.*, vol. 44, no. 1, pp. 37–70, 2018.

[57] I. Iakovou, E. Giannoula, A. Gkantaifi, S. Levva, and S. Frangos, "Positron emission tomography in breast cancer: 18F- FDG and other radiopharmaceuticals," *Eur. J. Hybrid Imaging*, vol. 2, no. 1, 2018.

[58] J. Vercher-Conejero,L. Pelegrí-Martinez, D. Lopez-Aznar, and M. Cózar-Santiago, "Positron Emission Tomography in Breast Cancer," *Diagnostics*, vol. 5, no. 1, pp. 61–83, Mar. 2015.

[59] R. Baker, K. D. Rogers, N. Shepherd, and N. Stone, "New relationships between breast microcalcifications and cancer," *Br. J. Cancer*, vol. 103, no. 7, pp. 1034–1039, 2010.

[60] A. S. Haka, K. E. Shafer-peltier, M. Fitzmaurice, J. Crowe, R. R. Dasari, and M. S. Feld, "Identifying Microcalcifications in Benign and Malignant Breast Lesions by Probing Differences in Their Chemical Composition Using Raman

Spectroscopy 1," pp. 5375–5380, 2002.

[61] A. Ghita, P. Matousek, and N. Stone, "High sensitivity non-invasive detection of calcifications deep inside biological tissue using Transmission Raman Spectroscopy," *J. Biophotonics*, vol. 11, no. 1, pp. 1–8, 2018.

[62] P. Matousek and N. Stone, "Prospects for the diagnosis of breast cancer by noninvasive probing of calcifications using transmission Raman spectroscopy," *J. Biomed. Opt.*, vol. 12, no. 2, p. 024008, 2007.

[63] P. Matousek and N. Stone, "Development of deep subsurface Raman spectroscopy for medical diagnosis and disease monitoring," *Chem. Soc. Rev.*, vol. 45, no. 7, pp. 1794–1802, 2016.

[64] K. Yeh, S. Kenkel, J. N. Liu, and R. Bhargava, "Fast infrared chemical imaging with a quantum cascade laser," *Anal. Chem.*, vol. 87, no. 1, pp. 485–493, 2015.

[65] L. M. Kehlet, N. Sanders, P. Tidemand-Lichtenberg, J. S. Dam, and C. Pedersen, "Infrared hyperspectral upconversion imaging using spatial object translation," *Opt. Express*, vol. 23, no. 26, p. 34023, 2015.

[66] M. J. Baker, H. J. Byrne, J. Chalmers, P. Gardner, R. Goodacre, A. Henderson, S. G. Kazarian, F. L. Martin, J. Moger, N. Stone, and J. Sulé-Suso, "Clinical applications of infrared and Raman spectroscopy: State of play and future challenges," *Analyst*, vol. 143, no. 8, pp. 1735–1757, 2018.

[67] M. H. Lyng, Fiona M., Traynor, Damien, Nguyen, Thi Nguyet Que, Meade, Aidan D., Rakib, Fazle, Al-Saady, Rafif, Goormaghtigh, Erik, Al-Saad, Khalid, Ali, "Discrimination of breast cancer from benign tumours using Raman spectroscopy," *PLoS One*, vol. 14, no. 2, pp. 1–13, 2019.

[68] K. Buckley, P. Matousek, A. W. Parker, and A. E. Goodship, "Raman spectroscopy reveals differences in collagen secondary structure which relate to the levels of mineralisation in bones that have evolved for different functions," *J. Raman Spectrosc.*, vol. 43, no. 9, pp. 1237–1243, 2012.

[69] S. J. Smith, R. Emery, A. Pitsillides, C. E. Clarkin, and S. Mahajan, "Detection of early osteogenic commitment in primary cells using Raman spectroscopy," *Analyst*, vol. 142, no. 11, pp. 1962–1973, 2017.

[70] E. Brauchle, D. Carvajal Berrio, M. Rieger, K. Schenke-Layland, S. Reinert, and D. Alexander, "Raman Spectroscopic Analyses of Jaw Periosteal Cell Mineralization," *Stem Cells Int.*, vol. 2017, 2017.

[71] A. C. S. Talari, C. A. Evans, I. Holen, R. E. Coleman, and I. U. Rehman, "Raman

spectroscopic analysis differentiates between breast cancer cell lines," *J. Raman Spectrosc.*, vol. 46, no. 5, pp. 421–427, 2015.

[72] N. Tkachenko, "Optical spectroscopy: methods and instrumentations," *Opt. Spectrosc. Methods Instrumentations*, pp. 15–38, 2006.

[73] Y.-P. Tseng, C. Pedersen, and P. Tidemand-Lichtenberg, "Upconversion detection of long-wave infrared radiation from a quantum cascade laser," *Opt. Mater. Express*, vol. 8, no. 5, p. 1313, 2018.

[74] L. L. McManus, F. Bonnier, G. A. Burke, B. J. Meenan, A. R. Boyd, and H. J. Byrne, "Assessment of an osteoblast-like cell line as a model for human primary osteoblasts using Raman spectroscopy," *Analyst*, vol. 137, no. 7, pp. 1559–1569, 2012.

[75] J. H. Solheim, E. Gunko, D. Petersen, F. Großerüschkamp, K. Gerwert, and A. Kohler, "An open-source code for Mie extinction extended multiplicative signal correction for infrared microscopy spectra of cells and tissues," *J. Biophotonics*, vol. 12, no. 8, pp. 1–14, 2019.

[76] P. Bassan, A. Kohler, H. Martens, J. Lee, H. J. Byrne, P. Dumas, E. Gazi, M. Brown, N. Clarke, and P. Gardner, "Resonant Mie Scattering (RMieS) correction of infrared spectra from highly scattering biological samples," *Analyst*, vol. 135, no. 2, pp. 268–277, 2010.

[77] R. G. Brereton, "Introduction to multivariate calibration in analytical chemistry," *Analyst*, vol. 125, no. 11, pp. 2125–2154, 2000.

[78] R. D. Tobias, "An introduction to Partial Least Squares Regression," *Mathemathics*, pp. 1–8, 1996.

[79] R. Z. LeGeros, "Apatites in biological systems," *Prog. Cryst. Growth Charact.*, vol. 4, no. 1–2, pp. 1–45, 1981.

[80] R. Z. LeGeros, "Formation and transformation of calcium phosphates: Relevance to vascular calcification," *Z. Kardiol.*, vol. 90, no. SUPPL. 3, pp. 116–124, 2001.

[81] T. Sakae, H. Nakada, and J. P. LeGeros, "Historical review of biological apatite crystallography," *J. Hard Tissue Biol.*, vol. 24, no. 2, pp. 111–122, 2015.

[82] R. Z. Legeros and J. P. Legeros, "Phosphate minerals in human tissues.," *Phosphate Miner.*, pp. 351–385, 1984.

[83] O. Gourgas, J. Marulanda, P. Zhang, M. Murshed, and M. Cerruti, "Multidisciplinary Approach to Understand Medial Arterial Calcification,"

Arterioscler. Thromb. Vasc. Biol., vol. 38, no. 2, pp. 363–372, 2018.

[84] A. McIntyre and A. L. Harris, “The role of pH regulation in Cancer Progression,” vol. 207, pp. 135–156, 2016.

[85] M. Damaghi, J. W. Wojtkowiak, and R. J. Gillies, “pH sensing and regulation in cancer,” *Front. Physiol.*, vol. 4 DEC, no. December, pp. 1–10, 2013.

[86] E. P. Paschalis, E. DiCarlo, F. Betts, P. Sherman, R. Mendelsohn, and A. L. Boskey, “FTIR microspectroscopic analysis of human osteonal bone,” *Calcif. Tissue Int.*, vol. 59, no. 6, pp. 480–487, 1996.

[87] M. M. Figueiredo, J. A. F. Gamelas, and A. G. Martins, “Characterization of Bone and Bone-Based Graft Materials Using FTIR Spectroscopy,” *Infrared Spectrosc. - Life Biomed. Sci.*, no. April, 2012.

[88] F. Z. Ren and Y. Leng, “Carbonated Apatite, Type-A or Type-B?,” *Key Eng. Mater.*, vol. 493–494, pp. 293–297, 2011.

[89] N. Pleshko, A. Boskey, and R. Mendelsohn, “Novel infrared spectroscopic method for the determination of crystallinity of hydroxyapatite minerals,” *Biophys. J.*, vol. 60, no. 4, pp. 786–793, 1991.

[90] H. Ou-Yang, E. P. Paschalis, W. E. Mayo, A. L. Boskey, and R. Mendelsohn, “Infrared microscopic imaging of bone: Spatial distribution of CO3-2-,” *J. Bone Miner. Res.*, vol. 16, no. 5, pp. 893–900, 2001.

[91] C. Rey, O. Marsan, C. Combes, C. Drouet, D. Grossin, and S. Sarda, *Characterization of Calcium Phosphates Using Vibrational Spectroscopies*, vol. 2, no. June 2016. 2014.

[92] J. A. Stammeier, B. Purgstaller, D. Hippler, V. Mavromatis, and M. Dietzel, “In-situ Raman spectroscopy of amorphous calcium phosphate to crystalline hydroxyapatite transformation,” *MethodsX*, vol. 5, no. July, pp. 1241–1250, 2018.

[93] P. Nandha Kumar, S. K. Mishra, and S. Kannan, “Structural Perceptions and Mechanical Evaluation of β-Ca3(PO4)2/c-CeO2 Composites with Preferential Occupancy of Ce3+ and Ce4+,” *Inorg. Chem.*, vol. 56, no. 6, pp. 3600–3611, 2017.

[94] B. O. Fowler, M. Marković, and W. E. Brown, “Octacalcium Phosphate. 3. Infrared and Raman Vibrational Spectra,” *Chem. Mater.*, vol. 5, no. 10, pp. 1417–1423, 1993.

[95] G. R. Sauer and R. E. Wuthier, “Fourier transform infrared characterization of

mineral phases formed during induction of mineralization by collagenase-released matrix vesicles in vitro," *J. Biol. Chem.*, vol. 263, no. 27, pp. 13718–13724, 1988.

[96] G. R. Sauer, W. B. Zunic, J. R. Durig, and R. E. Wuthier, "Fourier transform raman spectroscopy of synthetic and biological calcium phosphates," *Calcif. Tissue Int.*, vol. 54, no. 5, pp. 414–420, 1994.

[97] A. P. Duarte Moreira, M. Soares Sader, G. D. De Almeida Soares, and M. H. M. R. Leão, "Strontium incorporation on microspheres of alginate/β-tricalcium phosphate as delivery matrices," *Mater. Res.*, vol. 17, no. 4, pp. 967–973, 2014.

[98] S. J. Gadaleta, E. P. Paschalis, F. Betts, R. Mendelsohn, and A. L. Boskey, "Fourier transform infrared spectroscopy of the solution-mediated conversion of amorphous calcium phosphate to hydroxyapatite: New correlations between X-ray diffraction and infrared data," *Calcif. Tissue Int.*, vol. 58, no. 1, pp. 9–16, 1996.

[99] H. Boyar, B. Turan, and F. Severcan, "FTIR spectroscopic investigation of mineral structure of streptozotocin induced diabetic rat femur and tibia," *Spectroscopy*, vol. 17, no. 2–3, pp. 627–633, 2003.

[100] H. Madupalli, B. Pavan, and M. M. J. Tecklenburg, "Carbonate substitution in the mineral component of bone: Discriminating the structural changes, simultaneously imposed by carbonate in A and B sites of apatite," *J. Solid State Chem.*, vol. 255, no. May, pp. 27–35, 2017.

[101] C. Rey, B. Collins, T. Goehl, I. R. Dickson, and M. J. Glimcher, "The carbonate environment in bone mineral: A resolution-enhanced fourier transform infrared spectroscopy study," *Calcif. Tissue Int.*, vol. 45, no. 3, pp. 157–164, 1989.

[102] A. Antonakos, E. Liarokapis, and T. Leventouri, "Micro-Raman and FTIR studies of synthetic and natural apatites," *Biomaterials*, vol. 28, no. 19, pp. 3043–3054, 2007.

[103] A. Awonusi, M. D. Morris, and M. M. J. Tecklenburg, "Carbonate assignment and calibration in the Raman spectrum of apatite," *Calcif. Tissue Int.*, vol. 81, no. 1, pp. 46–52, 2007.

[104] E. Stewart, S., Shea, D. A., Tarnowski, C. P., Morris, M. D., Wang, D., Franceschi, R., Lin, D. L., Keller, "Trends in early mineralization of murine calvarial osteoblastic cultures: A Raman microscopic study," *J. Raman Spectrosc.*, vol. 33, no. 7, pp. 536–543, 2002.

[105] A. S. Haka, K. E. Shafer-Peltier, M. Fitzmaurice, J. Crowe, R. R. Dasari, and M. S. Feld, “Identifying microcalcifications in benign and malignant breast lesions by probing differences in their chemical composition using raman spectroscopy,” *Cancer Res.*, vol. 62, no. 18, pp. 5375–5380, 2002.

[106] Z. Movasaghi, S. Rehman, and I. U. Rehman, “Raman spectroscopy of biological tissues,” *Appl. Spectrosc. Rev.*, vol. 42, no. 5, pp. 493–541, 2007.

[107] Y. Chen, J. Dai, X. Zhou, Y. Liu, W. Zhang, and G. Peng, “Raman spectroscopy analysis of the biochemical characteristics of molecules associated with the malignant transformation of gastric mucosa,” *PLoS One*, vol. 9, no. 4, 2014.

[108] P. Gao, B. Han, Y. Du, G. Zhao, Z. Yu, W. Xu, C. Zheng, Z. Fan, “The Clinical Application of Raman Spectroscopy for Breast Cancer Detection,” *J. Spectrosc.*, vol. 2017, no. 1, 2017.

[109] B. Brozek-Pluska, J. Musial, R. Kordek, E. Bailo, T. Dieing, and H. Abramczyk, “Raman spectroscopy and imaging: Applications in human breast cancer diagnosis,” *Analyst*, vol. 137, no. 16, pp. 3773–3780, 2012.

[110] E. Ó Faoláin, M. B. Hunter, J. M. Byrne, P. Kelehan, M. McMamara, H. J. Byrne, F. M. Lyng, “A study examining the effects of tissue processing on human tissue sections using vibrational spectroscopy,” *Vib. Spectrosc.*, vol. 38, no. 1–2, pp. 121–127, 2005.

[111] L. Fernández-Carrasco, D. Torrens-Martín, L. M. Morales, and S. Martínez-Ramírez, “Infrared Spectroscopy in the Analysis of Building and Construction Materials,” *Infrared Spectrosc. - Mater. Sci. Eng. Technol.*, 2012.

[112] E. Landi, G. Celotti, G. Logroscino, and A. Tampieri, “Carbonated hydroxyapatite as bone substitute,” *J. Eur. Ceram. Soc.*, vol. 23, no. 15, pp. 2931–2937, 2003.

[113] J. Kunitake, S. Choi, K. X. Nguyen, M. M. Lee, F. He, D. Sudilovsky, P. G. Morris, M. S. Jochelson, C. A. Hudis, D. A. Muller, P. Fratzl, C. Fischbach, A. Masic, L. A. Estroff, “Correlative imaging reveals physiochemical heterogeneity of microcalcifications in human breast carcinomas,” *J. Struct. Biol.*, vol. 202, no. 1, pp. 25–34, 2018.

[114] R. Scott, N. Stone, C. Kendall, K. Geraki, and K. Rogers, “Relationships between pathology and crystal structure in breast calcifications: An in situ X-ray diffraction study in histological sections,” *npj Breast Cancer*, vol. 2, no. 1, pp. 1–6, 2016.

[115] R. Scott, C. Kendall, N. Stone, and K. Rogers, “Locating microcalcifications in breast histopathology sections using micro CT and XRF mapping,” *Anal. Methods*, vol. 6, no. 12, pp. 3962–3966, 2014.

[116] P. S. Hung, Y. C. Kuo, H. G. Chen, H. H. K. Chiang, and O. K. S. Lee, “Detection of Osteogenic Differentiation by Differential Mineralized Matrix Production in Mesenchymal Stromal Cells by Raman Spectroscopy,” *PLoS One*, vol. 8, no. 5, pp. 1–7, 2013.

[117] F. Langenbach, J. Handschel, “Effects of dexamethasone, ascorbic acid and β-glycerophosphate on the osteogenic differentiation of stem cells in vitro,” *Stem Cell Res. Ther.*, vol. 4, no. 5, p. 1, 2013.

[118] R. F. Cox, A. Hernandez-Santana, S. Ramdass, G. McMahon, J. H. Harmey, and M. P. Morgan, “Microcalcifications in breast cancer: Novel insights into the molecular mechanism and functional consequence of mammary mineralisation,” *Br. J. Cancer*, vol. 106, no. 3, pp. 525–537, 2012.

[119] S. O’Grady and M. P. Morgan, “Deposition of calcium in an in vitro model of human breast tumour calcification reveals functional role for ALP activity, altered expression of osteogenic genes and dysregulation of the TRPM7 ion channel,” *Sci. Rep.*, vol. 9, no. 1, pp. 1–12, 2019.

[120] R. F. Cox, A. Jenkinson, K. Pohl, F. J. O’Brien, and M. P. Morgan, “Osteomimicry of mammary adenocarcinoma cells in vitro; increased expression of bone matrix proteins and proliferation within a 3D collagen environment,” *PLoS One*, vol. 7, no. 7, 2012.

[121] C. A. Gregory, W. G. Gunn, A. Peister, and D. J. Prockop, “An Alizarin red-based assay of mineralization by adherent cells in culture: Comparison with cetylpyridinium chloride extraction,” *Anal. Biochem.*, vol. 329, no. 1, pp. 77–84, 2004.

[122] C. J. Frank, R. L. McCreary, and D. C. B. Redd, “Raman Spectroscopy of Normal and Diseased Human Breast Tissues,” *Anal. Chem.*, vol. 67, no. 5, pp. 777–783, 1995.

[123] J. Vongsvivut, D. Pérez-Guaita, B. Wood, P. Heraud, K. Khambatta, D. Hartnell, M. Hackett and M. Tobin, “Synchrotron macro ATR-FTIR microspectroscopy for high-resolution chemical mapping of single cells,” *Analyst*, vol. 144, no. 10, pp. 3226–3238, 2019.

[124] J. D. Schuttlefield and V. H. Grassian, “ATR-FTIR spectroscopy in the

undergraduate chemistry laboratory part I: Fundamentals and examples," *J. Chem. Educ.*, vol. 85, no. 2, pp. 279–281, 2008.

[125] M., Kansiz and C., Marcott, "Submicron simultaneous IR and Raman microscopy (IR+Raman): breakthrough developments in Optical Photothermal IT (O-PTIR) combined with Raman provide new capabilities," in *Proceedings of SPIE 11200*, 2020, no. December 2019, pp. 2019–2021.

[126] G.S. Mandair and M.D. Morris, "Contributions of Raman spectroscopy to the understanding of bone strength," *Bonekey Rep.*, vol. 4, no. January, pp. 1–8, 2015.

[127] N. J. Crane, V. Popescu, M. D. Morris, P. Steenhuis, and M. A. Ignelzi, "Raman spectroscopic evidence for octacalcium phosphate and other transient mineral species deposited during intramembranous mineralization," *Bone*, vol. 39, no. 3, pp. 434–442, 2006.

[128] S., Gosling, R., Scott, C., Greenwood, P., Bouzy, J., Nallala, I. D., Lyburn, N., Stone, K., Rogers, "Calcification Microstructure Reflects Breast Tissue Microenvironment," *J. Mammary Gland Biol. Neoplasia*, vol. 2, 2019.

[129] A. Zoladek, F. C. Pascut, P. Patel, and I. Notingher, "Non-invasive time-course imaging of apoptotic cells by confocal Raman micro-spectroscopy," *J. Raman Spectrosc.*, vol. 42, no. 3, pp. 251–258, 2011.

[130] L. M. Miller and P. Dumas, "Chemical imaging of biological tissue with synchrotron infrared light," *Biochim. Biophys. Acta - Biomembr.*, vol. 1758, no. 7, pp. 846–857, 2006.

[131] G. Theophilou, C. L. M. Morais, D. E. Halliwell, K. M. G. Lima, J. Drury, P. L. Martin-Hirsch, H. F. Stringfellow, D. K. Hapangama, and F. L. Martin, "Synchrotron- and focal plane array-based Fourier-transform infrared spectroscopy differentiates the basalis and functionalis epithelial endometrial regions and identifies putative stem cell regions of human endometrial glands," *Anal. Bioanal. Chem.*, vol. 410, no. 18, pp. 4541–4554, 2018.

[132] N. Benseny-Cases, E. Álvarez-Marimon, H. Castillo-Michel, M. Cotte, C. Falcon, and J. Cladera, "Synchrotron-Based Fourier Transform Infrared Microspectroscopy (μFTIR) Study on the Effect of Alzheimer's Aβ Amorphous and Fibrillar Aggregates on PC12 Cells," *Anal. Chem.*, vol. 90, no. 4, pp. 2772–2779, 2018.

[133] J. Doherty, A. Raoof, A. Hussain, M. Wolna, G. Cinque, M. Brown, P. Gardner,

and J. Denbigh, “Live single cell analysis using synchrotron FTIR microspectroscopy: Development of a simple dynamic flow system for prolonged sample viability,” *Analyst*, vol. 144, no. 3, pp. 997–1007, 2019.

[134] J. M. Dudley and G. Genty, “Supercontinuum light,” *Phys. Today*, vol. 66, no. 7, pp. 29–34, 2013.

[135] F. Borondics, M. Jossent, C. Sandt, L. Lavoute, D. Gaponov, A. Hideur, P. Dumas, and S. Février, “Supercontinuum-based Fourier transform infrared spectromicroscopy,” *Optica*, vol. 5, no. 4, p. 378, 2018.

[136] C. R., Petersen, N., Prtljaga, M. Farries, J. Ward, B., Napier, G. R., Lloyd, J., Nallala, N., Stone, and O., Bang, “Mid-infrared multispectral tissue imaging using a chalcogenide fiber supercontinuum source,” *Opt. Lett.*, vol. 43, no. 5, p. 999, 2018.

[137] N., Kröger-Lui, N., Gretz, K., Haase, B., Kränzlin, S., Neudecker, A., Pucci, A., Regenscheit, A., Schönhals, and W., Petrich, “Rapid identification of goblet cells in unstained colon thin sections by means of quantum cascade laser-based infrared microspectroscopy,” *Analyst*, vol. 140, no. 7, pp. 2086–2092, 2015.

[138] B. Bird and J. Rowlette, “High definition infrared chemical imaging of colorectal tissue using a Spero QCL microscope,” *Analyst*, vol. 142, no. 8, pp. 1381–1386, 2017.

[139] M. J. Pilling, A. Henderson, and P. Gardner, “Quantum Cascade Laser Spectral Histopathology: Breast Cancer Diagnostics Using High Throughput Chemical Imaging,” *Anal. Chem.*, vol. 89, no. 14, pp. 7348–7355, 2017.

[140] S. Mittal, K. Yeh, L. Suzanne Leslie, S. Kenkel, A. Kajdacsy-Balla, and R. Bhargava, “Simultaneous cancer and tumor microenvironment subtyping using confocal infrared microscopy for all-digital molecular histopathology,” *Proc. Natl. Acad. Sci. U. S. A.*, vol. 115, no. 25, pp. E5651–E5660, 2018.

[141] Y. P. Tseng, P. Bouzy, N. Stone, C. Pedersen, and P. Tidemand-Lichtenberg, “Long wavelength identification of microcalcifications in breast cancer tissue using a quantum cascade laser and upconversion detection,” in *Progress in Biomedical Optics and Imaging - Proceedings of SPIE*, 2018, vol. 10490.

[142] S. Ran, S. Berisha, R. Mankar, W.-C. Shih, and D. Mayerich, “Mitigating fringing in discrete frequency infrared imaging using time-delayed integration,” *Biomed. Opt. Express*, vol. 9, no. 2, p. 832, 2018.

[143] Y.-P. Tseng, P. Bouzy, C. Pedersen, N. Stone, and P. Tidemand-Lichtenberg,

"Upconversion raster scanning microscope for long-wavelength infrared imaging of breast cancer microcalcifications," *Biomed. Opt. Express*, vol. 9, no. 10, p. 4979, 2018.

[144] A., Ogunleke, V., Bobroff, H. H., Chen, J. Rowlette, M., Delugin, B., Recur, Y., Hwu and C. Petibois, "Fourier-transform vs. quantum-cascade-laser infrared microscopes for histo-pathology: From lab to hospital?," *TrAC - Trends Anal. Chem.*, vol. 89, pp. 190–196, 2017.

[145] C. Kuepper, A. Kallenbach-Thieltges, H. Juette, A. Tannapfel, F. Großerueschkamp, and K. Gerwert, "Quantum Cascade Laser-Based Infrared Microscopy for Label-Free and Automated Cancer Classification in Tissue Sections," *Sci. Rep.*, vol. 8, no. 1, pp. 1–10, 2018.

[146] V. K. Varma, A. Kajdacsy-Balla, S. Akkina, S. Setty, and M. J. Walsh, "Predicting Fibrosis Progression in Renal Transplant Recipients Using Laser-Based Infrared Spectroscopic Imaging," *Sci. Rep.*, vol. 8, no. 1, pp. 1–6, 2018.

[147] R.Z., Legeros, R.O. Trautz, J.P., Legeros, E. Klein and P. Shirra, "Apatite crystallites: Effects of Carbonate on Morphologgy," *Science (80-.).*, vol. 155, no. 3768, pp. 1409–1411, 1967.

[148] P. W. Brown, "Calcium Phosphates in Biomedical Engenieering," in *Encyclopedia of materials: Science and Technology*, 2001, pp. 893–898.

[149] M. P. Morgan, M. M. Cooke, and G. M. McCarthy, "Microcalcifications associated with breast cancer: An epiphenomenon or biologically significant feature of selected tumors?," *J. Mammary Gland Biol. Neoplasia*, vol. 10, no. 2, pp. 181–187, 2005.

[150] M.J., Favus, D.A., Bushinsky D.A., and J., Lemann, "Regulation of calcium, magnesium, and phosphate metabolism," *Disord. Bone Miner. Metab.*, pp. 76–117, 2006.

[151] O. Suzuki, *Evolution of octacalcium phosphate biomaterials*, no. 1. LTD, 2020.

[152] A. Lotsari, A. K. Rajasekharan, M. Halvarsson, and M. Andersson, "Transformation of amorphous calcium phosphate to bone-like apatite," *Nat. Commun.*, vol. 9, no. 1, 2018.

[153] M. S. A. Johnsson and G. H. Nancollas, "The role of Brushite and octacalcium phosphate in apatite formation," *Crit. Rev. Oral Biol. Med.*, vol. 3, no. 1–2, pp. 61–82, 1992.

[154] D. dos S. Tavares, L. D. O. Castro, G. D. de A. Soares, G. G. Alves, and J. M.

Granjeiro, “Synthesis and cytotoxicity evaluation of granular magnesium substituted β-tricalcium phosphate,” *J. Appl. Oral Sci.*, vol. 21, no. 1, pp. 37–42, 2013.

[155] J. Mansfield, J. Moger, E. Green, C. Moger, and C. P. Winlove, “Chemically specific imaging and in-situ chemical analysis of articular cartilage with stimulated raman scattering,” *J. Biophotonics*, vol. 6, no. 10, pp. 803–814, 2013.

[156] A. Jabłońska-Trypuć, M. Matejczyk, and S. Rosochacki, “Matrix metalloproteinases (MMPs), the main extracellular matrix (ECM) enzymes in collagen degradation, as a target for anticancer drugs,” *J. Enzyme Inhib. Med. Chem.*, vol. 31, pp. 177–183, 2016.